Hydroxyl Airglow Temperatures above Davis Station, Antarctica

W. John R. French. B.Sc (Hons)

William John Reginald

Submitted in fulfilment of the

requirements

for the Degree of

DOCTOR OF PHILOSOPHY

IASOS

in the

UNIVERSITY OF TASMANIA

and the

AUSTRALIAN ANTARCTIC DIVISION

September, 2001

Declaration

This thesis contains no material which has been accepted for a degree or diploma by the University of Tasmania or any other tertiary institution, and, to the best of the author's knowledge and belief, it contains no material previously published or written by another person, except where due reference is made in the text.

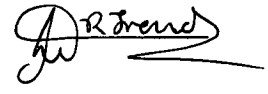

W. John R. French

18-Sep-01

Authority of Access

I consent to this thesis being made available for loan and limited copying in accordance with the Copyright Act 1968.

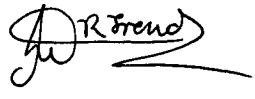

W. John. R. French

18-Sep-01

Abstract

The hydroxyl airglow (6-2) band has been monitored above Davis station, Antarctica (68.6°S, 78.0°E) by means of a Czerny-Turner spectrometer since 1990. This thesis is an investigation of the long-term trends and variability in OH(6-2) rotational-temperatures over an 11 year time span.

Tropospheric warming, due to increased greenhouse gases concentrations over the last 150 years, is expected to be associated with enhanced cooling in the stratosphere and mesosphere. Modelling studies indicate a maximum cooling response in the high latitude mesosphere. Some reported observations suggest that pronounced cooling, (up to 7 K/decade) in excess of model predictions, has already taken place.

Hydroxyl airglow emissions originate near 87 km. The layer is ideally located to monitor mesopause region temperatures by ground based spectroscopic means. The Davis OH(6-2) database contains 8 years of observations that span 1990 to 2000; over 126,000 spectra, which yield 1310 nightly averages. Observations are limited by day length at Davis. Night-time observations are possible between day-of-year 45 (14-Feb) and 300 (27-Oct).

Analysis techniques are developed to optimise the rotational temperature determinations for the $P_1(2)$, $P_1(4)$ and $P_1(5)$ ratio's in this band for climate change studies. Precise calibration of the instrument spectral response is important for long-term trend assessment. Inter-year spectral response variation of less than 0.3% has been achieved. Temperature errors associated with the response calibration amount to 1.5 K for earlier years and less than 0.3 K since 1996.

A detailed investigation of auroral and OH satellite line emissions, solar Fraunhofer and water vapour absorption across the OH(6-2) region (λ837.5-851.5 nm) is undertaken. These features can modify the apparent intensity of the P-branch lines. $P_1(3)$ is rejected from further analysis due to un-thermalised contributions from the OH(5-1)$P_1(12)$ lines. A correction is applied to account for the $Q_1(5)$ contribution under $P_1(2)$. N_2 1PG and N_2^+ Meinel auroral emissions and solar Fraunhofer absorption are accounted for by appropriate selection of the backgrounds for each line. Water vapour absorption is not found to be significant. Correction factors are also applied to account for the difference in Λ-doubling between the P-branch lines. These are derived from frequency-stabilised laser determinations of the instrument bandwidth (which is 0.15nm). Errors associated with each correction are assessed.

Serendipitously, auroral emissions due to atmospheric Argon are identified for the first time in this investigation. Two argon lines (at λ840.82 nm and λ842.46 nm, between $P_1(2)$ and $P_1(3)$) are apparent during intense auroral activity but do not influence the rotational temperatures at the resolution of the Davis instrument.

As a scanning instrument is used, a 'sampling' error is also associated with the time taken to acquire each spectrum due to possible intensity variations. A mean trend of –1.1 K due to an average intensity decrease across the night, with a 7 K standard deviation is found from coincident photometer observations. As a result of the investigation of background features, acquisition times were reduced from the order of 1 hour (in 1990) to 7.3 minutes (from the end of 1996) by scanning only selected P-branch lines and background regions, which reduces the standard deviation. Furthermore, an analysis technique for time interpolation of sampled branch lines and backgrounds between spectra is developed, which removes the trend component.

Three sets of published transitions probabilities yield a 12 K range in the absolute temperature derived. An experimental investigation of OH(6-2) Q_1/P_1 and R_1/P_1 emission intensity ratios, for rotational states up to j'=4.5, is undertaken to determine which set is most suitable for application to the OH(6-2) band.

Selection criteria are established to reject spectra that do not yield consistent temperatures for each of the three possible ratios, suffer low signal-to-noise, or are contaminated by strong aurora, scattered moonlight or changing cloud conditions.

Nightly averages are determined from spectra that pass all criteria. Annual variations are characterised by an extended warm (206 ± 4 K) winter period, with a gradual decline (-0.04 K/day) over the interval DOY 106-258 and including episodic 10-20 day (planetary scale) variations of amplitude up to 30 K. Equinoctial transitions from cold summer temperatures show a sharp rise in autumn (1.2 K/day; DOY 49-80) and a more gradual spring decline (-0.65 K/day; DOY 275-296). The autumn transition occurs earlier, and the spring transition later than either CIRA86 or MSISE-90 model predictions. The midwinter local minimum in MSISE-90 is also not supported.

Mean winter temperatures calculated from the daily averages for each year are consistent with a positive solar cycle association of 0.066 K/solar-flux-unit, considerably lower than most values reported in the literature. Multivariate analysis supports a long term cooling trend of the order of 0.5 K/year in the winter average temperatures over Davis.

Acknowledgements

There are many people I wish to sincerely thank for their contribution to this work.

I particularly thank Dr. Gary Burns, Principal Research Scientist at the Australian Antarctic Division for his highly enthusiastic supervision. Always helpful, always with new ideas and directions, a meticulous attention to detail and a tenacious desire to wring every last shred of information out of every photon collected. I have enjoyed being associated with Gary on various projects for thirteen years.

I was fortunate to also have Dr. Pene Greet as co-supervisor. Pene was principal investigator on the hydroxyl airglow project during most of my association with it. I greatly appreciate Pene's guidance and encouragement and her review and many constructive comments on this thesis.

Prof. Bob Lowe of the University of Western Ontario has openly and enthusiastically shared his wealth of knowledge on many OH matters with our group. His association has established a strong bond of collaboration between UWO and AAD that promises an exciting future. I thank him for his kindness, interest and insightful answers to many questions.

I joined the hydroxyl airglow project in late 1994 and enrolled in this degree part-time with the Institute of Antarctic and Southern Ocean Studies (IASOS) at the University of Tasmania. Prof. Garth Paltridge has kindly acted as my administrative supervisor at IASOS during my candidature. I am grateful to the University for HECS scholarship support during this degree.

I have been very fortunate to be able to complete this thesis while being employed full-time with the Atmospheric and Space Physics Group (ASP) at the Australian Antarctic Division. I am largely indebted to Dr. Ray Morris for this opportunity, who has steered the helm of ASP for over seven years. I would also like to thank Keith Finlayson, Damian Murphy, Andrew Klekociuk, John Innis, Pelham Williams and David Rasch for their friendship, valued opinions and assistance over the years. It has been a pleasure working with these people at ASP.

Two unforgettable years have been spent as ASP optical physicist at Davis station, Antarctica during the course of this project. I sincerely thank the extraordinary men and women of the Australian National Antarctic Research Expeditions (ANARE)

1995 and 1998 for their hard work, hard play, humour and company in the experience of a lifetime.

During these years I have had the distinct pleasure of working with ASP electronics engineers Lloyd Symons and Andrew Bish. Both demonstrated exceptional technical ability in support of ASP experiments and equipment. I appreciate their talent, enthusiasm and friendship.

I also wish to thank those dedicated ASP physicists who have contributed to the OH project at Davis; Pelham Williams (1984,1987,1990,1994), Keith Finlayson (1996), Pene Greet (1997), Frances Phillips (1999) and George Klich (2000). It is their careful operation and calibration of the scanning spectrometer and other instruments over the years that have made this project possible. Their efforts are also embodied in this thesis.

I am indebted to Mr Errol Atkinson of the National Measurement Laboratory (NML) in Sydney, Australia for many repeated and painstaking calibrations of our low brightness sources for instrument calibration.

I thank my parents, Reg and Llyween for their continued interest and support of all my endeavours. Finally, to my wife, Karen and my son, Matthew I owe special thanks. They have been my inspiration. I have had the unique privilege of spending both years at Davis with Karen. It was her observation of a noctilucent cloud in Feb-98 that has led to a renewed interest in southern hemisphere NLC's. Behind the scenes, while writing this thesis, we were married, moved into a new house, Matthew was born, we spent 3½ months as lighthouse caretakers on a remote southern Tasmanian island and Karen finished her teaching degree. I thank them for some wonderful times and for keeping life in perspective

John French.

11-Sep-2001

Table of Contents

1. Introduction and Review

1.1. Climate Change

Global warming, greenhouse gases and carbon credits are at the present time, subjects of intense political, social and economic debate. Understanding and monitoring climate change is a major focus of current atmospheric research. This project aims to contribute to this research effort through a monitoring program in a region of the atmosphere sensitive to the effects of climate change.

It is now widely accepted that anthropogenic emissions of carbon dioxide, methane and nitrous oxide are the most important contributors to climate change. The longest continuous record of CO_2 samples from Mauna Loa Observatory in Hawaii (Figure 1-1) reveals a steady increase from 315 to 370 ppmv (17%) in the last 40 years. [Keeling and Whorf (2000)].

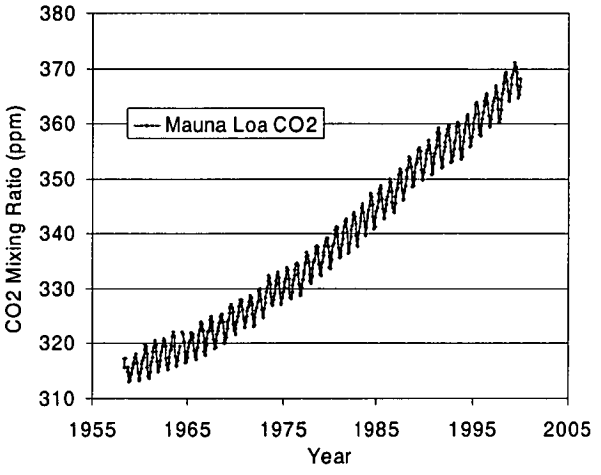

Figure 1-1. CO_2 samples collected at Mauna Loa, Hawaii (from Keeling and Whorf (2000))

Extraction of air from ice core samples, such as from the Law Dome site in Antarctica, [Figure 1-2] show pre-industrial CO_2 mixing ratios around 280 ppm and dramatic growth during the industrial period since 1800. [Etheridge *et al.* (1998)]

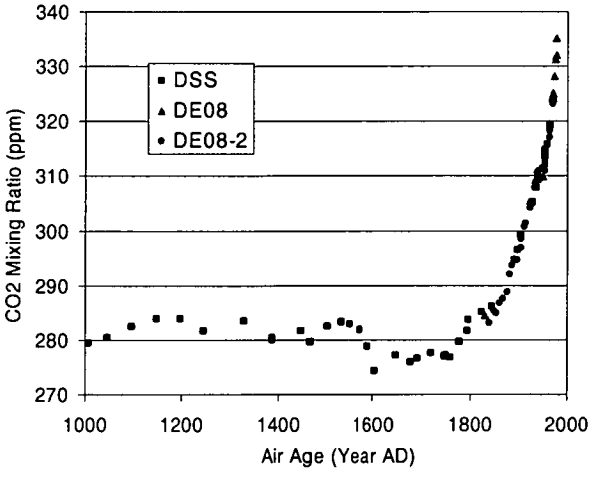

Figure 1-2. Historical CO_2 record from the Law Dome ice cores (from Etheridge et al. (1998)).

Further back however, analysis of the 3300-metre Vostok ice core yields a natural CO_2 variation between about 180 and 300 ppmv,

with a dominant period of about 100,000 years [Figure 1-3]. Both the inferred temperature and methane concentration are highly correlated with the CO_2 variation [Petit *et al.* (1999)]. CO_2 concentrations have never exceeded 300ppmv throughout the 420,000-year record, thus present-day values appear to be unprecedented.

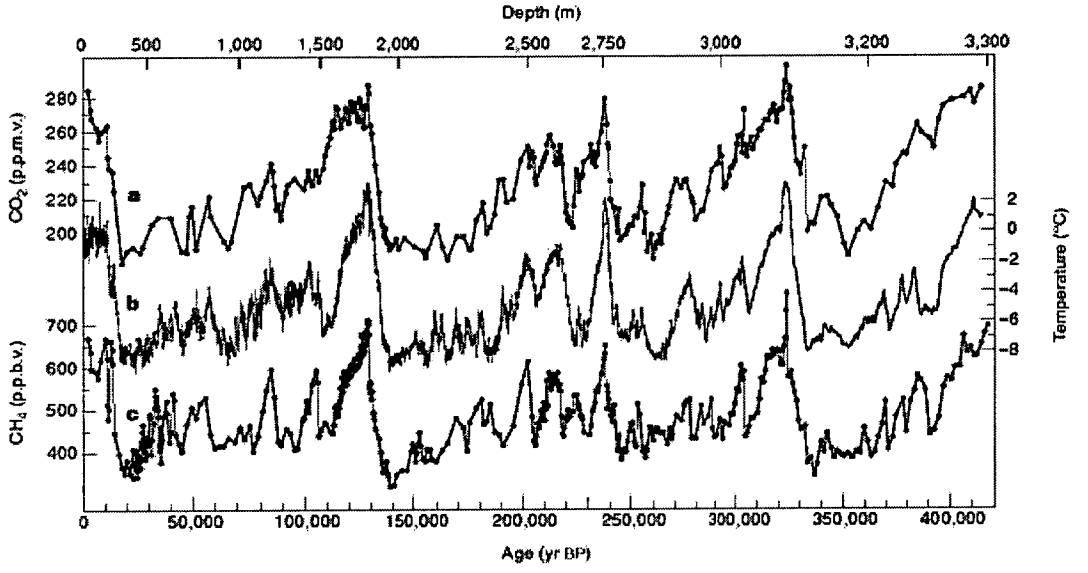

Figure 1-3. (a) CO_2 concentration (b) Isotopic temperature and (c) Methane concentrations from the Vostok Ice core over the last 420,000 years [Petit et al. (1999)].

Methane increases are even more dramatic, having not exceeded 800 ppbv throughout the Vostok record, they have more than doubled in the past 200 years to present levels around 1720 ppmv. [IPCC (1994)]. Methane's contribution to climate change is large because it is 22 times more effective as an absorber per molecule than CO_2. Its atmospheric lifetime is shorter however (of the order of 12 years compared to a very uncertain 50-200 years for CO_2). The molecule is oxidised in a long reaction chain starting with OH and eventually ends up as CO_2 and H_2O.

Nitrous Oxide (N_2O) also has a disproportionately large greenhouse effect. It is about 1100 times less abundant that CO_2, but it is about 200 times more effective as a greenhouse gas absorber. Increases are of the order of 14% from 275 ppbv in the pre-industrial era to a present value of about 312 ppbv. [IPCC (1996a)].

For the earth-atmosphere system, globally averaged, a radiative balance must exist between the incident solar radiation and that re-radiated to space. Currently, the Earth's mean surface temperature is near 288K (15°C), radiating about 390 Wm^{-2} in the infrared. However, when viewed from space, the *effective radiating temperature*

is only about 255 K (–18 °C), emitting about 240 Wm^{-2}. In effect, an apparent radiating altitude of about 5 km. The difference is maintained by the absorption and re-emission of infrared radiation by greenhouse gases. Net warming results at the surface and lower troposphere where excited gas molecules generally suffer collisions before radiating, and net cooling of the atmosphere above where the mean time between collisions exceeds the radiative lifetime. The dominant absorber in this process is water vapour, responsible for 60-70% of the natural greenhouse effect followed by CO_2, CH_4 and N_2O.

Increasing the number of absorbers renders the atmosphere more opaque to infrared radiation. The radiation to space and effective radiating temperature is therefore decreased or equivalently, the apparent radiating altitude increased. This *radiative forcing* is estimated to amount to 2.45Wm^{-2} for the increased anthropogenic emissions, of which CO_2 contributes 1.56Wm^{-2} (64%), CH_4 0.47Wm^{-2} (19%) and N_20 0.14 Wm^{-2} (6%). [IPCC (1996b)]

With constant solar input, a net radiation influx results until the climate system responds to restore radiative balance. This can occur via a temperature increase in the Earth's surface and troposphere or a change in the tropospheric lapse rate; both processes raising the temperature at the new apparent radiating altitude.

Abundant data demonstrate that global climate has warmed during the past 150 years by some 0.3-0.6C. The ten warmest years since 1860 have all occurred in the 1980s and 1990s. Figure 1-4, from Jones *et al.* (1999) shows the trend in global averaged[†] surface temperatures for this period.

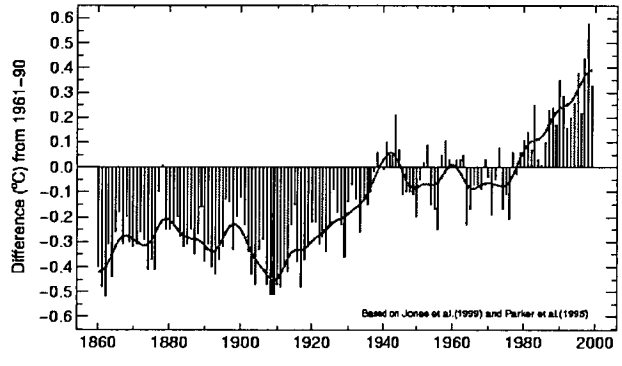

Figure 1-4. Trend in global average surface temperature 1860-1999 [Jones et al. (1999)]

[†] The global averaging procedure, first proposed by Hansen and Lebedeff (1987), and subsequently refined by Parker et al. (1994) consists of dividing the surface of the Earth into grids (currently 5° in latitude and longitude) and calculating a weighted average of the monthly averaged temperature records of the qualified measurement stations or sea-surface measurements within the grid. This average is then subtracted from the mean value of a similar average for the same grid over a reference period (currently 1961 to 1990). The figure obtained is the temperature anomaly for that grid for that month and year. The weighted annual average anomalies are then plotted as in Figure 1-4.

Other changes have also been noted in global precipitation and evaporation patterns, increased climate variability and extreme weather events, a sea level rise of between 10 and 25 cm in the last century and in circulation patterns of ocean currents.

Climate change problems are being addressed through the United Nations Framework Convention on Climate Change (UNFCCC), which was opened for signature in 1992 at the Rio Earth Summit. International research is directed to this body through the Intergovernmental Panel on Climate Change (IPCC). Its primary objective is to "*stabilize greenhouse gas concentrations in the atmosphere at a level that would prevent dangerous anthropogenic human-induced interference with the climate system*". The Kyoto Protocol, agreed to in December 1997, formalizes this commitment and calls for the industrialized nations to reduce their average national emissions over the period 2008-2012 to about five percent (on average) below 1990 levels.

Since then the UNFCCC has met in Buenos Aires, Argentina in November 1998, Bonn, Germany in October 1999 and The Hague, Netherlands in November 2000 to negotiate strategies to implement the main provisions of the Kyoto Protocol. With more than 180 member countries, and with the major players reluctant to reduce market competitiveness the negotiations were reportedly characterised by a lack of compromise and ended in deadlock.

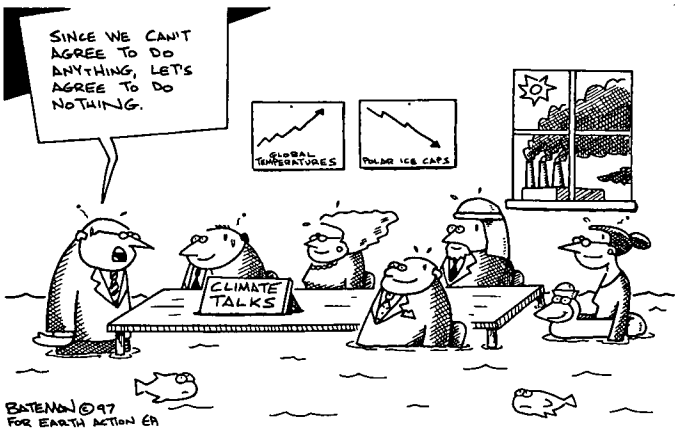

1.2. Modelling Trends

Climatic temperature changes in the troposphere are very small. Several generations of atmospheric general circulation models (GCMs) with various greenhouse gas scenarios predict future global warming trends of 0.1 to 0.3 K per decade. Most models attempt to predict the effects of doubled CO_2 or compounded 1% increases.

Examples of the most sophisticated ocean-atmosphere coupled models include those at NASA's Goddard Institute for Space Studies (GISS) [Hansen *et al.* (1988), Russell

et al. (1995), Rind *et al.* (1988a,b), http://aom.giss.nasa.gov/], the Hadley Center (climate-modelling arm of the United Kingdom Meteorological Office) [Johns *et al.*, (1997), Murphy (1992), http://www.met-office.gov.uk/research/hadleycentre/], the Japanese Meteorological Research Institute [Kitoh *et al.* (1995), http://www.mri-jma.go.jp/Dep/cl/cl4/GW/GW.html] and at the Geophysical Fluid Dynamics Laboratory (GFDL) at the National Climate Data Centre (NCDC) [Manabe *et al.* (1991), http://www.ncdc.noaa.gov/ol/climate/online/gcm1000.html]. Most of these may be accessed online at the noted web sites.

In general, these models agree on the global aspects of warming. It will not be uniform; significantly, it will be much greater at high latitudes than at the equator, larger over land surfaces than oceans, and cooling in the upper atmosphere is expected to be much greater than warming in the troposphere.

Computations for the troposphere and stratosphere are necessarily subject to large uncertainties due to inadequate data on competing radiative forcings and complex feedback mechanisms. Principally, these include sulphate aerosol, volcanic, CFC-ozone, land-use and solar cycle forcings, and water vapour, snow-ice albedo, cloud, oceanic and biological feedbacks [Hansen *et al.*, 1998]. Until these processes are better understood, future predictions of the atmospheres response to anthropogenic emissions are exceedingly difficult.

Models do indicate however the best place to detect early signatures of climate change: the high latitude mesosphere and lower thermosphere (MLT). Here, the tenuous atmosphere is most sensitive to change and less complicated by the forcing and feedback mechanisms of the lower atmosphere [see review by Thomas (1996a)]. It is a region of temperature extremes, with an annual range up to 100K and the coldest temperatures anywhere in the atmosphere observed at the polar summer mesopause [Figure 1-5]. It is also host to a variety of unique phenomena, including the hydroxyl (OH) airglow layer, sodium layer, auroral emissions, noctilucent clouds (NLC) and polar mesospheric clouds (PMC), which provide opportunities for remote sensing and hence long-term ground based studies of the region.

This is precisely the recommendation of the concluding priorities from IPCC Working Group I: (The Science of Climate Change) to encourage the *'Systematic collection of long-term instrumental and proxy observations of climate system*

variables for the purposes of model testing, assessment of temporal and regional variability, and for detection and attribution studies.' This project aims to contribute to that endeavour, through the long term monitoring of hydroxyl airglow at Davis station, Antarctica (68.6°S, 78.0°E) and the derivation of accurate rotational temperatures from spectral data.

The MLT region is not without its own complexities however. It lies between, and is coupled to, the radiatively heated regions of the stratopause (ozone absorption of solar ultraviolet radiation) and the thermosphere (strong absorption of solar extreme ultraviolet radiation, particularly by atomic and molecular oxygen). Consequently, one could expect ozone depletion and solar variability influences. It is also strongly dominated by dynamical heating and cooling, largely due to deposition of internal gravity wave energy in winter [Holton (1983)], resulting in the large seasonal temperature variation [Figure 1-5].

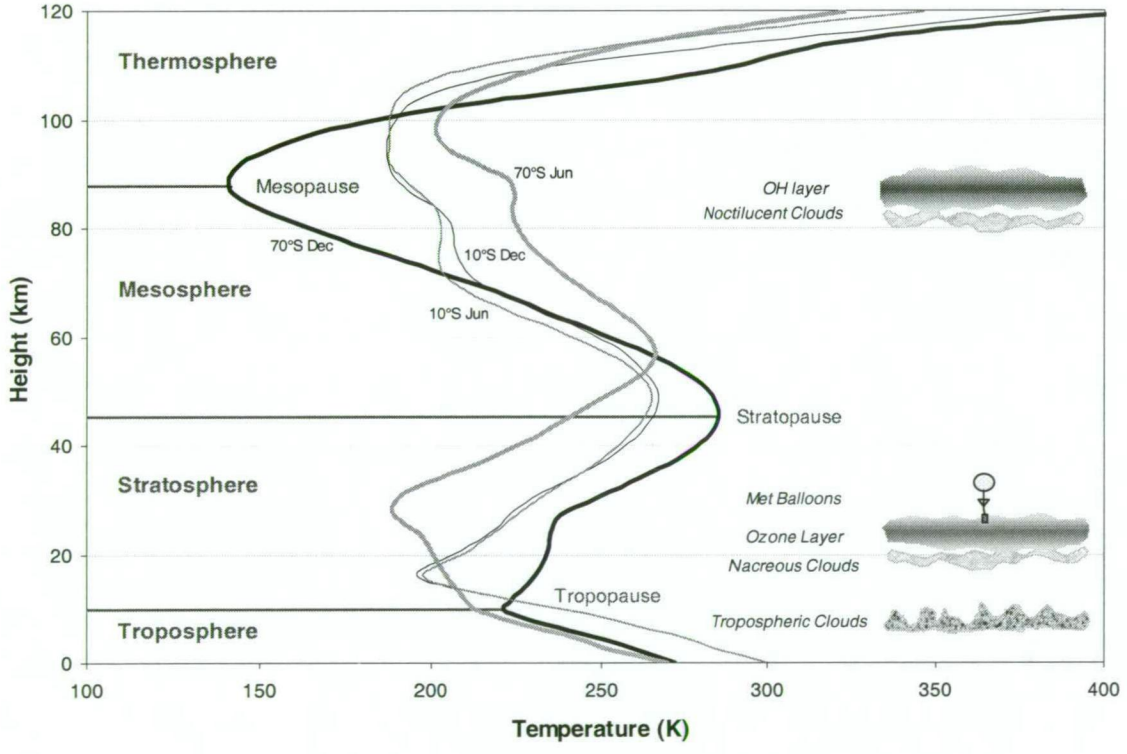

Figure 1-5. Atmospheric temperature profiles from the CIRA 1986 model [Fleming et al. 1988] illustrating the extremely cold summer mesopause and large seasonal variability at 70°S (thick lines), while the temperature structure at 10°S (thin lines) is virtually unchanged throughout the year. Key atmospheric features are also illustrated.

Several research groups have modelled the MLT region specifically. Most notably these include Roble and Dickinson (1989) [NCAR 1-D photochemical model], Rind

et al. (1990) [GISS Global Climate Middle Atmosphere model (GCMAM)], Berger and Dameris (1993) [Cologne Global 3-D Mechanistic Model], Portmann *et al.* (1995) [modified Garcia-Solomon 2-D model] and Akmaev and Fomichev (1998, 2000) [Spectral Mesosphere/Lower Thermosphere model (SMLTM)]. While a number of limitations and deficiencies exist in each of these models, predictions of enhanced cooling throughout the stratosphere and lower mesosphere (10-15K), upper mesosphere and mesopause (6-12K) and lower thermosphere (40-50K at 110 km altitude) are generally consistent for a doubled CO_2 atmosphere. All are considerably easier to measure than predicted tropospheric change.

Other changes in atmospheric parameters are also noted. The Roble and Dickinson (1989) radiative-photochemical model shows significant alteration of the compositional distributions of the major and minor species throughout the mesosphere and thermosphere and a reduction of atmospheric density by more than 40% in the thermosphere due to thermal compression.

Radiatively induced dynamical changes are also important. Planetary and gravity waves generated in the troposphere play an essential role in the thermal structure and large-scale circulation of middle atmosphere. More complete models must include the dynamical aspects of a doubled CO_2 atmosphere.

Rind *et al.* (1990) find a warming troposphere and cooling stratosphere leads to a decrease in static stability for the atmosphere as a whole. Tropospheric warming maximises around the equator, producing an increased latitudinal temperature gradient, improved propagation conditions for planetary waves and increased eddy energy in the middle atmosphere that acts to intensify meridional flow. Their simulations predict *cooling* of the winter upper mesosphere but a *warming* of the winter lower mesosphere and summer upper mesosphere as a result of dynamic feedbacks (increased gravity wave momentum deposition) for doubled CO_2. As they point out however, the upper mesosphere warming was not as expected and suggest it may be severely affected by the breakdown of local thermal equilibrium (LTE) above about 75km.

Accordingly, Berger and Dameris (1993) developed a detailed parameterisation for the terrestrial CO_2 radiation flux including non-LTE effects above 80km, to couple with the Cologne 3-D dynamical model extending from the surface to 150km. Both

pure radiative and radiative-dynamical coupled zonal mean model simulations were evaluated for doubled CO_2 and compared with Rind *et al.'s* results. It was apparent that the mesopause region cooled less than neighbouring regions but the warming of the summer upper mesosphere was not evident. These simulations were limited however by inadequate treatment of changes in the troposphere, no inclusion of gravity waves and large-scale planetary waves (only tides) and no account of chemical interactions.

Subsequently, Portmann *et al.* (1995) modified the Garcia-Solomon model [Garcia and Solomon (1983,1985)] to include non-LTE CO_2 cooling above 70km as well as feedbacks due to altered wave propagation characteristics, diabatic heating (solar and chemical heating, and infrared cooling), diffusive heating and chemistry, but not stratospheric ozone, planetary waves or changes in the gravity wave flux due to climate change in the troposphere. The effect of doubled CO_2 is modelled through the infrared cooling term of diabatic heating. Thomas (1996b) also discusses results from this model study.

Again, both radiative only (by means of fixed dynamical heating terms) and radiative-dynamical feedback simulations were run to isolate the effect of dynamic feedbacks. Both show regions of maximum cooling (10-12K) in the high latitude upper stratosphere, winter mesosphere and throughout the MLT region for doubled CO_2 [shaded in Figure 1-6]. Interestingly, the warming of the high latitude summer mesosphere observed by Rind *et al.* (1990) is reproduced in the fixed dynamical heating simulation, but is virtually eliminated when full dynamical feedbacks were included. The first conclusion drawn is similar to Rind *et al.* (1990). CO_2 increases lead to a strengthening of the (winter to summer hemisphere) meridional flow, increased upward motion (hence cooling) in the high latitude summer mesopause region and downward motion (warming) in the high latitude winter mesopause. The large meridional (winter-

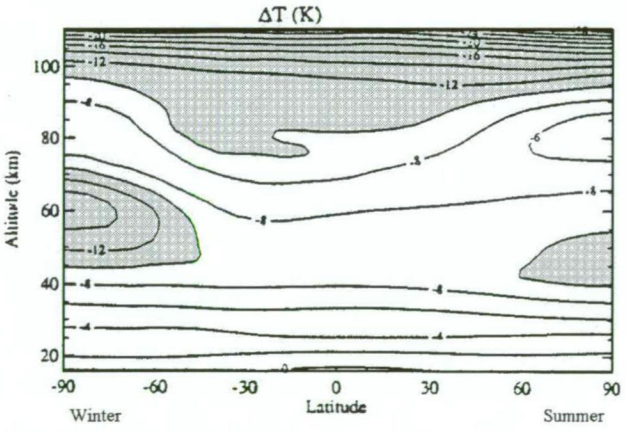

doubling of CO_2 from the modified Garcia-Solomon model with dynamical feedbacks [Thomas (1996b)]. Regions of enhanced cooling (>-10K) are shaded.

summer) variation in mesopause temperature changes of Rind *et al.* (1990) is consequently reduced. Secondly, the diffusive feedback process, dominated by the eddy mixing of breaking gravity waves, also acts to cool the high latitude summer mesopause as a result of the large rate of change of temperature above and below the mesopause level.

Most recently Akmaev and Fomichev (1998) have also incorporated new parameterisation of infrared radiative transfer in the 15 μm CO_2 band (including non-LTE effects) into the 3-D spectral mesosphere/lower thermosphere model (SMLTM) and have considered both doubled CO_2 and the actual measured increase in CO_2 over the last 3-4 decades for direct comparison with observations [Akmaev and Fomichev (2000)]. Akmaev and Fomichev (1998) also provide a very good review of the modelling attempts mentioned here and long-term observational evidence discussed in the next section. Significantly, the effects of strong diurnal and semidiurnal tides (important at low latitudes) and planetary scale motions are examined in this work for the first time. The model also incorporates parameterisation of solar heating due to UV absorption by O_2 and O_3 and EUV absorption by O, O_2 and N_2, infrared radiative transfer in the 9.6μm band of O_3, molecular viscosity and thermal conductivity, ion drag, a discrete spectrum gravity wave parameterisation with latitudinal and seasonal variations and interactive eddy diffusivity. Initial conditions were specified according to the MSIS-E-90 empirical model [Hedin (1991)] at a moderate solar activity level ($F_{10.7}$ = $150x10^{-22}$ $Wcm^{-2}Hz^{-1}$). They note several limitations of the current SMLTM model, particularly, no account of chemical feedbacks (mainly important for ozone in the stratosphere and potentially important in the mesosphere through changing temperature dependent reaction rates of exothermic processes), and no explicit account for radiative cooling in the 5.3 μm band of NO (may be important in the thermosphere).

Common features of previous models for doubled CO_2 were reproduced. Dynamical cooling feedbacks counteract radiative warming of the high latitude summer mesopause region such that net cooling results throughout the upper stratosphere and MLT. Radiative feedback due to heating in the 9.6 μm ozone band also damps the thermal response in the upper stratosphere and lower mesosphere. Zonal means were derived for the stratopause of –14 K, reducing to –8 K at the mesopause, and then increasing again to –40 K in the lower thermosphere. For a given geometric height,

thermal shrinking (due to cooling of the underlying atmosphere) also contributes to an apparent enhanced cooling where temperature gradient is negative with height in the mesosphere, and conversely, weaker cooling, or even apparent warming where the temperature gradient is positive in the lower thermosphere.

Calculations of the temperature response to doubled CO_2 greatly exaggerate the real changes that have occurred in the last 3-4 decades and as such cannot compare directly with current observational evidence. Akmaev and Fomichev (2000) have addressed this with a model simulation of a more realistic 15% increase. They find cooling maximises in the mesosphere at about 3K, practically vanishes at 100-120 km and grows again to 10-15K in the thermosphere [Figure 1-7]. This suggests an average cooling rate of about 0.8K per decade for comparison with observational data in the mesosphere. There are enough similarities to the doubled CO_2 case to suggest that the forcing is roughly proportional to the relative CO_2 increase.

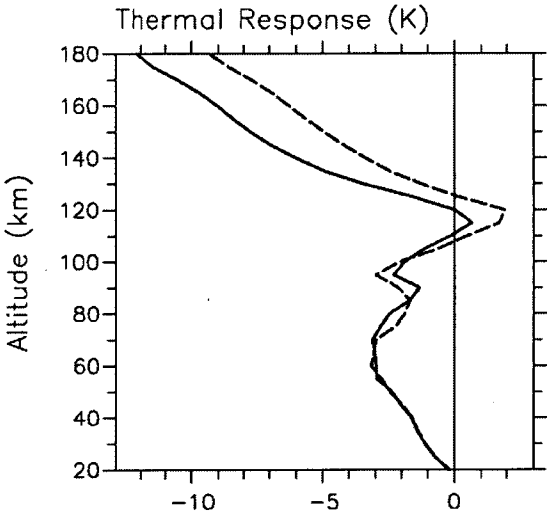

response for the change in CO_2 concentration that has occurred between 1955 and 1995, for January (solid) and April (dashed) [Akmaev and Fomichev (2000)]

At present, no model adequately describes all the complex radiative, dynamical and chemical interactions and feedback mechanisms for an atmosphere subject to perturbations of radiatively active trace gases. Comparisons of simulations performed with different models do however help clarify the role and importance of the various mechanisms and feedbacks of global change in the MLT.

1.3. Monitoring Trends

Modelling aside, a growing number of observational studies monitor trends in the MLT region and some now extend over several decades. Direct temperature measurements can be made by Rayleigh lidars, rocketsondes, by spectroscopic means for layered molecular species (OH, O_2) and Doppler means for layered atomic species (Na, O). Indirectly, temperature changes can also be inferred from changes in

natural phenomena like noctilucent cloud occurrences or from the changing height of atmospheric layers (such as lidar measurements of Na layer height or radio wave reflection heights of the ionospheric layers) as a consequence of the thermal shrinking discussed above. Good reviews of experimental observations of long-term trends are included in Akmaev and Fomichev (1998) and Lysenko *et al.* (1999). A summary of the measured trends is collated in Table 1-1.

Both the Russian, and US rocketsonde databases provide an invaluable record of trends extending back over 30 years for altitudes below about 75km. Although both databases contain difficulties associated with inevitable instrument improvements and sensor modifications, changes in measurement times, correction factors and data processing techniques, these have recently been addressed by special intercomparison experiments in the Russian case and detailed statistical modelling and error analysis in the US case.

Kokin and Lysenko (1994) analysed over 7000 weekly soundings made since 1964 from 5 Russian stations: Heiss Island (81°N, 58°E) and Molodezhnaya (68°S, 46°E) at high latitude, Volograd (49°N, 44°E) and Balkhash (47°N, 75°E) at mid latitudes and Thumba (8.5°N, 76.8°E) at low latitude. Cooling trends were found at all latitudes throughout the upper stratosphere (0.1-0.3 K per year) and mesosphere (0.3-1.0K per year) except for a consistent lack of trend around 45 km altitude. [see Figure 1-8]. Significant seasonal variability was also evident with the winter-autumn trend greater than in summer-spring.

The US rocketsonde measurements from six low latitude sites (8°S to 34°N) were analysed by Dunkerton *et al.* (1998) and Keckhut *et al.* (1999). In the latter, a total of 9647 of the 12215 profiles obtained between 1969 and 1993 were selected. They also find trend profiles are similar in pattern and magnitude at the different latitudes and consequently present a mean profile [Figure 1-8]. In contrast to the Russian study, they find much weaker cooling trends of 1.1±0.6 K per decade at 25 km, increasing with height to 1.7±0.7 K per decade in the altitude range 35-50 km (no trend minimum around 45km) and further to 3.3±0.9 K per decade near 60 km. These are approximately a factor of 3 less than the Russian study, but still a factor of 2 more than the model prediction of 0.8 K per decade in the mesosphere. Keckhut *et al.* (1999) specifically remove data following the major volcanic eruptions of Fuego

(Central Guatemala, 14-Oct-74), El Chichon (Mexico, 6-Apr-82) and Mt Pinatubo (Phillipines, 12-Jun-91) and the multiparametric adaptive model used for trend detection includes components for annual and semi-annual season, Quasi Biennial Oscillation[†] (QBO), solar cycle and step functions for known sensor or correction changes.

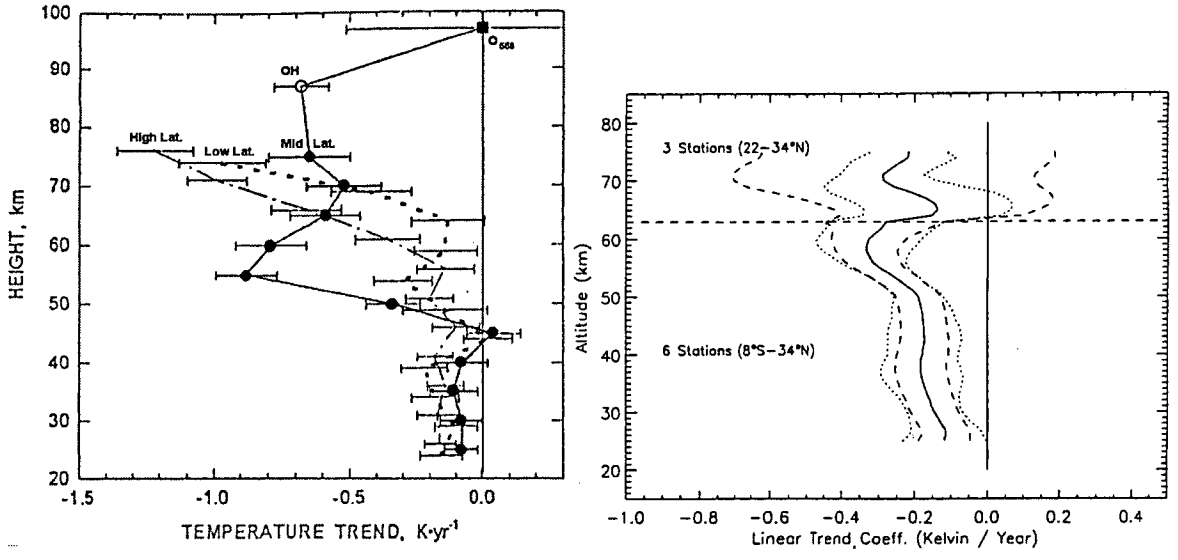

Figure 1-8. A comparison of cooling trends observed in Russian and US rocketsonde studies. The left panel from Golitsyn et al. (1996) shows the mean trends from two high-latitude, two mid-latitude and one low latitude stations and the right panel from Keckhut et al. (1999) shows the mean trend from six low latitude sites. Vertical scales have been aligned for comparison but the abscissas are not to scale. The mean trends from OH and 558nm measurements are also plotted on the left panel (see text).

Golitsyn *et al.* (1996) present analysis of the oldest series of direct measurements in the mesopause region using spectral measurements of hydroxyl airglow. These data are compared with the rocket profiles of Kokin and Lysenko (1994), the Fritz Peak Observatory (40°N, 106°W) interferometric measurements of the λ558 nm oxygen emission [Hernandez and Killeen (1988)] and the lidar measurements of She *et al.* (1993) from Fort Collins (41°N, 105°W). OH measurements at Abastumani (42°N, 43°E) and Zvenigorod (56°N, 37°E) extend back over 40 years to 1957. Several bands were observed at different periods, but the measurements were corrected to an OH(5-2) band equivalent. They derive a cooling of the mesopause region by some

[†] The QBO is a lower stratospheric equatorial wind that reverses its direction (east-west) with a period of approximately 26-months. Usually measured between 100-10 hPa (16-31km). It was discovered in 1961 but the forcing mechanism is still not fully understood.

27 K over this time; a trend of almost 7 K per decade, in agreement with the upper boundary of the rocket profiles. An increase in OH(5-2) emission intensity of 9.8±0.6 kR per year, with a prominent solar cycle correlation is also noted. No significant trend is detected in the lower thermosphere from the λ558 nm emission (at 97 km) however. [Figure 1-8].

The Rayleigh lidar at Haute Province (44°N, 6°E), operated since 1979, offers temperature measurements in the height range 30-80km. A long-term trend analysis is presented by Hauchecorne *et al.* (1991) and updated by Keckhut *et al.* (1995). They too use a multivariate analysis technique to account for natural variability, including solar cycle, QBO and volcanic eruptions. Particular attention is drawn to the choice of proxy for solar induced variations. Four are tested; the solar constant, MgII index, HeI λ1083-nm line and the 10.7 cm solar flux index. Smaller confidence in the solar constant and HeI indices and nonlinearities in the F10.7 index led them to prefer the MgII solar cycle proxy, which accurately tracks the flux in the photochemically important region. Figure 1-9 plots the fitted solar cycle response for winter (Oct-Mar) and summer (Apr-Sep) data. In winter a large positive solar cycle response is found for the mesosphere (7 K per solar cycle at 65km) and negative response in the stratosphere (-7 K per cycle at 40 km). The summer response is similar in direction but smaller magnitude.

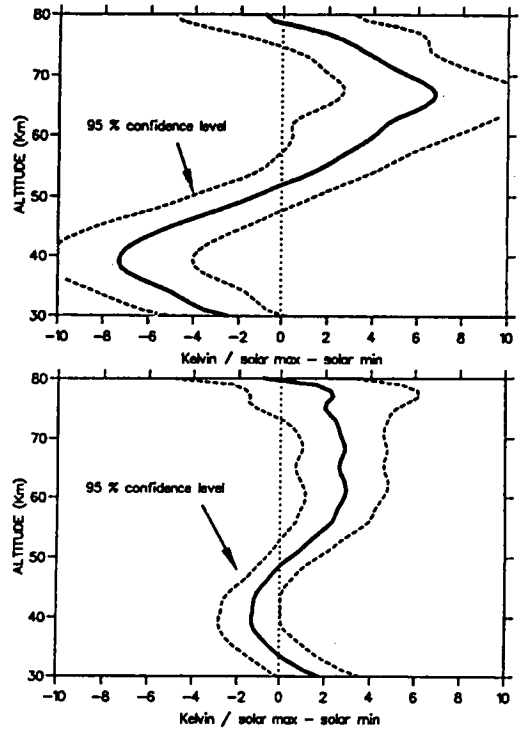

Figure 1-9 Temperature profiles of the solar cycle response (using MgII solar proxy) for winter (top panel) and summer (bottom panel) extracted from multivariate analysis of the Haute Province lidar data. [Keckhut et al. (1995)]

QBO effects were only found to be significant in the stratosphere where lidar temperatures were warmer by (3-5 K) during the east phase of the QBO. Following the eruption of Mt Pinatubo, a significant warming of the mesosphere (5K between 60-80 km) and cooling of the upper stratosphere (>1.5K less than 50 km) is observed in the summer of 1992 and 1993. In the 1991-1992 winter months the perturbed profile is reversed (6K warmer

upper stratosphere and 4 K cooler mesosphere). Extracting each of these influences from the lidar data yields a resultant linear trend profile. Appreciably greater variability was measured in winter as would be expected through dynamical effects. Figure 1-10 plots the trend profile considering only summer data between 1979 and 1991. (This may be compared to Figure 1-8.) The cooling trend maximises in the summer mesopause (60-70km altitude) at 4-5 K per decade. The minimum trend around 45 km is consistent with that derived in the Golitsyn *et al.* (1996) study. The trend at the top of the response profile is subject to noise, initialisation and sky background difficulties that give poor confidence.

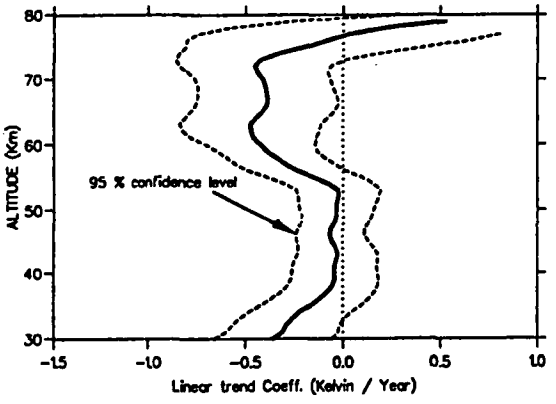

Figure 1-10. Cooling trend from the Haute Province summer lidar data 1979-1991 [Keckhut et al. (1995)]

Sodium lidar data from Fort Collins (41°N, 105°W), covering the period 1990-1997, has also been studied for long-term trends in the 84-102 km altitude region [Krueger and She (1999)]. In particular, the impact of the Mt Pinatubo eruption is investigated in their paper. With seasonal variations removed, the perturbation due to Pinatubo is fit with an episodic response function [She *et al.* (1998)]. A maximum warming response of 9.0±1.7 K at 86 km and 12.9±1.8 K at 100 km is found about 2 years after the eruption [Figure 1-11].

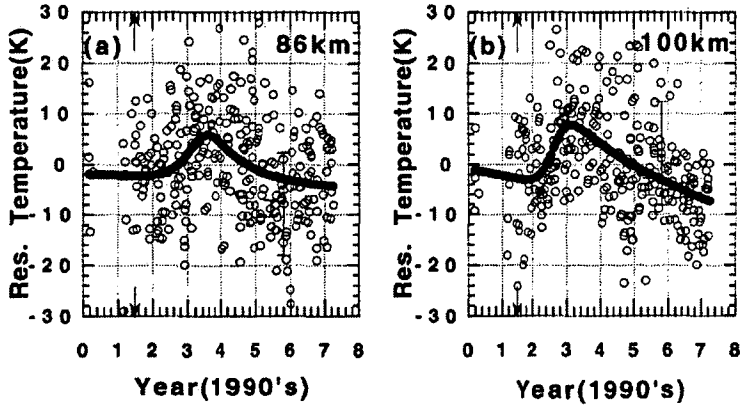

Figure 1-11. Time series of residual temperatures over Fort Collins (41°N) between 1990 and 1997 with a least squares fit including an episodic response function attributed to the Mt Pinatubo eruption (marked with arrow) from She et al. (1998)

An underlying cooling trend is evident in the figures above and is extracted from the fits at each altitude sampled by the lidar [Figure 1-12]. Without removing any solar cycle effect (data interval coincides with the declining phase of solar flux cycle 21) this yields cooling rates of 0.4±0.6 K per year at 86 km, increasing to 1.4±0.8 K per year at 100 km. Comparison with the modelled solar cycle effect of Huang and Brasseur (1993) (also plotted in Figure 1-12) shows that this could account for most of the trend, but continued observations are required to verify this.

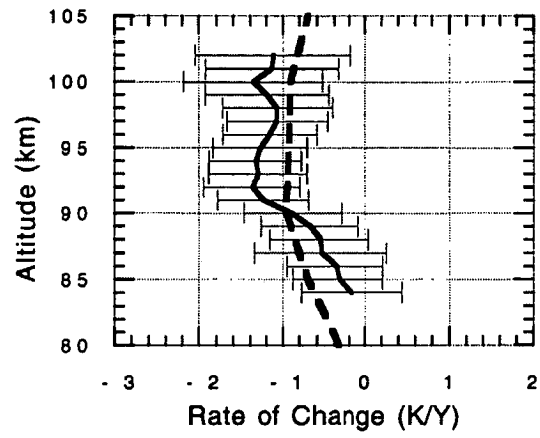

Figure 1-12. Observed cooling rate from the Fort Collins sodium lidar data 1990-1997. [Krueger and She (1999). Also plotted is a simulated cooling rate due to solar variability over the period [Huang and Brasseur (1993)]

Atmospheric physics groups at Stockholm University (from Sandkullen 59°N, 18°E, Stegman at http://www.misu.su.se/~jacek/Ground/index2.html), the University of Western Ontario (from Delaware Observatory 43°N, 81°W, Lowe (private comm.)), universities in Norway (from Adventdalen, Svalbard 78°N, 15°E, Sigernes *et al.* http://fred.unis.no/OHNobs/) and the University of Wuppertal, Germany (51°N 7°E, Bittner *et al.* (2000)) have all monitored temperatures using OH emissions over the last solar cycle.

The Stockholm group measured several OH infrared bands (among other atomic and molecular oxygen bands) using a Michelson Interferometer. Their time-series of derived OH rotational temperatures is shown in Figure 1-13. They find limited evidence for an *increase* in temperature of 5±3 K/decade.

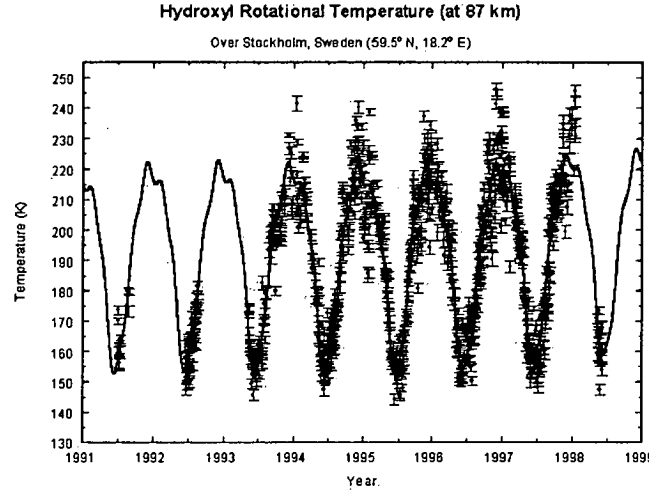

Figure 1-13. Hydroxyl rotational temperatures from Sandkullen 59°N [Stegman (from web site in text)]

Though their data span solar minimum (decreasing 1991-1996, increase 1996-1998) it was not yet possible to infer a rotational temperature – solar flux relationship.

Figure 1-14 shows the annual mean temperatures obtained from observations of OH(3-1) band emissions at Delaware Observatory, using a Fourier transform spectrometer. The data are detrended with fitted annual, semi-annual and ter-annual variations and yield a small positive linear trend of 0.7 (±1.3K per decade within 95% confidence limits). Again, the data interval spans the maximum of solar cycle 22, through its minimum and onto the peak of cycle 23 but any solar cycle relationship is still speculative.

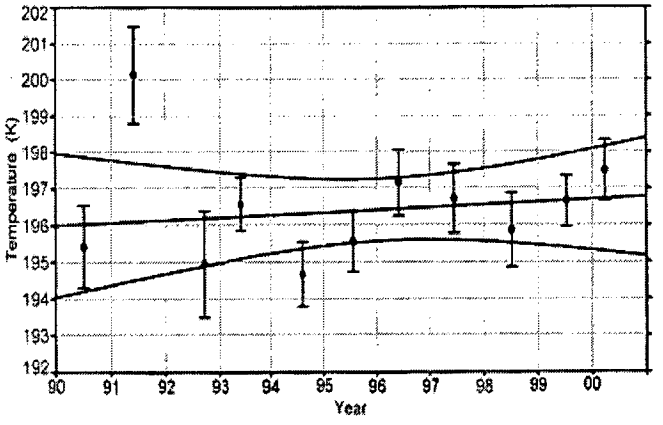

Figure 1-14. Seasonally detrended annual mean temperatures from the Delaware Observatory 43°N. Slope is 0.7 ±1.3 K per decade and 95% confidence limits are shown. [Lowe, private comm.]

Sigernes *et al.* (at http://fred.unis.no/OHNobs/) have measured winter (Dec-Jan) OH(6-2) and (8-3) rotational temperatures at Adventdalen since 1980. Their preliminary results are plotted in Figure 1-15. Annual mean winter temperatures show a nearly zero temperature trend (+0.03±0.002 Ka^{-1} weighted trend, dotted line in Figure 1-15) over twenty years. No obvious evidence of a solar cycle variation, but an association with stratospheric warmings is reported.

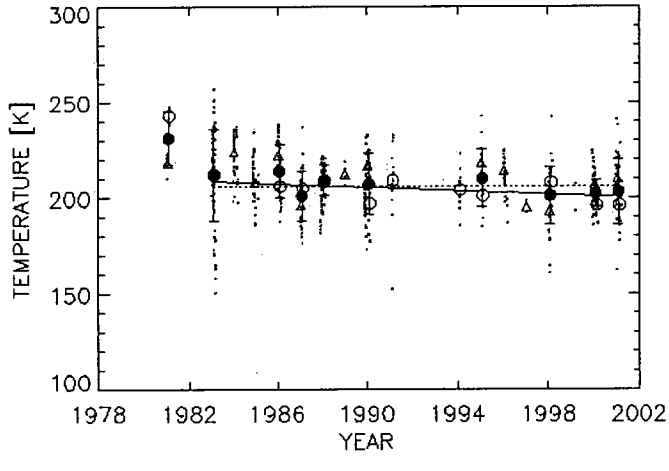

Figure 1-15. Trend in winter (Dec-Jan) OH temperatures over Svalbard 1980 - 2001. Daily mean temperatures are plotted as small dots. Monthly means are plotted for December (triangles) and January (circles). Seasonal averages (filled circles) have the standard deviation plotted as error bars. Solid and dashed lines represent linear and weighted trends, respectively (from http://fred.unis.no/OHNobs/).

Bittner *et al.* (2000) present a maximum entropy and wavelet analysis on more than 2000

nightly mean OH(3-1) temperatures obtained between 1987 and 1995 (using two different spectrometers) over Wuppertal, Germany. [Figure 1-16].

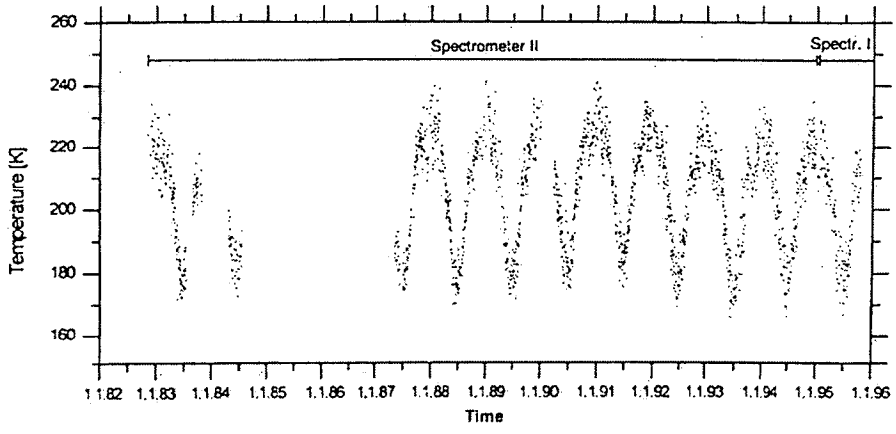

Figure 1-16. Time series of nocturnal temperatures from OH(3-1) emissions above Wuppertal (51°N) from Bittner et al. (2000).

This paper concentrates on the seasonal dependence of 4-50 day variations. Short period oscillations are found to dominate in summer and longer period (<20 day) variations dominate in winter. Neither a long-term temperature trend, nor solar cycle relationship are reported in the paper but both a trend toward increasing temperature *variability*, amounting to +0.8K per decade and a correlation with the QBO are found.

Long-term temperature trends have also been inferred indirectly from the occurrence frequency of noctilucent clouds[†] [Gadsden (1990, 1998)]. Noctilucent clouds form at 83 km, normally during the cold summer months, and require particularly low temperatures. Increased cloud sightings thus imply a cooler average summer mesopause region. Gadsden (1998) surveyed noctilucent cloud reports over NW Europe since 1964 [Figure 1-17] and found a 10-year cycle with an

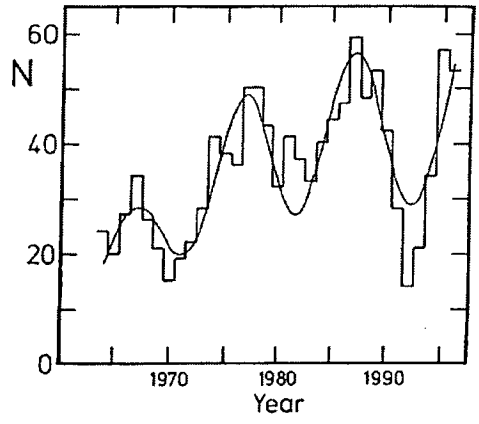

Figure 1-17. Number of nights on which noctilucent clouds were reported over NW-Europe as a function of year since 1964, with a least-squares log-sinusoid fit. [Gadsden 1998]

[†] A noctilucent cloud was observed by the author at Davis station in Feb-1998. OH temperatures were measured with the spectrometer at this time. A paper on this observation is included in Appendix-A.

underlying long-term trend. The decrease in 1992-93 may be associated with the eruption of Mt Pinatubo, but there is no corresponding decrease associated with El Chichon in 1982. A correlation with summertime mesopause temperatures from the rocket data of von Zahn (1990) is used to derive a median mesopause cooling from 144 to 127 K between 1964-95, or 5.5 K per decade. This is about twice the rate derived in Gadsden (1990) from thermodynamic calculations of the saturation vapour pressure and its rate of change with temperature (6.4 K over a 26 year period).

Long term trends based on the descent of various atmospheric layers have also been presented. This is interpreted as thermal contraction due to cooling of the underlying atmosphere. It is not possible by this means to attribute cooling to any particular level; instead trends are calculated assuming a uniform temperature change throughout the mesosphere (above 50km).

Clemesha *et al.* (1992, 1997) report a descent in the centroid height of the sodium layer (92 km altitude) at São José dos Campos (23°S, 46°W) by an average of 37±9 m yr^{-1} between 1972 and 1994 with a solar cycle related oscillation. They find a uniform cooling throughout the mesosphere of 5 K for this interval, or about 3 K per decade, would be necessary to account for the shift.

Taubenheim *et al.* (1990,1997) present a similar calculation based on the reflection heights of low frequency radio waves from about 80 km. They find a significant downward trend over the period 1962 to 1987 that would require a uniform cooling of 4K, or 1.5K per decade throughout the mesosphere. This smaller rate at 80km may not be at odds with the result of Clemesha *et al.* (1992) at 92 km if, as models suggest, cooling maximises above 80 km.

Danilov (1997) reviews the long-term trends in other atmospheric parameters, including various emission intensities, E and F2 layer critical frequencies, absorption measurements and ionospheric storm occurrence frequency.

In summary, the observational evidence of long-term trend estimates in the MLT region exhibit considerable variation [Table 1-1]. Nevertheless, data series that are long enough to account for solar cycle influences consistently point to pronounced cooling in the MLT region, perhaps at a greater rate than predicted by global change models. Further accurate, long-term and globally distributed observations in this

region are required to quantify seasonal, QBO, solar and latitudinal variability as well as episodic (volcanic) events that influence detection of any long-term anthropogenic changes. Ground based optical observations are ideally suited to this task, providing a more or less continuous inexpensive and easily calibrated method of monitoring atmospheric parameters.

Instrument	Latitude	Years	Height	Trend per decade	Reference
Direct Temperature Measurements					
Russian Rocket Radiosondes	High Med	1964-1990 (26 years)	60-70km	Cool 5-10K	Kokin and Lysenko (1994), Danilov (1997)
Rayleigh Lidar	44°N	1978-1994 (15 years) 1980-1990	60-70km 40-60km	Cool 4K Cool 2.5±1.0K	Hauchcorne *et al* (1991) Keckhut *et al.* (1995) Aikin *et al.* (1991)
Sodium Lidar	41°N	1990-1997 (7 years)	86km 100km	Cool 4±6K Cool 14±8K	Krueger and She (1999)
OH O green	42° and 56°N	1964-1990 1957-1994	87km 120km	Cool 7K No significant	Golitsyn *et al.* (1996)
US Rocket Radiosondes	8°S-38°N	1962-1991 1969-1993	30-60 km 35-50km 60km	Cool 1.7K Cool 1.7±0.7K Cool 3.3±0.9K	Dunkerton *et al.* (1998) Keckhut *et al.* (1999)
OH(3-1)	51°N	1987-1995	87km	+0.8K Increased varianced.	Bittner *et al.* (2000)
OH	43°N	1991-2000	87km	Warm 0.7±1.3K	Lowe (private comm.)
OH	59°N	1991-1998	87km	Warm 5±3K	Stegman (web)
OH	78°N	1980-2000	87km	No Significant	Sigernes (web)
Indirect Methods					
NLC obs	High	1964-1995	83km	Cool 5.5K	Gadsden (1998)
LF radio-wave reflection heights		1962-1987	80km	Cool 1.5K	Taubenheim (1990,1997)
Sodium layer centroid height		1972-1987	92km	Cool 3K	Clemesha *et al.* (1992, 1997)
Absorption		1959-1986	75-80km	Cool 2K	Nestorov *et al.* (1991)

Table 1-1. A summary of the observational studies of long-term temperature trends in the mesosphere and lower thermosphere.

The Antarctic mesopause region represents a temperature extreme in the Earth's atmosphere. Chemical reactions in the tenuous atmosphere at this altitude respond rapidly to change and can be further enhanced by unusual surface processes such as in the formation of noctilucent clouds. The mesopause is also a boundary between the atmosphere dominated by chemistry and dynamics and the thermosphere dominated by dissociation and diffusion. Coupling and energy transfer between the

solar wind, magnetosphere, ionosphere and neutral atmosphere occurs across this boundary.

The hydroxyl airglow layer is fortuitously positioned for studies of the mesopause region, at an altitude too low for in-situ measurements by satellites, too high for balloons and too expensive for long-term monitoring by rockets. Hydroxyl airglow is the most intense emission in the night sky spectrum, the order of 1 Mega-Rayleigh in total. The open structure of its emission bands allows it to be measured with relatively low-resolution instruments and techniques for the derivation of rotational temperatures are well established and understood.

With these considerations in mind, a long-term monitoring program for hydroxyl airglow was established at Davis station, initially with a filter photometer in 1983 and from 1990 with a scanning spectrometer that forms the basis of this work. The next chapter continues with a review and discussion of hydroxyl airglow; the development of techniques for its measurement in the infrared, OH molecular spectroscopy and nomenclature, the determination of rotational temperature and the photochemistry governing its production, loss and altitude distribution.

2. Hydroxyl Airglow

2.1. Historical Observations

The infrared emissions of hydroxyl airglow in night sky spectra were first identified by Meinel (1950), from Yerkes Observatory, Wisconsin [Figure 2-1] on a photographic plate spectrograph in January 1950. Several bands in the 7000 to 9000 Å region were recorded in which Meinel readily identified the P, Q and R branches within each group. For the stronger emission lines estimates were made of the relative intensities and wavelengths (accurate within a few Å) that showed excellent agreement with the extrapolated rotational-vibrational band positions of the OH molecule calculated by Herzberg (1939). Subsequent analysis of the rotational structure confirmed Meinel's identification and furthermore, provided refined values for the rotational and vibrational constants.

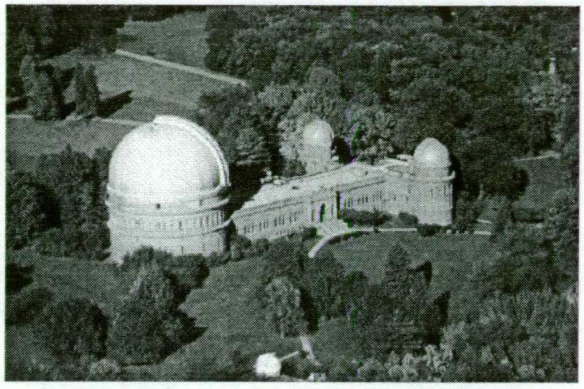

Figure 2-1. Yerkes Observatory, Wisconsin - site of the first OH observations by Meinel (1950).

Chamberlain and Roesler (1955) continued the spectrograph work at Yerkes to improve wavelength accuracy and in particular to resolve a wavelength discrepancy between measurements made on OH in airglow and those made in the laboratory using an oxyacetylene flame (Herman and Hornbeck, 1953). A micro-photometer tracing of their photographic plate between λ815 and λ900 nm, which includes the region of interest in this study, is reproduced in Figure 2-2.

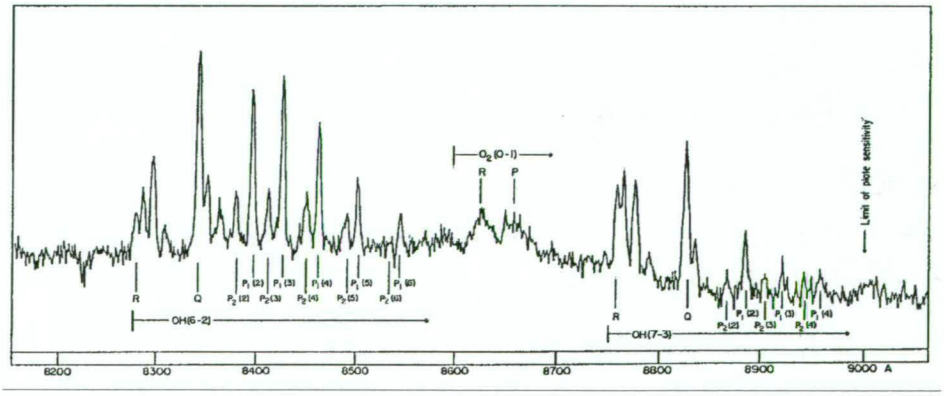

Figure 2-2. An infrared airglow spectrum (λ815-900 nm) obtained from a micro-photometer tracing of a photographic plate from the Yerkes spectrograph (Chamberlain and Roesler 1955)

The molecular bands of the OH Meinel system[†] appear above about 400 nm and are prominent through the infrared night airglow spectrum to about 4 microns [Figure 2-3]. Early estimates of the total system intensity were of the order of 4500-5000 kR [Chamberlain (1961), Wallace (1962)]. These estimates were usually made on the basis of one, or a few bands and could easily be in error by an order of magnitude with inaccurate data on the population of states (transition probabilities). Later calculations put the total intensity in the vicinity of 1000-1300kR (Evans and Llewellyn (1972), Good (1976), Meriwether (1989)), but this value nevertheless still constitutes the most intense feature in night airglow emissions.

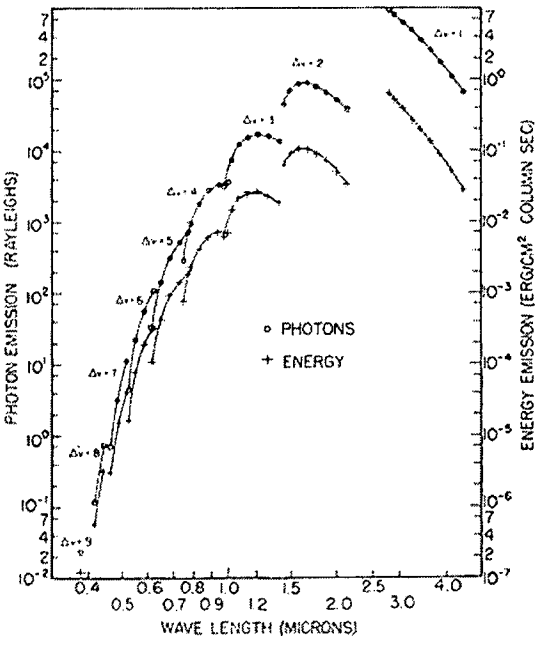

Figure 2-3. Predicted photon emission rates in Rayleighs and energy emission rates in erg/cm2 (column) sec for the OH Meinel band system. From Chamberlain (1961)

Chamberlain (1961) published the definitive text on atmospheric emissions a decade after OH was identified in the atmosphere. His book presents a comprehensive 'state of knowledge' on the emission at this time, including its band structure, wavelength tables, relative intensities, excitation mechanisms and rates, layer heights (determined, albeit with considerable uncertainty, via the van Rhijn method and rockets), transition probability calculations and various measurements of rotational temperature at mid latitudes that varied around 250 K.

2.2. *Instrumental Techniques*

Reviews of the early instrumental techniques applied to the study of infrared airglow are given in Vallance-Jones (1973), Meriwether (1985) and Forsyth and Wraight (1987).

[†] Meinel's name seems to have been first ascribed to the emissions in Chamberlain and Roesler (1955)

2.2.1. *Spectrometers*

Grating spectrographs with photographic plates, such as those used by Meinel (1950), Herman and Hornbeck (1953) and McPherson and Vallance-Jones (1960) or grating spectrometers with photomultiplier detectors [Kvifte (1967), Broadfoot and Kendall (1968), Shefov (1971), Sivjee *et al.* (1972)] provided spectra from the visible region out to about 1.1 μm. Beyond this limit solid-state photoconductive detectors (such as PbS, InSb, InGaAs and various varieties of doped Ge) must be used. The quantum efficiency of the photomultiplier (~20%) is about two orders of magnitude greater than the photographic plate. In general however, detector sensitivity decreases with wavelength and these devices must be operated at low temperatures to reduce thermal noise. Spectrometers commonly employed were of the Ebert-Fastie [Fastie (1952), Dick (1972), Armstrong (1975)] or Czerny-Turner [von Zahn *et al.* (1987), Conway *et al.* (1996), Elsworth (1997)] design. Instrument resolution, at a given wavelength, is principally determined by the grating characteristics, diffraction order, focal length and slit widths. These can normally be chosen to suit the wavelength region being investigated.

2.2.2. *Photometers*

Filter photometers, using similar detector systems, provide measurements at specific wavelengths with much greater throughput without the slit width limitations. Interference filters are manufactured to isolate the emission of interest, though sufficiently narrow filters are difficult far into the infrared region. Multi-filter and/or multi-field photometers can be used to monitor the relative intensities of various emissions simultaneously [Gattinger and Vallance Jones (1972), Wiens and Weill (1973), Meriwether (1975)]. If the filter is tilted relative to the incident light, a wavelength shift occurs which can be used to tune the filter, or to 'scan' across a small wavelength interval, such as used in tilting filter photometers [Eather and Reasoner (1969), Fiocco *et al.* (1970), Takahashi *et al.* (1974)]. Simple photometer systems can be made light, rugged and reliable, and are therefore ideal for balloon [Evans *et al.* (1973), Moreels *et al.* (1973)], aircraft or rocket [Heppner and Meredith (1958), Harrison (1970), Evans *et al.* (1973), Rogers *et al.* (1973), Good (1976), Watanabe *et al.* (1981), Lopez-Moreno *et al.* (1984)], and satellite [Shepherd *et al.* (1973)] studies.

2.2.3. *Camera Systems*

Photographic and TV camera systems, usually including interference filters for pass-band selection, have been used extensively to monitor wave fields and airglow structures over large regions of the sky. [Peterson and Kieffaber (1973), Moreels and Hersé (1977), Hersé *et al.* (1980), Hapgood and Taylor (1982)]. The invention of charge-coupled-device (CCD) detectors in 1970 [Boyle and Smith (1970)] greatly extended development and application of imaging instruments [Taylor *et al.* (1991), Hecht *et al.* (1997), Kubota *et al.* (1999)]. CCD detectors are particularly efficient in the infrared, with typical quantum efficiencies of 70% extending to 2μm (cooled CCDs behave as a photographic plate with an ISO rating of $3x10^6$). CCD detectors have also been fitted to grating spectrometers with the principle advantage of being able to collect the whole spectra at once across the array, although resolution is limited by the pixel size [Elsworth *et al.* (1997)].

2.2.4. *Fourier transform spectrometers*

Fourier transform spectrometers, (or FTIR spectroscopy) first conceived by Fellgett (1951) and put into practice by Connes and Gush (1960) are an adaptation of the Michelson interferometer [Figure 2-4]. The incident beam is split, and an optical path difference introduced by the moving mirror. An interferogram is produced as the beams recombine and interfere at the beamsplitter. For an increase in the path difference of λ there is one cycle in the intensity variation of that wavelength component. The detector measures the variation in energy versus time for all wavelengths simultaneously (a benefit called the *Fellgett advantage*). Signal-to-noise can be improved by time-averaging samples and the instrument resolution is proportional to the total path difference scanned. The intensity versus frequency spectrum is recovered by Fourier transform of the interferogram. A much larger throughput (or *etendue*) than equivalent grating

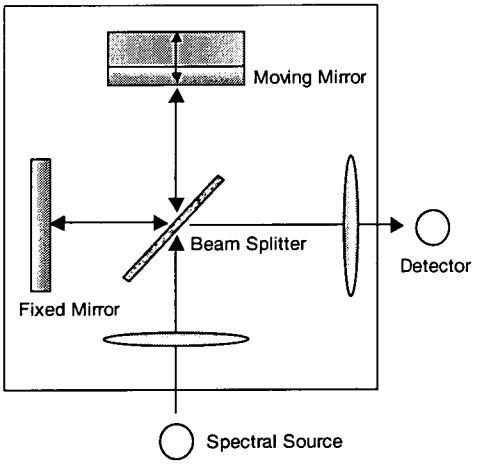

Figure 2-4. Fourier transform spectrometer Schematic.

instruments is achieved due to the area of the entrance aperture (known as the *Jacquinot advantage*). The method is particularly suited to the spectral region beyond 1 μm where solid-state IR (Ge or InGaAa) detectors (with noise independent of signal) can be employed. The Fellgett advantage is lost with shot-noise limited detectors such as photomultipliers. Lowe (1966), Mulligan *et al.* (1995) and Espy and Witt (1996) have used instruments of this type to study hydroxyl emissions.

2.2.5. *Fabry-Perot Spectrometers*

Fabry-Perot spectrometers (FPS) isolate particular wavelengths via interference in the cavity between two optically flat glass plates, known as *etalons*. The optical path length between successive rays is $2nd$, where n is the refractive index in the cavity and d is the plate separation [Figure 2-5]. Multiple pass-bands are transmitted (an Airy function), corresponding to where $k\lambda=2nd$, (k is the integer interference order), so it is usually necessary to isolate one pass-band with an interference filter, or second set of etalons. Resolution of the instrument increases with plate spacing, with a corresponding decrease in the free spectral range (wavelength between consecutive orders). FPS can thus offer low resolution over a wider wavelength range, suitable for rotational temperature measurements [Gattinger (1968)] or very high resolution over a limited wavelength range, sufficient to measure the Doppler temperature of an emission line directly. [Jacka (1984), Hecht *et al.* (1987), Greet *et al.* (1994), East *et al.* (1995)].

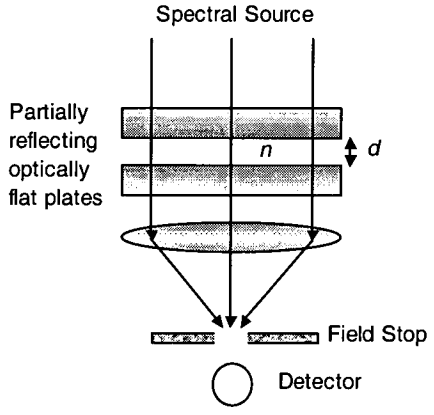

Figure 2-5. Schematic of the Fabry-Perot Spectrometer.

These instruments are mentioned specifically because of their direct association with this work. All of them have, or will in the near future, contribute to the OH monitoring program at Davis station. An overview of the Davis instrument suite and details of the Czerny-Turner spectrometer are given in the next chapter.

2.3. *Molecular Spectroscopy*

Molecular species dominate the composition of the Earth's atmosphere to altitudes around 100 km. In the upper stratosphere and mesosphere where physical parameters are difficult to measure directly, molecular spectroscopy provides a well-established and economical means of remote sensing. As molecules react, suffer collisions, vibrate and rotate, discrete quanta of energy are absorbed or emitted. Spectroscopy is the measurement and analysis of absorption and emission spectra to derive information about both the internal structure of the molecule (eg its energy states, bond strength, nuclear separation, symmetry and vibration frequency), and the bulk properties of the gas (eg energy state populations and transition probabilities, isotopic abundance and temperature).

The principles of atomic and molecular spectroscopy were pioneered by Herzberg (1939). With the variety of applications and a vast number of molecules to study, the field is enormously diverse. Different branches of spectroscopy express energy in units of ergs/molecule, calories/gm mole, eV, or joules depending on the magnitude of the energy involved. It is often convenient to express the quantity in terms of the frequency of radiation emitted or absorbed in the transition, since E = hν, or as a wavenumber (ν/c) in reciprocal centimetres.

Spectral characteristics of a particular molecule are governed by its energy states and transitions from one state to another. The total number of states in any molecule is extremely large as its total energy is the sum of all its quantised translational, electronic, vibrational, rotational and nuclear orientation energies;

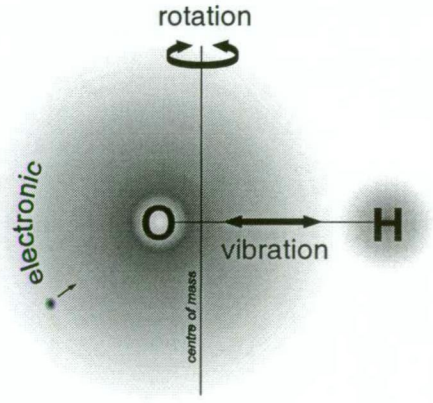

Figure 2-6. Energy modes in the OH molecule

$$E_{\text{total}} = E_{\text{translational}} + E_{\text{electronic}} + E_{\text{vibrational}} + E_{\text{rotational}} + E_{\text{nuclear orientation}}$$

The first describes the bulk motion of the molecule as a whole, the next three terms (in order of decreasing magnitude) involve the internal motion of the nuclear framework of the molecule and attractive and repulsive forces among the nuclei and electrons. The last includes the interaction of nuclear magnetic and electrostatic

moments (orientation) between themselves and with the electrons. These energy components are briefly described in the following section

2.3.1. Translational Energy

Classically, *translational energy* of a molecule of mass M and who's centre of mass travels with velocity **v** can be written $E_{translational} = {}^1/_2 M\mathbf{v}^2$ or, by the classical equipartition of energy theorem for a large number of molecules in a gas (having 3 degrees of freedom), the average translational kinetic energy is ${}^3/_2 kT$ at a given temperature T (~0.04eV at room temperature). All values of **v**, or T are allowed in classical mechanics, whereas solutions to quantum mechanical equations exist involving quantised energies. For practical situations, the number of energy levels is extremely large, and the interval between levels negligible, so that the range of translational energies available is essentially continuous. Few spectroscopic studies involve changes in translational energies.

2.3.2. Electronic Energy

Kinetic energy due to electron motion about each atom in the molecule and potential energy arising from mutual repulsion and nuclei attraction constitute the *electronic energy*. Nomenclature for electronic states varies among fields and authors but in general there are 3 cases considered with directly analogous notation. These are:

a) single electron states labelled with lower case letters eg. s, p, d, f;
b) states of a collection of atoms considered separately with many electrons labelled with upper case letters eg. S, P, D, F and;
c) molecular states with many electrons labelled with the Greek equivalent eg. Σ, Π, Δ, Φ.

Electrons orbit nuclei in *shells* labelled *K*, *L*, *M*, *N*, ... corresponding to the principle quantum number n = 1, 2, 3, 4, ... respectively. For simple hydrogen-like atoms energy in each shell can be written,

$$E_{electronic} = \frac{-2\pi^2 \mu e^4 Z^2}{h^2 n^2} \qquad \textit{Equation 2-1}$$

where Z is the atomic number, and μ is reduced mass, $m_e m_n/(m_e + m_n)$ for electron mass m_e and nuclear mass m_n. In this form the energies are negative, reaching the limit of zero as the electron becomes completely separated from the nucleus. Each electron possesses *orbital* angular momentum l with values 0, 1, 2, ...$(n-1)$ labelled *s,*

p, d, f ... and *spin* angular momentum *s* with values ±½, which divides the energy of electrons within each shell.

In the presence of a magnetic field, precession of orbital angular momenta and alignment of spin angular momenta takes place, which further splits the energy in each state (*Zeeman* splitting, and the *Paschen-Back* effect for stronger fields). Secondary splitting also occurs in an applied electric field (*Stark* effect). Two further magnetic quantum numbers m_l; with values $-l$, $-l+1$, .. $+l$ ($2l+1$ degenerate states) and m_s; with values +½ (up) and –½ (down) are used to distinguish these split states. In the absence of a magnetic or electric field all states with the same *n* and *l* have the same energy and are said to be *degenerate.*

Usually λ is used in place of m_l such that $\lambda = |m_l| = 0, 1, \ldots l$ with descriptors σ, π, δ, φ, ... with the understanding that each λ (apart from 0) is a doubly degenerate state. Electrons fill shells according to the Pauli exclusion principle such that no two electrons have the same value of n, *l*, m_l and m_s. Individual electrons are labelled with numerical *n*, the angular momentum label (*s*, *p*, *d*, *f*) and the degenerate λ (σ,π,δ,φ), such as a 3*p*σ electron (one of six 3p degenerate states with $m_l = -1, 0, +1$ each with $m_s = +½$ and $-½$). [Table 2-1]

Principle Quantum. No.	*n*	1 K	2 L				3 M								
Orbital Angular Momentum	*l*	0 s	0 s	1 p			0 s	1 p			2 d				
Spin Angular Momentum	*s*	±½	±½	±½	±½	±½	±½	±½	±½	±½	±½	±½	±½	±½	±½
Magnetic Q. No. (degeneracy)	m_l	0	0	-1	0	+1	0	-1	0	+1	-2	-1	0	+1	+3
Magnetic Spin (multiplicity)	m_s	↑↓	↑↓	↑↓	↑↓	↑↓	↑↓	↑↓	↑↓	↑↓	↑↓	↑↓	↑↓	↑↓	↑↓
Lambda = $\lvert m_l \rvert$	λ	σ	σ		σ	π	σ		σ	π			σ	π	δ
State		1sσ	2sσ		2pσ	2pπ	3sσ		3pσ	3pπ			3dσ	3dπ	3dδ

Table 2-1. Possible electron states for the first 3 principle quantum numbers.

In many electron systems, vector addition of the orbital angular momenta for each electron l_i produces a resultant orbital angular momenta *L* (positive integrals) with labels *S, P, D, F* and magnitudes $\sqrt{l(l+1)}\ h/2\pi$. Similarly, the spin angular momenta, s_i add to produce resultant spin angular momenta *S* (integral or half integral) with magnitudes $\sqrt{s(s+1)}\ h/2\pi$. When a shell contains the maximum number of electrons

(a *closed* shell) the resultant L and S values are zero. Thus, closed shell electrons need not be taken into account when deriving resultant angular momenta.

The *total* angular momentum $J = L + S$ has integer or half integer values. The number of ways L and S can be added together to yield a quantised J is $2S+1$ (termed the *multiplicity*). Degenerate states are normally labelled as ${}^{2S+1}L_J$. For example, if an atom contained one unfilled p-shell and one unfilled d-shell electron $l_1 = 1$, $l_2 = 2$, thus $L = 3$, 2 or 1 and $J = 3$, 2, or 1 for $S = 0$ (singlet) and $J = 4$, 3, 2, 1, or 0 for $S=1$ (triplets) thus the states ${}^1F_{3,2,1}$, ${}^1D_{3,2,1}$, ${}^1P_{3,2,1}$, ${}^3F_{4,3,2,1,0}$, ${}^3D_{4,3,2,1,0}$, and ${}^3P_{4,3,2,1,0}$ are all possible. In a magnetic field, the degeneracy in each state is resolved by the quantum number $M_J = M_L + M_S$, the sums of the m_l *and* m_s, having $2J+1$ values (J, $J-1,..,-J$).

Now, several atoms with different L, S, M_L and M_S can be brought together and vector added to define the molecular states. Without the spin coupling, the number of states is defined by the quantum number $\Lambda = |M_{L1} + M_{L2}|$, analogous to λ, which has values 0, 1, 2, 3 ... and labels Σ, Π, Δ, Φ... where values of $\Lambda > 0$ are doubly degenerate as before. In this case, as there are two nuclei, the Σ ($\Lambda = 0$) state may add in a symmetric or anti-symmetric manner with respect to a plane through the internuclear axis. Σ states are thus split and Σ^+ and Σ^- are used to express the symmetry property.

Including spin coupling defines the quantum number $\Omega = \Lambda + S = |M_{J1} + M_{J2}|$ which is the total electronic angular momentum of the molecule along the internuclear axis and determines the *multiplicity* of the resultant molecular state. S has values ($S_1 + S_2$), (S_1+S_2-1), ... $|S_1-S_2|$ and the states are termed singlet, doublet, triplet ... etc.

Molecular states are labelled with ${}^{2S+1}\Lambda_\Omega$ in a similar way to multi-electron states. Not all predicted states of the molecule are observed. Often a prefix is added to indicate that particular state is observed in the spectra. X is prefixed to indicate an observed ground state, followed by A, B,C ... for observed electronic excited states.

Let us consider now the ground state of OH. Taken as separate atoms we have ground state O in a ${}^3P$ state ($L_O = 1$) and the H atom in a ${}^2S$ state ($L_H = 0$). We have $M_{LO} = -1,0,+1$ and $M_{LH} = 0$, therefore Λ has values 0 and 1 corresponding to a Σ and the doubly degenerate Π states. Since the sum of L_O and L_H is odd the Σ state

symmetry is negative. For spin, $S_O = 1$ and $S_H = {}^1/_2$ therefore S has values ${}^1/_2$ and ${}^3/_2$. Accordingly, the molecule has four electronic states $^2\Pi$, $^2\Sigma^-$, $^4\Sigma^-$ and $^4\Pi$ all feasible from the electron configuration $(1s\sigma)^2(2s\sigma)^2(2p\sigma)^2(2p\pi)^3$ (where superscripts indicate the number of electrons in each state).

The first excited state has one electron promoted from $2p\sigma$ to a $2p\pi$ state, so the molecule has the electron configuration $(1s\sigma)^2(2s\sigma)^2(2p\sigma)^1(2p\pi)^4$. The $2p\pi$ electrons are now both paired and one unpaired $2p\sigma$ electron is left. O is in a ^1D state ($L_O = 2$) and H remains in a ^2S state ($L_H = 0$). Symmetry is positive, spin $S_O = 0$ and $S_H = {}^1/_2$ and Λ has values 0 and 2. States $^2\Sigma^+$ and $^2\Delta$ are therefore possible for the first electronic excited state.

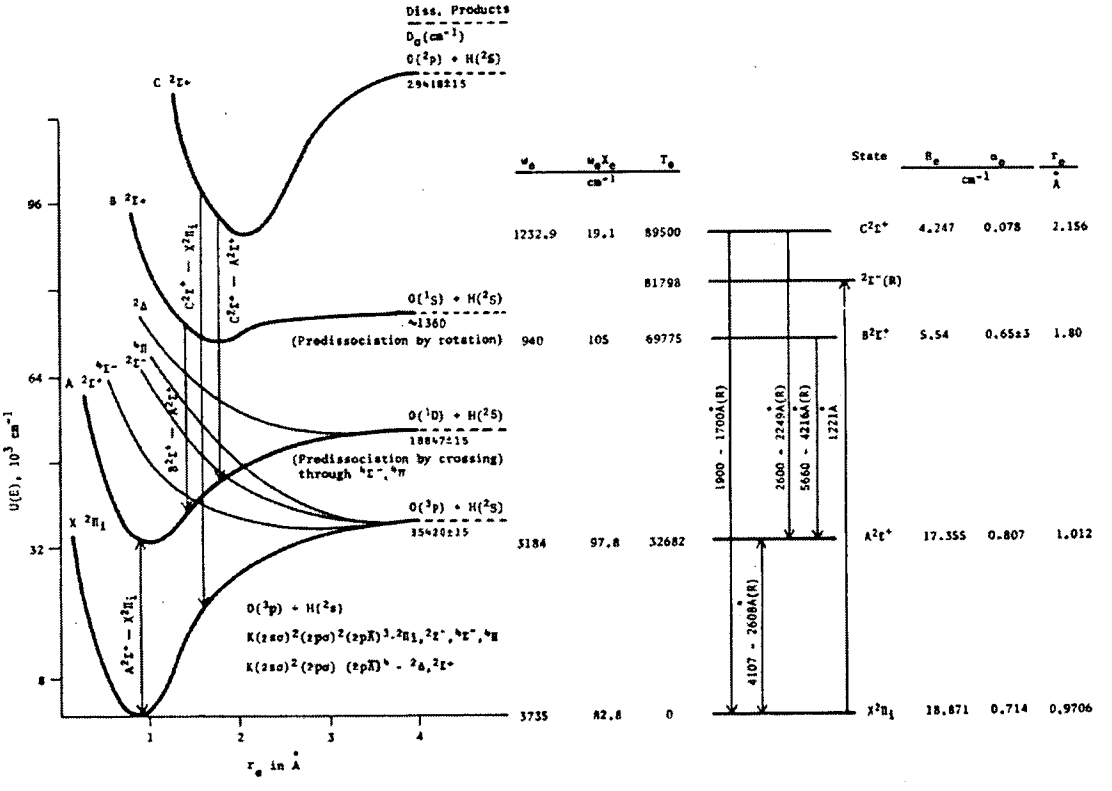

Figure 2-7. Electronic states of OH, observed states are prefix with letters X, A, B and C. Various vibrational and rotational constants are also shown [from Mohan and Shardanand (1975)].

Figure 2-7, from Mohan and Shardanand (1975), illustrates energy potential curves of the ground and excited states of OH with transitions that occur between them. Clearly there is no potential 'well' for the $^2\Sigma^-$, $^4\Sigma^-$ and $^4\Pi$ ground states or the $^2\Delta$ first excited state so the atoms will rapidly dissociate. For the observed ground state, spin-splitting (from the electron spin – orbital electronic angular momentum interaction along the internuclear axis) results in the two sub-states labelled $X^2\Pi_{1/2}$ and $X^2\Pi_{3/2}$.

For OH $^2\Pi$ state is 'inverted' (written $^2\Pi_i$) rather than a 'regular' state as the $X^2\Pi_{1/2}$ is higher in energy than the $X^2\Pi_{3/2}$ state. The first excited state possesses no resultant orbital angular momentum and is thus labelled $A^2\Sigma^+$.

If the nuclei are the same (forming a homonuclear molecule) symmetry with respect to the centre of the molecule is indicated by the subscripts *u* and *g*. For example, an observed molecular state of say N_2 may be described as $A^3\Sigma_u^+$.

2.3.3. Vibrational energy

Molecules are not rigid structures and their *vibrational energy* is manifested as the stretching and bending oscillations along the atomic bond axes. These vibrations, for the simplest case of a diatomic molecule can be treated as a simple harmonic oscillator. Quantised vibrational energy can be written

$$E_{\text{vibrational}} = h\nu_{\text{osc}}(v + \tfrac{1}{2}) \qquad \textit{Equation 2-2}$$

where $v = 0,1,2,..$ is the vibrational quantum number, ν_{osc} is the vibration frequency = $(1/2\pi)\sqrt{k/\mu}$, with reduced mass μ and k is the *force constant* of the bond, a characteristic of the particular molecule. As is customary in spectroscopy, this expression may be written as in the form of *term values* (in cm^{-1} units), by dividing by hc. Thus

$$G(v) = E_{\text{vibrational}}/hc = \nu_{\text{osc}}(v + \tfrac{1}{2})/c = \omega(v + \tfrac{1}{2}) \qquad \textit{Equation 2-3}$$

Where ω is the vibration frequency in cm^{-1}. Transitions from one vibrational level to another are subject to the selection rule that v must change by one ($\Delta v = \pm 1$), and the condition that a change in dipole moment occurs as the molecule undergoes vibration.

In reality the vibration is not harmonic as the atoms dissociate at some limit in separation. Anharmonic oscillation may be approximated by adding terms to $G(v)$:

$$G(v) = \omega_e(v + \tfrac{1}{2}) - \omega_e x_e(v + \tfrac{1}{2})^2 + \omega_e y_e(v + \tfrac{1}{2})^3 + \ldots \qquad \textit{Equation 2-4}$$

and results in perturbed energy levels, which decrease in separation with increasing vibrational level (v) and allow modification of the selection rules such that Δv may equal $\pm 2, \pm 3$ ... Transitions for which $\Delta v=1$ are termed *fundamental* transitions and for $\Delta v>1$ are termed *overtone* transitions.

2.3.4. *Rotational energy*

Molecules in a gas state are also free to undergo rotation about their axes. If the diatomic molecule is treated as a rigid rotator (vibration ignored) it can be characterised by a moment of inertia $I = \mu r^2$, where μ is the reduced mass and r is the atomic separation. *Rotational energies* are also quantised and defined by the *rotational* quantum number J = 0,1,2,3 such that

$$E_{\text{rotational}} = J(J + 1)(\hbar^2/2I) \qquad \textit{Equation 2-5}$$

where $\hbar$ is Planck's constant on 2π. In term values form this expression becomes

$$F(J) = E_{\text{rotational}}/hc = (h/8\pi^2cI)J(J + 1) = BJ(J + 1) \qquad \textit{Equation 2-6}$$

where B is termed the rotational constant. Similar to vibrational transitions, selection rules require $\Delta J = 0, \pm 1$ and the transition will only occur if the diatomic molecule possesses a permanent dipole moment.

Non-rigidity of the molecular bond allows stretching with higher rotational energy due to centrifugal force, increasing the internuclear separation and consequently the molecules moment of inertia. As for vibration, adding higher order terms can approximate non-rigid rotation:

$$F(J) = BJ(J + 1) - DJ^2(J + 1)^2 + \ldots \qquad \textit{Equation 2-7}$$

where D is a small correction term, and a function of the rotation frequency.

Moreover, vibration and rotation in a molecule take place simultaneously and interactions occur between them. As a result, equilibrium separation varies with vibrational level and rotational constants for each level (B_v, D_v) can be defined accordingly

$$B_v = B_e - \alpha_e(v + \tfrac{1}{2}) + \gamma_e(v + \tfrac{1}{2})^2 \ldots \qquad \textit{Equation 2-8}$$

$$D_v = D_e + \beta_e(v + \tfrac{1}{2}) + \ldots \qquad \textit{Equation 2-9}$$

where the subscript e signifies the equilibrium level and α_e , γ_e and β_e are constants that describe the anharmonicity. B_v and D_v are substituted to derive $F_v(J)$

In addition to the spin multiplet structure due to spin-orbit interactions, another form of splitting arises out of the interaction between nuclear rotation and orbital angular momentum of the electrons *L*. This is known as *Λ-doubling* and is present for all

states where $\Lambda \neq 0$. Splitting increases with greater rotational speed (higher J values) and is represented with Λ-doubling constants p_v and q_v, which are different for each electronic and spin-split component.

Labelling for Λ-doubled components are either + and – depending on whether symmetry is the same or inverted on reflection at the origin (i.e. the eigenfunction describing the state changes sign on reflection), or alternatively with *e* and *f* depending on whether the resultant state is decreased or increased in energy respectively.

2.3.5. Nuclear Orientation

Nuclei of each atom may also possess their own intrinsic spin (the proton magnetic moment), which will split energy states depending on the orientation of the nucleus. This is known as *hyperfine splitting*. It is characterised by the *nuclear* angular momentum, I, with magnitude $\sqrt{I(I+1)}\ h/2\pi$, and its quantum number M_I which may have values +I, +I-1, +I-2,.. -I. Including nuclear spin the total angular momentum then becomes F = J+I (a total of 2I+1 states). However, coupling between J and I is very weak, thus the energy splitting involved is extremely small, and each state is equally populated at all temperatures just above absolute zero. Hyperfine splitting can only be observed in spectra from instruments with very great resolving power.

2.3.6. OH Vibrational and Rotational Constants

Molecular quantities for $^{16}O^{1}H$ and the vibrational and rotational constants for the $^2\Pi_i$ and $^2\Sigma^+$ states are summarised in Table 2-2. These values are from Huber and Herzberg (1979). The energy of a particular vibrational-rotational level may be expressed as

$$
\begin{aligned}
H(v) = {} & T_e \ (electronic) \\
& + \omega_e(v + \tfrac{1}{2}) - \omega_e x_e(v + \tfrac{1}{2})^2 + \omega_e y_e(v + \tfrac{1}{2})^3 + \ldots \ (vibrational) \\
& + B_{ev}J(J+1) - D_{ev}J^2(J+1)^2 + \ldots \ (rotational) \\
& + q_v J(J+1) + p_v J(J+1) \ (\Lambda\text{-}doubling) \\
& + (hyperfine)
\end{aligned}
\qquad \text{Equation 2-10}
$$

Quantity	Symbol	$^{16}O^{1}H$		Unit
O mass	O	15.9994		amu
H mass	H	1.00794		amu
Reduced mass	μ	0.948204436		amu
Ionization Potential	IP	12.9		eV
Quantity	Symbol	$^2\Pi_i$	$^2\Sigma^+$	Unit
Dissociation Energy	D_o	4.392	2.337	eV
		35420	18847	cm^{-1}
Internuclear distance	R_e	0.96966	1.0121	Å
Electronic Energy	T_e	0	32684.1	cm^{-1}
Vibrational Constants	ω_e	3737.76	3178.8	cm^{-1}
	$\omega_e x_e$	84.881	92.91	cm^{-1}
	$\omega_e y_e$	0.540	1.791	cm^{-1}
	$\omega_e z_e$	0.0213	0.3236	cm^{-1}
Rotational Constants	B_e	18.910	17.358	cm^{-1}
	D_e	1.938×10^{-3}	2.039×10^{-3}	cm^{-1}
	α_e	0.7242	0.786	cm^{-1}
	β_e	-4.3×10^{-5}		cm^{-1}
	γ_e	0.00207		cm^{-1}
Λ-doubling constants	p_v	0.235–0.006v		cm-1
	q_v	-0.0391+0.0018v		cm^{-1}

Table 2-2. Molecular quantities for $^{16}O^{1}H$ and the vibrational and rotational constants for the $^2\Pi_i$ and $^2\Sigma^+$ states.

2.3.7. Transitions between states

Transitions between electronic, vibrational and rotational states result in emission or absorption of radiation. Electronic transitions for OH, e.g. between the ground and first excited states ($A^2\Sigma^+ \leftrightarrow X^2\Pi_i$), result in ultraviolet emission bands (2444-4107Å). Electronic spectra are detailed in, for example Mohan and Shardanand (1975).

Transitions also occur between vibrational and rotational levels of OH molecules in any given electronic state (as they possess a permanent dipole moment). Transitions are governed by selection rules. For total angular momentum, $\Delta J = 0, \pm1$ (except if J'=0 and J''=0) is the most rigorous and results in P, Q and R branches for $\Delta J = +1, 0, -1$ respectively. Figure 2-8 shows a schematic of the transitions between vibrational-rotational energy levels for the $X^2\Pi_i$ electronic states for lower J values.

Nomenclature for labelling transitions within one state is of the form $(v'\text{-}v'')\Delta J_S(L'')_\Lambda$ where v' and v'' are upper and lower state vibrational quantum numbers, ΔJ is the label P, Q, R. Spin angular momentum S, lower state Λ-doubling $\Lambda=e$ or f and lower state orbital angular momentum L'', for example $(6\text{-}2)P_1(2)_e$. Notation differs considerably between texts, for example Osterbrock *et al.* (1996) use J'' in place of

L" which has half integer values and upper state Λ instead of lower state Λ. Often the letter *k* or N is used in place of L also.

Typically also ΔL = 0, ±1 and ΔS = 0 also hold as long as the spin-orbit coupling is weak. Transitions for which ΔL = ±2, ±3, ... do sometimes occur. For atomic transitions these are said to be *forbidden*, for example the atomic oxygen $^1S \rightarrow {}^1D$ (ΔL = 2) which produces the λ558 nm auroral emission. Between molecular spin-split states these are called *satellite transitions*. In this case the labelling convention is of the form $(v'\text{-}v'')^{\Delta L}\Delta J_{S',S''}(L'')_{\Lambda}$ where ΔL can have labels O,P,Q,R,S corresponding to values -2,-1,0,1,2 and S', S" are the upper and lower spin quantum numbers. For example $(6\text{-}2)^{S}R_{21}(1)_e$ or $(5\text{-}3)^{P}Q_{12}(2)_f$ lines.

Symmetry selection rules require a change of symmetry in the Λ-doubled component +↔– for the transition. This corresponds to *e*↔*e* or *f*↔*f* transitions for P and R branches and *e*↔*f* transitions for the Q branch.

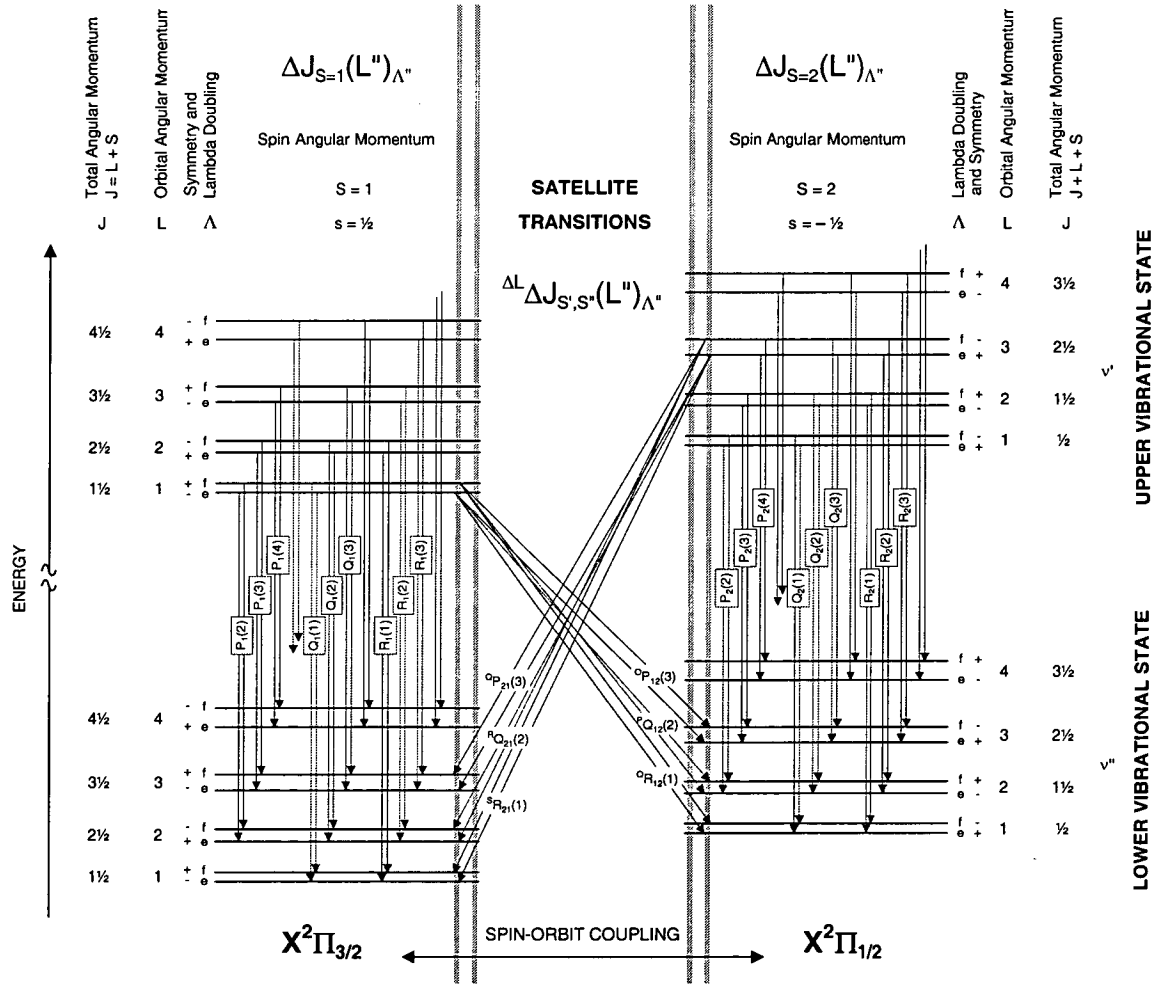

Figure 2-8. Schematic of the transitions between vibrational-rotational energy levels for the $X^2\Pi_i$ electronic states and lower J values.

2.3.8. *Transition probability*

Consider now a population of molecules in a variety of electronic and vibrational-rotational states. If the population of molecules per unit volume in an upper vibrational-rotational state is $N_{v'J'}$ and a lower state is $N_{v''J''}$ in an incident radiation field of energy density ρ we can write the rate of change of population due to state transitions as

$$\frac{dN_{v'J'}}{dt} = \frac{-dN_{v''J''}}{dt} = A_{v'J'\rightarrow v''J''}N_{v'J'} - B_{v'J'\rightarrow v''J''}\rho N_{v'J'} + B_{v''J''\rightarrow v'J'}\rho N_{v''J''} \qquad \textit{Equation 2-11}$$

where the coefficients $A_{v'J'\rightarrow v''J''}$, $B_{v'J'\rightarrow v''J''}$ and $B_{v''J''\rightarrow v'J'}$ are Einstein coefficients or *transition probabilities* for spontaneous emission, induced absorption and induced or stimulated emission respectively.

If the radiation energy density $\rho = 0$ then we have simply

$$\frac{dN_{v'J'}}{dt} = A_{v'J'\rightarrow v''J''}N_{v'J'} \qquad \textit{Equation 2-12}$$

which has a solution of the form $N_{v'J'}(t) = N_{v'J'}(0)e^{-At}$ so that $A_{v'J'\rightarrow v''J''}$ is inversely proportional to the radiative lifetime of the upper state ie

$$\tau_{v'} = [\sum_{v'} A_{v'J'\rightarrow v''J''}]^{-1}. \qquad \textit{Equation 2-13}$$

The radiative lifetime decreases with vibrational level, for example OH v'=1 is approximately 80 milliseconds and v'=6 approximately 10 milliseconds. Turnbull and Lowe (1989) give a comparison of different v' radiative lifetimes between published transition probability sets. $A_{v'J'\rightarrow v''J''}$ can be determined for each transition from a knowledge of the molecule's electric dipole moment function (EDMF). We can write

$$A_{v'J'\rightarrow v''J''} = \frac{64\pi^4 E^3_{v'J'\rightarrow v''J''}}{3h^4(2J'+1)} |< v'J' \,|\mu(r)|\, v''J''>|^2 S_{J'J''}, \qquad \textit{Equation 2-14}$$

where $E_{v'J'\rightarrow v''J''}$ is the energy difference between the states, $\mu(r)$ is the EDMF in matrix element form and $S_{J'J''}$ is the line strength factor. The choice of theoretical, or empirical EDMF that have been used in published sets of transition probabilities are listed in Table 2-3. The EDMF for OH is particularly difficult to determine because of the large curvature near r_e (equilibrium separation) which results in the intense overtone ($\Delta v>1$) transitions and also the vibrational-rotational interaction and spin uncoupling strongly modify the line strengths as a function of rotation. Consequently large numbers of line strength measurements are necessary to characterize the EDMF. Nelson *et al.* (1990) have made a comparison of the published EDMFs, which show considerable differences.

Transition Probability Set	EDMF
Heaps and Herzberg (1952)	
Murphy (1971)	Ferguson and Parkinson (1963)
Mies (1974)	Stevens *et al.* (1974)
Langhoff, Werner, Rosmus (1986)	Werner *et al.* (1983) MCSCF(7)-SCEP
Langhoff Bauschlicher, Taylor (1989)	
Turnbull and Lowe (1989)	Turnbull and Lowe (1988) empirical
Nelson *et al.* (1990)	Empirical

Table 2-3. Electric Dipole Moment Functions used in the published sets of transition probabilities.

2.3.9. Rotational temperature

Intensity of an observed spectral line for a spontaneous emission involving energy $E_{v'J'\rightarrow v''J''}$, logically depends on the number of molecules in the upper state v'J' and on the probability of their transition to v"J", thus in photons.s^{-1}.cm^{-3} units we can write

$$I_{v'J'\rightarrow v''J''} = N_{v'J'}\, A_{v'J'\rightarrow v''J''}. \qquad \textit{Equation 2-15}$$

The population in any vibrational-rotational level ($N_{v'J'}$) may be determined from the total population of the upper vibrational state ($N_{v'}$) with knowledge of the rotational *partition function* Q_r, thus

$$N_{v'J'} = N_{v'}\,(2J'+1)\,exp(-E'_{v'J'}/kT_{rot})/Q_r \qquad \textit{Equation 2-16}$$

where the partition function is written

$$Q_r = \sum_{J'}^{\infty}(2J'+1)exp(-E_{v'J'}/kT_{rot}) \qquad \textit{Equation 2-17}$$

k is Boltzmanns constant, T_{rot} is termed the *rotational temperature* and $E_{v'J'}(J')$ is the rotational energy in the form hcF(J').

Combining these equations we can write the intensity of a given transition as

$$I_{v'J'\rightarrow v''J''} = A_{v'J'\rightarrow v''J''}\, N_{v'}\,(2J'+1)\,exp(-E'_{v'J'}/kT_{rot})/Q_r \qquad \textit{Equation 2-18}$$

For a ratio of any two lines within the same vibrational band $N_{v'}$ and Q_r cancel so that

$$\frac{I_n}{I_m} = \frac{A_n\,(2J_n+1)}{A_m\,(2J_m+1)}\,exp\left(\frac{E_m-E_n}{kT_{rot}}\right) \qquad \textit{Equation 2-19}$$

which may be re-written in terms of the rotational temperature as

$$T_{rot} = \frac{E_m-E_n}{k\,ln\left(\frac{I_n\,A_m(2J'_m+1)}{I_m\,A_n(2J'_n+1)}\right)} \qquad \textit{Equation 2-20}$$

Figure 2-9 plots the intensity distribution of the OH(6-2) P-branch rotational transitions as a function of wavelength at selected temperatures [obtained with the

Mies (1974) transition probabilities]. Clearly, the greatest temperature sensitivity is shown by ratios that span the peak of the intensity distribution (e.g. $P_1(2)/P_1(3)$ or $P_1(2)/P_1(4)$ ratios are much more sensitive to temperature than the $P_1(4)/P_1(5)$ ratio at these temperatures).

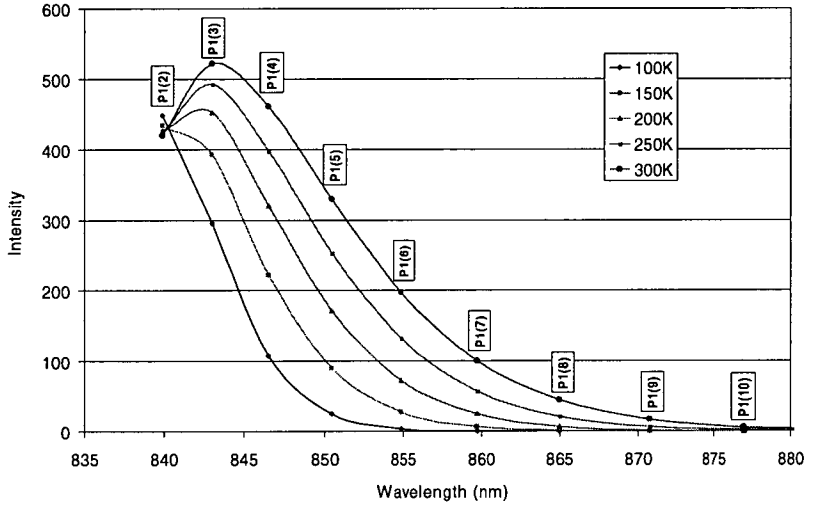

Figure 2-9. Intensity distribution for the P-branch rotational levels of OH(6-2) at various rotational temperatures using the transition probabilities of Mies (1974).

An assumption is made here that the distribution of rotational states (J') is Boltzmann like (i.e. the rotational state population attains a Boltzmann distribution equal to the kinetic temperature of the bulk gas). However, the creation process for OH^* (see section 2.4.1) is highly exothermic. The total energy available for populating vibrational and rotational states is the sum of the reaction exothermicity (~26939 cm^{-1}) and the translational (kinetic) energy ($^3/_2kT \approx 208$ cm^{-1} at 200K) of the reactants (Polanyi and Woodall, 1972).

Figure 2-10 shows the energy levels of the OH $X^2\Pi_{3/2}$ state for v'=4 to 9 and J' = 1.5 to 15.5. The exothermic and kinetic energy levels available for populating states are also plotted as horizontal lines. It is apparent that all states below v' = 9, J' = 8.5 should be populated in a kinetic energy field at 200K.

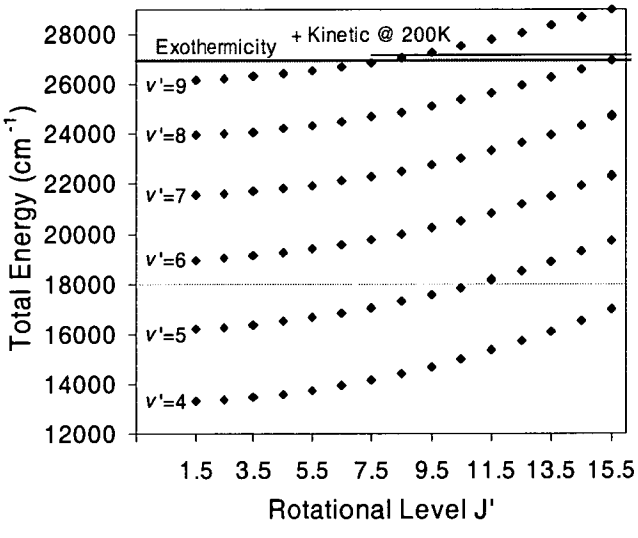

Figure 2-10. Energy levels of the OH $X^2\Pi_{3/2}$ state for v'=4 to 9 and J' = 1.5 to 15.5 and showing the exothermic and kinetic energy available for populating states.

A Boltzmann-like distribution of rotational state populations is only attained through collision with other gas molecules (mainly N_2 and O_2). Walterscheid *et al.* (1986) calculate that the collision frequency in the mesopause is $\sim 10^4\ s^{-1}$ [Weast *et al.* (1987) gives a collision frequency of $3.76\times10^4\ s^{-1}$ at 85 km from the mean speed $371.6\ ms^{-1}$ divided by the mean free path of 9.9×10^{-3} m]. Thus for v'=6 with an average radiative lifetime of ~10 ms the molecule undergoes about 100 collisions before radiating. This is generally sufficient for rotational *thermalisation* to occur, but as the transition process is stochastic, a small percentage of radiative transitions will occur before thermalisation of the rotational levels is attained.

More importantly, population re-distribution through collisions is poor where the separation between adjacent rotational energy levels is much greater than the local kinetic energy (as noted by referee 1 in the review of this thesis). Figure 2-11 plots the energy separation between adjacent rotational states for the v'=6 vibrational level. Energy separation increases in a near linear manner with J'. Kinetic energy levels ($^3/_2$kT) at temperatures from 100 to 300 K are also plotted.

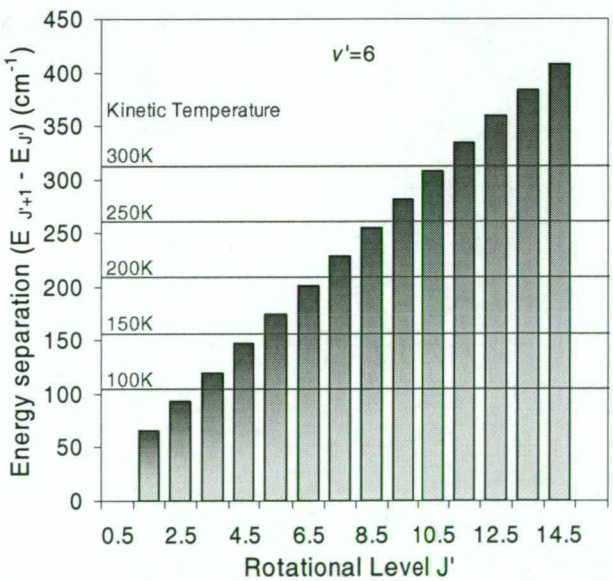

Figure 2-11. The separation between adjacent rotational energy levels in the v'=6 vibrational level. Kinetic energy levels for 100 to 300 K are also shown. Exchange between rotational and translational energy is good where the rotational state separation is less than the kinetic energy.

Where the separation between adjacent rotational states is less than the kinetic energy, good exchange between rotational and translational energy occurs and a Boltzmann-like distribution (in local thermodynamic equilibrium) of rotational state populations is obtained. Where the separation is greater than the kinetic energy, re-distribution to lower levels does not readily occur and as a result populations in these higher J' states remain greater than expected from Boltzmann collisional equilibrium and this leads to un-thermalised emissions.

In Figure 2-11 for example we can see that if the kinetic temperature field is at 200K, we would expect rotational levels up to J'=6.5 to be well thermalised, but J' greater than 7.5 may exhibit unthermalised behaviour. However, at 100K, levels above J'=3.5 may be unthermalised. The bulk gas of course has a Boltzmann distribution of kinetic energy so that the transition to un-thermalised rotational levels is indistinct.

Unthermalised behaviour is nevertheless shown increasingly for higher J' values and at lower temperatures. Pendelton *et al.* (1993) have examined un-thermalised behaviour in the OH (3-1), (6-3) and (7-4) bands. At v'=7 they find ~10% of the rotational population is in J' levels greater than 6.5, compared to ~1% if all states were in local thermodynamic equilibrium. Figure 2-12 shows the rotational population distribution for v'=6 and the departure from thermodynamic equilibrium at J' > 4.5 determined from experimental measurements [Pendelton *et al.* (1993)]. The populations of high J' values (9.5 and 10.5) are found to be more than 3 orders of magnitude greater than expected in thermodynamic equilibrium.

In this work, only rotational states with $J' \leq 4.5$ are used to derive temperatures and the kinetic temperature in the mesopause region is of the order of 200K. It can therefore be assumed that T_{rot} represents adequately the kinetic temperature of the atmosphere integrated over the OH emission profile.

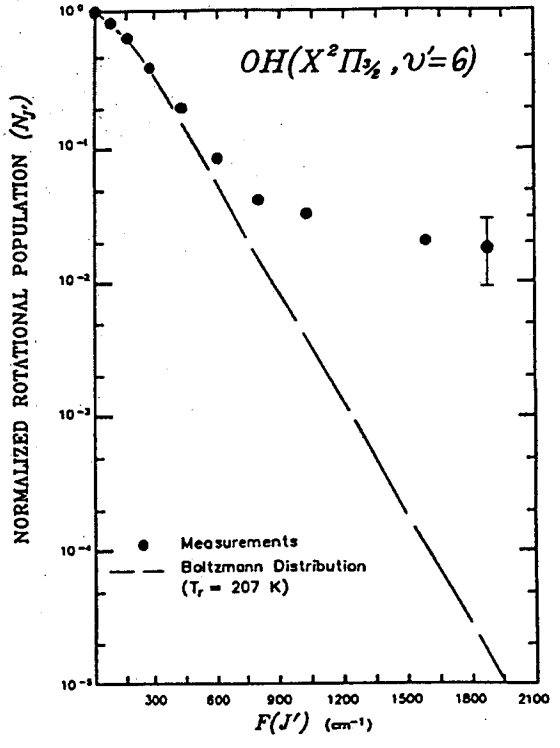

Figure 2-12. OH $X^2\Pi_{3/2}$ v'=6 rotational population distribution extending to J'=10.5 showing departure from a Boltzmann distribution at 207 K. [from Pendelton et al. *(1993)].*

2.4. OH Photochemistry

2.4.1. Hydrogen-Ozone reaction

Bates and Nicolet (1950) and Herzberg (1951) independently proposed reaction of hydrogen with ozone as the principle formation mechanism for vibrationally excited OH in the upper atmosphere:

$$H + O_3 \rightarrow OH^*(v' < 10) + O_2 \qquad \textit{Equation 2-21}$$

The exothermicity of this reaction (3.34 eV) is sufficient to excite vibrational levels up to v' = 9 (G_9 = 26196 cm^{-1} = 3.25 eV). This is the largest level observed in airglow emissions and the predominance of this process is now widely accepted. Relative yields of the different vibrational levels were estimated by Evans and Llewellyn (1972) and shown to exclusively excite v'=6-9, though some evidence of direct excitation of v'=4 and 5 was found by Ohoyama *et al.* (1985).

Reported determinations of the reaction rate for 2-21, listed in Table 2-4, give a wide range of values with temperature dependence, and yield a variation in the total emission of the Meinel system of about a factor of 4 (Lopez-Moreno *et al.* (1987)).

Source	Reaction Rate ($cm^3 s^{-1}$)	Equivalent at 200K
Phillips and Schiff (1962)	2.6×10^{-11}	2.6×10^{-11}
Greenblatt and Wiesenfeld (1982)	1.5×10^{-11}	1.5×10^{-11}
Nicolet (1971)	1.5×10^{-12}sqrt(T)	2.1×10^{-11}
Clyne and Monkhouse (1977)	9.89×10^{-11}exp(-516/*T*)	7.5×10^{-12}
Lee *et al.* (1978)	1.33×10^{-10}exp(-449/*T*)	1.4×10^{-11}
Keyser (1979)	1.47×10^{-10}exp(-496/*T*)	1.2×10^{-11}
Winick (1983), Clancy *et. al.* (1994)	1.4×10^{-10}exp(-470/*T*)	1.3×10^{-11}

Table 2-4. Reaction rates for the ozone-hydrogen reaction (Lopez-Moreno et al. 1987)

Following excitation, the molecule may radiate to a lower vibrational state, suffer vibrational de-excitation by collisional quenching or destruction by atomic oxygen

$$OH^*(v') \rightarrow OH^*(v'') + h\nu \qquad \textit{Equation 2-22}$$

$$OH^*(v') + M \rightarrow OH^*(v < v') + M \qquad \textit{Equation 2-23}$$

$$OH^*(v') + O \rightarrow O_2 + H \qquad \textit{Equation 2-24}$$

where M is generally O_2 or N_2. Collisional quenching may de-excite over several vibrational levels, thus populating lower vibrational levels (Llewellyn *et al.* 1978), or completely deactivate the molecule (Moreels *et al.*, 1977). Collisional quenching processes are examined in section 2.4.4 below.

The reactants H and O_3 leading to the production of OH^* in reaction 2-21 are minor constituents in the mesopause region and their production and loss needs to be understood in order to appreciate the importance of OH emissions and its altitude distribution. Good reviews of the mesopause photochemistry are provided by Torr (1985) and Meriwether (1989) and Figure 2-13, reproduced from Torr (1985), presents an overview of the various reaction pathways associated with OH.

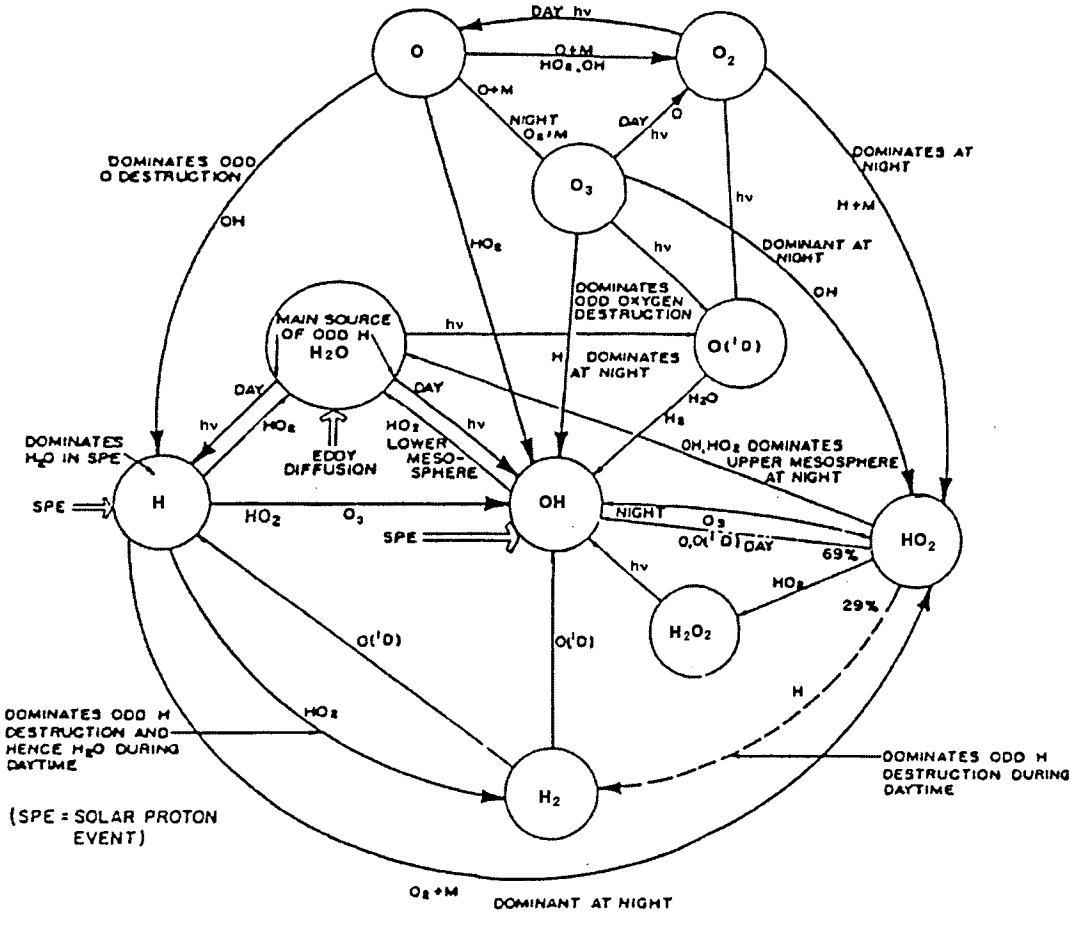

Figure 2-13. Reaction pathways associated with the OH photochemistry in the mesopause region, Torr (1985).

2.4.2. O_2^* hypothesis

Two alternative mechanisms for the production of OH^* have been suggested. Bates and Moiseiwitsch (1956) deal with the O_2^* hypothesis, proposed by Krassovsky (1956) where O_2^* is formed through the three-body reaction

$$O + O + M \rightarrow O_2^* + M \qquad \textit{Equation 2-25}$$

and is lost, depending on its vibrational excitation, according to

$$O_2^*(v' \geq 26) + O_2 \rightarrow O_3 + O \quad \text{and} \qquad \textit{Equation 2-26}$$

$$O_2^*(v' < 26) + H \rightarrow OH^*(v' < 10) + O \qquad \textit{Equation 2-27}$$

Bates and Moiseiwitsch (1956) find, from rocket observations, that the yield of O_2^* from reaction 2-25 is too low and is rapidly quenched by O. Reaction 2-26 is also relatively slow so that the absence from the nightglow spectrum of hydroxyl bands with vibrational level v>10 is not an immediate consequence of reaction 2-27.

2.4.3. Perhydroxyl mechanism

The second alternative, proposed by Nicolet (1970) introduces the perhydroxyl radical, HO_2, formed via the three-body reaction

$H + O_2 + M \rightarrow HO_2 + M$ followed by reaction with O *Equation 2-28*

$HO_2 + O \rightarrow O_2 + OH^*(v' < 7)$ *Equation 2-29*

In this process, the exothermicity (2.4 eV[†]) is only sufficient to excite vibrational levels up to v' = 6 (G_6 = 18958 cm^{-1} = 2.35 eV).

Suzuki and Tohmatsu (1976) calculated rotational temperatures using spectroscopic data from 6 observational sources, and covering upper vibrational levels 3 to 9. The temperatures derived were found to depend systematically on that vibrational level, decreasing quickly from 9 to 7, and then from 6 to 3 after an abrupt rise at v' = 6. Their interpretation was in favour of there being two routes to the excitation of OH.

Using multi-channel tilting filter photometer observations covering the OH(9-4), (8-3), (7-2), (6-2) and (5-1) bands, Takahashi and Batista (1981) also observed an increase in the excitation rate in the v' = 5 and v' = 6 levels, consistent with enhanced production via the perhydroxyl mechanism. The increased excitation rate for v' = 6 is less that for v' = 5, but a possible explanation is that the OH does not receive all the energy of the reaction; some may go into excitation of the O_2 molecule. The partitioning of released energy between the reaction products is not well understood.

From oxygen-hydrogen chemical model calculations Sivjee and Hamwey (1987) found that the perhydroxyl source must be invoked in order to account for the observed column abundance of $OH^*(v'<7)$, inferred from photometric observations of the OH(6-2) band intensities over Longyearbyen, Spitzbergen, and in fact, may contribute up to 50% of the $OH^*(v'<7)$ airglow observed in the dark winter polar

[†] There is some degree of uncertainty in the measurement of exothermicity of reaction 2-29, current thermodynamic data has this value slightly less than required for excitation to v'=6, but with the upper error limit extending just above it. (see Le Texier *et al.*,1987)

mesopause. Turnbull and Lowe (1983) found similar evidence of enhanced v'=5 and v'=6 vibrational level populations.

Several other applications of the perhydroxyl reaction in OH photochemical and dynamical coupled numerical models have been made eg. Moreels *et al.* (1977), Le Texier *et al.* (1987) and Walterscheid *et al.* (1987), further developed by Hickey (1988a,b). Le Texier *et al.* (1987) investigate the importance of this reaction in explaining observed difference in seasonal behaviour between lower and higher vibrational level bands (Shefov, 1969b). The higher levels are populated by the hydrogen-ozone mechanism alone, but atomic oxygen and atomic hydrogen compete in driving the seasonal variation in the lower vibrational levels and thus will exhibit features of both O and H seasonal variations.

On the other hand, there is a growing body of evidence against the perhydroxyl reaction producing significant vibrationally excited OH as so much depends on the way the reaction proceeds, and on the wide choice of rate coefficients due to inaccurate kinetic data.. Direct microwave (λ~1.2mm) measurements of HO_2 abundances below 70km have been made by Clancy *et. al.* (1994) and its diurnal variation at 50-80km altitude by Sandor and Clancy (1998). They find OH_2 abundances are roughly twice those predicted by standard models and a 40% decrease in the model rate coefficient of reaction 2-29 [$3.0\times10^{-11}e^{200/T}$] is required for agreement with observed O_3 and H_2O abundances.

The reviews of Kaye (1988) and Meriwether (1989) both argue that the reaction proceeds via the intermediate complex HO_3, and with experimental evidence from isotope labelling studies (Sridharan *et al.* (1985)), the break-up of this species strongly favours O atom transfer rather than H atom transfer. In highly exothermic reactions, it is well known that most exothermicity is channelled into the newly formed molecule, in this case into O_2 vibrational excitation rather than OH excitation. On this basis, the reaction should not contribute substantially to the emission from OH(v'=5 and 6). Meriwether (1989) goes so far as to say it "plays a negligible role in the vibrational excitation of OH and the production of OH optical emissions in the mesopause region". A crude statistical calculation by Kaye (1988) suggests that less than 1% of the OH would be produced with v'≥4 (although considerable amounts in lower vibrational states).

2.4.4. *Collisional Quenching by N_2 and O_2*

Given that the dominant OH^* formation mechanism produces mainly vibrational levels $5<v'<10$, two collisional processes may contribute to the observed vibrational level distribution. Both reviews by Kaye (1988) and Meriwether (1989) examine the vibrational level dependence of collisional quenching (deactivation or relaxation) by O_2 and N_2 (via reaction 2-23) and promote that quenching may occur as a single or multi-level stepwise fashion (*collisional cascading*) thereby populating lower v' levels or in the loss of all vibrational energy in a single collision (*sudden death*) thereby decreasing the relative population at higher levels.

The interpretation depends very strongly on choice of quenching rates, both for O_2/N_2 and for atomic oxygen discussed later. The quenching rates originally derived by Streit and Johnston (1976), Nagy (1976) and later Llewellyn *et al.* (1978) and Lopez-Moreno *et al.* (1987) all considered only the single quantum ($v'\rightarrow v'-1$) collisional cascade.

Llewellyn *et al.* (1978) use a steady state concentration calculation (excluding the perhydroxyl mechanism) where the rate constants for N_2 and O_2 quenching were varied until good agreement between derived OH^* concentrations and observed nightglow intensities were obtained. The resulting rates showed a vibrational level dependence from 8×10^{-13} cm^3s^{-1} at v'=1, increasing to 5.8×10^{-12} at v'=7, then decreasing again to 4×10^{-12} at v'=9. Of the models mentioned above in support of the perhydroxyl mechanism, LeTexier *et al.* (1987) used Streit and Johnston's quenching rates, both Takahashi and Batista (1981) and Sivjee and Hamwey (1987) used Llewellyn *et al.*'s rates, and Walterscheid *et al.* (1987) and Hickey (1988a,b) did not consider the collisional quenching.

Moreels *et al.*'s (1977) model assumed only the complete deactivation (sudden death) pathway for N_2/O_2 quenching, and arrived at a quenching rate of 5×10^{-14} cm^3s^{-1} in order that the observed noon integrated emission rate approximately matched the night-time value.

McDade and Llewellyn (1987) modelled both scenario's, with the view that the hydrogen-ozone reaction is the *only* source of vibrationally excited OH, and have re-evaluated the collisional deactivation coefficients to match observational data in each case, similar to approach of Llewellyn *et al.* (1978). They concluded that both

models could adequately explain the observed Meinel band vibrational distribution without the need to include a second chemical source (perhydroxyl mechanism).

Their cascade model showed a total collisional loss rate maximum at v'=7 with monotonic decrease on either side, but it is not clear why there should be a vibrational level dependence (Figure 2-14).

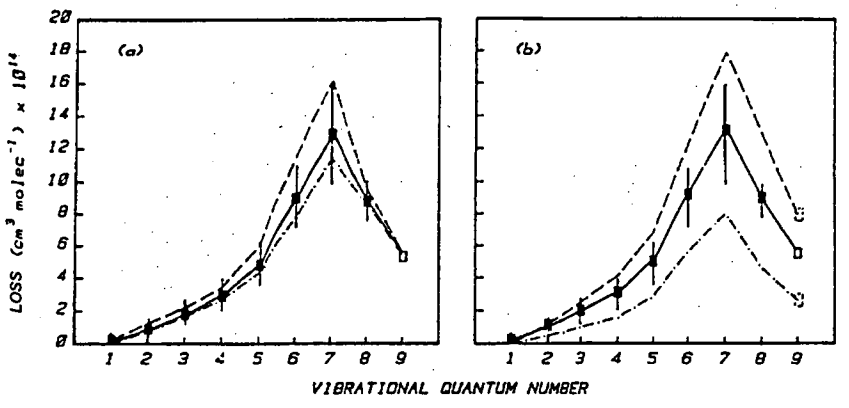

Figure 2-14. Collisional loss rates (lower limit) for O_2 via the COLLISIONAL CASCADE mechanism from McDade and Llewellyn (1987). Dashed and dash-dotted lines show 2x and 0.5x the O_2 density in (a) and the limits of the uncertainty of the reaction rate coefficient in (b).

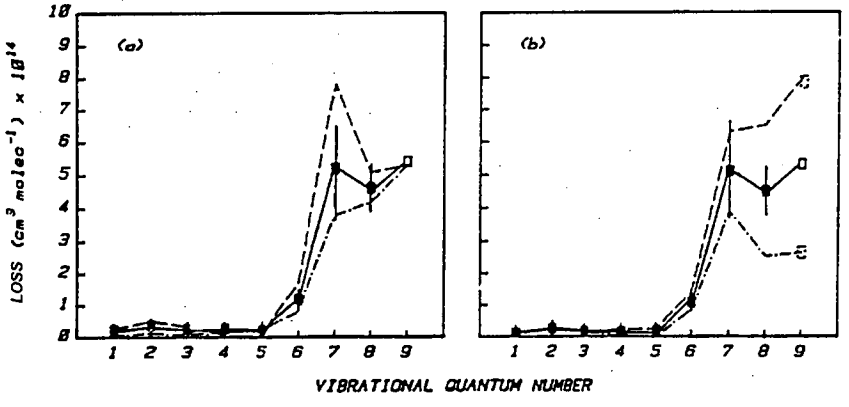

Figure 2-15. As for Figure 2-14 but for the SUDDEN DEATH mechanism.

Sudden death coefficients (Figure 2-15) exhibit an obvious discontinuity at v'=6 and approximately equal loss rates above, consistent with a physical explanation that all OH^* produced by the hydrogen-ozone mechanism suffer equal loss rates. They also put forward that in addition to vibrational *relaxation* by O_2, OH^* may be quenched by *reaction* with O_2 as well, in the reverse process to 2-29, ie

$$OH^*(v' \geq 6) + O_2 \rightarrow O + OH_2 \qquad \textit{Equation 2-30}$$

which becomes energetically possible at v'≥6 and thus also contributes to the discontinuity observed there. Therefore if the forward perhydroxyl reaction is

unimportant, this reverse process may be an important sink of $OH^*(v'\geq 6)$ in the mesosphere. Kaye (1988) points out that this process is expected to be fast if the reaction proceeds via formation of an HO_3 complex, and it has already been established that this is likely.

It was not possible in the McDade and Llewellyn (1987) study to identify a preferred model, although to be acceptable a radiative lifetime for OH(v'=7) of less than ~15 ms was implied for the cascade mechanism, and less than ~3 ms for the sudden death process. Turnbull and Lowe (1989) give a radiative lifetime of about 5ms for v'=7.

More recent laboratory measurements of OH quenching rates, which specifically explore the collisional cascade and sudden death models, have been carried out by Sappey and Copeland (1990), Chalamala and Copeland (1993), Knutsen *et. al.* (1996) and Dyer *et. al.* (1997) for v'=12, v'=9, v'=7 and v'=8,10,11 respectively using pulsed laser excitation of OH^*. A summary of the rate constants determined for collision with O_2, N_2, CO_2 and N_2O are listed in Table 2-5. Vibrational level dependence is found for the total removal rates by all species. O_2 is about an order of magnitude more efficient at quenching all vibrational levels than N_2 and appeared to increase consistently up to v'=9 and then stabilize at around $2x10^{-11}$ cm^3s^{-1}. CO_2 and N_2O were more efficient at lower v' and contained enhanced rates (or resonances), by at least a factor of 3, over the maximum O_2 rate for v' around 8. By examination of the energy of single quantum steps in v', they interpret these resonances as support for the collisional cascade model, whereas the absence of resonant enhancements in O_2 collisions is support for the sudden death model. It follows that, as both CO_2 and N_2O are not significant in the OH region of the atmosphere and N_2 is an order of magnitude less efficient, collisional quenching of OH, through the sudden death mechanism, is dominated by O_2.

v'	O_2 (cm^3s^{-1})	N_2 (cm^3s^{-1})	CO_2 (cm^3s^{-1})	N_2O (cm^3s^{-1})
7	$7\pm2x10^{-12}$	$<6x10^{-13}$	$6.7\pm1.0x10^{-11}$	$3.0\pm0.6x10^{-11}$
8	$8.0\pm1.0x10^{-12}$	$7\pm4x10^{-13}$	$6.4\pm0.4x10^{-11}$	$6.2\pm0.7x10^{-11}$
9	$1.7\pm1.1x10^{-11}$	$<5x10^{-13}$	$5.7\pm0.6x10^{-11}$	$6.4\pm1.0x10^{-11}$
10	$1.50\pm0.12x10^{-11}$	$1.6\pm0.6x10^{-12}$	$1.86\pm0.34x10^{-11}$	$3.7\pm0.3x10^{-11}$
11	$2.79\pm0.14x10^{-11}$		$1.9\pm0.4x10^{-11}$	
12	$1.6\pm0.2x10^{-11}$	$2.5\pm0.7x10^{-12}$	$5.6\pm1.5x10^{-11}$	

Table 2-5. Rate constants (and 2 sigma errors) for OH quenching by collision with O_2, N_2, CO_2 and N_2O, determined from laboratory measurements.[see references in the text]

2.4.5. *Atomic Oxygen production and loss*

During the day, photolysis of ozone and molecular oxygen by solar UV radiation produce the active chemical radical atomic oxygen that is of fundamental importance in the OH photochemical cycle

$O_2 + h\nu \rightarrow O + O$ and *Equation 2-31*

$O_3 + h\nu \rightarrow O_2(^1\Delta_g) + O(^1D)$. *Equation 2-32*

Eddy and molecular diffusion generate a downward flux of these atoms into the mesopause region where O_3 is formed by the three-body association

$O + O_2 + M \rightarrow O_3 + M$, *Equation 2-33*

and, H is released in reactive quenching with OH^* via 2-24. During the night the equilibrium rate of formation of ozone by 2-33 must balance its destruction in the hydrogen-ozone reaction (2-21). Consequently hydroxyl emission depends principally on the atomic oxygen concentration, the background atmosphere (O_2, N_2) and the temperature (as the rate coefficient for 2-33 is temperature dependent).

Conflicting conclusions have been drawn as to the relative importance of atomic oxygen reactive quenching (via 2-24) for different vibrational levels. A lot depends on the radiative lifetimes used. If the lifetime is long (for lower v'), quenching rates are necessarily slower if they are not to react before radiating.

Early work by Evans and Llewellyn (1973) concluded that O quenching must be negligible, from observations that there was little change in OH intensity from day to night despite the large variation in atomic oxygen production, and calculations that population rates for vibrational levels were in agreement with laboratory measurements without O quenching.

Moreels *et al.* (1977) assumed the relatively long radiative lifetime of Potter *et al.* (1971) and were forced to use rate coefficients almost an order of magnitude *slower*, for levels $v' \geq 1$, than for the fundamental, otherwise the quenching of OH^* was so severe that nightglow emission was reduced to a negligible level.

Alternatively, if the lifetime is short, the quenching rate may be higher and therefore constitute an important sink for OH^*. Spencer and Glass (1977) were first to report a reaction rate enhancement of 2 to 3 times for $v'=1$ compared to $v'=0$, and Llewellyn *et al.*'s (1978) efforts to fit model results to observations led them to derive reaction

rates increasing with vibrational level (see Table 2-6). Sivjee and Hamwey (1987) forward a rather simple but reasonable physical explanation for this; the higher the vibrational state, the larger the stretching of the O–H bond and the higher the probability of the bond breaking in the reaction with O.

v'	Moreels *et al.* (1977) [cm^3s^{-1}]	Llewellyn *et al.* (1978) [cm^3s^{-1}]	Lopez-Moreno *et al.* (1987) [cm^3s^{-1}]
0	$1.8\times10^{-12}\sqrt{T}$		
1	↑	4×10^{-11}	9.8×10^{-11}
2	|	5.4×10^{-11}	8.6×10^{-11}
3	|	6.8×10^{-11}	7.4×10^{-11}
4	8×10^{-12}	8.1×10^{-11}	6.2×10^{-11}
5	|	9.5×10^{-11}	5.0×10^{-11}
6	|	10.9×10^{-11}	3.8×10^{-11}
7	|	12.3×10^{-11}	2.6×10^{-11}
8	|	13.6×10^{-11}	1.4×10^{-11}
9	↓	15×10^{-11}	0.2×10^{-11}

Table 2-6. Reported rate coefficients for the quenching of OH by atomic oxygen, for the various vibrational levels.

On the other hand, most supporting observational evidence for quenching rate calculations comes from the rocket photometer measurements of layer height for different vibrational states. Lopez-Moreno *et al.* (1987) confirmed the conclusion of Rogers *et al.* (1973) that the upper edge of the OH emission profiles extend higher in altitude with higher vibrational state and, as the abundance of atomic oxygen increases with height in the mesopause-lower thermosphere, resolved that the quenching was in fact faster, for lower vibrational states than for higher ones, completely opposite to those derived by Llewellyn *et al.* (1978), (Table 2-6)

2.4.6. Production of Hydrogen

Production of odd H is dominated by photolysis of H_2O during the day via

$$H_2O + h\nu \rightarrow OH + H \qquad \textit{Equation 2-34}$$

with a contribution from

$$H_2 + O(^1D) \rightarrow OH^*(v'<5) + H \qquad \textit{Equation 2-35}$$

and loss processes competing with the H-O_3 reaction via

$$H + HO_2 \rightarrow H_2 + O_2 \qquad \textit{Equation 2-36}$$

during the day, and the three body reaction with O_2 (reaction 2-28) at night.

2.5. *Altitude Profile*

An understanding of the processes that define the shape of the OH emission layer and its diurnal variation directly follows from the discussion of photochemistry. References to night-time OH emission height profile invariably mention the review of rocket photometer observations by Baker and Stair (1988). On the basis of 34 rocket flights from mid and high latitudes, at various times of the year and solar depression angles they derive a mean altitude of 86.8±2.6 km with a mean emission layer thickness of 8.6±3.1 km from selected profiles. These values have essentially not changed with subsequent rocket and global scale satellite observations [eg Lowe *et al.*(1996), She and Lowe (1998)] over all latitudes and seasons.

Lubken *et al.* (1999) have shown that this is very close to the summer mesopause (88 km) from the first in-situ temperature measurements in Antarctica, based on rocket-borne falling spheres launched from Rothera (68°S, 68°W). Von Zahn *et al.* (1996) report from ship-borne lidar observations that the winter mesopause is considerably higher; in-fact mesopause altitude exhibited a strong bi-modal character worldwide, either 100±3 km in winter or 86±3 km in summer.

OH concentration, for a given vibrational level (v''), can be described knowing the concentration of reacting species and their corresponding reaction rate coefficients (k). A simple steady state scheme, following reactions 2-21 to 2-24, may be written

$$[OH_{v''}] = \frac{k_{1_{v''}}[O_3][H] + k_{2_{v'>v''}}[OH_{v'>v''}][M] + \sum_{v'+1}^{9} A_{v'v''}[OH_{v'}]}{k_{3_{v''}}[O] + k_{4_{v''}}[M] + \sum_{v'} A_{v'v''}} \qquad \textit{Equation 2-37}$$

where production terms for the hydrogen-ozone reaction (at rate k_1 from Table 2-4), collisional quenching (cascade, at rate k_2) and radiative cascade (photon emission to lower vibrational level) are balanced with loss terms for destruction by atomic oxygen (rate k_3), vibrational de-activation by collision with O_2/N_2 (rate k_4) and radiative deactivation to an unexcited state. Obviously, a more complex scheme could include all reaction pathways in Figure 2-13. Moreels *et al.* (1977) for example include 21 constituents in 52 reactions.

If the height distribution and diurnal variation of the major reacting species is known, the OH profile can be modelled according to 2-37 [for example Gattinger (1969),

Battaner and Lopez-Moreno (1979) and Lopez-Moreno *et al.* (1987)]. Figure 2-16 shows nighttime height profiles of v'=2-9 from Lopez-Moreno *et al.* (1987) with profiles of reacting species from Battaner and Lopez-Moreno (1979).

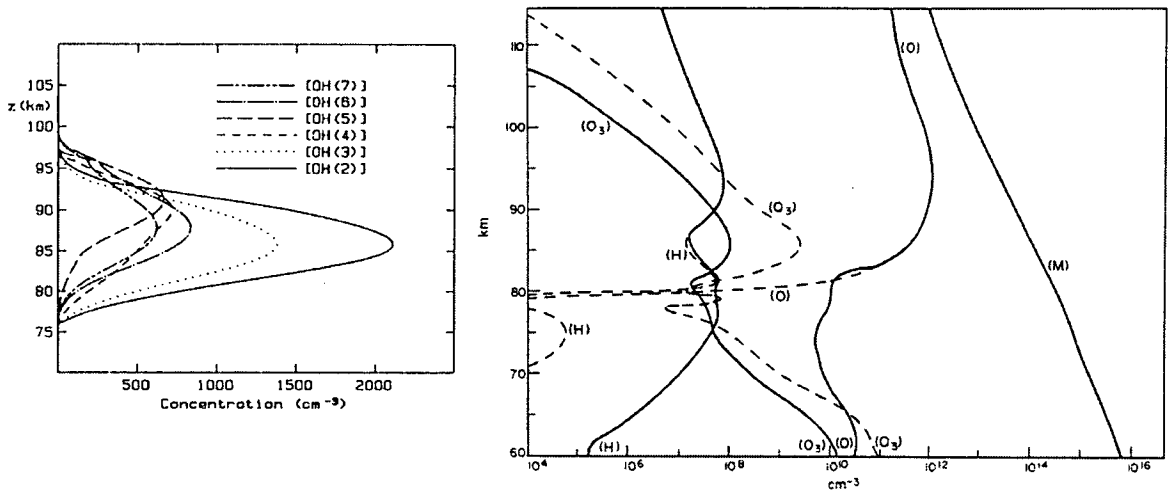

Figure 2-16. Vertical profiles of OH for v' = 2-7 from Lopez-Moreno et al. (1987) and major reacting species in the OH photochemical scheme for daytime (solid) and nighttime (dashed) conditions from Battaner and Lopez-Moreno (1979). Vertical scales have been aligned for comparison, horizontal axes are not to scale.

On the topside of the layer quenching by atomic oxygen is dominant. Above about 86 km atomic oxygen lifetime exceeds 24 hrs, so that no significant change in altitude profile is expected over a diurnal cycle [Lowe *et al.* (1996)]. Atomic oxygen concentration reaches a stable maximum at about 95km. Vibrational dependence in the quenching process (greater for low v') leads to a separation of vibrational levels with higher v' extending to greater altitudes.

On the bottom side collisional quenching by M becomes the dominant factor due to the exponential increase in $[O_2]$ and $[N_2]$. The opposite vibrational level dependence (greater for high v') leads to lower vibrational levels extending down as low as 50-60 km during the day [Moreels *et al.* (1977)].

A combination of other factors also influences the shape of the bottom side at night. Below 86km both atomic oxygen and hydrogen are used up in three-body associations with O_2 after sunset in the absence of photolysis, thus [O] and [H] decrease exponentially into the night, with time constants equal to $1/k_{O,H}[O_2][M]$. These odd O and H decreases lead pure photochemical models to predict a steady decrease in OH emission over the night. This is not the case for a large body of

observations and most models employ an increase in eddy diffusion coefficient (vertical mixing rate), to compensate for the decrease. Physically, this increases downward transport of O and contributes to both increases in H (via reaction with OH and HO_2) and O_3 (via reaction with O_2). Ozone concentrations are relatively high at night in the absence of photolysis and the OH peak coincides with a local peak in ozone concentration. A minimum in ozone around 80 km altitude is caused by the presence of water vapour that acts as a source of atomic hydrogen, which in turn converts O_3 to molecular O_2. Not surprisingly, the most significant local time variation occurs on the bottom side in the pre-midnight period [Lowe *et al.* (1996)]

Double peaked profiles have been frequently observed [Baker and Stair (1988)]. Melo *et al.* (2000) have examined the WINDII/UARS database and calculated occurrence frequencies for double peaked layers between 5 and 25% with seasonal maximum at middle to low latitudes during equinox and diurnal migration from medium latitudes early in the night toward the equator by midnight. Examples of double peak profile shapes are shown in Figure 2-17. They propose and investigate three possible explanations for this characteristic; a mesospheric temperature inversion layer, perturbation in the gradient of the atomic oxygen profile due to turbulence, or the propagation of short vertical wavelength gravity waves through the layer. Any of the three were found capable of producing double peaks, but gravity waves were unlikely to be the source of large horizontal scale, long duration structures.

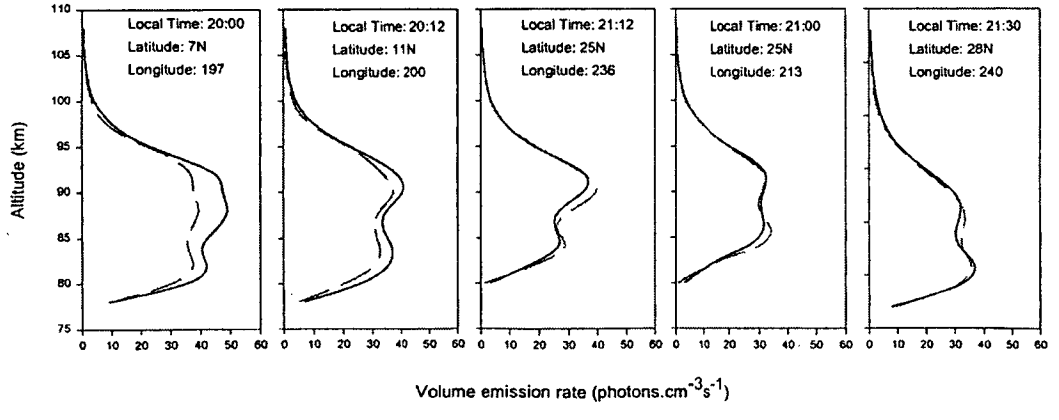

Figure 2-17. Examples of double peaked OH volume emission rate profiles in the WINDII OH(8-3) $P_1(3)$ line. The solid and dashed profiles are two fields of view of the same spatial region viewed 8 min apart. Data are from April 10, 1992. [from Melo et al. (2000)]

3. Instrumentation, Calibrations and Data

This chapter is primarily focused on the Davis hydroxyl airglow scanning spectrometer, its calibration and the data collected. Several other co-located optical instruments contribute to the OH database, analysis and data selection procedures and to collaborative studies. A brief overview of the Davis optical instrument suite, operated by the author during 1995 and 1998, is given here.

Figure 3-1. Aerial views of Davis station in summer and winter. The ASP laboratory is the yellow building at centre in each picture.

3.1. Optical Instruments at Davis.

The new Atmospheric and Space Physics laboratory was opened at Davis in 1992 to replace a collection of modified shipping containers. The building itself is a very comfortable and high standard facility, comprising separate office, electronics workshop, computer room, darkroom and temperature controlled optics labs.

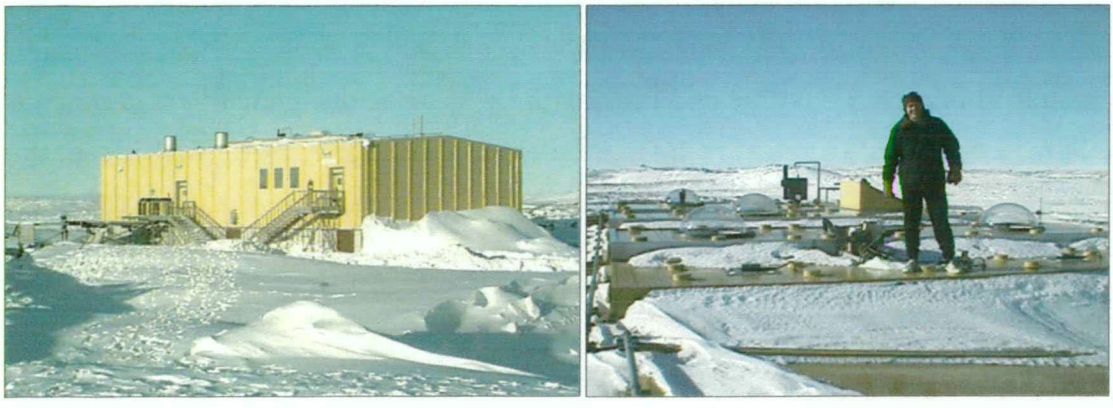

Figure 3-2. The ASP building in winter, and on the roof of the laboratory showing the optical ports (Perspex domes).

As mentioned previously, initial hydroxyl airglow observations at Davis were made in 1984 with a six-filter photometer system that monitored OH(8-3) $P_1(2)$, $P_1(4)$ and $P_1(5)$ lines and the λ630 nm auroral emission [Williams (1987)]. The same instrument was previously used at Mawson from 1979-1981 [Stubbs *et al.* (1983)]. Photometer measurements offer much greater time resolution for short period wave studies than is possible with a scanning spectrometer. Simultaneous photometer-spectrometer data from 1990 is used in this work to assess temperature errors associated with time taken for the spectrometer to scan a spectrum.

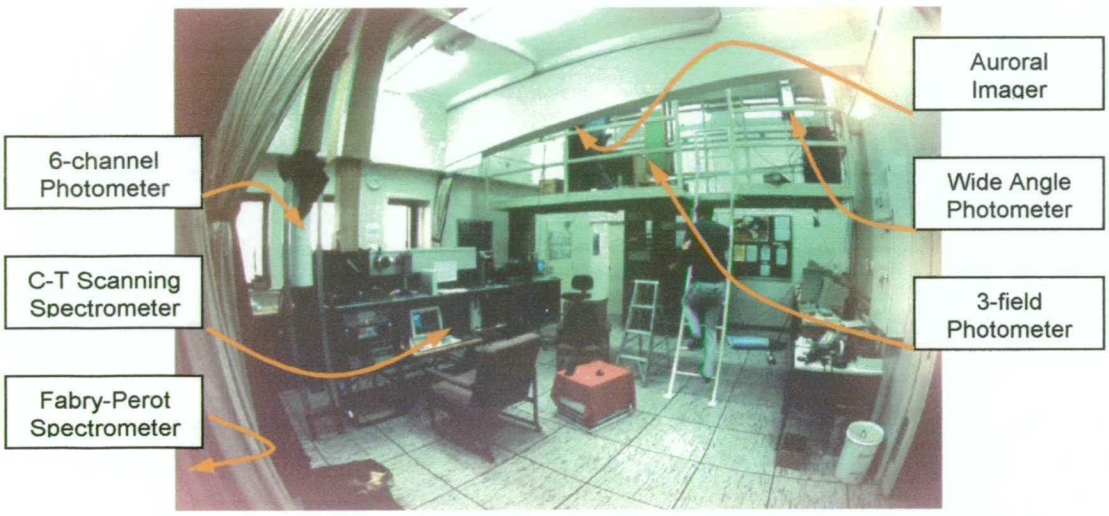

Figure 3-3. A fisheye view inside the Atmospheric and Space Physics optics laboratory at Davis in 1995 showing locations of optical instruments discussed in the text. An OH scanning radiometer was installed in a spare hatch at top-centre in 1999 with a new gantry for access. A Fourier-transform spectrometer will be installed in place of the 6-channel photometer for 2002.

The Czerny-Turner spectrometer was supplied by Spex industries in 1986 and deployed at Davis to monitor OH(8-3) emissions in 1987, and OH(8-3) and OH(6-2) bands consecutively in 1990. Both the spectrometer and photometer were returned to Australia between 1991-1993 and fitted with GaAs detectors. New filters to monitor OH(6-2) band $P_1(2)$, $P_1(3)$, $P_1(4)$ and $P_1(5)$ lines were also installed in the photometer. The spectrometer was used briefly at the Buckland Park field station near Adelaide to study tidal variations and compare with MF radar winds [Hobbs *et al.* (1996)]. Both instruments returned to Davis and were re-located in the new lab in 1994. The photometer was decommissioned at the end of that year while the spectrometer control system and software were upgraded. The spectrometer has continued to monitor OH(6-2) each year since that time, although changes to

acquisition parameters and other system components have occurred which will be detailed later in this chapter.

A twin-channel wide-angle (30° fov at zenith) photometer and a 3-field photometer (3° fov, 5° off zenith, 60° azimuth separation) were installed at Davis in 1994 and 1995 respectively. Both are operated routinely during darkness hours to monitor λ630, λ558 and λ428 nm airglow and aurora activity and the λ731 nm OH emission. Data from these instruments are available to assess auroral activity and intensity variations during acquisition of OH airglow spectra.

A 6-filter CCD all-sky auroral imaging system has also operated routinely at Davis since 1994 and replaced an earlier single filter model used since 1992 and various all-sky camera photographic systems prior to that. Filters were also available for monitoring λ731, λ630, λ558 and λ428 nm emissions. Data is optionally stored as digital images [Figure 3-4] or on videotape. Its particular contribution to this work is in assessment of cloud conditions at the time of observations. Time-lapse video for each observing night was reviewed and cloud classified as clear, haze, patchy, overcast (or unknown). The image intensified time-lapse picture often enabled more accurate cloud assessment than the naked eye, especially on moonless nights, as motion of cloud across the image was readily apparent against the stellar background.

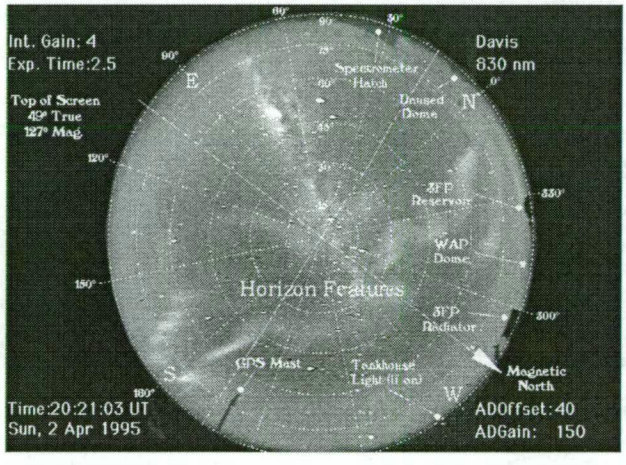

Figure 3-4. An auroral video image from 1995, overlaid with orientation information.

In 1997 a dual-channel high-resolution Fabry-Perot spectrometer commenced routine observations at Davis after several years of development and problem solving since its installation in 1994. The instrument could be configured to measure Doppler winds and temperatures from the λ630, λ558 and λ834 nm [OH(6-2)Q_1(1) line] emissions [Greet *et al.* (1994)]. A comparison of temperatures derived from the Czerny-Turner and FPS instruments has recently been made [Innis *et al.* (2001)].

Three other instruments rate a mention for their potential contributions to the hydroxyl airglow project.

A scanning radiometer was added to the instrument suite in 1999 as a collaborative project with the University of Western Ontario. The instrument consists of a InGaAs detector optimised to measure the OH bands in the 1.2-1.6 μm region ($\Delta v = 2$ and 3 sequences) and a telescope which scans the sky ±8 degrees from the zenith in a 16x16 grid with an integration time of 0.22 sec per point. Cross correlation analysis of intensity variations yields information on the propagation of wave structures through the OH layer.

A Fourier transform spectrometer is currently under construction to add to the Davis optical instruments. This instrument will measure OH emissions in the 1.5 μm region also using a thermoelectrically cooled InGaAs detector. It is intended to extend our seasonal coverage of OH observations at Davis (further into the daytime and summer period) through the rejection of scattered sunlight with a polarising filter. This instrument is also discussed further in the future work chapter.

In addition, a Lidar has recently been installed at Davis and commenced operation in February 2001. It is comprised of a 30 W pulsed Nd:YAG laser, 1 metre tiltable telescope and a Fabry-Perot Spectrometer. The instrument is capable of measuring density, temperature, wind speed and direction as a function of altitude between 10km and the upper mesosphere. It can identify regions of significant aerosol concentration and measure the altitude, thickness and direction of clouds, certainly through the lower atmosphere and potentially at NLC heights. Comparison with the rotational temperatures derived from this work enables a valuable and important proofing study for the lidar system.

I will continue with a detailed description of the scanning spectrometer system components and software, instrument changes and calibrations and diffraction theory.

3.2. The Davis Scanning Spectrometer

Figure 3-5. Pictures of the spectrometer at Davis in Dec 1998.

3.2.1. Overview

Figure 3-5 shows the Davis spectrometer, which employs a single plane diffraction grating, two concave collimating mirrors and entry and exit slits in a Czerny-Turner configuration [schematic Figure 3-6]. In normal observing configuration, light is accepted vertically from the sky through a Perspex window and a telescoping baffled light-column suspended from the laboratory ceiling. A 45-degree mirror directs it horizontally through a blocking filter and the entrance slit of the spectrometer, to the first mirror lens. Collimated light is then directed onto the diffraction grating. The second mirror lens re-focuses the light onto the exit slit.

All light passing through the exit slit is gathered via a pair of lenses, which focuses an image of the second mirror lens, through an electronic shutter, onto the cathode of a cooled GaAs photomultiplier tube (PMT). The PMT is operated in pulse mode. Detected pulses pass through pre-amplifier and discrimination electronics before being counted onboard the control computer.

A low brightness source can be mounted in place of the entrance column for periodic calibration. In addition the 45-degree mirror in the entrance system can be swung away to permit response calibrations with a secondary reference source or instrument function measurements using a frequency stabilised laser via a Lambertian screen.

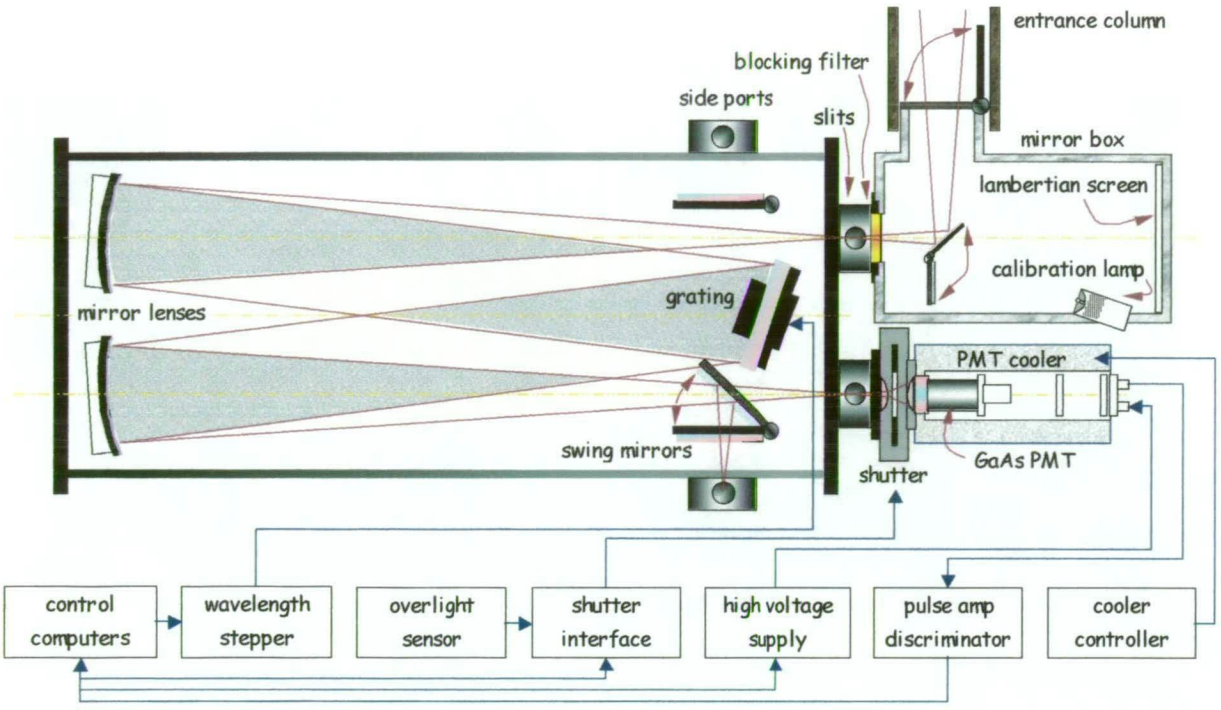

Figure 3-6. Schematic diagram of the Scanning Spectrometer

3.2.2. System Components.

The main spectrometer unit is a Spex Industries model 1269 with a 1.26 m focal length and equivalent f-number (focal length/aperture) of 9. It is an off-Littrow configuration with the incident beam at 4.9° to grating normal. The entrance column and mirror box were manufactured to suit the installation. The entire instrument is mounted on an optical table that is fixed through the floor to a separate foundation pedestal so that mechanical separation from the building can be maintained.

3.2.2.1. Ports and Slits

Both front and side entrance ports are fitted. Front ports are always used for hydroxyl airglow observations as they contain 50 mm-high curved slits. Curved slits correct for instrument astigmatism and enable the full 50 mm height to be used for maximum throughput. Side ports were fitted with 20 mm-high straight slits, which are adequate for calibration of interference filters used in other optical instruments.

Slit widths are manually adjustable with vernier screws and slit height on the front entrance port by a gated shutter (see Figure 3-8). For the great majority of OH routine observations both entrance and exit slits were set to 250 μm giving a

maximum theoretical (fwhm) resolution of 1.523 Å at a laser calibration wavelength (6238 Å) or 1.417 Å at the OH(6-2)$P_1(4)$ line (8465 Å). Some data have been collected with 100 μm slit widths giving a theoretical resolution of 0.609 Å at the laser wavelength and 0.567 Å at the $P_1(4)$ line.

Correct alignment or parallelism of the slits is critical to obtain a good (near theoretical) instrument function at a given slit width. Convolution of the two slit functions, and minor components due to errors in focusing the mirror lenses and stray light from the grating (both ghosts and scattered light from dust or irregular ruling errors) defines the instrument function shape.

Slit alignment was the most awkward and fickle of the optical alignment procedures. Adjustment is allowed for only through the 'slop' in the boltholes (in Figure 3-8) that hold the entire slit assembly onto the instrument's front plate. The entrance box and shutter/detector assemblies must be removed, slit bolts loosened and an eyepiece fitted to the exit slit [Figure 3-7]. Alignment is set by viewing an image of the entrance slit (illuminated with an emission line) through the exit slit and rotating the slit barrel to maximise parallelism. Tightening the bolts, and reinstalling the entrance box and detector assemblies was often enough to shift the alignment. With the detector back on, a laser scan reveals the alignment success. If it was moved during re-assembly the whole procedure had to be restarted. You could either be very lucky or, even with utmost care, it could take a few days!

Figure 3-7. Setup for the slit alignment procedure.

A redesign of the slit housing and connections to the shutter/detector assembly was considered in Jan 2001 with the intention of providing a micrometer adjustment for the rotation of the slit barrel that would enable precise control while the photomultiplier assembly is still in place. This modification is still under construction and has yet to be tested.

3.2.2.2. *High Order Blocking Filters*

Blocking filters may be installed immediately in front of the entrance slit (Figure 3-8) to reject higher order diffraction. In particular, auroral contamination from second order N_2^+ 1NG(0,1) and (1,2) bands (with band heads at λ424 and λ428 nm respectively) and several minor N_2 Vegard-Kaplan band emissions could be rejected. A low wavelength cut-off of λ470 nm was appropriate for this purpose.

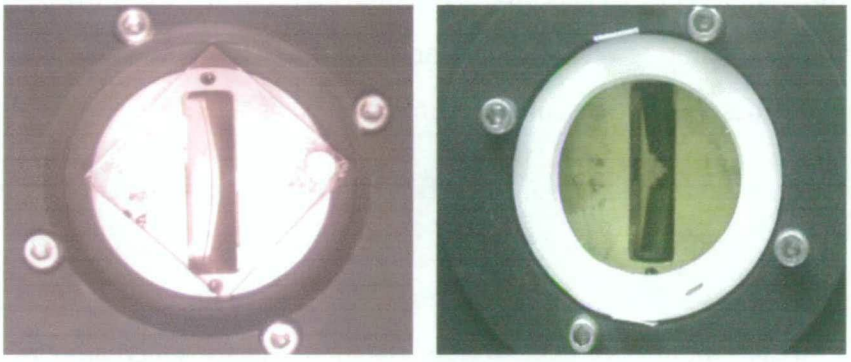

Figure 3-8. Views of the single blocking filter in front of the entrance slit as used prior to 1996 (left) and the double set fitted in a Teflon ring mount after 1996 (right).

Although a suitable filter was available in 1990 it was apparently not installed that year. A single filter was used for 1994 and 1995. Four new filters were manufactured during 1995, of which two were mounted together in the instrument for 1996 and subsequent years. Filter transmission characteristics for the single and double configurations used, are plotted in Figure 3-9. Transmissions fall slightly across the OH(6-2) region from 86% and 90% respectively

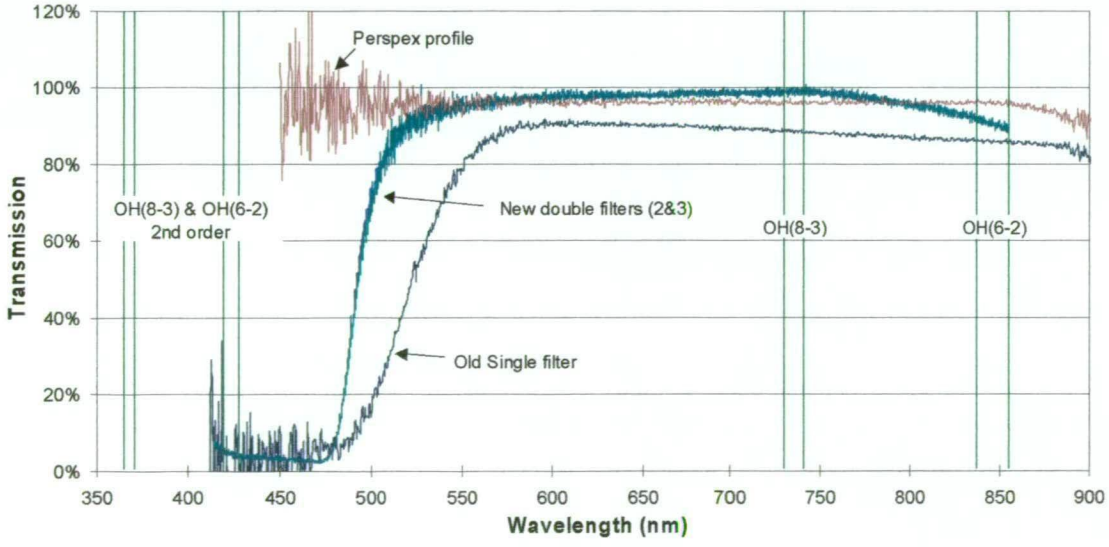

Figure 3-9. Transmission profiles of the blocking filters and Perspex front viewing window.

3.2.2.3. *Perspex viewing hatch*

Perspex was chosen for the viewing hatch due to its high infrared transmission characteristics. Its transmission was measured in 1995 and is also plotted in Figure 3-9. It is around 96% across the OH(6-2) region. This window is the only element in the optical path not taken into account with a low brightness source calibration and therefore the correction for it is applied separately in the analysis routine. The Perspex window and other observing domes are regularly cleaned and polished during the observing season [Figure 3-10].

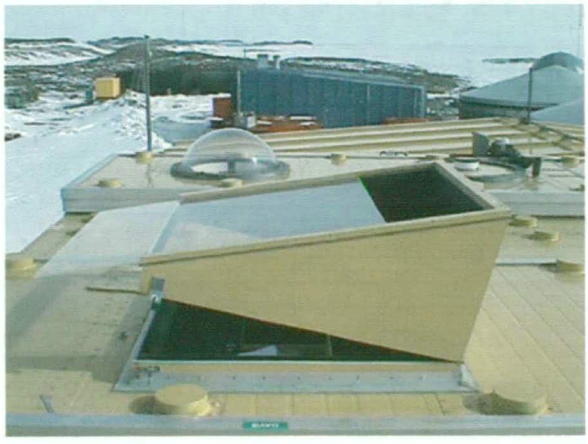

Figure 3-10. View of the viewing hatch showing the hatch unfastened and tilted back and the Perspex partially removed.

3.2.2.4. *Field of View*

The entrance column and mirror box were designed so as not to limit the normal instrument view. Acceptance angle of the front port is thus defined by the width of the grating and is consequently wavelength dependent in horizontal aspect as the grating rotates. Table 3-1 summarizes field of view for zenith observations at a few wavelengths of interest and the calculated area of view at 87 km altitude.

			Horizontal NW-SE		Vertical NE-SW	
Wavelength	Feature	Grating °	View Angle °	Width (km)	View Angle °	Width (km)
427.8	N_2	14.929	5.970°	9.074	5.271°	8.010
557.7	O	19.624	5.820°	8.845		
632.8	Laser	22.400	5.713°	8.682		
730.5	OH(8-3)	26.098	5.549°	8.433		
744.5		26.637	5.524°	8.394		
837.5	OH(6-2)	30.288	5.336°	8.109		
855.5		31.010	5.297°	8.048		

Table 3-1. Grating rotation angle, field of view and area at 87km for various wavelengths of interest. Horizontal and vertical refer to the directions measured from the optical axis of the spectrometer. After re-direction through the 45° entrance mirror, vertical becomes the plane in the NE-SW direction, and horizontal the plane in the NW-SE direction.

Prior to 1994 the instrument viewed at 30° elevation above the SE horizon (130° azimuth) by means of a second mirror mounted on the roof. This was primarily to take advantage of van-Rhijn effect but also to minimise auroral and station light

contamination. Area of view becomes a trapezium 8 times as large as the zenith area, with dimensions 32.5 km long (NW-SE direction) by 14.8 km on the near side and 17.4 km on the far side (NE-SW direction) at λ840 nm. Centre of the field is located at 69.4°S, 80.8°E (152 km from Davis).

3.2.2.5. Diffraction Gratings

Two diffraction gratings (specified in Table 3-2) have been used over the course of this work. The old grating was replaced prior to the 1996 observing season.

Manufacturer	Milton Roy Analytical products.
Material	Borosilicate Crown type 2
Grooves/mm	1200
Blank size	140x120x30 mm
Ruled area	136x116 mm
Blaze wavelength	7500 Å
Blaze Angle	26.7°
Maximum ghost intensity	0.087% of parent @6000A[†]

Table 3-2 Diffraction grating parameters.

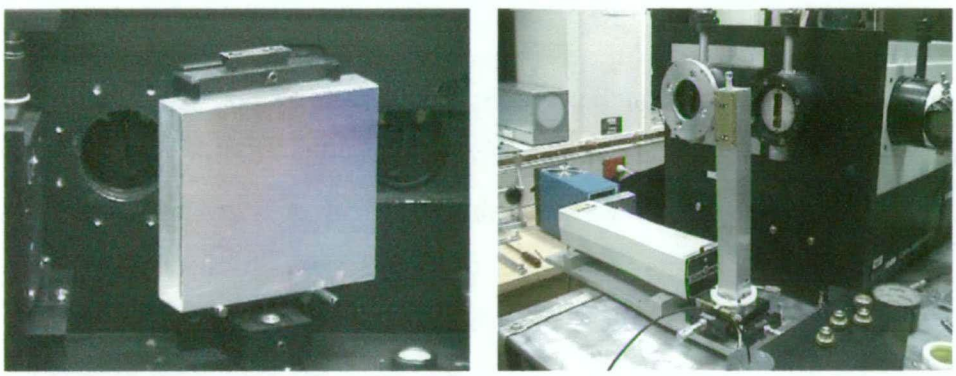

Figure 3-11. The diffraction grating installed on a 3-axis adjustable mount (left) and the laser alignment kit set up for optical alignment (right).

Optical alignment of the grating, slits and mirror lenses is carried out each year. A laser alignment kit (manufactured in-house) directs a beam through targets on the entrance slit and first mirror, onto the grating [Figure 3-11]. Post and grub screws provide fine adjustment of the gratings yaw, tilt and rocking axes to position the beam correctly on the exit slit target with the grating in plane reflection, and rotated for first and second order diffraction, at the laser wavelength.

Diffraction characteristics of the Davis gratings are examined further in section 3.3.

[†] This specification was much lower than ghosts actually observed, see section 3.3.6

3.2.2.6. *Shutter and Over-light Interface*

An electronic shutter is positioned immediately after the exit slit and forward of the photomultiplier housing. This is a 'normally shut' device, providing protection for the photomultiplier in the event of power loss. Interface electronics constructed in Feb-95 allows routine control of the shutter from the control computer so that dark counts can be obtained each spectrum cycle. A daylight detector (photo resistor) overrides operation of the shutter.

3.2.2.7. *Photomultiplier detector*

An EMI 9658A S20-type photomultiplier was used in 1987, which restricted observations to OH(8-3) due to the fall-off in detector sensitivity at about λ800 nm. In 1990 it was replaced by a Hamamatsu R943-02 GaAs[†] tube with an extended wavelength response to enable OH(6-2) observations. A comparison of typical spectral response characteristics for these two detectors is shown in Figure 3-12.

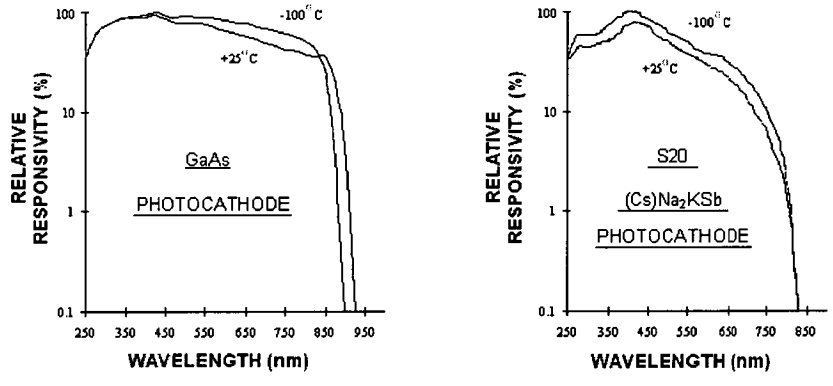

Figure 3-12. Typical spectral response characteristics for GaAs and S20 type photomultipliers.

Operating voltage (typically 1840V DC) and pulse height discrimination level (typically 1 mV) are set to optimise signal-to-noise ratio at average OH airglow signal levels. Photomultiplier output is typically 10-20 mV pulses. The pulse amplifier/discriminator unit was changed in Nov 1994.

Replacement of the GaAs tube occurred in Feb-1994, Dec-1994 and in Dec-2000. Differences between tubes are accounted for in instrument response calibrations. Deterioration of a photomultiplier (decrease in signal-to-dark count ratio) is primarily caused by damage to the last dynode by heavy electron bombardment

[†] using Gallium Arsenide activated in Caesium as the photocathode.

(Hamamatsu Photonics (1990)). This process is more dependent on the magnitude of the anode current than on applied voltage, tube life is therefore shortened by exposure to high light levels.

As pulse generation is a stochastic process, photomultipliers operating in pulse counting mode are subject to 'pulse-pileup' when exposed to high light levels. This occurs when pulses are so frequent that they overlap and cannot be distinguished by the pulse amplifier electronics, resulting in a lower than actual count rate. For this system, pulse pileup becomes a significant problem above 200,000 counts/sec which is much higher than OH rates (400 counts/sec) and three times the low brightness source intensity (65,000 counts/sec) so does not require further consideration.

Thermionic emission of electrons from the photocathode and dynodes contribute most to the dark current. Other factors, such as ionisation of residual gases within the tube, glass scintillation, ohmic leakage from imperfect insulation and field emission from electrons ejected from the electrodes also contribute minor amounts. Hamamatsu Photonics (1990).

Cooling the photomultiplier reduces the major thermionic component by several orders of magnitude [Figure 3-13]. The Davis detector is cooled by a series of Peltier devices and initially operated at around -25 °C, with dark counts of the order of 40 counts/sec. A number of improvements in the cooling system have led to improved stability and lower dark counts over the years. Since 1996 the coolers have typically maintained –25 to –30°C and dark counts of about 5 counts/sec.

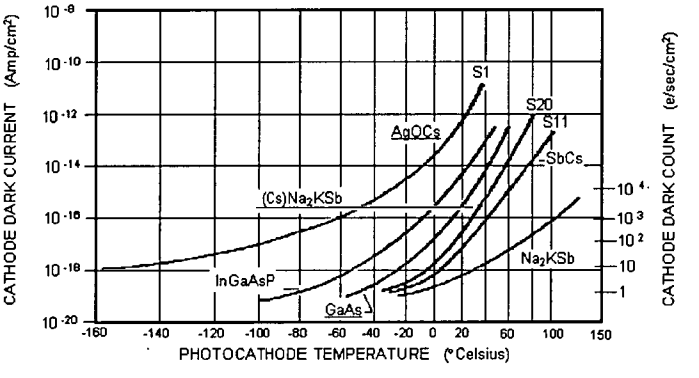

Figure 3-13. Dark-current temperature characteristics for common detectors. (from http://www.photocool.com/)

3.2.2.8. Control computers and software

Several generations of control computers and hardware upgrades have occurred during the course of this project. The author undertook a major upgrade from a SPEX DM1B laboratory coordinator to a SpectrAcq/PC based system in Nov-1994.

The latter system employs a 'host' and 'interface' PC configuration. High-level control software runs on the host PC and issues instructions to initiate a scan procedure through serial commands to the interface PC (SpectrAcq). It also controls add-on devices such as a parallel shutter/overlight interface and time synchronisation via IRIG-b time code to a GPS clock. It receives and stores scan data after each step. Low-level instructions on the SpectrAcq interface PC control the scan requested. It contains an EHT card for photomultiplier supply, a counter card connected to the pulse-amp/discriminator output and serial connections to the grating-rotation stepper-motor driver and to the host PC.

The system is run continuously during the February to November observing period each year, and at least partially over summer months for calibrations and training. Few failures have occurred over the seven years of system operation since 1995. Some problems are attributable to static damage in the dry environment.

Automated control software and scan procedures to accompany the hardware upgrade in Nov-1994 were developed by the author. Spex Industries DM3000 software supplied with the SpectrAcq hardware offers a fairly rudimentary keyboard driven control structure in which collections of keystrokes may be saved in a file and run in a loop for repetitive scanning. No internal access to the parallel I/O port was provided, so control of the shutter/overlight interface and synchronisation to the lab GPS clock were written as external shell programs. Data are stored in a custom binary format, which replaced the plain ASCII format of the DM1B software.

A newer version of the Spex control software (SpectraMax) was also purchased with the hardware upgrade. It offered a much nicer menu-driven layout and contained a command interpreter language for automatic script based operation and internal control of the parallel interface port. Several scripts for routine scanning were also developed by the author but unfortunately the software contained several bugs that precluded its use for routine observations; the most important being a half second delay between successive data points that doubled the length of time for a complete scan and a bug in the parallel I/O command set making them unusable. Despite several attempts to get these problems rectified by the supplier, it was not resolved and eventually this software was abandoned.

3.3. Diffraction Characteristics

This section examines diffraction characteristics with respect to the Davis spectrometer. Wave theory treatment of diffraction is presented in standard optics texts. Discussion in the following section is extracted from Hecht and Zajac (1974), Jenkins and White (1976) and Wolfe (1997) except where otherwise noted.

Diffraction results from the interaction of propagating waves with some physical obstruction or aperture. Interference of various wavefront segments propagating beyond the obstruction produce an energy-density distribution known as a *diffraction pattern.* If the obstructing elements are periodic, constructive interference occurs in several discrete directions, known as *diffraction orders*, where the path difference between adjacent elements is equal to some multiple of the wavelength. Within each order the wave field is dispersed in angular space to form a *spectrum.* A very large number of parallel and equidistant grooves on a grating[†] obstruct the wavefront in a precise manner. Formulation is least complex for Fraunhofer diffraction, where a plane wavefront (parallel light) is incident on a plane diffracting surface. The Fresnel case involves convergent and divergent beams where the curved surfaces of the wavefront must be taken into account. In many optical systems a plane wavefront is generated from a divergent beam with the use of collimating lenses or mirrors. Such is the case for the Davis spectrometer.

[†] Astronomer David Rittenhouse is credited with the construction of the first diffraction grating, in 1786. Joseph von Fraunhofer produced a reflection grating by ruling grooves with a diamond point on a mirror surface in 1821. This enabled him to measure, for the first time, the wavelength of light. He went on to derive the grating equation, explain diffraction orders, discovered the absorption features in solar radiation which bear his name, and consider the effects on the spectrum of groove shape and errors in groove position. Little was done after his death in 1826, principally because of the difficulty in producing gratings that would outperform the spectral dispersion of simple prisms, until Professor Henry Rowland of Johns Hopkins University began producing gratings on sophisticated ruling engines in the 1880's. (Rowland 1882)
An ideal grating contains grooves that are perfectly parallel, equidistant and the profile of each groove is constant, therefore any wear on the ruling tool must be excluded. To this end a soft aluminium coating is usually vacuum deposited onto the flat (to within $\lambda/10$) glass substrate into which the grooves are ruled with a diamond tipped tool. The advancing mechanisms on most sophisticated ruling engines today are controlled with double Michelson interferometers ensuring precise parallelism and displacement accuracy is maintained within the order of a nanometre. Typically they rule about 600 lines per hour, so a grating such as installed in the Davis spectrometer containing over 163,000 lines would have taken over 11 days to rule.
Gratings are now also produced holographically with the use of laser interference fringes recorded on a photosensitive coating. Holographic gratings can be generated on plano, spherical, toroidal and many other surfaces and can be made with as many as 6000 grooves per mm. Furthermore, as the 'grooves' are an optical interference pattern, they are perfectly constant and the gratings have extremely low stray light and no ghosts due to random and periodic errors in the groove spacing respectively. As a result holographic gratings have a higher signal to noise ratio than ruled gratings.

3.3.1. The Grating Equation

With reference to the Czerny-Turner schematic in Figure 3-14, a plane wave is incident on the grating from the first collimating mirror. For a diffracted order to occur in the direction of the second mirror requires contributions from each groove to be in phase, i.e. optical path difference between successive grooves is some multiple (m) of the wavelength. This fundamental principle of diffraction is described by the *grating equation* -:

$$m\lambda = d(\sin\alpha + \sin\beta) \qquad \textit{Equation 3-1}$$

where α is the angle of incidence is, β is angle of diffraction, m is diffraction order, λ is wavelength and d is grating spacing.

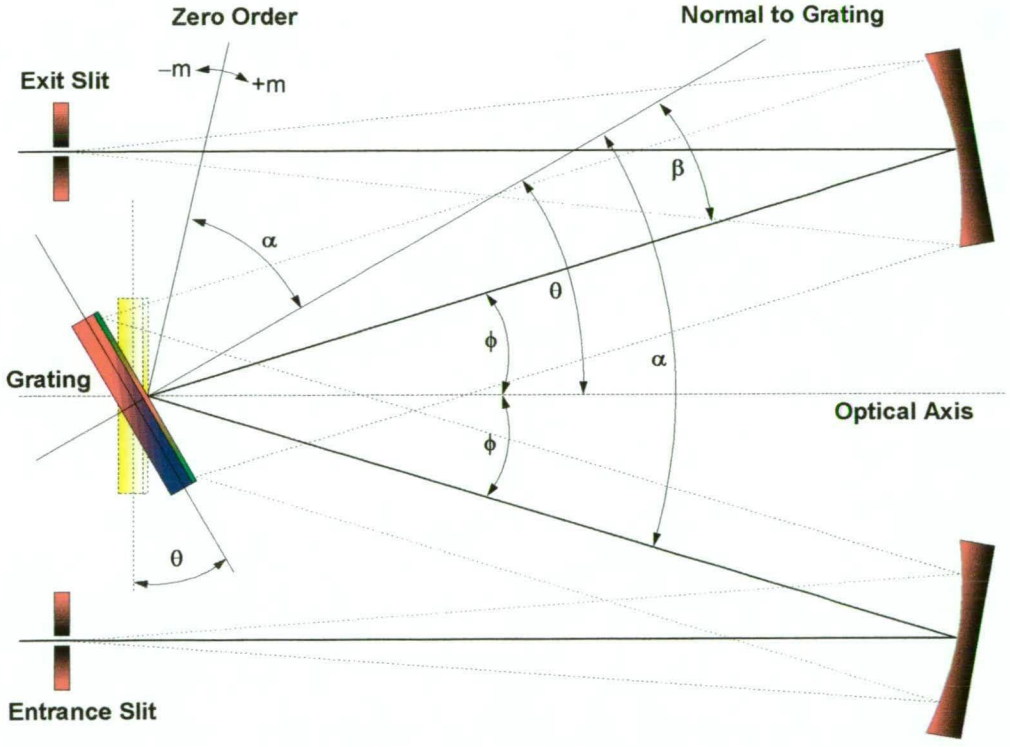

Figure 3-14. Schematic diagram for the grating equation

Diffraction order can be positive or negative. By convention, m is positive when the diffracted order is on the same side of the zero order as the grating normal. The convention for the sign of angles of incidence (α) and diffraction (β) varies between texts, either Cartesian, where angles in the 1st and 3rd quadrants are positive, or where the angles have the same sign if they are on the same side as the grating normal. The latter is adopted here.

Relative to the optical axis of the instrument, we have $\alpha = \theta + \phi$ and $\beta = \theta - \phi$, thus equation 3-1 may be rewritten as

$$m\lambda = 2d\sin\theta\cos\phi \qquad \textit{Equation 3-2}$$

where θ is the grating rotation angle and ϕ is the angle between the optical axis and the incident and diffracted rays, known as an off-Littrow angle. For the Davis system ϕ is 4.9° and the grating contains 1200 lines/mm, thus spacing d is 833.3 nm.

Figure 3-15 plots the grating rotation angle against wavelength for m=1 to 5 and demonstrates overlapping of orders. If the grating is rotated to 30° to select 830 nm in 1st order for example, wavelengths at $\lambda/2$ = 415 nm in 2nd order, $\lambda/3$ at 277 nm in 3rd order, etc, will also appear at the exit slit. Rotation angles for the wavelength scan regions of interest are given in Table 3-3.

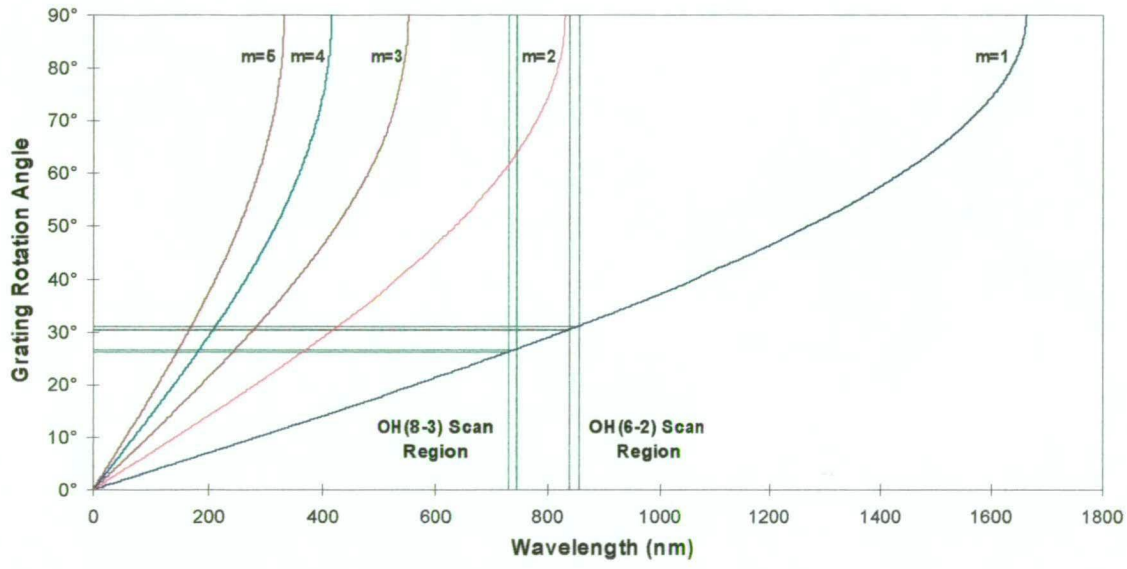

Figure 3-15. The grating equation applied to the Davis spectrometer with d = 1/1200 grooves/mm ϕ=4.9° for diffraction orders 1-5.

	Scan Region	OH(6-2)	OH(8-3)
Wavelength Region	Start	837.5 nm	730.5 nm
	Stop	855.5 nm	744.5 nm
	Range	18 nm	14 nm
	Step	0.005 nm	0.005 nm
Grating Rotation Angle θ	Start	30.2878°	26.0980°
	Stop	31.0097°	26.6371°
	Range	0.72191°	0.53914°
	Step	0.000195°	0.000186°

Table 3-3. Grating rotation angles for the OH(6-2 and OH(8-3) scan regions.

It follows from equation 3-2 that the maximum wavelength in a given order occurs as $\theta \rightarrow 90°$ and is governed by the grating spacing such that $\lambda_{max} \cong 2d/m$ for small ϕ. In practice a grating angle of 90° is impossible, as the incident and diffracted rays are parallel to the grating surface and no light is diffracted. Experimentally, the maximum grating rotation angle achievable is of the order of 65°.

The precision required to step the grating in milli-degree steps is achieved by means of a 'sine drive' mechanism. A long arm is attached between the grating mount and a slider guide on a fine pitch lead screw. A stepper motor controls the rotation of the lead screw such that the sine of the grating rotation angle is equal to the distance the slider guide moves along the lead screw divided by the length of the arm.

3.3.2. Angular and Linear Dispersion

Differentiation of the grating equation (3-1) with respect to the diffraction angle β, yields

$$m\frac{\partial\lambda}{\partial\beta} = d\cos\alpha\frac{\partial\alpha}{\partial\beta} + d\cos\beta\,, \qquad \textit{Equation 3-3}$$

and thus the quantity

$$\frac{\partial\beta}{\partial\lambda} = \frac{m}{d\cos\alpha\dfrac{\partial\alpha}{\partial\beta} + d\cos\beta}. \qquad \textit{Equation 3-4}$$

Consider in the case of the Davis instrument, as the grating rotates, the diffracted beam sweeps through twice the incident angle, thus $\partial\beta = 2.\partial\alpha$ and we have

$$\frac{\partial\beta}{\partial\lambda} = \frac{m}{\dfrac{d\cos\alpha}{2} + d\cos\beta} \qquad \textit{Equation 3-5}$$

which is the *angular dispersion*, a measure of the gratings ability to separate wavelengths differing by a small amount $\partial\lambda$, in angular space, thereby forming a spectrum for each order. Note that it is the change of diffraction angle with wavelength, not the change in grating angle. From the differentiation of equation 3-2 we may however write the equivalent expression

$$\frac{\partial\beta}{\partial\lambda} = 2\frac{\partial\theta}{\partial\lambda} = \frac{m}{d\cos\theta\cos\phi} \qquad \textit{Equation 3-6}$$

in terms of the grating rotation angle. Thus $\partial\beta = 2\partial\theta$ (the beam is diffracted at twice the angle of rotation of the grating). Angular dispersion is plotted against grating

rotation angle in Figure 3-16 for orders m = 1 to 5. As it is inversely proportional to cosθ, dispersion increases with angle and tends to infinity as θ tends to 90°. An increase in dispersion is also gained by increasing the groove density (i.e. decreasing the groove spacing d) or observing at higher orders, (i.e. separation of wavelengths in second order is twice as great as in first order).

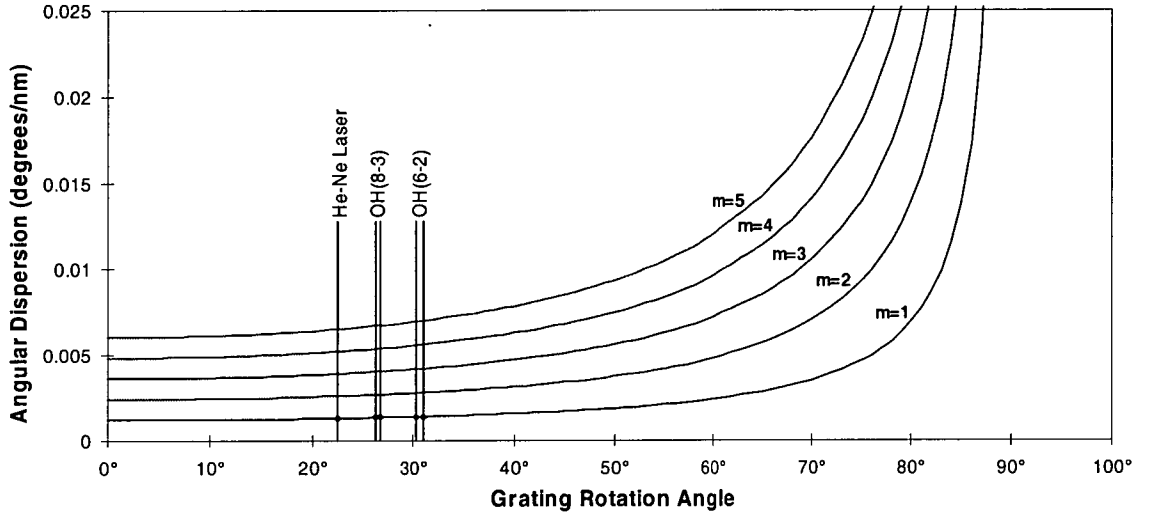

Figure 3-16. Angular dispersion curves for the Davis spectrometer

What is often more useful to know is dispersion across the focal plane at the exit slit, i.e. what is the wavelength spread, $\partial\lambda$, for a given distance, ∂x, in the plane of the exit slit. This is termed the *linear dispersion* and is obtained by multiplying equation 3-7 by the focal length f (in this case f of the second mirror is 1260 mm), thus

$$\frac{\partial x}{\partial \lambda} = f\frac{\partial \beta}{\partial \lambda} = 2f\frac{\partial \theta}{\partial \lambda} = \frac{mf}{d\cos\theta\cos\phi}. \qquad \textit{Equation 3-7}$$

The reciprocal of linear dispersion (in nm/mm) is more often quoted by grating manufacturers, as it can be considered as the wavelength spread per millimetre of slit width, i.e. if the small ∂x is taken to be slit width, then $\partial\lambda$ is a measure of wavelength spread or *bandpass* which results. Thus if s is slit width, bandpass can be calculated from equation 3-7 as

$$\mathrm{BP} = \partial\lambda = \frac{sd\cos\theta\cos\phi}{mf}. \qquad \textit{Equation 3-8}$$

Figure 3-17 plots both reciprocal linear dispersion (RHS axis) and bandpass (LHS axis) for the Davis instrument with a slit width of 250 μm. Table 3-4 also lists dispersion and bandpass quantities for regions of interest.

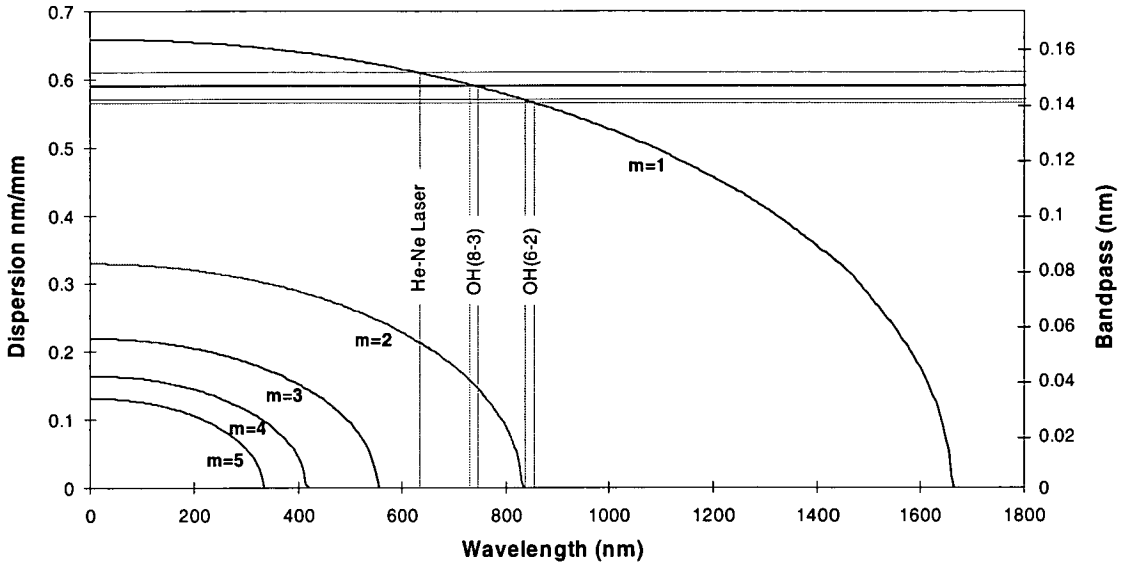

Figure 3-17. Linear dispersion of the Davis system (f = 1260 mm) and bandpass, for 250μm slits.

Region	Wavelength (nm)	Angular Dispersion (°/nm)	Linear Dispersion (mm/nm)	Reciprocal LD (nm/mm)	Bandpass (nm)	Resolving Power @250μm
OH(6-2)	837.5	0.0013948	1.7556	0.5696	0.1424	5881.4
	855.5	0.0014052	1.7702	0.5649	0.1412	6057.7
OH(8-3)	730.5	0.0013411	1.6896	0.5919	0.1480	4936.9
	744.5	0.0013474	1.6952	0.5899	0.1475	5048.2
HeNe Laser	632.8	0.0013027	1.6402	0.6097	0.1524	4151.6

Table 3-4. Dispersion and bandwidth parameters for the Davis instrument in the regions of interest.

The term *bandpass* is used here, as distinct from *instrument function width*, as it defines the theoretical lower limit to instrument function width, for a given slit width. Where two slits are employed, the instrument function becomes a convolution of the entrance and exit slit functions and is further broadened by the focussing precision of the diffracted beam onto the exit slit plane, including spherical and chromatic aberrations and astigmatism. Effective width is also a function of the degree of parallelism between entrance and exit slits. The instrument function is discussed further in section 3.4

3.3.3. Resolution and Resolving Power

Instrument *resolution* refers to its ability to distinguish adjacent lines in a spectrum and is usually expressed as a wavelength. The point at which two adjacent spectral

lines can be resolved is quantified, somewhat arbitrarily, by the Rayleigh criterion; where a principle maximum of one spectral line falls in the first minimum of another. This is the same distance as the instrument function full-width-at-half-maximum (fwhm), thus is determined by the grating, focal length and slit parameters.

Chromatic resolving power is defined as a ratio of wavelength over resolution $\lambda/\Delta\lambda$ and is therefore a dimensionless quantity. Figure 3-18 plots resolving power as a function of wavelength for the Davis spectrometer with 250 μm slits. Values at wavelengths of interest are also listed in Table 3-4.

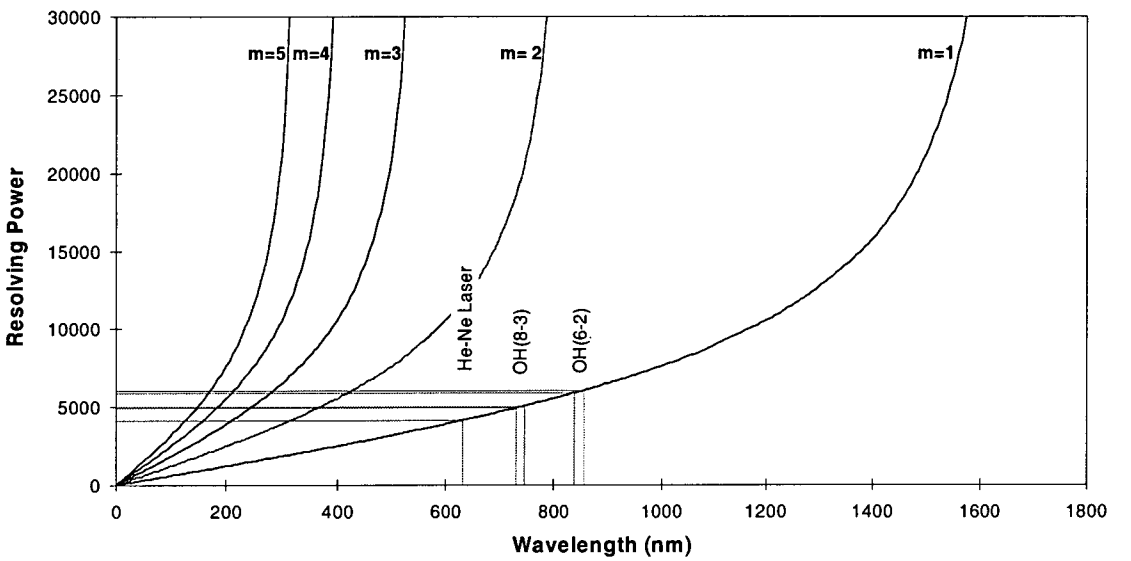

Figure 3-18. Resolving power of the Davis spectrometer with 250 μm slits

The grating itself is certainly capable of much greater resolving power. For this element resolving power is shown to be equal to the product of angular dispersion and the width of the diffracted beam. For a grating of width W, beam width is given by $W.\cos(\theta-\phi) = N.d.\cos(\theta-\phi)$ for N grooves at separation d. Thus resolving power of the grating element is

$$\frac{\lambda}{\Delta\lambda} = \frac{\partial\beta}{\partial\lambda}.W\cos(\theta-\phi) = \frac{m.Nd\cos(\theta-\phi)}{d\cos\theta\cos\phi} \approx mN \qquad \textit{Equation 3-9}$$

i.e. for $\phi \approx 0$ (Littrow case) resolving power in a given order is only dependent on the number of grooves. In our case W is 136 mm, thus N is 163200, giving a resolving power in first order about 27 times greater than for the whole instrument with 250 μm slits.

3.3.4. Throughput and Etendue

Spectral throughput and etendue are measures of the ability of an instrument to accept or pass light. Throughput is a value per unit bandwidth (i.e. independent of slit width) given by

$$U = \varepsilon.A_g \frac{m\, h_s}{d\, f} \qquad \textit{Equation 3-10}$$

where ε is the grating efficiency, A_g is the projected area of the grating = $A\cos(\theta-\phi)$, m is order, h_s is slit height, d is grating spacing and f is focal length [Myrabo and Harang (1988)]. It has units of $mm^2.str.nm^{-1}$. Figure 3-19 plots the throughput of the Davis instrument assuming a grating efficiency of 1.

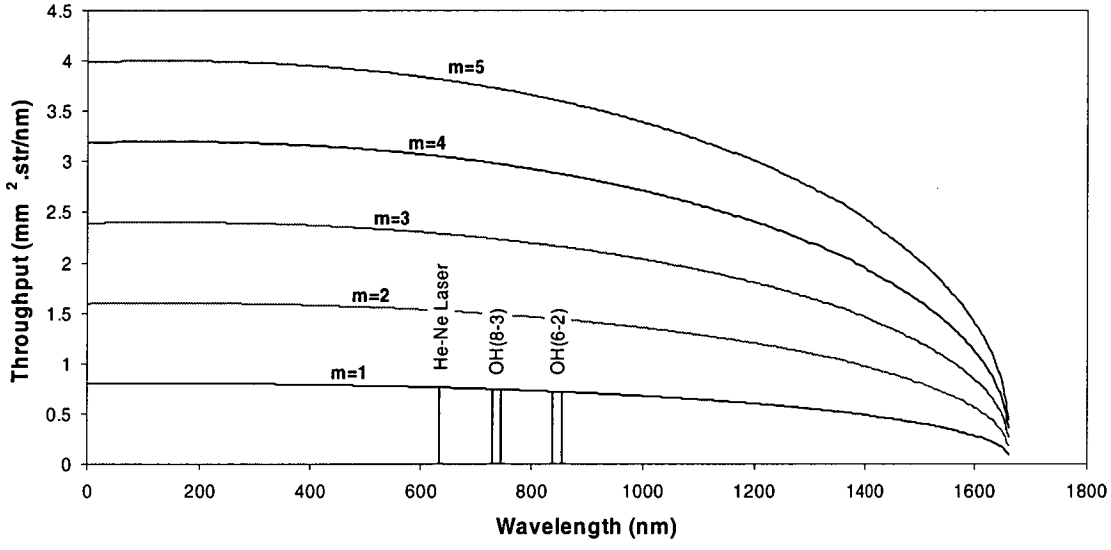

Figure 3-19. Throughput of the Davis spectrometer versus wavelength for m=1-5

Etendue simply includes bandwidth to yield a value in $mm^2.str$. Thus we can write

$E = U.BP =$

$$\varepsilon A_g \frac{m\, h_s}{d\, f} \cdot \frac{s d \cos\theta \cos\phi}{mf} = \varepsilon A_g \frac{s.h_s}{f^2} \cos\theta\cos\phi = \varepsilon A_g \Omega \cos\theta\cos\phi \qquad \textit{Equation 3-11}$$

where the solid angle Ω is that subtended by slit area $s.h_s$ at the collimating mirror. [see http://www.instrumentssa.com/systems/theory/oos/oos.htm]. Etendue for the Davis instrument with 250 μm slit widths is plotted in Figure 3-20.

Instrument etendue [in $mm^2.str$] can be considered as a factor which when multiplied by the radiance [in units $Wmm^{-2}str^{-1}$] of a uniform field viewed by the instrument, yields the radiant flux [in Watts or equivalently photons with energy hc/λ per second] at the detector.

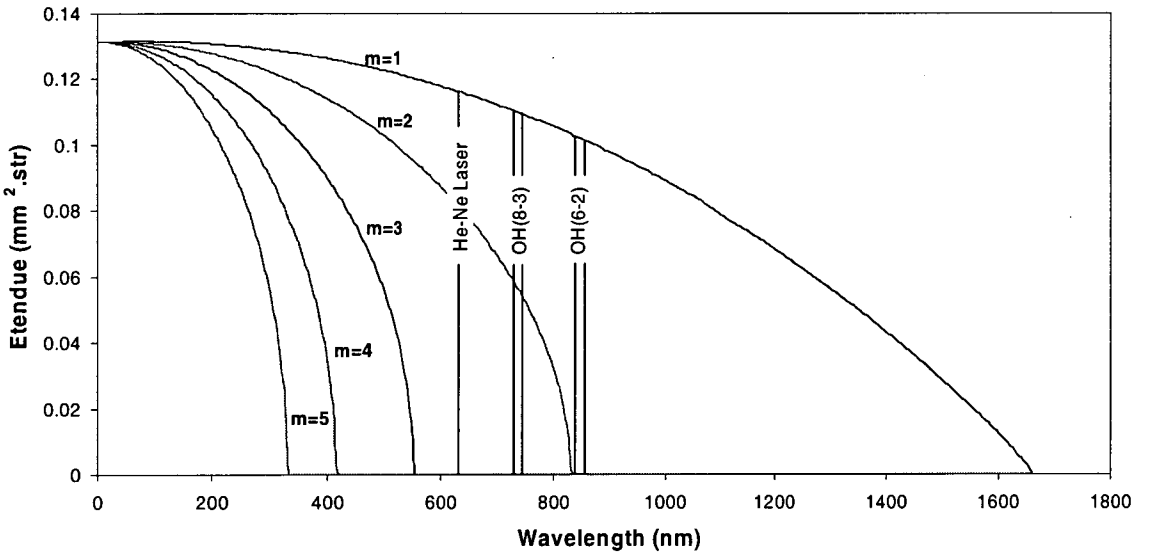

Figure 3-20. Etendue of the Davis instrument with 250 μm slit widths

3.3.5. Blazing and Woods Anomalies

In the calculations above a grating efficiency ε of 1 is assumed, which is certainly not the case across a wide wavelength range. A typical ruled grating efficiency curve, eg from http://www.isainc.com/systems/theory, is shown in Figure 3-21. The grating efficiency can be maximised at a particular wavelength by *blazing*. Triangular grooves are ruled into the grating surface such that the energy distribution to a particular order is enhanced by specular reflection from the groove surface. Diffraction order remains relative to the grating normal, but energy distribution among orders shifts relative to the angle of the groove surface and the grating is said to show a *blaze* of light at the desired angle. The blaze-angle blaze-wavelength relationship is simply the grating equation (3-2) since for reflection the groove surface is equal to the grating rotation angle. For the Davis system the blaze angle is 26.75°, which yields a blaze wavelength of λ750.2 nm in first order for Littrow conditions (or λ747.4 nm for our 4.9° off-Littrow configuration). Note that the grating is also blazed for λ375 nm in 2nd order and λ250 nm in 3rd order etc.

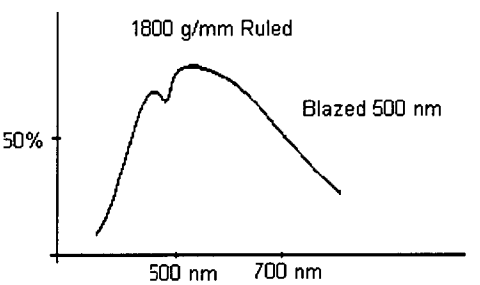

Figure 3-21. Typical blaze efficiency for a ruled grating (http://www.isainc.com /systems/theory)

Wood (1937) first succeeded in ruling grooves with a controlled shape in 1910. His name is given (Woods Anomalies) to deviations in the grating efficiency profile

(such as depicted in Figure 3-21 at about 500 nm), which occur when the angle of refraction (β in Figure 3-14) passes through 90° for integer order (ie the diffracted beam is parallel to the grating surface. Plotted in Figure 3-22 is the function

$$m = \frac{d(\sin\beta - \sin 90)}{\lambda}$$ *Equation 3-12*

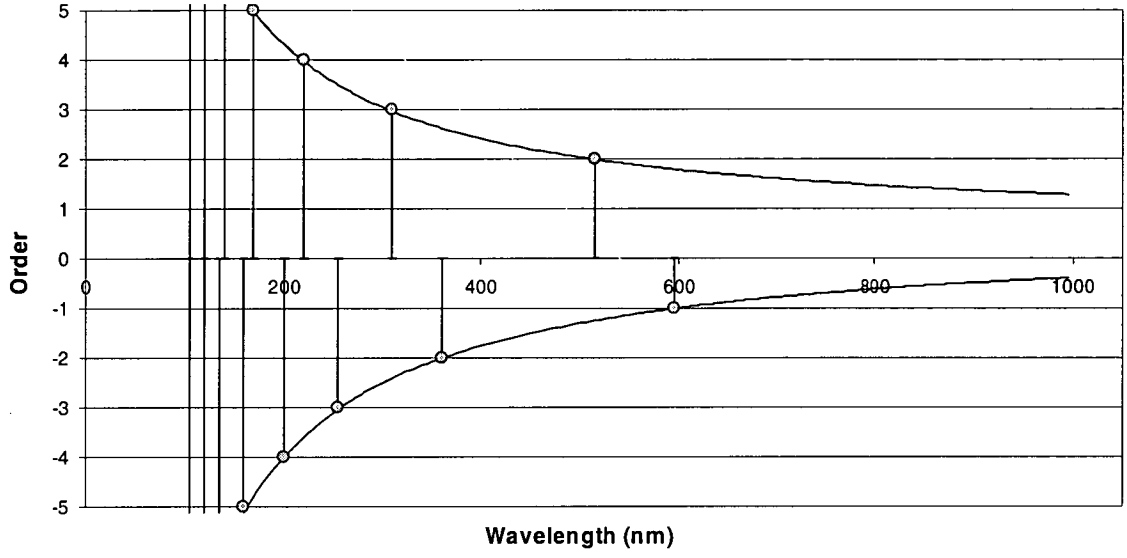

Figure 3-22. Woods Anomalies for the Davis grating.

Woods anomalies for positive orders thus occur at λ515, λ310, λ220 and λ170 nm for orders 2,3,4 and 5 respectively.

3.3.6. Ghosts

Periodic defects formed in diffraction gratings produce multiple minor copies of the primary image called *Rowland ghosts*, displaced small distances in wavelength (Longhurst, 1957). These may be characterised by obtaining a high signal to noise profile of a narrow spectral source, such as a laser or argon discharge lamp. A frequency-stabilised laser has been available at Davis since 1995 for this purpose. Figure 3-23 shows examples of the Rowland ghosts in laser scans of the old grating in 1995 and the new grating in 1998, normalised to 100 at the primary peak for comparison. Values for each grating are summarised in Table 3-5 and are determined by fitting a convolution of instrument functions at primary line and ghost positions.

It is apparent from the fit in Figure 3-23 that the primary instrument function does not well represent the shape of the ghosts, which appear increasingly broadened. This

effect may be due to a small component from focussed stray light, due to non-periodic errors in the grating rulings (Sharpe and Irish (1978)). In any case, ghost separation (~0.35 nm) is very small compared to P-branch line separations (3-4 nm) and very large compared to their Λ-doubling (0.01-0.04 nm). Hence contributions to the P-branch intensities are negligible and can be ignored. Q- and R-branch line separations are much smaller. Rowland ghosts are accounted for when deriving transition probability ratios in chapter 5.

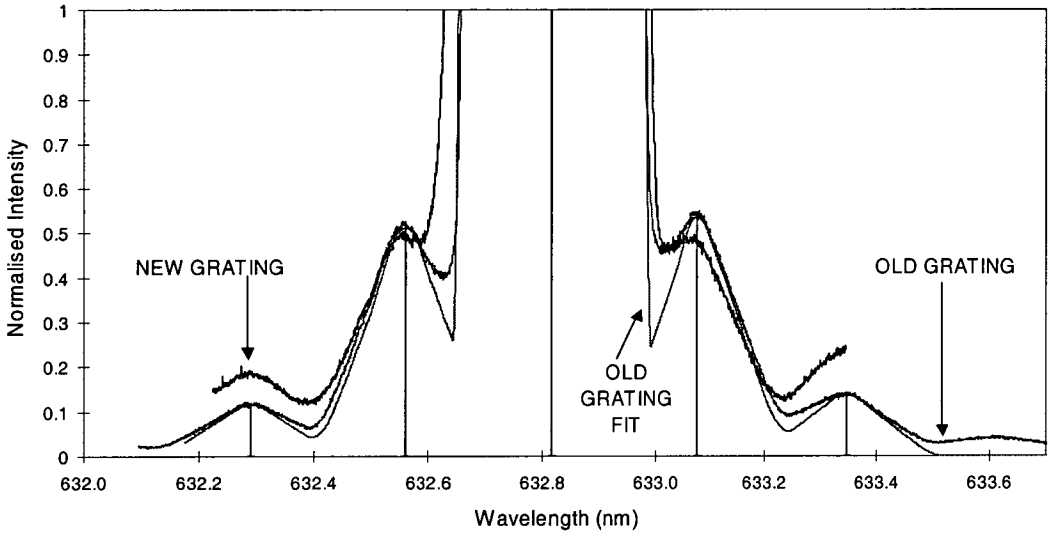

Figure 3-23. Frequency-stabilized laser profiles showing the Rowland ghosts for the old and new gratings at the operating resolution (250 μm slits) and a fit to the old grating profile (see text).

	Ghost	2nd lower λ		1st lower λ		1st higher λ		2nd higher λ	
Grating	λ	Offset Δλ nm	%of peak	Offset Δλ nm	%of peak	Offset Δλ nm	%of peak	Offset Δλ nm	%of peak
Old	632.8	-0.527	0.116%	-0.257	0.513%	0.264	0.536%	0.529	0.138%
	846.5	-0.705		-0.344		0.353		0.708	
New	632.8	-0.517	0.182%	-0.252	0.481%	0.264	0.475%	0.539	0.240%
	846.5	-0.692		-0.337		0.353		0.721	

Table 3-5. Summary of the offset and peak heights (relative to primary) of the first and second ghosts for the old and new gratings at the laser and OH(6-2) $P_1(4)$ wavelengths.

3.4. Instrument Function Calibrations

Accurate characterization of the instrument function is required to correct for differences in the Λ-doubling separation of P-branch lines and to allow for the contribution of background features in close proximity to the integration region around each line.

Regular scans of a frequency-stabilized laser, dispersed over the field of view via a Lambertian screen, have been made since 1995 for this purpose. As dispersion increases with grating rotation angle, the instrument function at the laser wavelength is substantially wider than in the OH(6-2) region. Conversion of the laser profile, to an instrument function at the observing wavelengths has been approached in several different ways.

3.4.1. Intrinsic Width Method

The first was to consider the measured fwhm of the laser profile (F_{laser}) to be composed of an in-quadrature sum of the theoretical bandwidth B_{laser} and an intrinsic error term δW, i.e.

$$F_{laser}^2 = B_{laser}^2 + \delta W^2. \qquad \textit{Equation 3-13}$$

Theoretical bandwidth can be scaled to any wavelength by equation 3-8 and, if δW is assumed to be independent of λ, the fwhm at the new wavelength can be calculated. The ratio F_{laser} to F_{sample} gives the magnification in the wavelength domain by which to scale the laser profile to derive the instrument function at the sample wavelength.

Calculated width, for the two Λ-doubled components at OH(6-2)$P_1(4)$ turned out to be wider than the measured fwhm for $P_1(4)$, indicating that δW does in-fact vary with wavelength and this method is inappropriate.

3.4.2. Empirical Fit Method

A better method was to take the full measured laser profile (including ghosts and any asymmetry) and using a multi-parameter least squares method varying the width (wavelength scale) and amplitude, fit a sum of two replica

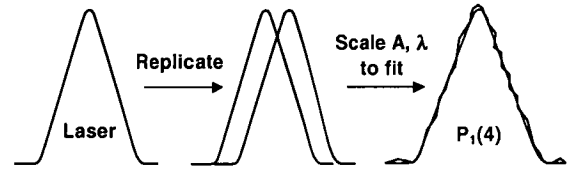

Figure 3-24. Empirical laser profile fit to $P_1(4)$

profiles centred at the Λ-doubling wavelengths to a high signal to noise $P_1(4)$ profile [Figure 3-24].

$P_1(4)$ was chosen specifically due to the lack of satellite lines and minimal auroral contamination in the background region around this line. Representative high-signal-to-noise $P_1(4)$ profiles were generated from routine observations for each year (or part-year when the instrument configuration was changed) by summing multiple profiles aligned in offset.

The fitted width can then be described as an in-quadrature sum of the theoretical bandwidth and an error term, as for the intrinsic width method. A resulting instrument function fwhm is calculated for other P-branch lines from a scaled bandwidth and the error term, assuming that differences in the error term over the OH(6-2) wavelength range is very small. The wavelength domain is again scaled by the ratio $F_{P1(4)}$ to $F_{P\text{-line}}$ so that the instrument profile shape is preserved.

This method has an advantage over the slit rotation method discussed below, in that profile asymmetry and ghosts are accounted for, but it requires high-signal-to-noise $P_1(4)$ profiles to be generated from selected profiles each time the instrument configuration is changed.

3.4.3. Slit Rotation Method

An alternative is to consider the instrument function as a convolution of theoretical bandwidths of a straight and a rotated slit function as illustrated in Figure 3-25. By the symmetry relationship the rotated slit can be approximated as a trapezium with sides angled at the rotation angle. The convolved function is fitted to a laser profile by adjusting the rotation angle, offset and amplitude using a reduced-squares method to yield a best-fit slit rotation angle. It is assumed that this rotation angle does not change with wavelength (or grating rotation angle) so that the instrument function at any wavelength can be reconstructed using the theoretical bandwidth at the new wavelength. Fitted fwhm

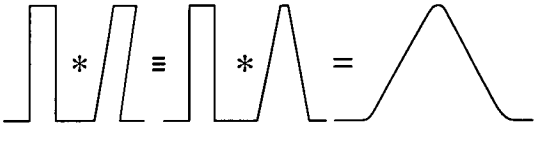

Figure 3-25. Convolution of a slit and rotated slit function.

and slit rotation angle for all laser profiles scanned at 250 μm slit widths since 1995 are shown in Figure 3-26. Theoretical width is 1.52Å.

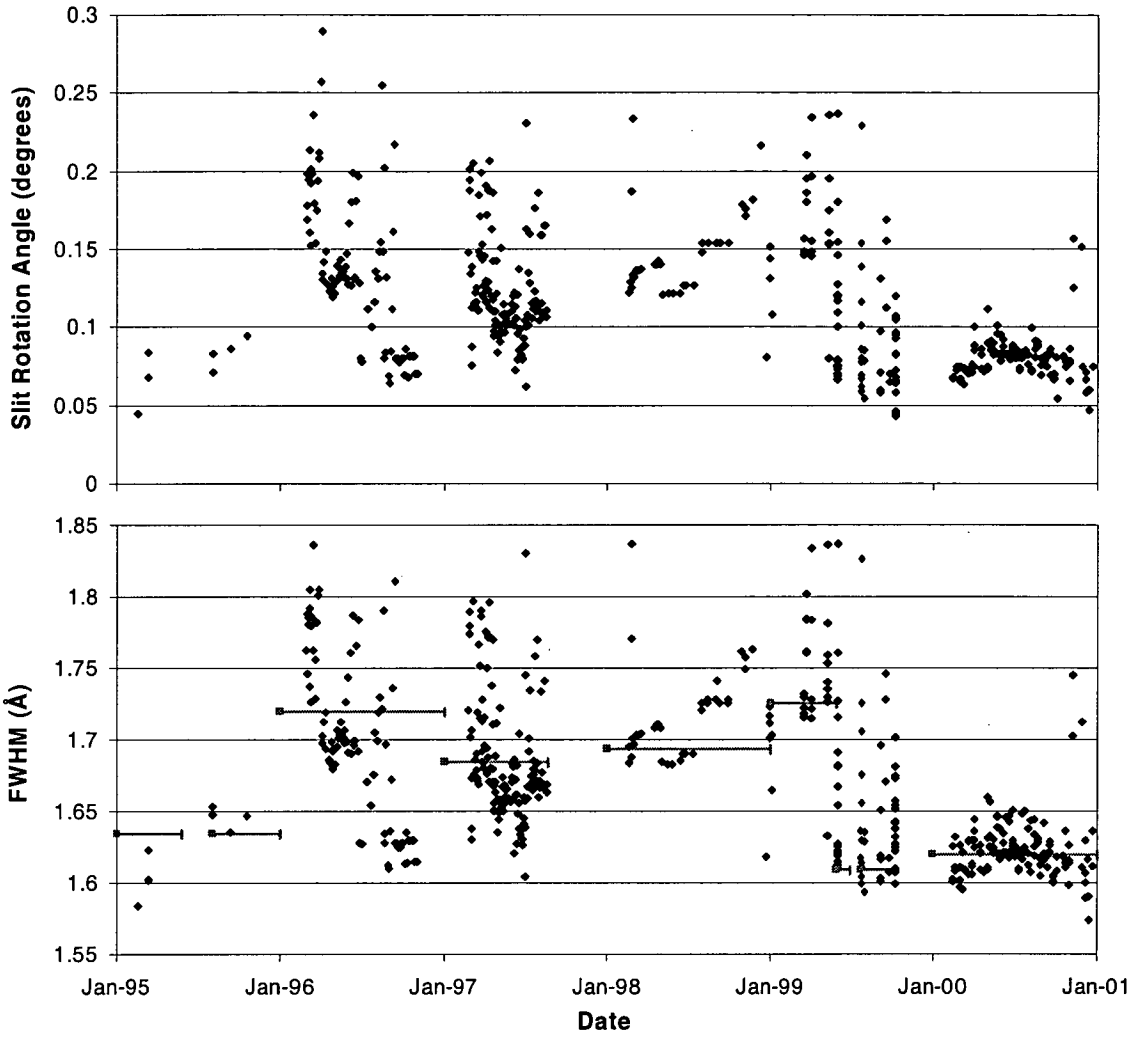

Figure 3-26. Fitted slit rotation angle (top) and fwhm (bottom) from frequency-stabilized laser profiles at 250μm slit widths from 1995-2001. Mean fwhm values derived using the empirical fit method are also shown in the bottom panel for the periods covered.

On 27-May-1995 (D147) the instrument suffered a knock during the process of fitting a stabilizing bracket to the entrance column (the entrance column vibrated considerably during blizzards). As a result the entrance slit was bumped out of alignment (rotation ~0.54° and the instrument function considerably broadened (fwhm ~2.59Å). The following period was characterized by frequent blizzards and overcast sky such that diminished signal to noise and broadened instrument function was not recognized until the end of July. This period is not shown in Figure 3-26. Regular laser scans became part of the routine operational requirements after this time.

This slit rotation method has an advantage that an instrument function at a given wavelength can be re-created from a single parameter; the slit rotation. Furthermore, slit rotation and laser fwhm are linearly related by the equation shown in Figure 3-27. With regular laser scans the variation of the slit rotation parameter keeps an up-to-date track of instrument performance as it is not necessary to compute a representative $P_1(4)$ profile over a given time. It does not however account for profile asymmetry or ghosts.

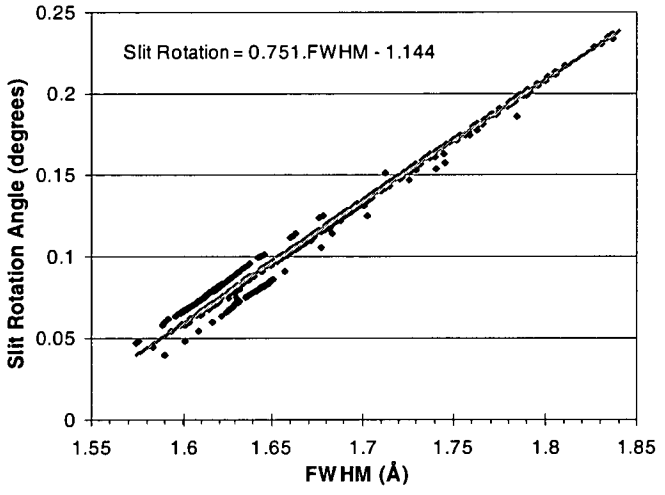

Figure 3-27. Slit rotation and laser fwhm relationship. The incremental offset from the best fit line are due to the sampling resolution on some laser scans..

3.4.4. Λ-doubling correction factors

Either of the latter two methods is able to adequately reproduce the instrument function across the OH(6-2) region. With this information correction factors can be calculated for each line to account for the difference in Λ-doubling separation.

For a given integration width, centred on the mean of the Λ-doubled components for each line, correction factors represent the percentage of the total emission summed [Figure 3-28]. The wider the Λ-doubling, the smaller the percentage summed. Derivation of an optimum summing width is discussed in section 4.3.8.

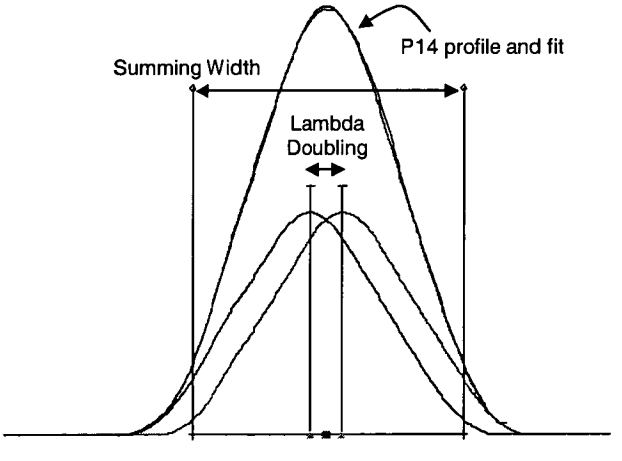

Figure 3-28. Λ-doubling correction factors.

Where the measured instrument functions for a given period are similar, an average value was selected to represent all data within that interval, for the analysis. Selected fwhm values and the time interval spanned (derived from the empirical fit method) are shown on Figure 3-26 and listed in Table 3-6 for each year, or part year where

the instrument configuration is changed significantly. Values for 1990 and 1994, when no laser scans are available were chosen from the best match of instrument configuration from other years, adjusted for the different step sizes.

For the slit rotation method, the fraction of each line within the sum interval is a smooth function of the slit rotation (and consequently laser fwhm). These curves are plotted in Figure 3-29 and compared with those derived from the empirical fit method.

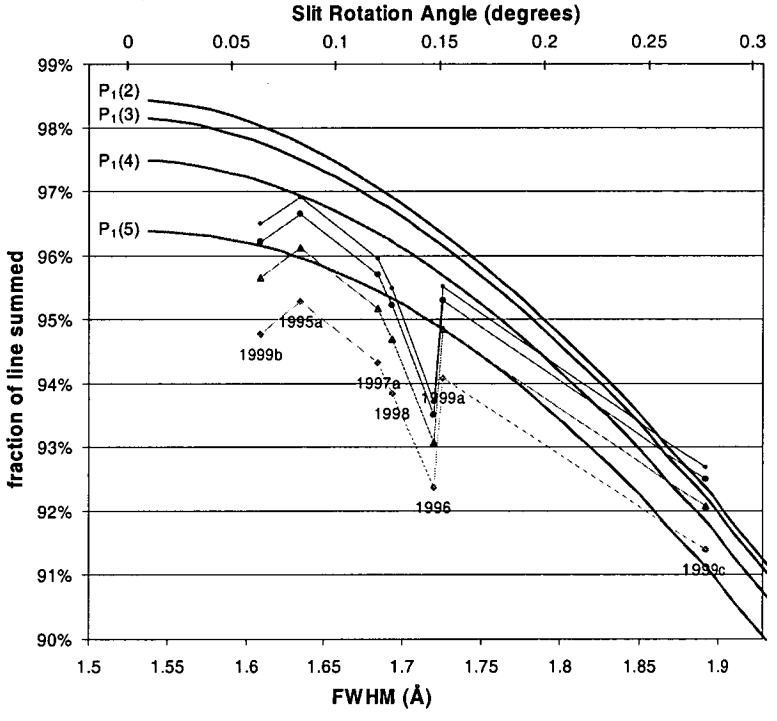

Figure 3-29. Correction factors, derived from the slit rotation method (smooth curves labelled with branch lines) compared to those derived from the empirical fit method (labelled with year).

Considering the different approaches the two methods compare well. The empirical fit method yields slightly lower fractions for each line, which is expected as ghost contributions are outside the summing interval. These curves are not smooth, largely due to profile asymmetries.

Rotational temperatures are derived from the ratio of two emission intensities. Line fraction ratios are also listed in Table 3-6 with average values for 250 μm slit widths. Not accounting for Λ-doubling differences yields temperatures that are on average 1.4 K, 2.0 K and 1.6 K too low for $P_1(2)/P_1(4)$, $P_1(4)/P_1(5)$ and $P_1(2)/P_1(5)$ ratio's respectively at 200 K. Variability in factors between years amounts to 0.36 K, 0.52 K and 0.41 K, for respective ratio's.

Year	From Day	From Date	Slit Width μm	Step size Å	Sum Width Å	Slit Rotation degrees	Laser fwhm Å	Fraction of Line summed						Ratios		
								$P_1(2)$ %	$P_1(3)$ %	$P_1(4)$ %	$P_1(5)$ %	$Q_1(5)_f$ %	$Q_1(5)_a$ %	$P_1(2)/P_1(4)$	$P_1(4)/P_1(5)$	$P_1(2)/P_1(5)$
1990	1	1-Jan-90	250	0.05	2.55	N/A	N/A	96.91%	96.65%	96.12%	95.29%	96.94%	48.82%	1.0082	1.0088	1.0170
1994a	1	1-Jan-94	250	0.05	2.55	N/A	N/A	96.91%	96.65%	96.12%	95.29%	96.94%	48.82%	1.0082	1.0088	1.0170
1994b	100	10-Apr-94	250	0.1	2.5	N/A	N/A	95.95%	95.70%	95.17%	94.33%	95.99%	47.17%	1.0083	1.0089	1.0173
1994c	182	1-Jul-94	250	0.2	2.6	N/A	N/A	97.88%	97.69%	97.24%	96.48%	97.94%	50.82%	1.0066	1.0079	1.0145
1995a	1	1-Jan-95	250	0.05	2.55	0.0831	1.6345	96.91%	96.65%	96.12%	95.29%	96.94%	48.82%	1.0082	1.0088	1.0170
1995b	147	27-May-95	250	0.05	2.55	0.5465	2.5937	80.45%	80.37%	80.13%	79.69%	80.47%	48.94%	1.0040	1.0056	1.0095
1995c	214	2-Aug-95	250	0.05	2.55	0.0831	1.6345	96.91%	96.65%	96.12%	95.29%	96.94%	48.82%	1.0082	1.0088	1.0170
1996	1	1-Jan-96	250	0.05	2.55	0.1471	1.7196	93.70%	93.49%	93.07%	92.36%	93.73%	48.01%	1.0067	1.0076	1.0144
1997a	61	2-Mar-97	250	0.1	2.5	0.1206	1.6844	95.95%	95.70%	95.17%	94.33%	95.99%	47.17%	1.0083	1.0089	1.0173
1997b	234	22-Aug-97	100	0.05	2.55			98.67%	98.67%	98.67%	98.66%	98.67%	47.99%	1.0001	1.0001	1.0002
1998	1	1-Jan-98	250	0.1	2.5	0.1272	1.6931	95.49%	95.23%	94.70%	93.84%	95.55%	47.21%	1.0084	1.0091	1.0175
1999a	1	1-Jan-99	250	0.1	2.5	0.1515	1.7255	95.51%	95.30%	94.85%	94.09%	95.55%	47.88%	1.0070	1.0080	1.0151
1999b	146	26-May-99	250	0.1	2.5	0.0642	1.6094	96.49%	96.21%	95.65%	94.77%	96.55%	47.47%	1.0087	1.0094	1.0181
1999c	178	27-Jun-99	250	0.1	2.5	0.2765	1.8916	92.68%	92.49%	92.07%	91.39%	92.72%	47.68%	1.0065	1.0075	1.0141
1999b	146	23-Jul-99	250	0.1	2.5	0.0642	1.6094	96.49%	96.21%	95.65%	94.77%	96.55%	47.47%	1.0087	1.0094	1.0181
1999d	287	14-Oct-99	250	0.1	2.5			96.92%	96.64%	96.07%	95.16%	96.97%	47.68%	1.0088	1.0095	1.0184
2000	1	1-Jan-00	250	0.1	2.5	0.0722	1.6200	97.92%	97.65%	97.07%	96.13%	97.99%	47.56%	1.0087	1.0098	1.0186
												250 μm average		1.0080	1.0087	1.0168

Table 3-6 Correction factors for the percentage of each line contained within the summing width for each year, or part year when the instrument configuration changed significantly. No laser scans are available prior to 1995, these values are estimated from the best match instrument configuration from other years, adjusted appropriately for the different step sizes.

3.5. Low Brightness Source Calibration Lamps

Spectral response of the instrument is characterised by reference to a low brightness source of known radiant intensity and traceable to international standards. Stability and longevity of the calibration lamp is an important factor for inter-year comparisons. Factors affecting the lifetime of lamps are discussed in Appendix B. Significant problems were experienced with the consistency of low brightness source calibrations and as a result, three different sources were used over the years. These lamps, and their calibration at various standards laboratories are discussed here.

3.5.1. Primary Tungsten-Filament Lamps

A Siemens type-83 12V 60W tungsten filament lamp, fitted in a purpose built housing (Figure 3-30) and powered by a precision current source at 4.595A was calibrated in Dec-1987 by the colour measurement unit of the Australian Broadcasting Corporation (ABC). Initial work with the spectrometer concentrated on the OH(8-3) band so the lamp was only calibrated up to λ770 nm.

Figure 3-30. Primary tungsten filament lamp

Response calibrations were made on the spectrometer at Davis in 1990 and 1994. Several neutral density filters were required to reduce the emission intensity to a suitable level for the spectrometer in observing configuration. Light was also distributed over a Lambertian screen covering the spectrometer's field of view.

Recalibration of the lamp was not made until May-1996, and then at the Commonwealth Scientific and Industrial Research Organization (CSIRO) National Measurement Laboratory (NML). Results were largely inconsistent over the range of the ABC's measured values including the OH(8-3) region as shown in Figure 3-31 (both curves are normalised to unity at λ750 nm). It was not possible to determine if one calibration had been in error, or the spectral character of the lamp had changed. Consequently, no reasonable assessment of the spectrometer spectral response over either the OH(8-3) or OH(6-2) scan region could be made using this lamp.

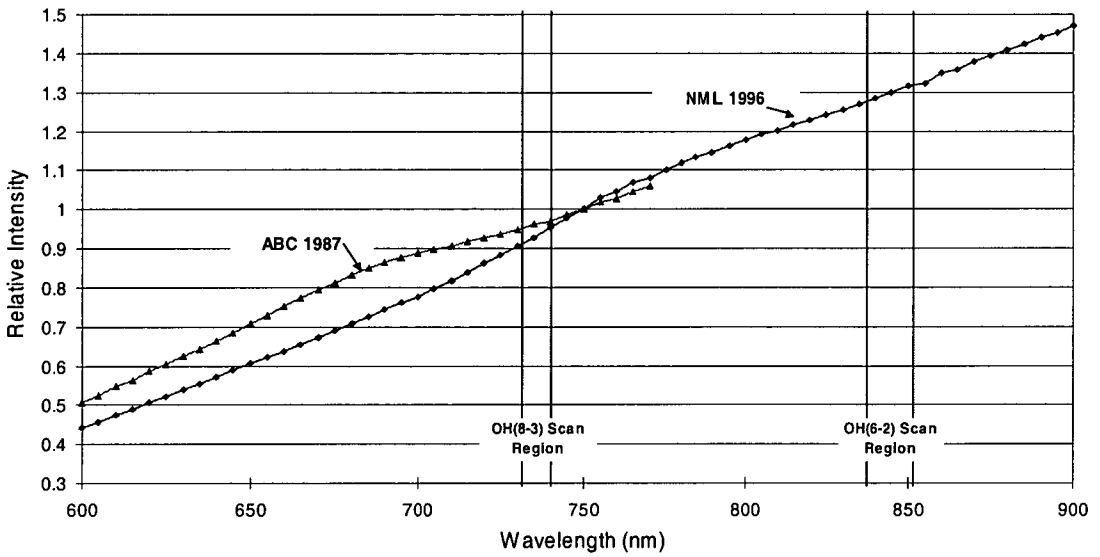

Figure 3-31. Inconsistent calibrations precluded the use of the primary calibration lamp for spectral response calibrations. Curves are normalized to unity at λ750 nm.

3.5.2. Secondary Calibration Lamp

Due to time constraints in setting up and performing a primary instrument response calibration, and the objective of extending the life of that lamp, it was intended to calibrate against the primary source only 3 or 4 times per year and assess shorter time scale variability with more frequent observations of a secondary calibration lamp.

For this purpose a quartz-halogen lamp (Osram type HLX 64250 20W 6V) was built into the entrance box assembly and introduced into the instrument via the front swing mirror and Lambertian screen. This lamp was driven with a precision DC current source at 2.00A, about 60% of it nominal rating, again to preserve lamp life. Considering the difficulty experienced with primary calibrations it turned out to be very fortunate that these calibrations were made, and furthermore, that the same lamp was used for each year of observations between 1987 and 1996.

With the assumption that the relative radiant spectral intensity of the secondary lamp had not changed over this period, these measurements provide a consistent means of determining relative spectral response of the instrument for years prior to 1996, by reference to a new low-brightness source introduced in that year. These retrospective calibrations and associated errors are discussed further in section 3.6.1.

3.5.3. McEwen Portable Low Brightness Source

At the end of 1995 a portable low brightness source (PLBS), donated by Dr. Don McEwen's group at the Institute for Space and Atmospheric Studies, University of Saskatchewan, Canada, was sent to Davis and measured on the spectrometer over the OH(6-2) and OH(8-3) scan regions. At this stage the radiance of the PLBS had only been calibrated between λ400 and λ660 nm (in 1990) but it was intended to re-calibrate it to λ900 nm at a later date so that a response function for the instrument could be determined across both regions of interest.

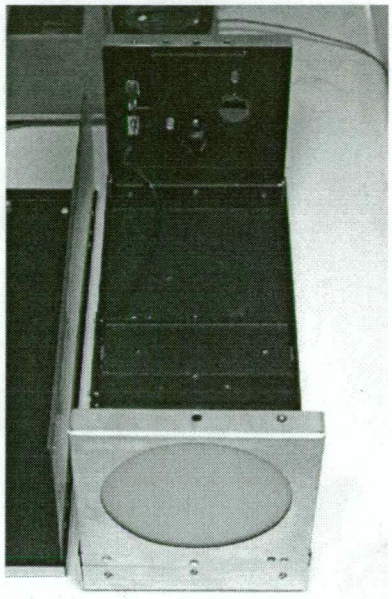

Figure 3-32. The McEwen LBS, opened for inspection.

This unit consists of a battery powered, Tungsten filament lamp, housed in an aluminium box of dimensions 170×200×420 mm and illuminating a glass diffusing screen of diameter 127 mm (Figure 3-32). Separation between the lamp and diffusing screen is about 400mm. A neutral density filter may be rotated into position over the lamp to reduce radiance by approximately a factor of 10. A solid-state regulator controls voltage across the lamp at 4.965 V. The unit is mounted on top of the entrance box for measurement.

In December 1996 radiance calibrations of the PLBS was made over the range λ350-900 nm at NML, no measurement errors were given at this time. A relative intensity measurement was repeated four times over the λ700-900 nm range in January 1997. The mean of the Jan-97 measurements is scaled to fit the Dec-96 absolute units at λ840 nm, and is plotted for comparison in Figure 3-33. Error bars plotted on the Jan-97 fit are the standard deviation of the four measurements at each wavelength.

Good agreement was obtained between the 1996 and 1990 calibrations for the limited wavelength range below λ660 nm over which they can be compared. The Jan-97 scaled curve also agrees well with the 1996 result and provides some estimate of measurement repeatability. Poor signal to noise above λ870 nm is due to fall off in detector response.

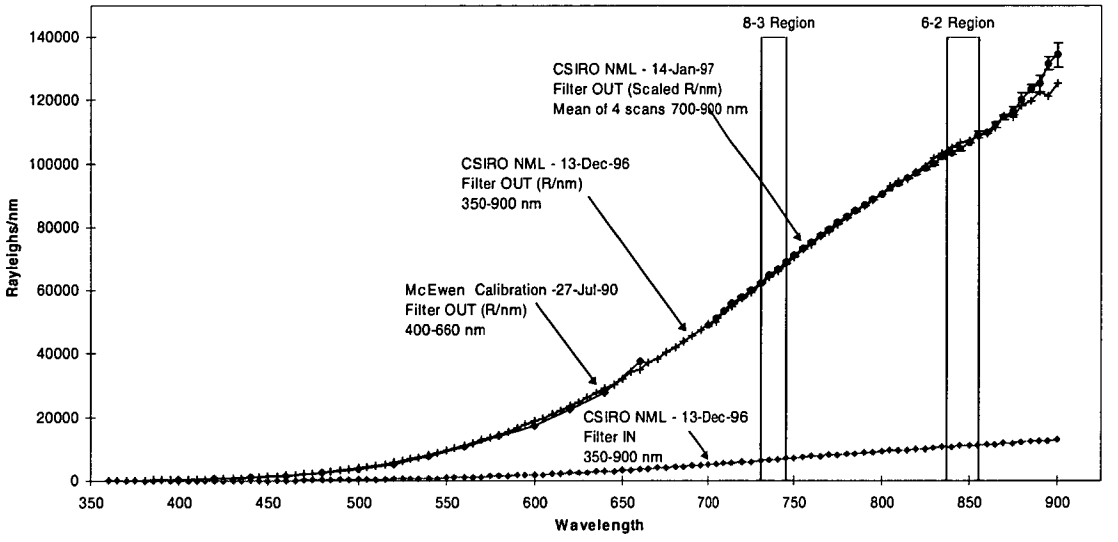

Figure 3-33. Spectral radiance of the McEwen portable low brightness source, tested with and without the neutral density filter.

Ultimately a choice was made not to pursue calibrations with this unit for several reasons:

1. The low power (~1 Watt) lamp contained a thin and fragile filament, an undesirable property for extended lifetime considering the stress and vibration it would encounter twice annually transported between Australia and Antarctica.
2. A good set of calibration scans take at least several hours to complete. After the batteries ran down midway through calibrations at Davis the battery power supply option was also considered undesirable.
3. The single diffusing screen in the McEwen design was also a drawback as it resulted in a non-uniform intensity distribution across the front aperture. The Davis spectrometer and the NML instrument viewed different areas of this diffusing screen and it was not determined whether any spectral differences resulted.

As a better choice became available, no calibrations were done on the McEwen portable low brightness source after Jan-97.

3.5.4. Eather Low Brightness Source

In December 1995 a third low brightness source was obtained from Dr Bob Eather of KEO Consultants - Photometric, Camera and TV Systems, Massachusetts, USA. This LBS is a coiled-coil filament tungsten-halogen lamp powered by an external supply and housed in a metal box of dimensions 525×162×162 mm. (Figure 3-34). Internally the box is divided into 3 sections. The first, containing the lamp is painted black and allows air circulation (by natural convection) around the lamp through side vents. Light passes through to the second section via a small diffusing screen and an aperture disk. A rotary switch on the rear panel selects the aperture size. Second and third sections are painted a diffuse white and are divided by a ground glass diffusing screen. A white target plate inside the second section prevents light from directly irradiating the diffusing screen. The third section is sealed by another diffusing screen, which is viewed by the spectrometer from the front.

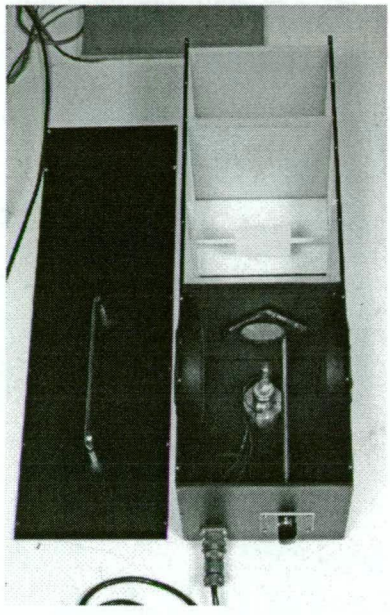

Figure 3-34. The Eather LBS with lid removed.

3.5.4.1. A change from AC to DC operation

Calibration by KEO Consultants in Dec-95 was conducted at 1.900 amps (115V AC) in 10 nm steps over the range λ380 to λ850 nm and is shown in Figure 3-35. The unit was delivered to Davis for the 1996 winter season where a great deal of effort was devoted to defining the instrument spectral response, not only for the current system but retrospectively for all previous years of operation by reference to the quartz-halogen secondary calibration lamp. This is described in section 3.6.

After returning from Davis in December 1996 the unit was re-calibrated at NML at 1.900A and at 1.800A in 5 nm steps between λ360 and λ900 nm. These measurements were repeated four times each at two different aperture settings over the λ700-900 nm range in January 1997. These results are also plotted in Figure 3-35. Although consistent results were obtained between Dec-96 and Jan-97 they were substantially different from the earlier KEO consultants calibration.

Further investigation revealed that the external power supply for the unit had been changed at the beginning of 1996. The original supply was an autotransformer on mains supply, and the voltage was adjusted to set a current of 1.900 Amps (AC). A stop was added to the adjustment so that when connected to the Australian 240V mains standard it could not be turned up above 115V. As voltage adjustment on the power supply was fairly coarse and there was a safety hazard issue within the unit, the 1996 engineer and physicist at Davis exchanged the autotransformer with a precision current source. Unfortunately, the supply was changed from AC to DC current in this process.

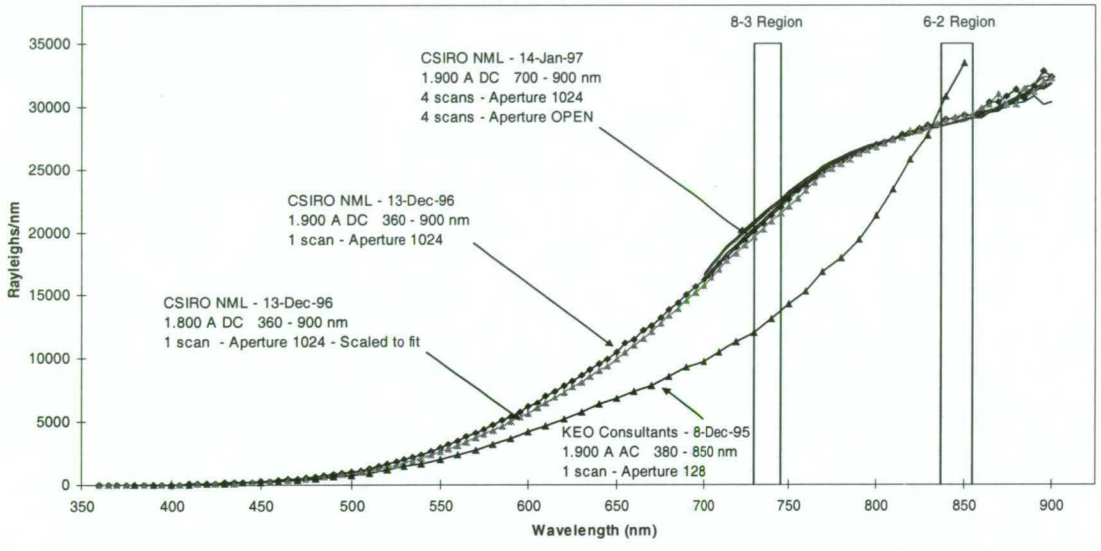

Figure 3-35 Spectral radiant intensity of the Eather low brightness source. The change from AC to DC lamp operation is responsible for the difference in the KEO and NML curves.

That this should result in such a dramatic change in spectral shape is perhaps surprising, considering that at 1.9 A RMS AC the same power should be dissipated as at 1.9 A DC providing the current and voltage were in phase. An intensity enhancement at lower wavelengths is consistent with the lamp operating at a higher temperature when DC voltage is applied. The scan at 1.8 A DC shows a slight spectral change towards the AC profile, and suggests, that when using AC supply, the lamp was operating well below its power rating. The consequences of this in terms of the *halogen cycle* and some disadvantages of DC operation in terms of filament lifetime (in particular DC notching) are discussed in Appendix B. Despite this, and due to the fact that DC notching persists after its formation, it was decided not to revert to AC for further calibrations.

3.5.5. Annual NML Calibrations: Comparisons, Problems and Tests

Table 3-7 shows a log of the annual low brightness source calibrations at NML. Series labels in column 2 are referred to throughout this section. A calibration is made using source substitution with a lamp of known spectral radiant intensity.

Operating current and voltage of each lamp was recorded at the start and end of each scan. Although manually set, fine adjustment on the power supply could set the current to 1 part in 10^5.

Each scan also began and ended with a measurement at a reference wavelength, (normally at λ700 nm in our case), which was also sampled during the scan. This was to assess the drift in detector response during the course of the calibration. A linear interpolation between the reference samples, as a percentage change from the mid-scan sample, was applied as a correction at each wavelength. The reference wavelength samples and percentage drift are also included in the last columns of Table 3-7 to enable a comparison of the relative signal levels and drift rates.

Dark (or zero level) currents were measured at the start, mid-scan and end of each scan by closing the shutter. A linear interpolation between the dark count samples was subtracted from the measured current at each wavelength.

3.5.5.1. Measurement Errors

For each measurement, the detector current was sampled until the standard deviation in the measurement was better than 0.1% or to a maximum of 800 times. Calculation of the LBS source function is given by

$$LBS_{source}(\lambda) = \frac{(LBS_{meas}(\lambda) - D_{lbs}) / S_{lbs}}{(REF_{meas}(\lambda) - D_{ref}) / S_{ref}} \times REF_{source}(\lambda) \qquad \textit{Equation 3-14}$$

where $LBS_{meas}(\lambda)$ and $REF_{meas}(\lambda)$ are the measured detector currents for the LBS and the reference lamp respectively. D_{lbs} and D_{ref} are the time interpolated dark currents from samples taken during the LBS and reference scans respectively. S_{lbs} and S_{ref} are the time interpolated scaling factors for the drift in the measured current at the reference wavelength, taken during the LBS and reference lamp scans respectively. $REF_{source}(\lambda)$ is the known spectral radiant intensity of the reference lamp.

Scan	Label	Lamp	V	A	Time	Shielding	Aperture	Bandwidth	Detector	Start	End	Reference Currents				
										λ	λ	Start	700	End	Increase from start	
1990																
01-Jan-90																
1	AK	McEwen LBS	4.965			Filter OUT			Saskatoon	400	660					
1995																
01-Jan-95																
1	Eureka	McEwen LBS	4.965						Hammel – Eureka	482	660					
08-Dec-95																
1	KEO	Eather LBS M27610	AC	1.9			128		Keo Consultants	380	850					
1996																
13-Dec-96																
1		McEwen LBS	4.965			Filter IN			Hamamatsu R562 s/n SA4965	360	900					
2		McEwen LBS	4.965			Filter OUT			Hamamatsu R562 s/n SA4965	360	900					
	1.9A	Eather LBS M27610		1.9			1024		Hamamatsu R562 s/n SA4965	360	900					
	1.8A	Eather LBS M27610		1.8			1024		Hamamatsu R562 s/n SA4965	360	900					
	E LBS (5)	Eather LBS M27610	105.152	1.9			1024		Hamamatsu R562 s/n SA4965	700	900	16239.9741	16239.9741	16239.97419	0.00%	0.00%
1997																
Tue 14-Jan-1997																
1		SI26 Reference	100.757	5.069	?	none			Hamamatsu R562 s/n SA4965							
2	R1	SI26 Reference	100.762	5.069	12:19	none			Hamamatsu R562 s/n SA4965	700	900	0.00001097	0.00001096	0.000010833	-0.05%	-1.27%
3	E Full (1)	Eather LBS M27610	105.153	1.9	13:02	none	1		Hamamatsu R562 s/n SA4965	700	900	6.1586E-09	6.149E-09	6.143E-09	-0.16%	-0.25%
4	E 1024 (1)	Eather LBS M27610	105.194	1.9	15:26	none	1024		Hamamatsu R562 s/n SA4965	700	900	1.9573E-09	1.9589E-09	1.962E-09	0.08%	0.24%
Wed 15-Jan-1997																
5	E Full (2)	Eather LBS M27610	105.153	1.9	7:52	none	1		Hamamatsu R562 s/n SA4965	700	900	6.1277E-09	6.1223E-09	6.1663E-09	-0.09%	0.63%
6	E 1024 (2)	Eather LBS M27610	105.182	1.9	10:16	none	1024		Hamamatsu R562 s/n SA4965	700	900	1.9664E-09	1.967E-09	1.9687E-09	0.03%	0.12%
7	E Full (3)	Eather LBS M27610	105.179	1.9	12:39	none	1		Hamamatsu R562 s/n SA4965	700	900	6.1805E-09	6.179E-09	6.179E-09	-0.02%	-0.02%
8	E 1024 (3)	Eather LBS M27610	105.184	1.9	15:03	none	1024		Hamamatsu R562 s/n SA4965	700	900	1.9645E-09	1.966E-09	1.968E-09	0.08%	0.18%
Thu 16-Jan-1997																
9	McEwen (1)	McEwen LBS	4.965		7:57	none			Hamamatsu R562 s/n SA4965	700	900	4.9868E-10	4.9753E-10	4.9857E-10	-0.23%	-0.02%
10	E Full (4)	Eather LBS M27610	105.149	1.9	10:23	none	1		Hamamatsu R562 s/n SA4965	700	900	6.0038E-09	6.0039E-09	6.0411E-09	0.00%	0.62%
11	McEwen (2)	McEwen LBS	4.965		12:47	none			Hamamatsu R562 s/n SA4965	700	900	5.4016E-10	5.3969E-10	5.3992E-10	-0.09%	-0.04%
12	E 1024 (4)	Eather LBS M27610	105.161	1.9	15:15	none	1024		Hamamatsu R562 s/n SA4965	700	900	2.0485E-09	2.048E-09	2.0581E-09	-0.02%	0.47%
13	McEwen (3)	McEwen LBS	4.965		17:42	No filter			Hamamatsu R562 s/n SA4965	700	900	4.9299E-10	4.9256E-10	4.9224E-10	-0.09%	-0.15%
Fri 17-Jan-1997																
14	McEwen (4)	McEwen LBS	4.965		6:58	No filter			Hamamatsu R562 s/n SA4965	700	900	4.9172E-10	4.9128E-10	4.9023E-10	-0.09%	-0.30%

Scan	Label	Lamp	V	A	Time	Shielding	Aperture	Bandwidth	Detector	Start	End	Reference Currents				
												Start	700	End	Increase from start	
1998																
Mon 8-Dec-1997																
1	R1	SI26 Reference	100.844	5.069	14:56	none			LAH1PF5	700	900	1.0306	1.0307	1.0311	0.01%	0.05%
2	Full(1)	Eather LBS M27610	105.091	1.9	15:12	none	1		LAH1PF5	700	900					
3	Full(2)	Eather LBS M27610	105.094	1.9	15:46	none	1		LAH1PF5	700	900					
Tue 9-Dec-1997																
4	R2	SI26 Reference	100.843	5.069	9:06	none			Hamamatsu R562 s/n SA4965	700	900	0.80561	0.8039	0.80378	-0.21%	-0.23%
5	Full(3)	Eather LBS M27610	105	1.9	9:23	none	1		Hamamatsu R562 s/n SA4965	700	900					
6	Full(4)	Eather LBS M27610	105	1.9	9:53	none	1		Hamamatsu R562 s/n SA4965	700	900					
7	1024(1)	Eather LBS M27610	105	1.9	11:00	none	1024		Hamamatsu R562 s/n SA4965	700	900					
8	1024(2)	Eather LBS M27610	105	1.9	11:56	none	1024		Hamamatsu R562 s/n SA4965	700	900					
7	1024(3)	Eather LBS M27610	105	1.9	12:41	none	1024		Hamamatsu R562 s/n SA4965	700	900					
8	1024(4)	Eather LBS M27610	105	1.9	13:51	none	1024		Hamamatsu R562 s/n SA4965	700	900					
Thu 15-Jan-98																
1	CRESTech	Eather LBS M27610	105.4	1.9			1	6.2 nm	Hamamatsu R562 s/n SA4965	501	1101					
2	CRESTech	Eather LBS M27610	105.4	1.9			1	3.1 nm	Hamamatsu R562 s/n SA4965	700	900					
3	CRESTech	Eather LBS M27610	105	1.9			all		Hamamatsu R562 s/n SA4965							
1999																
Mon 25-Jan-1999																
1	R1	SI29 Reference	100.91	5.079	10:12	full			Hamamatsu R562 s/n SA4965	380	900	3.9583	3.931	3.9347	-0.69%	-0.60%
2	A	Eather LBS M27610	105.33	1.9	10:44	mostly	1		Hamamatsu R562 s/n SA4965	380	900	0.46446	0.46803	0.46995	0.77%	1.18%
3	B	Eather LBS M27610	105.33	1.9	12:27	none	1		Hamamatsu R562 s/n SA4965	380	900	5.0517	5.0634	5.0667	0.23%	0.30%
4	C	Eather LBS M27610	105.33	1.9	14:17	none	1024		Hamamatsu R562 s/n SA4965	380	900	1.6146	1.6188	1.6225	0.26%	0.49%
5	D	Eather LBS M27610	105.33	1.9	15:43	none	128		Hamamatsu R562 s/n SA4965	380	900	0.57186	0.5721	0.57376	0.04%	0.33%
Mon 1-Feb-1999																
1	R2	SI26 Reference	101.04	5.069	14:55	full			Hamamatsu R562 s/n SA4965	600	900	5.7128	5.6841	5.7056	-0.50%	-0.13%
2	E	Eather LBS M27610	105.298	1.9	15:55	mostly	1024		Hamamatsu R562 s/n SA4965	600	900	0.0158	0.0158	0.0159	0.00%	0.63%
Fri 5-Feb-1999																
1	R3	SI26 Reference	101.04	5.069	11:31	full			Hamamatsu R562 s/n SA4965	600	900	6.4477	6.4172	6.4318	-0.47%	-0.25%
2	F	Eather LBS M27610	105.3	1.9	12:06	mostly	1		Hamamatsu R562 s/n SA4965	600	900	1.3528	1.3553	1.3595	0.18%	0.50%
3	G	Eather LBS M27610	105.3	1.9	14:06	none	1		Hamamatsu R562 s/n SA4965	600	900	1.7961	1.7973	1.8001	0.07%	0.22%
4	H	Eather LBS M27610	105.3	1.9	14:43	none	1024		Hamamatsu R562 s/n SA4965	600	900	0.56904	0.56921	0.57003	0.03%	0.17%
5	I	Eather LBS M27610	105.3	1.9	15:33	none	128		Hamamatsu R562 s/n SA4965	600	900	0.73362	0.73467	0.73595	0.14%	0.32%

Scan	Label	Lamp	V	A	Time	Shielding	Aperture	Bandwidth	Detector	Start	End	Reference Currents				
												Start	700	End	Increase from start	
Mon 8-Feb-1999																
1	R4	SI26 Reference	101.05	5.069	9:16	full			AAD cooled GaAs 0°C	600	900	2.6846	2.5767	2.457	-4.02%	-8.48%
2	J	Eather LBS M27610	105.3	1.9	9:35	mostly	1		AAD cooled GaAs 0°C	600	900	0.32361	0.33547	0.34728	3.66%	7.31%
3	K	Eather LBS M27610	105.3	1.9	10:25	none	1		AAD cooled GaAs 0°C	600	900	4.2492	4.2631	4.2792	0.33%	0.71%
4	L	Eather LBS M27610	105.3	1.9	10:57	none	1024		AAD cooled GaAs 0°C	600	900	1.3992	1.4043	1.4216	0.36%	1.60%
5	M	Eather LBS M27610	105.3	1.9	11:46	none	128		AAD cooled GaAs 0°C	600	900	0.23692	0.23881	0.24103	0.80%	1.73%
6	R5	SI29 Reference	100.925	5.0797	14:52	full			AAD cooled GaAs 0°C	600	900	2.0059	1.943	1.8595	-3.14%	-7.30%
7	N	Eather LBS M27610	105.3	1.9	15:15	mostly	1		AAD cooled GaAs 0°C	600	900	0.35143	0.35538	0.36252	1.12%	3.16%
8	O	Eather LBS M27610	105.3	1.9	16:31	none	1		AAD cooled GaAs 0°C	600	900	3.7282	3.7217	3.7311	-0.17%	0.08%
9	P	Eather LBS M27610	105.3	1.9	17:13	none	1024		AAD cooled GaAs 0°C	600	900	1.2276	1.2319	1.24	0.35%	1.01%
10	Q	Eather LBS M27610	105.3	1.9	18:19	none	128		AAD cooled GaAs 0°C	600	900	0.22051	0.22254	0.2255	0.92%	2.26%
Mon 05-Jul-99																
1	R1	Test Lamp	14.4745	4.999201	15:11	Full @ 56 cm			LAH1PF5 Silicon	700	900					
2	A	Test Lamp	14.4805	5	15:21	Full @ 56 cm			LAH1PF5 Silicon	700	900					
3	B	Test Lamp	14.4795	5.00005	15:40	Mostly @ 56 cm			LAH1PF5 Silicon	700	900					
4	C	Test Lamp	14.477	5.0001	16:09	None @ 56cm			LAH1PF5 Silicon	700	900					
5	D	Test Lamp	14.467	4.99995	16:38	None @ 33 cm			LAH1PF5 Silicon	700	900					
6	E	Test Lamp	14.477	5.0001	16:50	None @ 100 cm			LAH1PF5 Silicon	700	900					
7	F	Test Lamp	14.4755	5	17:24	Full @ 100 cm			LAH1PF5 Silicon	700	900					
2000																
Mon 13-Dec-99																
1	R1	SI29 Reference	101.022	5.079	8:42	mostly		1700um=5nm	Hamamatsu R562 s/n SA4965	700	900	4.1067	4.1134	4.1117	0.16%	0.12%
2	A	Eather LBS M27610	105.631	1.9	9:03	mostly	1	1700um=5nm	Hamamatsu R562 s/n SA4965	700	900	0.18606	0.18645	0.18799	0.21%	1.04%
3	B	Eather LBS M27610	105.33	1.9	9:38	mostly	1	1700um=5nm	Hamamatsu R562 s/n SA4965	700	900	0.18795	0.18808	0.18862	0.07%	0.36%
4	C	Eather LBS M27610	105.33	1.9	10:16	none	1	1700um=5nm	Hamamatsu R562 s/n SA4965	700	900	0.9753	0.97789	0.97787	0.27%	0.26%
5	R2	SI29 Reference	101.025	5.079	11:11	mostly		1700um=5nm	Hamamatsu R562 s/n SA4965	700	900	3.6233	3.6289	3.6297	0.15%	0.18%
6	R3	SI29 Reference	101.022	5.079	11:36	mostly		1700um=5nm	LAH1PF5 Silicon	700	900					
7	R4	SI29 Reference	101.0355	5.0796	11:52	mostly + filter		1700um=5nm	LAH1PF5 Silicon	700	900					
8	D	Eather LBS M27610	105.613	1.9	13:35	mostly + filter	1	1700um=5nm	LAH1PF5 Silicon	700	900	USELESS				
9	E	Eather LBS M27610	105.611	1.9	14:17	none + filter	1	1700um=5nm	LAH1PF5 Silicon	700	900	USELESS				
10	R5	SI29 Reference	101.029	5.079	15:08	mostly		1700um=5nm	LAH1PF5 Silicon	600	900					
11	F	Eather LBS M27610	105.582	1.9	15:30	none	1	1700um=5nm	LAH1PF5 Silicon	600	900					
12	G	Eather LBS M27610	105.61	1.9	16:18	none	1	1700um=5nm	LAH1PF5 Silicon	600	900					

Scan	Label	Lamp	V	A	Time	Shielding	Aperture	Bandwidth	Detector	Start	End	Reference Currents				
												Start	700	End	Increase from start	
13	H	Eather LBS M27610	105.609	1.9	17:02	none	1	1700um=5nm	LAH1PF5 Silicon	600	900					
14	R6	SI29 Reference	101.0295	5.079	17:56	mostly		1700um=5nm	LAH1PF5 Silicon	600	900					
15	R7	SI29 Reference	101.057	5.07537	18:08	none		1700um=5nm	LAH1PF5 Silicon	600	900					
Tue 14-Dec-99																
1	R8	U153 Reference				mostly		1700um=5nm	LAH1PF5 Silicon	600	900					
2	I	Eather LBS M27610				mostly	1	1700um=5nm	LAH1PF5 Silicon	600	900					
3	J	Eather LBS M27610				mostly	1	1700um=5nm	LAH1PF5 Silicon	600	900					
4	K	Eather LBS M27610				none	1	1700um=5nm	LAH1PF5 Silicon	600	900					
5	R9	U153 Reference				none		1700um=5nm	LAH1PF5 Silicon	600	900					
6	R10	U153 Reference				mostly		1700um=5nm	LAH1PF5 Silicon	600	900					
Wed 15-Dec-99																
1	G1	Eather LBS M27610	105	1.9	12:07	mostly	1	850um=2.5nm	Cooled GaAs -25.6°	600	900					
2	G2	Eather LBS M27610	105	1.9	12:35	mostly	1	850um=2.5nm	Cooled GaAs -26.5°	600	900					
3	G3	Eather LBS M27610	105	1.9	13:53	mostly	1	850um=2.5nm	Cooled GaAs -26.7°	600	900					
4	G4	Eather LBS M27610	105	1.9	15:11	mostly	1	850um=2.5nm	Cooled GaAs -26.7°	600	900					
5	R11	SI29 Reference at 10m	101	5.079	16:31	full+2x40% scrn		850um=2.5nm	Cooled GaAs -27.0°	600	900					
6	R12	SI29 Reference at 10m	101	5.079	17:10	full+2x40% scrn		850um=2.5nm	Cooled GaAs -26.6°	600	900					
7	R13	SI29 Reference at 10m	101	5.079	17:43	mostly		300um=15/17nm	Cooled GaAs -26.6°	600	900					
Thu 16-Dec-99																
1	R14	SI29 Reference at 10m	101	5.0796	10:34	mostly		300um=15/17nm	Cooled GaAs -27.2°	600	900					
2	G5	Eather LBS M27610	105	1.9	11:37	mostly	1024	850um=15/17nm	Cooled GaAs -27.3°	600	900					
3	G6	Eather LBS M27610	105	1.9	12:27	mostly	1	850um=15/17nm	Cooled GaAs -27.3°	600	900					
4	R15	U153 Reference	101.0645	5.090	14:40	mostly		1700um=5nm	Hamamatsu R562 s/n SA4965	600	900	9.71E-01	9.68E-01	9.70E-01	-0.25%	-0.04%
5	L	Eather LBS M27610	105.573	1.9	15:12	mostly	1	1700um=5nm	Hamamatsu R562 s/n SA4965	600	900	1.1981	1.1992	1.2022	0.09%	0.34%
6	M	Eather LBS M27610	105.616	1.9	15:56	mostly	1	1700um=5nm	Hamamatsu R562 s/n SA4965	600	900	1.2078	1.2074	1.178	-0.03%	-2.47%
7	N	Eather LBS M27610	105.614	1.9	16:43	none	1	1700um=5nm	Hamamatsu R562 s/n SA4965	600	900	5.7585	5.7654	5.7628	0.12%	0.07%
8	R16	U153 Reference	101.067	5.090	17:30	mostly + filter		1700um=5nm	Hamamatsu R562 s/n SA4965	600	900	9.46E-01	9.44E-01	9.46E-01	-0.24%	-0.04%
9	O	Eather LBS M27610	105.59	1.9	17:46	mostly + filter	1	1700um=5nm	Hamamatsu R562 s/n SA4965	600	900	1.1686	1.1669	1.1695	-0.15%	0.08%
10	P	Eather LBS M27610	105.619	1.9	18:30	mostly + filter	1	1700um=5nm	Hamamatsu R562 s/n SA4965	600	900	1.171	1.172	1.1727	0.09%	0.15%
11	Q	Eather LBS M27610	105.617	1.9	19:14	mostly + filter	1	1700um=5nm	Hamamatsu R562 s/n SA4965	600	900	1.1734	1.1726	1.1734	-0.07%	0.00%
12	R	Eather LBS M27610	105.617	1.9	19:59	none + filter	1	1700um=5nm	Hamamatsu R562 s/n SA4965	600	900	5.3863	5.3874	5.387	0.02%	0.01%

Table 3-7. A log of the annual calibrations of the Eather LBS. Series labels in column 2 are referred to in the text.

3.5.5.1.1. Relative Errors

Ignoring the error in the reference wavelength scaling, the relative error in $LBS_{meas}(\lambda)$ is taken as the square root of the sum-of-the-squares of the standard deviations in the measurement of the LBS and the dark current, reduced by the square root of the number of samples at each wavelength $N_{lbs}(\lambda)$

$$RE_{lbs\ meas}(\lambda) = \frac{\sqrt{\delta LBS_{meas}(\lambda)^2 + \delta D_{lbs}^2}}{LBS_{meas}(\lambda) - D_{lbs}} \cdot \frac{1}{\sqrt{N_{lbs}(\lambda)}} . \qquad \textit{Equation 3-15}$$

Similarly for the relative error in the measurement of the reference lamp $RE_{ref\ meas}(\lambda)$. An error in the determination of the reference source function is not specified by NML, but we can take the difference from a smooth polynomial fit as an estimate of $RE_{ref\ source}(\lambda)$. (In practice a 4th order polynomial fit to the source function is used instead of the source values themselves. The motivation for this is described later in section 3.5.5.9.)

Relative error in the intensity at any given wavelength is thus approximated by

$$RE_{lbs\ source}(\lambda) = \sqrt{RE_{lbs\ meas}(\lambda)^2 + RE_{ref\ meas}(\lambda)^2 + RE_{ref\ source}(\lambda)^2} \qquad \textit{Equation 3-16}$$

and applies to each individual calibration of the LBS source.

3.5.5.1.2. Repeatability Uncertainty

From the Jan-97 calibrations, we have opted to repeat the same measurement multiple times, so that an estimate of calibration repeatability can be made.

Each of the $LBS_{source}(\lambda)$ in a collection can be normalised to unity, at say the $P_1(3)$ wavelength, and averaged. The *repeatability uncertainty* is taken as the standard deviation of a set of normalised $LBS_{source}(\lambda)$ profiles for each wavelength (it has zero value at the normalisation wavelength). It thus refers to the uncertainty in the mean of a collection of calibrations determined in the same way. The mean annual source functions are determined in this way, and also groups of scans made for comparison to characterize various features of the measurement technique.

3.5.5.2. Inter Year Comparisons

During the course of annual NML calibrations appreciable inconsistencies in inter-year comparisons were revealed. Mean annual source functions are plotted in Figure 3-36, scaled to unity at the $P_1(3)$ wavelength. Errors plotted are the repeatability

uncertainty as described above. The trend from Dec-96 to Dec-98 decreased the slope across the OH(6-2) region in a reasonably consistent manner, which perhaps could be interpreted as an ageing effect of the bulb. However, this trend was not confirmed by measurements on the spectrometer at Davis, which were highly consistent over all years (see section 3.6).

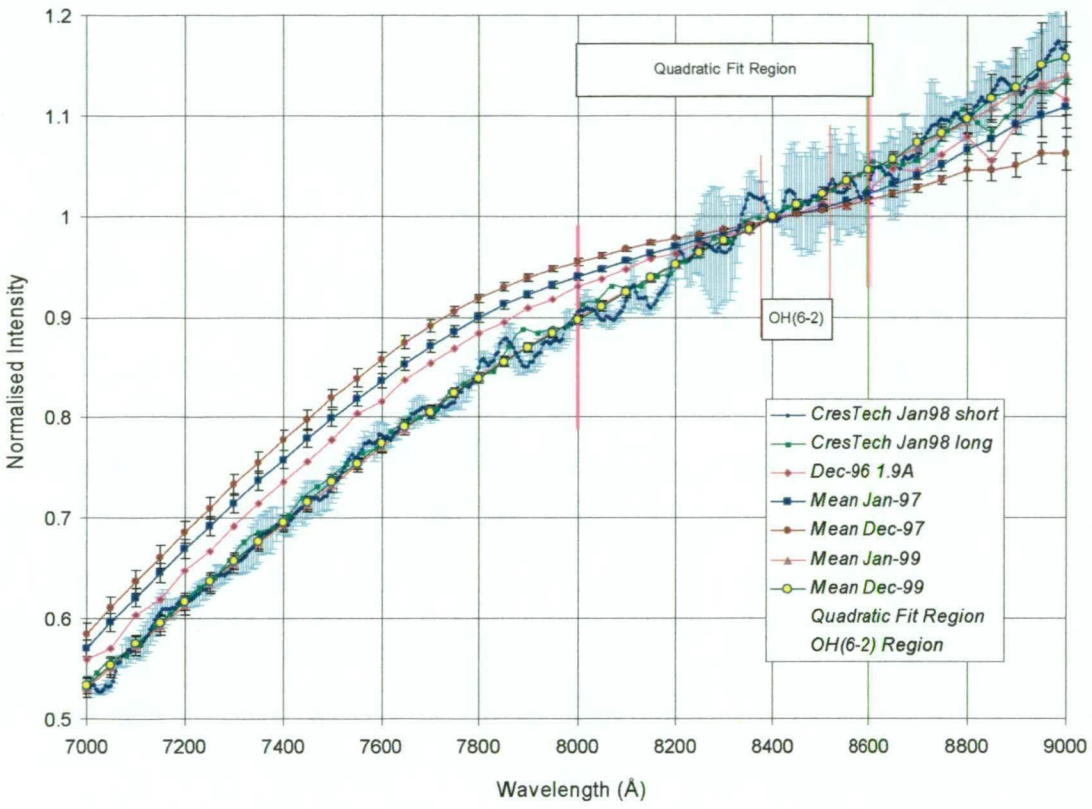

Figure 3-36. Mean annual Eather LBS source functions Dec-96 to Dec-99. Errors plotted on the NML measurements are repeatability uncertainties as described in the text. Measurement standard deviations are plotted for the CRESTech short-range curve, as only one scan was made in that configuration.

Following the Dec-97 calibrations the LBS was sent for cross-calibration at the Centre for Research in Earth and Space Technology (CRESTech) in Ontario, Canada with assistance from Prof. Bob Lowe at University of Western Ontario. Calibrations were made on an Aries FF250 spectrometer (f/4, 1200 lines/mm, 3.1 nm/mm reciprocal linear dispersion) with a silicon photodiode detector. The reference standard was a NIST traceable lamp (Epply type EN68) coupled with a Labsphere Spectralon panel (type LS 4085), viewed at 45°.

Two scans were made on the full aperture setting, one broad range from λ501 to λ1101 nm at 3 nm intervals with 6.2 nm spectral bandwidth and one short range λ700 to λ900 nm at 0.5 nm intervals with 3.1 nm bandwidth. The broadband radiances for

other LBS aperture settings were also measured to allow them to be scaled. Both calibrations are also plotted on Figure 3-36. Errors plotted on the short-range scan are standard deviations.

Although CRESTech results suffer poor signal to noise (due to short dwell time at each wavelength) both calibrations failed to match the Dec-97 NML result, and this was in retrospect, the first indication that something was wrong with the radiance calibrations at NML.

In the meantime, the LBS returned to Davis for the 1998 season and it was not until January 1999 that it was remeasured at NML. Surprisingly, the Jan-99 result reversed the 1996 to 1998 trend (the slope across OH(6-2) *increased*) and the calibration now matched the CRESTech result.

In terms of temperature analysis (chapter 4), the effect of the Jan-99 calibration was to *increase* the mean OH(6-2) temperatures derived by about 1.6 K, and in terms of the transition probability ratios (chapter 5), the most widely separated ratio $R_1(3)/P_1(5)$ *decreased* by 3.1%.

First suggestion of a systematic error in LBS measurement came from Errol Atkinson at NML. In 1998 he had considered that the blackout curtains enclosing the test lamp and spectrometer system at NML might not be 'black' in the infrared. He had installed a shield on the input to his spectrometer to stop the possibility of scattered light from the blackout curtains from entering the entrance slit directly.

Shielding consisted of a black box enclosing the entrance slit, reflecting mirror and diffusing screen. Two different apertures on the front of the box allowed only direct light from the reference source to illuminate the screen. A small aperture (referred to as FULL shielding) only allowed light to illuminate the centre of the diffusing screen, while a larger aperture (referred to as MOSTLY shielded) illuminated the whole diffusing screen. NO shielding referred to a configuration with the whole box removed.

All scans of the reference standard in Jan/Feb 1999 were done with full shielding in place while the LBS scans were made in the mostly shielded, or no shielding configuration, as the light level was reduced too much with full shielding.

By the time I had re-checked the Jan/Feb-99 calculations and unravelled what scan was done in what configuration the LBS was back down at Davis for another year. A definitive answer on the shielding effect could not be determined from scans we had and a consistent NML calibration over consecutive years was yet to be achieved.

The importance of resolving any error in the measuring technique called for a visit to NML when the LBS was returned from Davis in Dec 1999. In addition to standard calibration scans, several tests were conducted to identify and quantify effects of instrument configuration and measurement technique on the calibrations obtained. These are described here.

3.5.5.3. Reference Lamp Shielding

The primary task was to quantify the effect of shielding installed on the NML spectrometer during 1998. When the problem became apparent following the Jan-99 calibrations, Errol Atkinson at NML ran several test scans with a spare reference source to investigate scattering effects in Jul-99 (see listings in Table 3-7). Ratios of each test scan (A-F) to the fully shielded reference scan (R1) are plotted in Figure 3-37, normalised to λ840 nm.

The effect on ratios for unshielded scans C, D and E is obvious. Intensities towards the low wavelength end of the spectrum are substantially lower than for shielded scans (thus a LBS source function would appear to be *enhanced* at the low wavelength end when derived from an unshielded reference, which is consistent with the shape of the Dec-96, Jan-97 and Dec-97 results).

For scan D the test lamp was at a distance of 33 cm from the diffusing screen, C at 56 cm and E at 100 cm. Deviation from the reference scan increases in each case. This is an expected result as the further the distance, the greater the amount of scattering possible from the blackout curtains. Differences between Dec-96, Jan-97 and Dec-97 results is therefore easily explained by positioning of the reference source, although orientation of folds in the curtains would also presumably have some effect on scattering each year.

Series A, which was a repeat of the *fully shielded* reference scan, series B in the *mostly shielded* configuration and series F with *full shielding* at a greater distance all matched the fully shielded reference scan to less than 0.8% across the whole scan

range. It is therefore reasonable to assume that the 'mostly' shielded configuration eliminates scattering from the curtains just as efficiently as full shielding.

These results were confirmed in Dec-99 with unshielded/shielded ratios using the SI29 and U153 reference lamps (against which the Eather LBS is calibrated). Both are also plotted in Figure 3-37 and although they show a greater scattering effect, agree with the Jul-99 curve shapes.

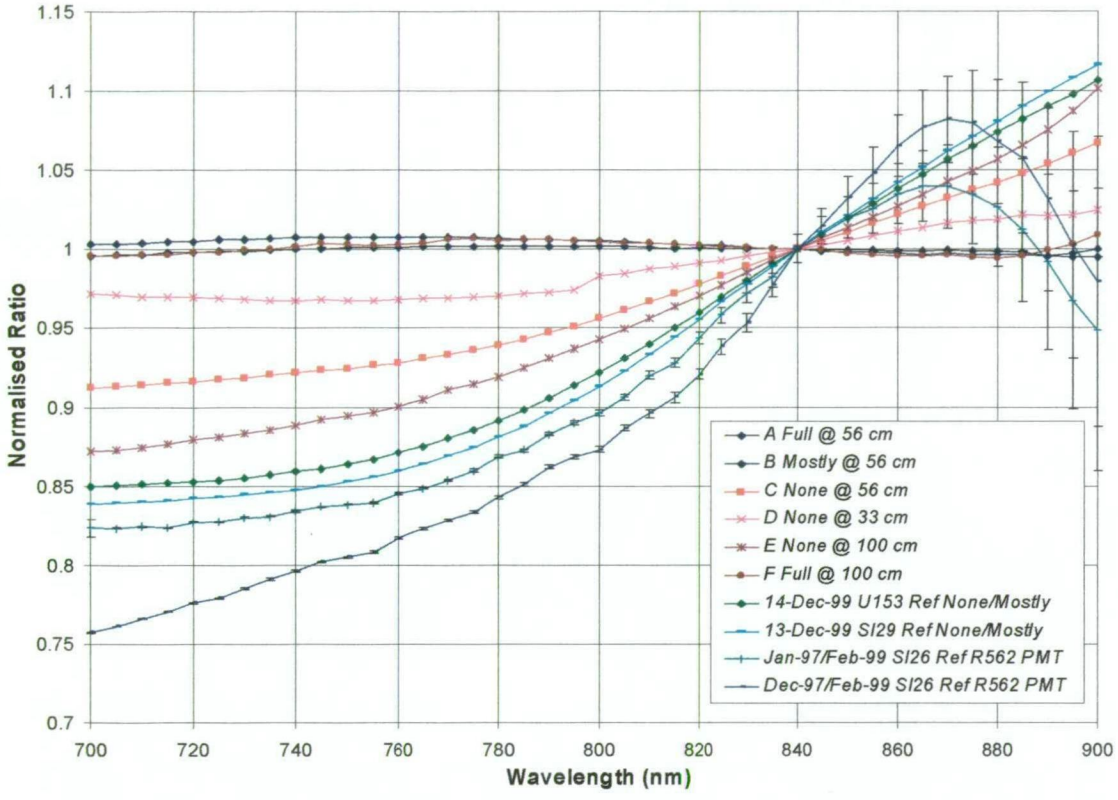

Figure 3-37. Ratios of Unshielded to Shielded Reference scans on the NML instrument

A silicon photodiode detector was used for all scans mentioned above. This is fine for the high intensity reference lamps but unsuitable for the Eather LBS calibrations as noise dominates the signal. A Hamamatsu R562 photomultiplier has much better signal-to-noise, at least below λ850 nm.

Due to the combination of different detectors and reference standards used over the years, only two sets of reference scans with the Hamamatsu R562 detector were available to assess shielding effect. Both sets used the SI26 reference lamp. Unshielded scans in Jan-97 (R1) and Dec-97 (R2) are compared with the fully shielded scan R3 in Feb-99. These ratios are plotted in Figure 3-37 together with their combined (square root of the sum-of-the-squared) relative errors.

Both show an even greater scattering effect but are consistent with previous results below about λ850 nm. Above λ850 nm the photomultiplier response falls off steeply and is responsible for the deviation from other curves.

Eather source functions derived from Jan-97 and Dec-97 unshielded references were used for initial temperature analysis of 1997 and 1998 data. Table 3-8 lists the error in OH(6-2) temperature for profiles at 150, 200 and 250K due to the scattering effect in Jan-97 and Dec-97 calibrations. Resulting temperature errors if the LBS source is assumed to be spectrally flat, and if no response correction is made (the instrument response is spectrally flat) are also listed for comparison.

150K	$P_1(2)/P_1(4)$	$P_1(4)/P_1(5)$	$P_1(2)/P_1(5)$	Mean
Jan-97	-0.7K	-0.5K	-0.6K	-0.6K
Dec-97	-0.9K	-0.7K	-0.8K	-0.8K
Spectrally flat source	-1.5K	-1.1K	-1.3K	-1.4K
No response correction	-4.0K	-4.4K	-4.2K	-4.1K
200K	$P_1(2)/P_1(4)$	$P_1(4)/P_1(5)$	$P_1(2)/P_1(5)$	Mean
Jan-97	-1.2K	-0.9K	-1.1K	-1.1K
Dec-97	-1.6K	-1.2K	-1.4K	-1.4K
Spectrally flat source	-2.6K	-2.0K	-2.4K	-2.4K
No response correction	-7.1K	-7.8K	-7.4K	-7.3K
250K	$P_1(2)/P_1(4)$	$P_1(4)/P_1(5)$	$P_1(2)/P_1(5)$	Mean
Jan-97	-1.9K	-1.4K	-1.7K	-1.7K
Dec-97	-2.5K	-1.9K	-2.2K	-2.3K
Spectrally flat source	-4.1K	-3.2K	-3.7K	-3.8K
No response correction	-10.9K	-12.1K	-11.4K	-11.3K

Table 3-8. Temperature errors for profiles at 150, 200 and 250K, resulting from the scattering effect in NML calibrations compared to 1999 measurements. Errors assuming a spectrally flat LBS and a spectrally flat instrument are also listed for comparison.

3.5.5.4. Eather LBS Shielding

The effect of shielding on Eather LBS measurements was also investigated. Radiant intensity of this source is ~1800 times less than the reference sources at λ700 nm. A mostly shielded configuration further reduces lamp intensity by a factor of ~5. Signal-to-noise level is so severely reduced that measurements with the silicon detector are not worthwhile and with the Hamamatsu R562 are difficult.

Ratios of averaged unshielded-to-shielded LBS source functions obtained in Jan-99 and Dec-99 are plotted in Figure 3-38. All measurements are derived from a shielded

reference and normalised to λ840 nm. Errors plotted are in-quadrature repeatability uncertainties. Scans with both GaAs and Hamamatsu R562 detectors were made in Jan-99 but the GaAs tube was insufficiently cooled to reduce dark current properly. The only comparative measurements in Dec-99 were made with the R562 detector.

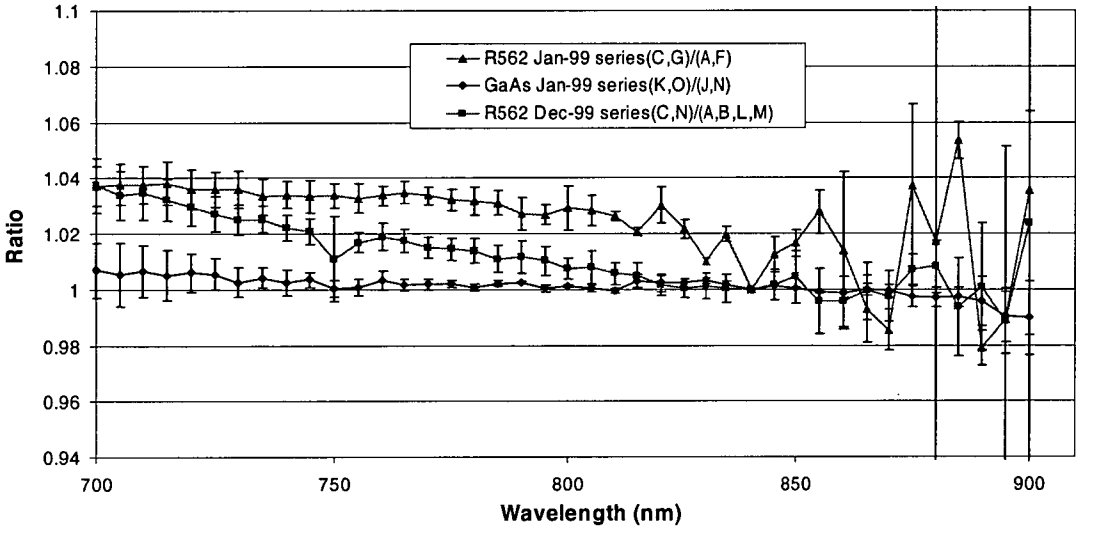

Figure 3-38. LBS source function ratios (unshielded over shielded) for Jan-99 and Dec-99, normalized to λ840nm. Series labels are listed in Table 3-7. Error bars are in-quadrature repeatability uncertainties.

Overall trend is an apparent intensity enhancement at lower wavelengths for unshielded scans, consistent with the effect of shielding on the reference source. The GaAs ratio shows least effect, probably due to the LBS being positioned close to the front diffusing screen for those scans, such that scattering is minimal. Over the small λ800-860 nm region of interest the LBS shielding effect is very small compared to the uncertainty and can be disregarded for these calibrations.

For future calibrations, a properly cooled GaAs photomultiplier operated in pulse counting mode should provide sufficient signal-to-noise so that the mostly shielded configuration can be employed for all reference and LBS calibration scans.

3.5.5.5. Aperture effect

A rotating switch is used to select an aperture size on the Eather LBS. The aperture disk has 11 settings, each of which approximately doubles the intensity. Calibrations on the instrument at Davis are normally done on the 128 or 1024 setting, which give approximately 6,400 or 65,000 counts per second at λ840 nm respectively.

Initial calibrations at NML in Dec-96 were done on the highest intensity setting (1024), but these results were marginal due to the lower sensitivity of the NML instrument. Prior to the Jan-97 calibrations, a larger hole was drilled in the aperture disk (in place of aperture setting 1) to provide greater intensity for NML. A 12 mm hole was intended, to match the size of the holes in the aperture disk housing, but when it came back from the workshop it had a 14 mm hole through it due to a drill bit mix-up! It was decided too difficult to put some of the hole back, so the new setting 1 became a 14 mm, fully open aperture for calibrations at NML.

Broadband intensity comparisons of the different aperture settings on the LBS have been made at each calibrating institution. These are listed in Table 3-9 scaled to the 1024 setting, but relative to 100% at the new Full aperture setting.

Aperture	KEO Dec-95	NML Dec-96	CRESTech Jan-98
Full			100.00%
1024	32.30%	32.30%	32.30%
512	10.53%	12.23%	11.10%
256	5.491%	6.570%	6.430%
128	2.674%	3.387%	3.270%
64	1.428%	1.754%	1.650%
32	0.1877%	0.2011%	0.2110%
16	0.1008%	0.0966%	0.1010%
8	0.0572%	0.0514%	0.0523%
4	0.0339%	0.0265%	0.0269%
2	0.0158%	0.0080%	0.0082%
1	0.0105%	0.0033%	

Table 3-9. Broadband intensity ratios of the Eather LBS aperture settings.

Somewhat later when the lamp was powered up it was noted that the geometry of the fully open aperture allowed some light to miss the target plate inside the second section of the LBS and directly irradiate the first diffusing screen. It was conceivable the spectral radiance of the output would change if the target plate had some spectrally reflective characteristic.

This effect was first tested in Jan-97 with 4 alternate scans on the full and 1024 aperture settings and the process was repeated in the Dec-98 calibrations. Tests in Jan-99 also include the 128 aperture settings and some measurements with the inadequately cooled GaAs photomultiplier, which were repeated in Dec-99 with the GaAs detector properly cooled.

All ratios are plotted in Figure 3-39 and yield a somewhat surprising but consistent result. The radiant intensity on the full aperture setting is *enhanced* at the blue end of the spectrum relative to both the 1024 and 128 settings. The magnitude is almost 4% at 700 nm compared to the normalisation wavelength at λ840 nm.

Given that the 1024 and 128 settings are the same implies the assumption of a spectral characteristic in the reflectivity of the target plate must be correct. The small component directly illuminating the first diffusing screen around the edges of the target plate modifies the spectral characteristic of the lamp in a significant way.

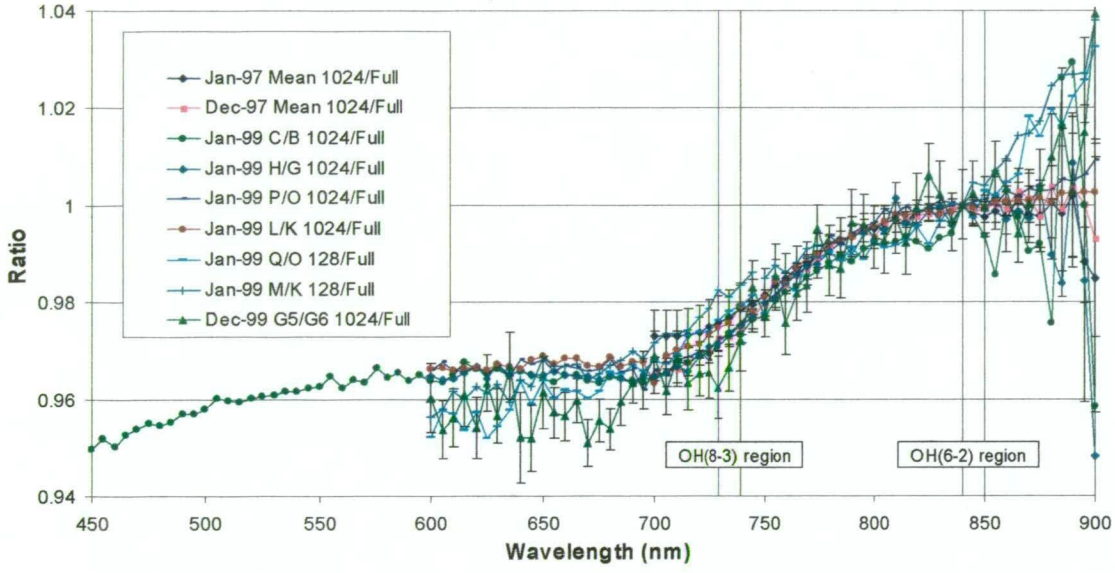

Figure 3-39. LBS Source function ratios of the 1024/Full and 128/Full apertures, normalized to λ840nm. Ratio labels refer to Table 3-7. Error bars plotted for the mean ratios are in-quadrature repeatability uncertainties and for the Dec-99 ratio only are combined relative errors.

Temperature errors associated with LBS calibration on the full aperture setting, compared to measurement on aperture setting 1024 are listed in Table 3-10 for the OH(6-2) band (using scans O(Full) and P(1024) from Jan-99 as a representative ratio). Temperatures are underestimated, but fortunately the error is small (in the most part negligible) as the ratio is reasonably flat across the OH(6-2) region.

OH(6-2) Temperature	$P_1(2)/P_1(4)$	$P_1(4)/P_1(5)$	$P_1(2)/P_1(5)$	Mean
150K	-0.037K	-0.027K	-0.033K	-0.034K
200K	-0.066K	-0.048K	-0.058K	-0.060K
250K	-0.103K	-0.075K	-0.091K	-0.094K

Table 3-10. Temperature errors for the OH(6-2) band resulting from calibration of the Eather LBS on the Full aperture setting, and measurement on the Davis instrument on the 1024 aperture setting, for profiles at 150, 200 and 250K.

Across the OH(8-3) region however, the slope is much more significant. If the curves are renormalised at the OH(8-3) $P_1(3)$ wavelength temperature errors associated with the full aperture effect on OH(8-3) analysis are listed in Table 3-11. These should be taken into account.

OH(8-3) Temperature	$P_1(2)/P_1(4)$	$P_1(4)/P_1(5)$	$P_1(2)/P_1(5)$	Mean
150K	-0.200K	-0.178K	-0.191K	-0.193K
200K	-0.355K	-0.317K	-0.339K	-0.342K
250K	-0.555K	-0.494K	-0.529K	-0.535K

Table 3-11. As for Table 3-10 but for the OH(8-3) band.

It is recommended that future calibrations be carried out on the 1024 aperture setting both at Davis and at NML.

3.5.5.6. Detector Comparison

Four different detectors have been used at NML to cross-reference the Eather LBS calibrations. These include a Hamamatsu R562 and LAH1 Silicon detector owned by NML, and two Hamamatsu R943-02 GaAs photomultipliers supplied by Australian Antarctic Division. Typical instrument response to the Eather LBS, normalised at λ700 nm, are plotted in Figure 3-40. The feature at λ640 nm is a Woods anomaly. (see section 3.3.5).

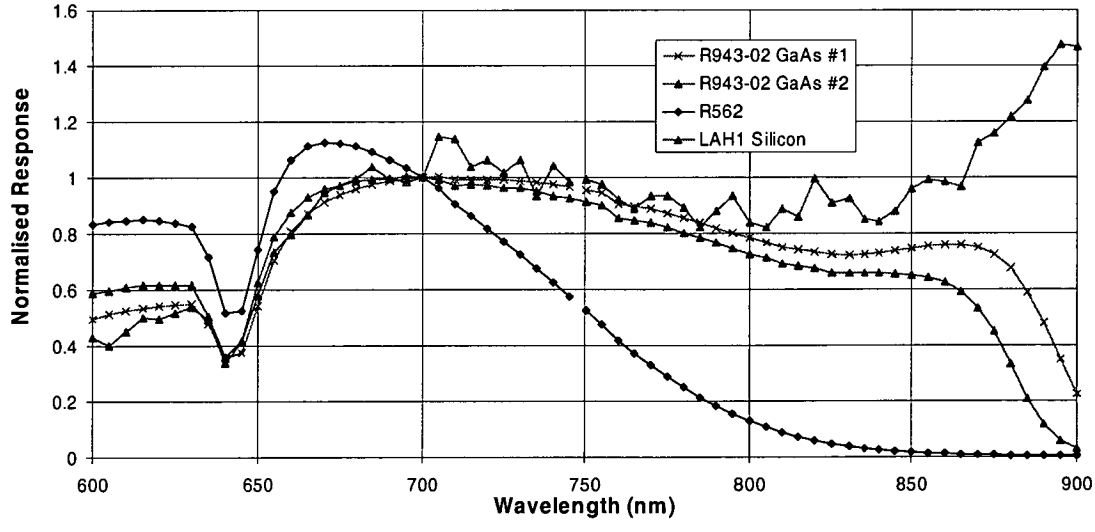

Figure 3-40. Typical instrument response to the Eather LBS on the NML system normalized to 700 nm. The feature at 640 nm is a Woods anomaly.

Due to different lamp positions, slit widths, offset and amplification electronics used in each case a proper detector efficiency comparison has not been determined. However, a comparison of signal-to-noise at the normalisation wavelength (λ700

nm) for series G2 (GaAs), L (R562) and J (Silicon) in Dec-99 yields ~2800 for the GaAs detector system, ~30 for the R562 detector and ~4 for the Silicon detector (each scaled to a 5 nm bandwidth).

Initial measurements with the GaAs detector in Jan-99 (operated by NML in current mode and with inadequate cooling) suffered low signal-to-noise and substantial drift in reference wavelength (up to 8%) during the course of the scan. In Dec-99 I visited NML to investigate the scattering problem, set-up the photomultiplier in pulse counting mode and ensure it was properly cooled (about -26°C was maintained). Vastly improved signal-to-noise and reference wavelength drift rates of less than 1% were achieved.

Comparison of LBS source functions derived from the different detectors is made from the average of five GaAs scans (Dec-99 series G1-G4,G6), four R562 scans (Dec-99 series A,B,L,M) and four Silicon detector scans (Dec-99 series F,G,H,K). Shielding was used for all scans except for the LBS with the Silicon detector. Ratios of the averaged source functions are plotted in Figure 3-41, normalized to λ840 nm. Errors plotted are the combined repeatability uncertainties.

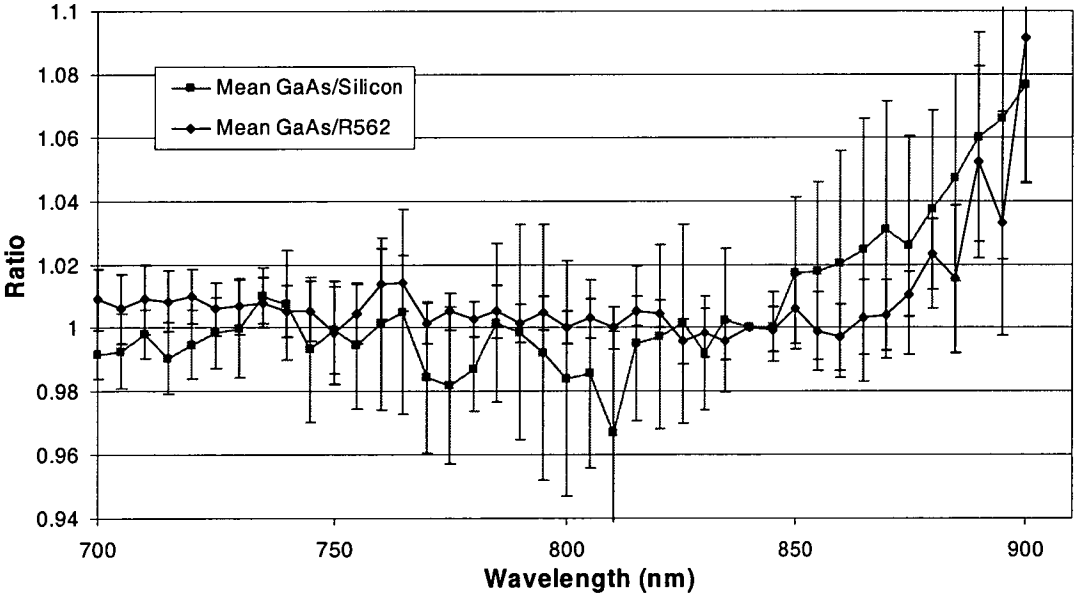

Figure 3-41. Detector Comparison - ratios of mean Eather source functions derived using GaAs, R562 and Silicon detectors. Errors plotted are combined repeatability uncertainties.

As one would expect, determination of the LBS source function is *not* dependent on choice of detector to within the repeatability uncertainty. Departure from unity above λ860 nm is due to the rapid response fall-off of the GaAs detector at this point.

3.5.5.7. Instrument Bandwidth

Bandwidth of the NML instrument is 5 nm with the slits set at 1700 μm for normal calibrations. In comparison, the Davis instrument has a 0.16 nm bandwidth with slits at 250μm. Dec-99 calibrations at NML also attempted to determine if instrument bandwidth has any consequence on measured spectral response.

Measured response is a convolution of the source and instrument functions, where the instrument function is a collective convolution of the front diffusing screen transmission, mirror reflectivity, slit function, grating efficiency, second order blocking filter transmission and detector efficiency. A difference in measured response with bandwidth may result, if any component contains rapid variations with wavelength.

Consecutive scans were made of the reference source with slit widths at 850μm and at 300μm, corresponding to bandwidths of 2.5 and 0.88 nm respectively (Dec-99 series R11-R14). The reference source was shielded and positioned 10 metres from the front diffusing screen in each case. With slits at 850 μm, two 40% transmission wire screens further reduced intensity to a suitable level. Ratios are plotted in Figure 3-42. Error bars are the combined relative errors. An inverse ratio for Eather source functions derived as the mean of G3, G4 and G5 (at 2.5 nm bandwidth) over G6 (at 0.88 nm bandwidth) is also plotted.

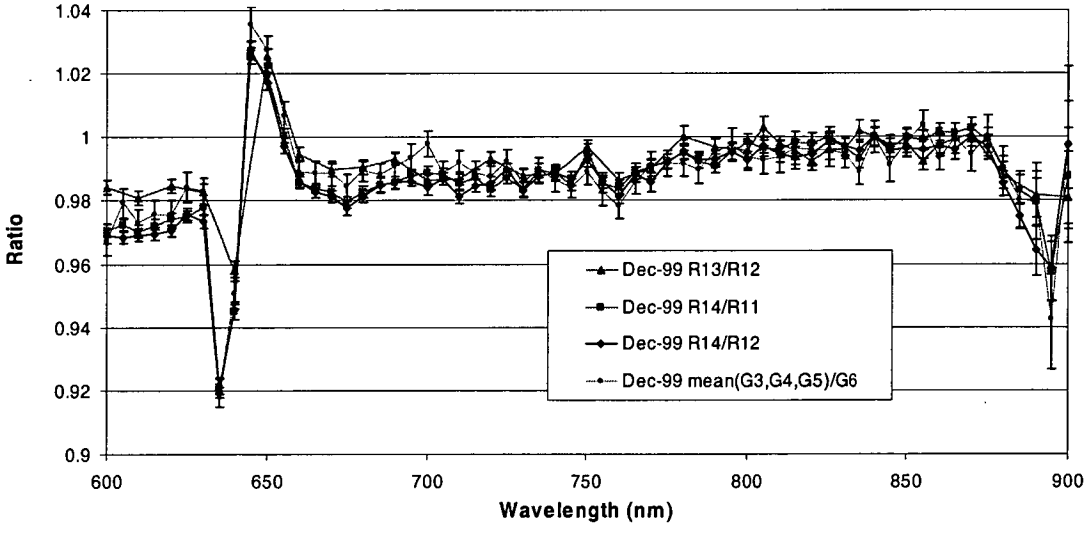

Figure 3-42. Ratios of the measured reference response at bandwidth 0.88 nm to bandwidth 2.5 nm, and the inverse ratio for the Eather source function derived. The effect of the Woods anomaly in the grating and the detector response fall-off about λ870 nm are apparent. Error-bars shown are combined relative errors.

An effect of the Woods anomaly is obvious at around λ640 nm, as is the effect of the rapid fall-off in detector response above λ870 nm. Over the λ780-870 nm interval however, ratios are constant (to within measurement error) so we can be confident that differences in instrument bandwidth have no effect over the λ800-860 nm fit region for OH(6-2) analysis. Ratios are also reasonably constant over the λ670-760 nm interval which covers the OH(8-3) region. Between these two intervals (~λ770 nm) a step of ~1.5% is coincident with a small anomaly in the instrument response function at that point (see GaAs curves in Figure 3-40). It is suspected this is a result of switching second order blocking filters at that point. This is examined next.

Even though a reasonably comfortable wavelength interval around both OH(6-2) and OH(8-3) regions are not affected by bandwidth selection, a general recommendation for future LBS calibrations would be to set bandwidth on the NML instrument as close as practicable to the 0.16 nm used for measurements on the Davis instrument.

3.5.5.8. Blocking Filters

Multiple blocking filters for rejection of higher order diffraction are contained in the NML instrument and are automatically switched depending on the wavelength selected. Wary of the importance of blocking filters on the Davis instrument, a check was made on the rejection efficiency of NML filters by adding a blocking filter of same the type used at Davis for comparison.

Ratios of averaged Eather source functions determined with and without the additional blocking filter (Dec-99 shielded scans O+P+Q over L+M and unshielded scans R over N) showed no consistent trend, or stepping between filter changes over the λ600-900 nm interval and confirm that the NML filters are sufficient to remove higher-order diffraction.

3.5.5.9. NML Reference Lamps

A final comparison is made to assess the consistency of Eather LBS calibrations between the three different NML reference lamps used thus far. All reference lamps are the same type of 500W quartz halogen lamps (filament type CC-8, envelope T4, distribution temperature 3100 to 3150K) operated with DC current.

Each reference lamp is traceable to the Australian primary legal spectral irradiance standard, derived using a high temperature Planckian source. They have also undergone comparison with the units maintained at all other major international laboratories responsible for maintaining spectral irradiance standards for their own countries, including NIST (USA), PTB (Germany), NPL (Britain) and NRC (Canada). The actual spectral irradiance values placed on the reference lamps for these calibrations were based on the international mean values of an inter-comparison that took place in August 1989. A report on the last inter-comparison in 1998 has yet to be released.

All LBS calibrations prior to Jan-99 were referenced to the NML SI26 lamp, which apparently became 'unstable' during 1999. Fortunately, the SI29 reference was introduced in Jan-99 so a comparison could be made. In order that a future reference source comparison could be maintained, U153 was also introduced in Dec-99.

Derived values for the SI26 source function contained a curious structure in the form of alternate 'notching' up to about 2% in magnitude every 50 nm. In Figure 3-43, a 4^{th} order polynomial it fitted to the SI26 source function. Residuals are plotted below to emphasize the notching. Although it was brought to the attention of NML the characteristic was not explained. I suspect it is a systematic measurement error although neither SI29 nor U153 lamps exhibit the same structure.

If the derived SI26 source values are used the Eather source function determined contains inverse notching. Therefore all calibrations were re-worked to reference a smooth polynomial fit to the reference source functions, instead of the raw source values.

Results of the reference source comparison are plotted in Figure 3-44. For the SI26/SI29 comparison, Eather source functions are taken from the Jan-99 calibration set and the ratio is the mean of series G, J and K for SI26 and series B, N and O for SI29. For the SI29/U153 comparison source functions are taken from the Dec-99 set and is the ratio of the mean of series A and B for SI29 to the mean of L and M for U153. Errors plotted for both ratios are repeatability uncertainties. Both ratios are consistent to within measurement uncertainty and it is concluded that each of the currently used reference sources yields consistent Eather LBS calibrations.

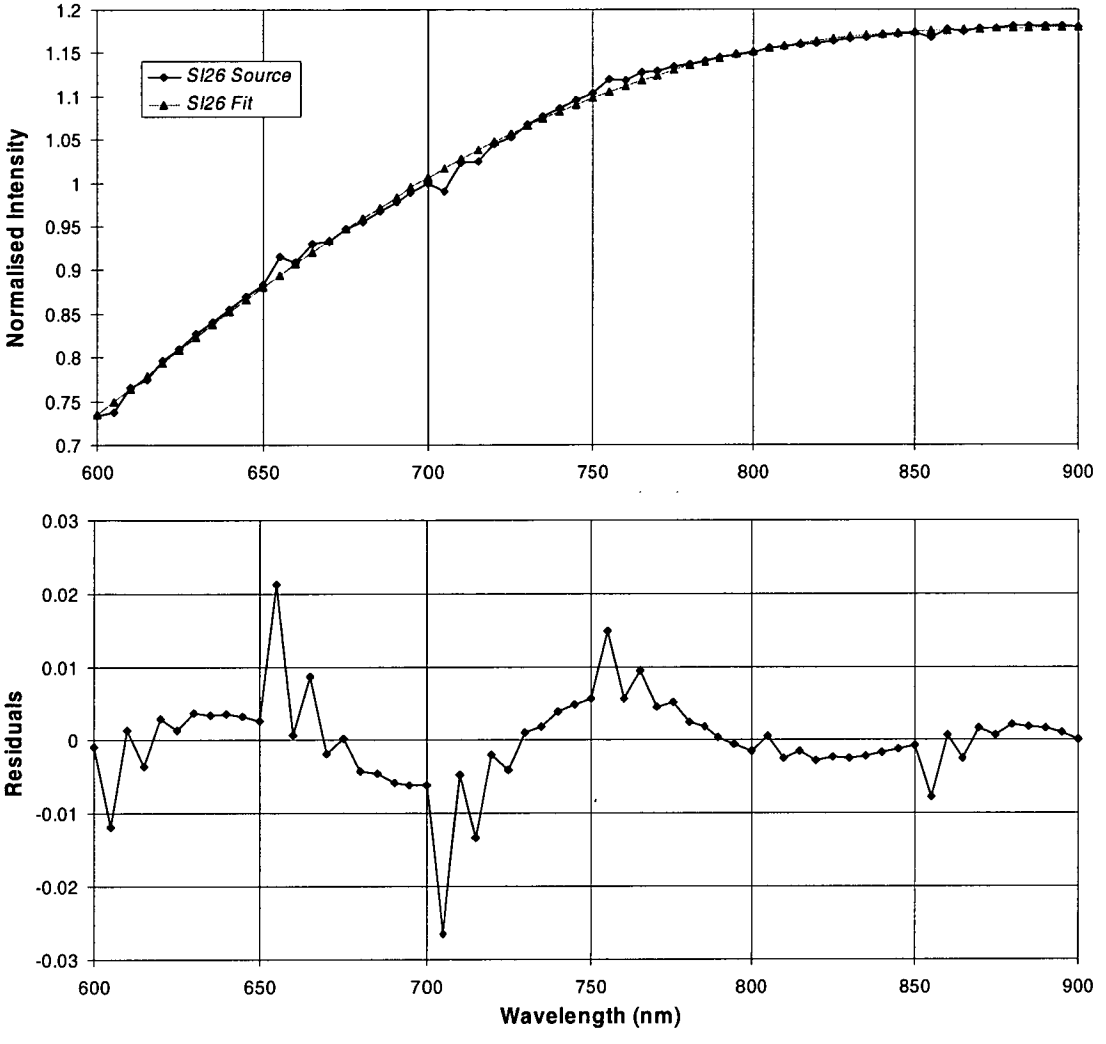

Figure 3-43. Top panel is the SI26 reference source function fitted with a 4th order polynomial. In the bottom panel the fit residuals emphasize the 50 nm alternate 'notching', believed to be a systematic measurement error.

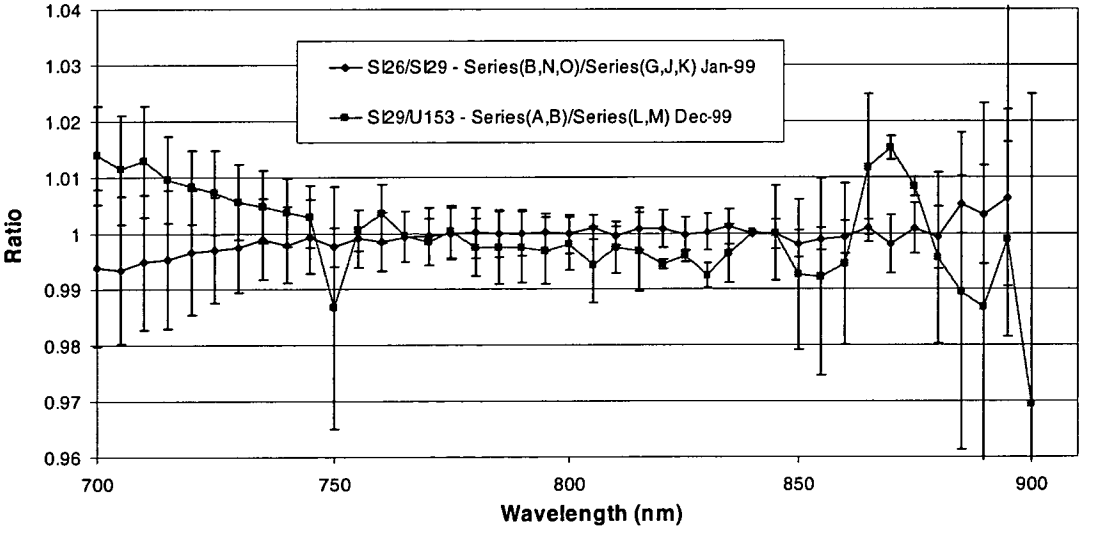

Figure 3-44. Ratios of the Eather source functions determined using the SI26 to SI29 reference sources and the SI29 to U153 reference sources.

3.5.5.10. Recommendations for future calibrations.

In summary the following recommendations are made for future LBS calibrations at NML.

- A cooled GaAs detector, operating in pulse counting mode should be used. Superior signal-to-noise will allow for implementation of other recommendations which all reduce signal level. Adequate time (~1 day) for the detector to cool and stabilize must be allowed to minimise reference wavelength drift.
- Some scans using the Hamamatsu R562 detector should be continued for comparison. There is no value in using the silicon detector.
- Shielding of scattering from the blackout curtains should be used for all scans of the reference and LBS sources. This reduced the intensity by a factor of about 5.
- Aperture setting 1024 on the Eather LBS should be used at both NML and Davis. Lamp intensity is reduced by a factor of 3 but spectral modification due to light directly irradiating the first diffusing screen on the 'full' setting is eliminated.
- Reduce bandwidth on the NML instrument to something more comparable to the Davis instrument. A 1 nm bandwidth is suggested, which will further reduce the intensity by a factor of 5.
- Maintain calibrations against two reference lamps for comparison.
- Construct and calibrate two more LBS units of the same design. The Eather LBS is currently the *only* source used for relative intensity calibration and is transported annually between Davis and NML as the shipping season permits. Several units would provide insurance against loss or damage of the existing unit and allow for inter-comparisons.

Total intensity reduction by implementation of the above recommendations is a factor of ~75, however gain in signal-to-noise provided by using a GaAs tube over the Hamamatsu R562 is a factor of ~95 which will adequately compensate.

3.5.5.11. Selection of calibrations for the annual mean

Having identified which elements of the measurement procedure affect LBS calibrations an appropriate selection of scans can be made to derive annual mean source functions.

Of the Dec-99 series only one measurement satisfied the recommendations entirely, and that was G5. G1-G4 and G6 were all done on the full aperture setting but may be

included if the calibration is applied only to OH(6-2) analysis. Of the Hamamatsu R562 series all were made with wider bandwidth and on the full aperture setting. Series C, N and R had no LBS shielding and O to R included the second blocking filter. Strictly, all of these can be included as bandwidth, aperture, LBS shielding and blocking filter made no difference within the repeatability uncertainty across the OH(6-2) region. All measurements made with the silicon detector (D to K) are rejected on signal-to noise grounds. A weighted mean for Dec-99, derived from scans (G5 + mean(G1-G4,G6) + mean(A,B,C,L,M,N,O,P,Q,R))/3 is plotted in Figure 3-45 with a quadratic fit across the λ800-860 nm and repeatability uncertainties.

For Jan-99 series A, D, E, F and I, using the Hamamatsu R562 detector, were rejected on signal-to-noise grounds. These scans were made with either the LBS shielded or on aperture setting 128. All others are included with equal weight, (there was no preference for weighting GaAs scans as they were made with inadequate cooling and suffered considerable drift). The mean, quadratic fit and repeatability uncertainties for Jan-99 are also plotted in Figure 3-45.

Both annual means agree extremely well, certainly within repeatability uncertainty and they represent the first consistent set of Eather LBS source calibrations in four years. Response calibrations on the Davis spectrometer can now be assess with good confidence that the Eather LBS had not changed significantly in spectral character since it was introduced in 1996. These are discussed next.

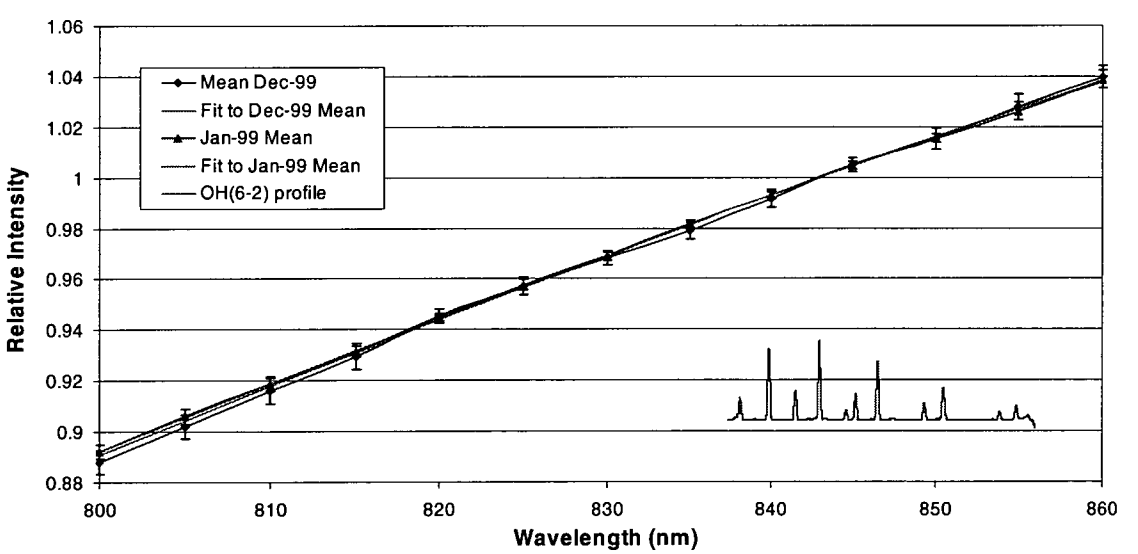

Figure 3-45. Mean annual source functions for the Eather LBS, normalised at λ840 nm with quadratic fits used in the OH(6-2) analysis. Errors plotted are repeatability uncertainties.

3.6. Instrument Response Calibrations at Davis

With a consistent and repeatable calibration of the Eather reference source finally established at NML, the lamp can now be employed to measure response characteristics of the Davis spectrometer. This section deals with source measurement, error assessment and inter-year comparison of the instrument response corrections. Figure 3-46 shows the Eather LBS mounted above the spectrometer entrance box for calibration. The lamp is powered by a precision DC supply at 1.900A/105V, the instrument is otherwise configured the same as for routine observations. No spectral response sensitivity to LBS orientation (diffusivity), off axis tilt (multiple reflections) or view area of the front diffusing screen (uniformity) was observed for these calibrations.

Figure 3-46. The Eather LBS mounted above the mirror box for calibration.

3.6.1. Retrospective Calibrations

On first inspection of an averaged OH(6-2) spectra the background over the small 15-20 nm scan range appears flat, suggesting that a variation in instrument response is not significant. As a consequence, initial analysis work made no allowance for it and previous results from this instrument published by Williams (1996) and Hobbs *et al.* (1996) do not include an instrument response correction.

Dark-sky background (without twilight or moon contamination) is however mostly due to dark counts, which do not have a spectral dependence. To a certain extent also, the fall off in detector response with wavelength was compensated by the increase in N_2 1PG band emissions (and 2nd order N_2^+ 1NG bands in 1990).

With the acquisition of the Eather LBS in early 1996 a calibration program was undertaken to retrospectively determine instrument response corrections for all previous years of operation. This was possible by referencing the Eather LBS instrument response calibration in 1996 to quartz halogen secondary calibration lamp responses measured each year, i.e. the secondary calibration lamp *source* profile was determined in 1996 and compared to measured response profiles for other years.

Thus, if $E(\lambda)$ denotes the Eather source function determined at NML (the first source derived without scattering in Jan-99 is used) and $R_{E96}(\lambda)$ the response to the Eather source (both in counts/sec) then the instrument response function in 1996, $I_{96}(\lambda)$ [a dimensionless quantity] is given by

$$I_{96}(\lambda) = \frac{R_{E96}(\lambda)}{E(\lambda)} \quad . \qquad \textit{Equation 3-17}$$

Then, if $R_{Q96}(\lambda)$ denotes the response to the quartz-halogen secondary calibration lamp in 1996 then the quartz-halogen source function $Q(\lambda)$ is determined by

$$Q(\lambda) = \frac{R_{Q96}(\lambda)}{I_{96}(\lambda)} = \frac{R_{Q96}(\lambda).E(\lambda)}{R_{E96}(\lambda)} \quad \text{[counts/sec]}. \qquad \textit{Equation 3-18}$$

Given that we have measured $R_Q(\lambda)$ for each observing year with the same lamp, we can then use $Q(\lambda)$ to determine the instrument response for any year $I_{YR}(\lambda)$ via

$$I_{YR}(\lambda) = \frac{R_{QYR}(\lambda)}{Q(\lambda)} = \frac{R_{QYR}(\lambda).R_{E96}(\lambda)}{R_{Q96}(\lambda).E(\lambda)} \quad . \qquad \textit{Equation 3-19}$$

It is assumed in this procedure is that the relative spectral intensity of the secondary calibration lamp $Q(\lambda)$ remained unchanged.

For the 1990 to 1995 data sets, an instrument response *correction* (reciprocal of $I_{YR}(\lambda)$) is applied to each profile after subtraction of dark counts, by means of four best fit quadratic equations for $R_{Q\,YR}(\lambda)$, $R_{E\,96}(\lambda)$, $R_{Q\,96}(\lambda)$ and $E(\lambda)$. Of course, for 1996 and subsequent years, $I_{YR}(\lambda)$ is determined directly from the Eather source and measured response functions. An error associated with each component is determined from the standard deviation of quadratic fits to each scan.

3.6.2. Response to the Eather Source - $R_{E96}(\lambda)$

An added complexity for the retrospective determinations of $I_{YR}(\lambda)$ (for years prior to 1996) was that both the diffraction grating and pre-filters were replaced for observations in 1996. Therefore LBS calibrations had to be performed with both old and new system components in 1996. Figure 3-47 plots the broad range response to the Eather LBS determined with the old grating and with and without the old pre-filter and Perspex viewing window in place.

$R_{E96}(\lambda)$ for the old system was determined from a set of 426 scans across the interval λ837.5-855.5 nm recorded over a 4 day period in 1996 (days 187 -190). 116 scans were also made without the blocking filter to derive the filter and Perspex transmission profiles shown in section 3.2.2.2.

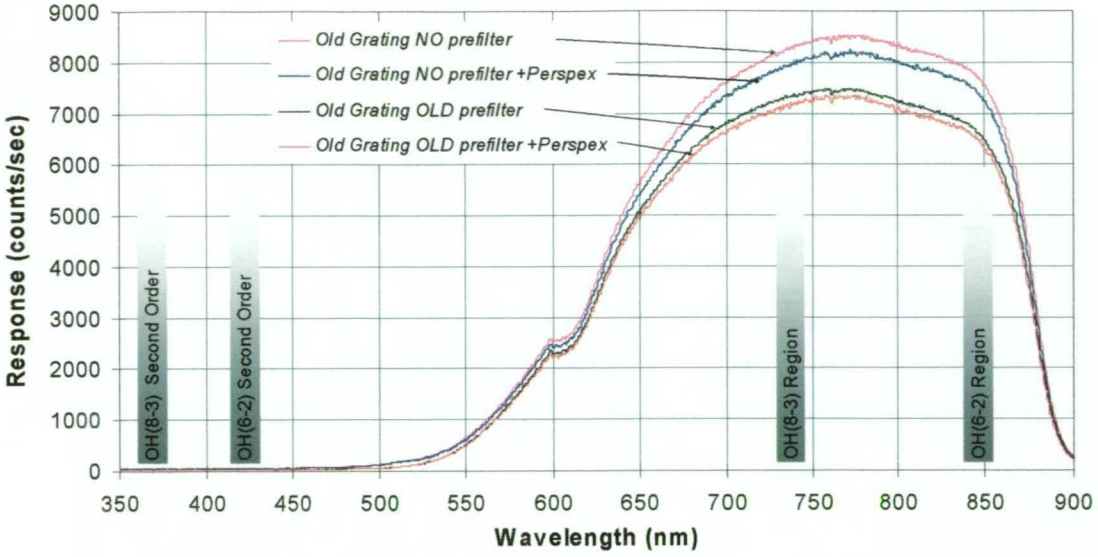

Figure 3-47. Broad range spectrometer response to the Eather LBS, with and without the blocking filter and perspex window. Collected on days 190-193, 1996 with LBS aperture 128.

Figure 3-48 plots the function $R_{E96}(\lambda)$ over the OH(6-2) scan region for the old system. It is determined as follows. A quadratic fit is made to each of the 426 scans. Each fit is normalised to unity at the $P_1(3)$ peak wavelength. Mean and standard deviation is then calculated across the wavelength interval. Error bars plotted are one standard deviation in the range of fits. $R_{E96}(\lambda)$ in the analysis is represented as a single quadratic fit to this mean profile. This function is used only for the retrospective instrument function [$I_{YR}(\lambda)$] determinations for years prior to 1996 via equation 3-19.

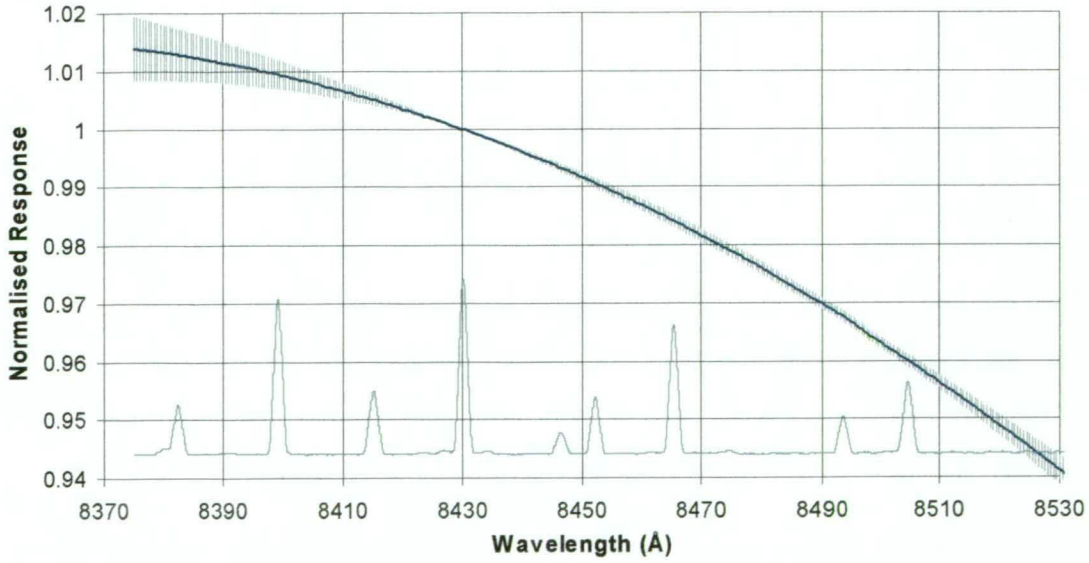

Figure 3-48. Mean response to the Eather LBS [$R_{E96}(\lambda)$], *normalised at the* $P_1(3)$ *wavelength and* 1σ *errors for the old system. A total of 426 scans collected on days 187-190 1996 with aperture 128. An OH(6-2) profile is also plotted for reference.*

3.6.3. Response to the Secondary Calibration Lamp - $R_{Q\,YR}(\lambda)$

Normalised means of the response to the secondary calibration lamp made each year [$R_{QYR}(\lambda)$] are plotted in Figure 3-49 and summarised in Table 3-12.

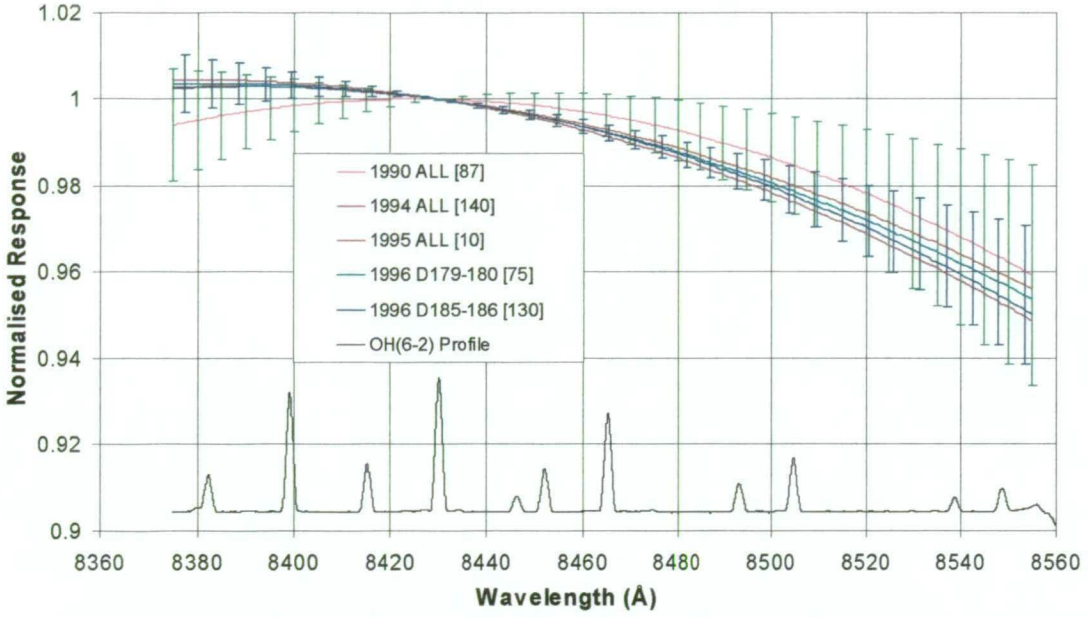

Figure 3-49. Comparison of $R_Q(\lambda)$ for the old system configuration 1990 to 1996. Errors plotted are one standard deviation for 1990 and 1996 profiles only, 1994 and 1995 are within these limits.

				Evaluation of $R_{QYR}(\lambda)$			Relative Errors		
Year DAY	Scans	Prefilter	Step Å	$P_1(2)$	$P_1(4)$	$P_1(5)$	$P_1(2)$%	$P_1(4)$%	$P_1(5)$%
1990 225-288	45	None	0.5	0.9980	0.9961	0.9841	0.491%	0.345%	0.757%
1990 85-212	42	None	0.05	0.9985	0.9961	0.9848	0.671%	0.548%	1.249%
1990 ALL	87	None	Both	0.9984	0.9961	0.9846	0.627%	0.503%	1.143%
1994 ALL	140	Old	0.5	1.0038	0.9913	0.9759	0.234%	0.111%	0.512%
1995 ALL	20	Old	0.5	1.0028	0.9929	0.9798	0.633%	0.559%	0.981%
1996 179-180	75	Old	0.05	1.0033	0.9923	0.9784	0.310%	0.185%	0.586%
1996 185-186	130	None	0.05	1.0028	0.9921	0.9773	0.276%	0.177%	0.597%

Table 3-12. Summary of $R_Q(\lambda)$ for each year. Evaluations are normalised to unity at $P_1(3)$.

$R_{Q\,96}(\lambda)$ was characterised by a set of 75 profiles obtained with the blocking filter in place on days 179-180, and 130 profiles without it on days 185-186. Those with the blocking filter are applicable to 1994 and 1995 data sets, and without it to 1990. Differences between 1990 curve and 1996 no-blocking-filter curves are most likely attributable to the change in photomultiplier tube at the beginning of 1994.

Uncertainties are clearly much larger than for the Eather source (compare Figure 3-48), due mainly to the difference in lamp intensities. Typical count rates for the secondary calibration lamp are 700-800 counts/sec, compared with 6,400 counts/sec for the Eather lamp on aperture 128 or 65,000 counts/sec on 1024.

3.6.4. *Inter-year Comparisons of $R_E(\lambda)$*

As we do not have a long-term record of the $E(\lambda)$ source function variation, we can only compare the inter-year $R_E(\lambda)$ response functions with the assumption that $E(\lambda)$ has not changed. Significant long term change in $R_E(\lambda)$ would imply an indistinguishable change in either the spectrometer or the Eather LBS, but no change would imply that both were stable (it is unlikely that they would have changed an equal amount in opposite directions).

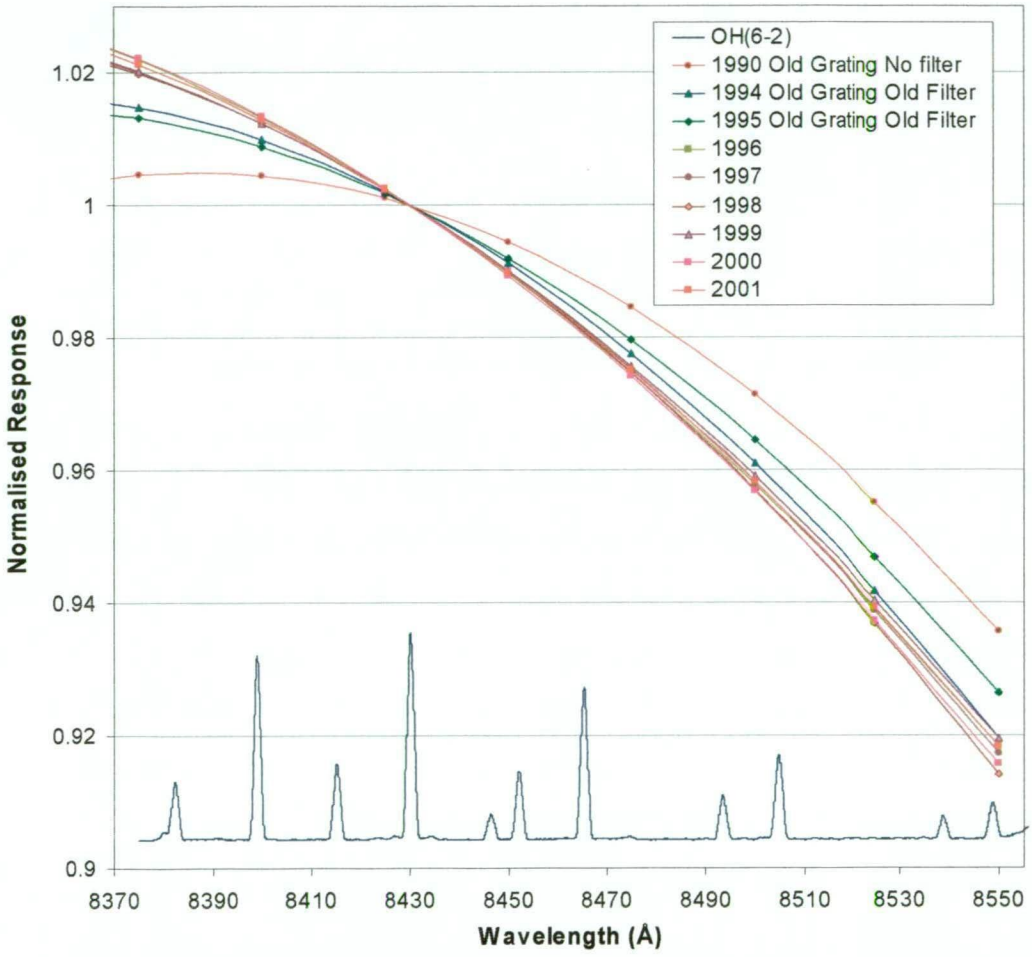

Figure 3-50. Quadratic fits to the Eather LBS mean annual response functions from 1990-2000 across the OH(6-2) band.

Figure 3-50 plots the quadratic fits to measured annual mean $R_E(\lambda)$ from 1996 to 2000 together with calculated (from $R_{QYR}(\lambda)/R_{Q96}(\lambda)$ ratios via equation 3-19) response curves for 1990, 1994 and 1995, all normalised to unity at $P_1(3)$. Table 3-13 summarises the evaluation of $R_E(\lambda)$ at P-branch lines and their relative errors, quadratic fit coefficients and resultant temperature corrections at 200K for each year. Full instrument response corrections include an additional 2.4 K due to the increase in $E(\lambda)$ across the region (Jan-99 NML calibration, see Table 3-8).

Year	Instrument Set			Evaluation of $R_{EYR}(\lambda)$			Quadratic Fit Coefficients			Resultant Temp. Correction
	Scans	Grating	Prefilter	$P_1(2)$ Error	$P_1(4)$ Error	$P_1(5)$ Error	λ^2	λ	c	
1990	87	Old	None	1.0045 0.722%	0.9887 0.543%	0.9686 1.296%	-2.5855E-06	0.04336	-180.825	+3.51K
1994	140	Old	Old	1.0100 0.464%	0.9832 0.245%	0.9576 0.786%	-2.2992E-06	0.03837	-159.067	+5.32K
1995	20	Old	Old	1.0090 0.749%	0.9847 0.600%	0.9613 1.148%	-2.1471E-06	0.03584	-148.579	+4.82K
1996	113	New	New	1.0135 0.184%	0.9807 0.115%	0.9540 0.288%	-1.6253E-06	0.02692	-110.398	+6.16K
1997	121	New	New	1.0127 0.106%	0.9811 0.067%	0.9541 0.162%	-1.8681E-06	0.03103	-127.820	+6.04K
1998	24	New	New	1.0127 0.040%	0.9807 0.045%	0.9528 0.132%	-2.0376E-06	0.03388	-139.826	+6.17K
1999	43	New	New	1.0127 0.027%	0.9814 0.023%	0.9551 0.047%	-1.7315E-06	0.02873	-118.142	+5.94K
2000	65	New	New	1.0137 0.0440%	0.9802 0.0493%	0.9527 0.1159%	-1.7305E-06	0.02868	-117.792	+6.32K

Table 3-13. Mean annual Eather LBS response functions, normalised at $P_1(3)$. 1990-1995 functions are derived via secondary calibration scans. Quadratic fits are plotted in Figure 3-50. Temperature corrections are for the $R_E(\lambda)$ component only (assumes a spectrally flat source). Increase in $E(\lambda)$ across the region contributes another 2.4 K to the instrument response correction.

Changes in the measured response are readily apparent following installing of the blocking filter after 1990, and the new grating and filter after 1995. Calibrations since 1996 are highly consistent however, which gives confidence that neither the LBS nor the instrument have changed significantly in spectral character since that time. Figure 3-51 plots the difference in response between 1996 and the four subsequent years across the OH(6-2) band. Errors shown are standard error in the difference between two means ($=\sqrt{SD_1^2/N_1+SD_2^2/N_2}$). The variation is around the 0.2% level between $P_1(2)$ and $P_1(5)$ but no consistent trend is evident.

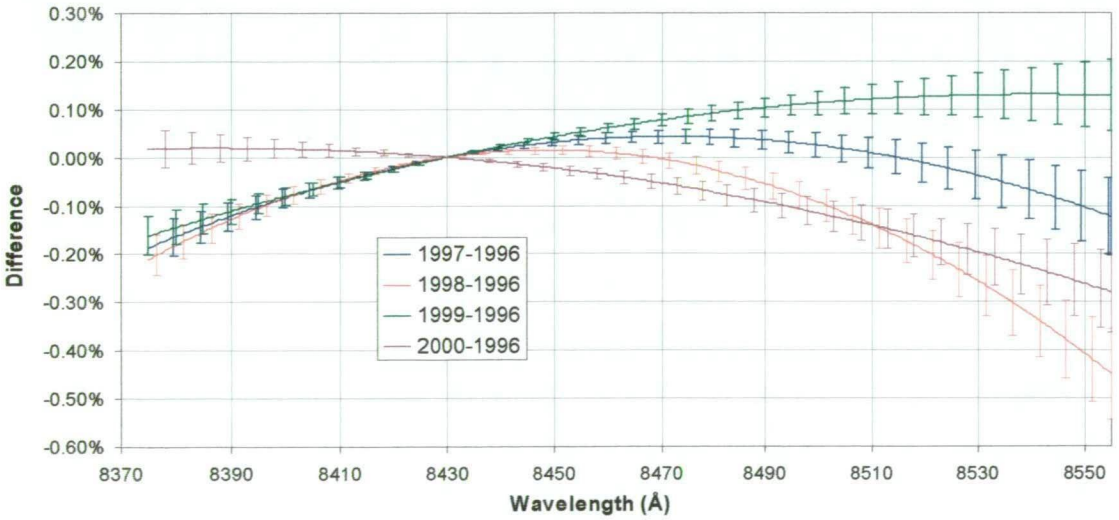

Figure 3-51. The change in response between 1996 and the four subsequent years. Error bars are the standard error in the difference between two means.

3.6.5. Errors in Line Ratios

Rotational temperature is proportional to the intensity ratio of any two P-branch lines. The error in each ratio is calculated by renormalizing the curves in Figure 3-50 at each of the branch line wavelengths. Table 3-13, normalized to $P_1(3)$ thus contains the error in $P_1(2)/P_1(3)$, $P_1(3)/P_1(4)$, and $P_1(3)/P_1(5)$ ratios. Renormalising to $P_1(2)$ yields $P_1(2)/P_1(4)$, $P_1(2)/P_1(5)$ (and $P_1(2)/P_1(3)$ again) etc.

Table 3-14 lists relative uncertainties in each intensity ratio due to the instrument response calibrations each year. Substitution of the intensity ratio, plus or minus the relative error in the ratio into the rotational temperature equation derives the equivalent temperature error for each ratio at 200K. Equivalent errors in deriving the Eather source function, $E(\lambda)$ (Jan-99 and Dec-99 calibrations) are also listed for comparison. Largest errors are for earlier years, but the response correction can now be quantified to around the 0.2 K uncertainty level. This is a minor contributor to overall temperature errors discussed in section 4.4

Ratio	$\frac{P_12}{P_13}$	$\frac{P_12}{P_14}$	$\frac{P_12}{P_15}$	$\frac{P_13}{P_14}$	$\frac{P_13}{P_15}$	$\frac{P_14}{P_15}$	Mean Error
$R_E(\lambda)$							
1990	0.722% 4.09 K	1.205% 2.11 K	1.592% 1.59 K	0.543% 1.41 K	1.296% 0.82 K	0.850% 1.97 K	2.00 K
1994	0.464% 2.63 K	0.644% 1.13 K	0.689% 0.69 K	0.245% 0.64 K	0.786% 0.50 K	0.483% 1.12 K	1.12 K
1995	0.749% 4.24 K	1.192% 2.09 K	1.613% 1.61 K	0.600% 1.56 K	1.148% 0.72 K	0.422% 0.98 K	1.87 K
1996	0.184% 1.04 K	0.278% 0.49 K	0.340% 0.34 K	0.115% 0.30 K	0.288% 0.18 K	0.222% 0.52 K	0.48 K
1997	0.107% 0.61 K	0.156% 0.27 K	0.183% 0.18 K	0.066% 0.17 K	0.153% 0.10 K	0.118% 0.27 K	0.27 K
1998	0.040% 0.23 K	0.075% 0.13 K	0.145% 0.14 K	0.045% 0.12 K	0.132% 0.08 K	0.093% 0.22 K	0.15 K
1999	0.027% 0.15 K	0.048% 0.08 K	0.067% 0.07 K	0.023% 0.06 K	0.047% 0.03 K	0.028% 0.06 K	0.08 K
2000	0.044% 0.25 K	0.091% 0.16 K	0.151% 0.15 K	0.049% 0.13 K	0.116% 0.07 K	0.070% 0.16 K	0.15 K
$E(\lambda)$							
Jan-99	0.037% 0.21 K	0.082% 0.14 K	0.137% 0.14 K	0.045% 0.12 K	0.100% 0.06 K	0.055% 0.13 K	0.13 K
Dec-99	0.050% 0.28 K	0.111% 0.19 K	0.185% 0.18 K	0.061% 0.16 K	0.135% 0.08 K	0.074% 0.17 K	0.18 K

Table 3-14. Relative errors in line-ratios, and equivalent 200K temperature errors due to instrument response calibrations for both measured response, $R_E(\lambda)$ and determination of source, $E(\lambda)$ functions.

3.6.6. Absolute Instrument Response.

While an absolute measure of line intensities are not necessary to derive rotational temperatures, the Dec-96 Eather LBS calibration at NML [Figure 3-35] was referenced to absolute intensity units (Rayleighs/nm) and can be used to give a approximate measure (some scattering included) of the absolute instrument response.

Figure 3-52 shows the measured absolute response (in counts s^{-1}/Rayleigh) assuming a 0.15 nm bandwidth between 350 and 950 nm and also the calculated response excluding the blocking filter and Perspex viewing window. Typical photomultiplier quantum efficiency, combined reflectivity of the 3 front surface aluminium mirrors (one plane entrance and two collimating), and a beam width correction factor (due to grating rotation) are also shown against the RHS axis. Aluminium reflectivity exhibits a local minimum around 825 nm, so was perhaps an unfortunate choice for OH(6-2) observations. The Woods anomaly for order -1, is a prominent feature at 595 nm and the +2 order is also just visible at 515 nm.

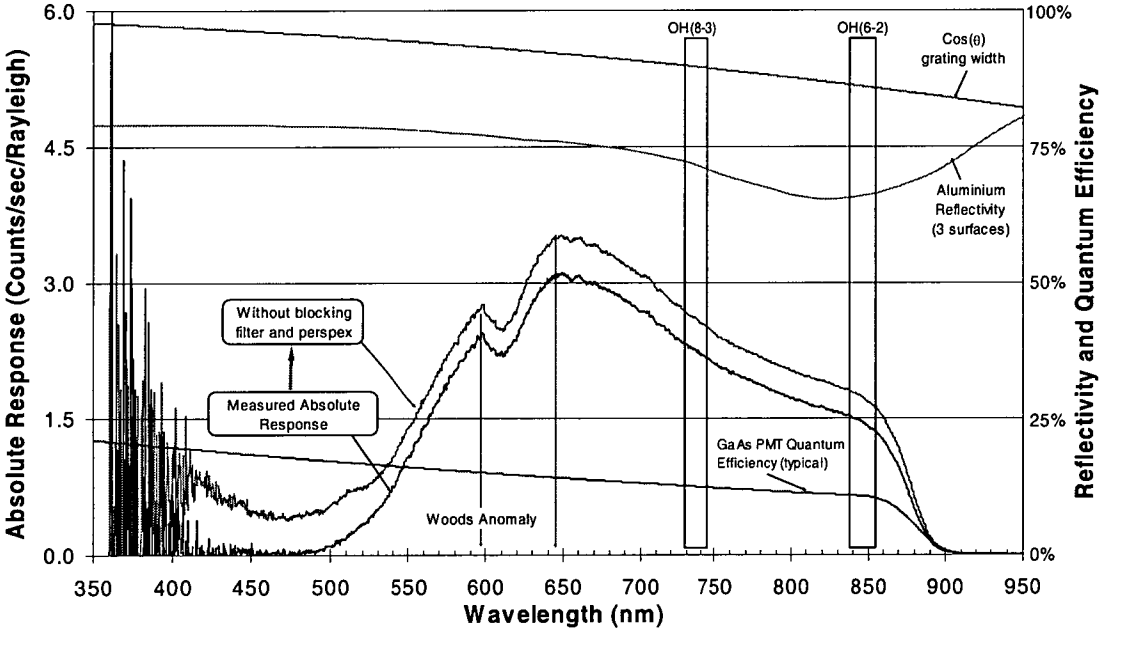

Figure 3-52. Absolute instrument response curves for the Davis spectrometer

Overall measured absolute instrument response is around 1.5 counts.s^{-1}.Rayleigh^{-1} in the OH(6-2) region and slightly better in the OH(8-3) region. An average $P_1(3)$ count rate of 300 counts s^{-1} implies 200R of $P_1(3)$ or 1.7kR for the whole OH(6-2) band at 200K (equivalent to Krassovsky *et al.* (1962)). Peak response, at around 650 nm, is somewhat lower than expected, as the grating is blazed for 750 nm. The response increases toward the low wavelength side due to the second order blaze at 375nm.

3.7. Data Sets and Scan Parameters

The final section in this chapter is a description of the data sets from which OH rotational temperatures are determined.

3.7.1. Data formats

As a consequence of numerous changes to instrumentation, control software and operating parameters, spectra have been stored in a variety of formats over the years. Managing multiple file formats and various scan parameters in analysis programs is not ideal and some early misinterpretation of error calculations directly resulted from it. Most changes however came about in a reasonably logical way considering the instrument improvements and observational goals.

3.7.1.1. DM1B format.

A plain ASCII format for the original DM1B coordinator and micro-PDP computer system contained a simple header with scan start and stop times, filename, number of scans, slit widths, step size, dwell time per step, number of samples, start wavelength and wavelength offset correction, followed by the data in counts per second for each scan. These easily readable files (about 64Kb in size for routine scans) were a great advantage during the development and proofing of analysis programs. This format was used until the end of 1994 when the DM1B was replaced by the SpectrAcq and DM3000 software.

3.7.1.2. DM3000 format

In contrast the new DM3000 software stored binary format files, which were about 12Kb in size for a comparable DM1B scan. Stored values were different from DM1B format when multiple scans were accumulated. Normally five scans were accumulated together with DM1B in 1990 and 1994 and individual scans were stored with DM3000, but groups of five were accumulated together later for comparison with 1990 data). Errors are calculated on total counts acquired at each step. Different conversions are required for DM3000 (stored as total counts/sec) and DM1B (stored as scans×counts/sec) for proper error analysis.

File timing accuracy is maintained by reference to an IRIG-B time code from the laboratory GPS clock.

3.7.1.3. Concatenated format

Original DM1B and DM3000 scan routines recorded a continuous block of data across the OH(6-2) or OH(8-3) region and stored one spectrum per file. These files were important during analysis development to identify and understand background features and contaminants, but only about 23% of the recorded data contributed to an actual rotational temperature derivation. With background contaminants well understood by mid 1996, fragmenting the scan block to cover just those intervals used for temperature calculation provided an obvious opportunity to increase the time-resolution of temperature measurements.

To do this using DM3000 software meant scanning and recording each individual segment to a separate file. Consequently, 8 files (typically) were produced for each spectrum cycle, which included a darks file, three P-branch lines, three background regions and a region to estimate auroral contamination. In 1998 for example this regime produced about 204,000 individual files.

Post acquisition programs concatenated the scan-segment files together, to construct a complete spectrum file for analysis. This system was introduced at the end of 1996 and has continued to the present time (with various scan region adjustments)

3.7.2. Data Catalogue

A catalogue of all data collected on the Davis spectrometer is presented in Table 3-16. Only OH(6-2) data is analysed in this work. Figure 3-53 shows examples of continuous scan spectra acquired until the end of 1996 and fast scan-segment spectra acquired subsequently for comparison. Table 3-15 lists scan parameters for the individual scan-segments used.

A scan segment at a prominent line in the N_2 1PG(2-1) band was introduced in 1998 to monitor N_2 aurora as the N_2 1PG(3-2) band is a significant contributor to the background in the OH(6-2) region. After D146 the scan segment was shifted down in wavelength to a prominent line in the N_2 1PG(5-4) band as the low PMT response in the higher region significantly diminishes the advantage gained in band strength.

Both atomic oxygen and Fraunhofer segments were included at the start of 2000 to monitor auroral activity and scattered moon and twilight respectively.

Feature	Label	Start λ	Stop λ	Step Å	Dwell sec
$P_1(2)$ Line	P12	8396.5	8401.5	0.1	1
$P_1(2)$ Background	BP12	8405.4	8409.4	0.1	0.5
$P_1(4)$ Background	BP14	8437.5	8441.5	0.1	0.5
$P_1(4)$ Line	P14	8462.5	8468	0.1	1
$P_1(5)$ Background	BP15	8477.5	8487	0.1	0.5
$P_1(5)$ Line	P15	8502.1	8507.7	0.1	1
N_2 1st POS (1-2) auroral band	N2PG	8689.5	8693.5	0.1	1
N_2 1st POS (5-4) auroral band	N2PG	8114.0	8120.0	0.2	1
Fraunhofer absorption region	FRA	8497.0	8499.5	0.1	0.5
Fraunhofer absorption region	FRA	8494.5	8501.6	0.1	0.5
Atomic oxygen auroral line	OI	8443.8	8448.9	0.1	0.5

Table 3-15. Scan parameters for the various spectral segments.

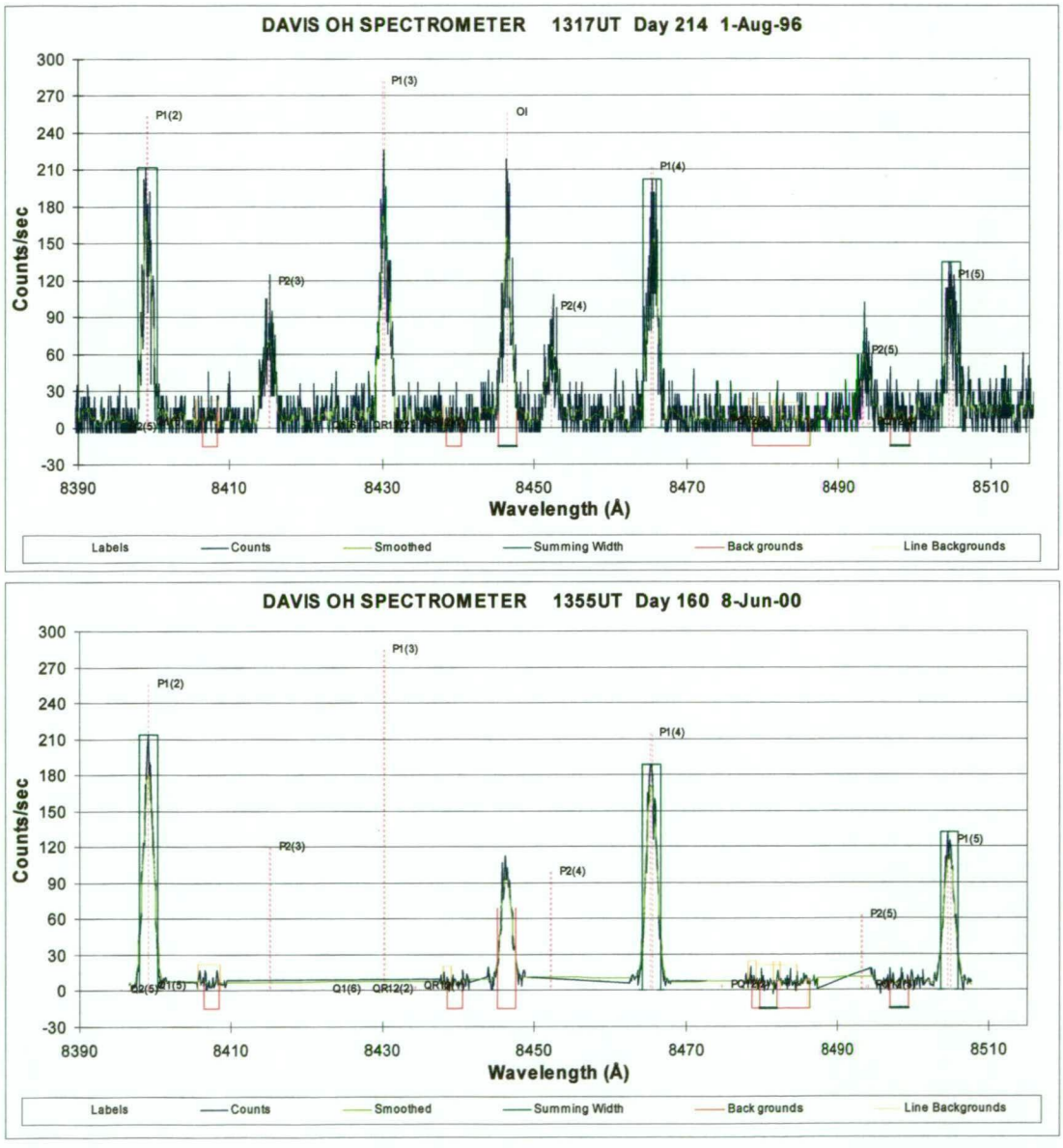

Figure 3-53. A comparison of typical continuous spectra acquired up until the end of 1996 over about 1 hour with scan-segment spectra acquired subsequently in about 7.5 minutes.

Year	Operator	Prefilter	Branch	Data Format	Files or cycles	Size (Mb)	Total Days	Day Start	Day Stop	Minutes per spectra	Dwell sec	Step size Å	Summed Scans	Seconds per nm	Scan Features
1987	P. Williams	Single	8-3	DM1B	537	8.04	112	96	285	92:00	1	0.2	5	250	Continuous Spectra 7300-7410 60°zenith angle to SE
1990	P. Williams	None	6-2	DM1B	466	27.80	97	83	282	57:00	0.5	0.05	5	100	Continuous Spectra 8375-8560 60°zenith angle to SE
			8-3	DM1B	381	18.40	85	90	282						Continuous Spectra - Various Operating Modes
1994	P. Williams	Single	6-2	DM1B	2305	66.50	123	99	99	65:00	0.1	0.05	5	100	Continuous Spectra 8375-8515
								100	167	41:00	0.2	0.1	5	100	Continuous Spectra 8375-8515
								182	193	21:30	0.2	0.2	5	50	Continuous Spectra 8375-8515
								194	194	41:00	0.1	0.1	5	50	Continuous Spectra 8375-8515
								195	209	20:15	0.2	0.2	5	50	Continuous Spectra 8375-8515
								210	211	4:55	0.3	0.2	1	15	Continuous Spectra 8375-8515
								212	216	20:10	0.2	0.2	5	50	Continuous Spectra 8375-8515
								217	294	4:36	0.3	0.2	1	15	Continuous Spectra 8375-8515
1995	J. French	Single	6-2	SpectraMax	9	0.10	3	56	58	28:00	0.1	0.05	1	20	Continuous Spectra 8375-8515
				DM3000	18657	213	241	59	303	7:48	0.1	0.05	1	20	Continuous Spectra 8375-8515
				DM1B 5sums	3883	138	241	59	297	39:54	0.1	0.05	5	100	Continuous Summed Spectra 8375-8515
1996	K. Finlayson	Double	6-2	DM3000	16773	191	248	57	269	7:48	0.1	0.05	1	20	Continuous Spectra 8375-8515
				DM3000	1824	13.7	36	269	306	6:17	1	0.1	1	100	$P_1(2),P_1(4),P_1(5),BP_1(2),BP_1(4),BP_1(5)$,BA
				DM1B 5sums	3354	123	248	57	268	38:59	0.1	0.05	5	100	Continuous Summed Spectra 8375-8515
1997	P. Greet	Double	6-2	DM3000	17751	122.0	154	55	233	6:37	1	0.1	1	100	$P_1(2)$, $P_1(4),P_1(5),BP_1(2),BP_1(4),BP_1(5)$,DARK
				DM3000	2330	27.8	53	235	295	11:05	1	0.05	1	200	$P_1(2)$, $P_1(4),P_1(5),BP_1(2),BP_1(4),BP_1(5)$,DARK,Ratios
1998	J. French	Double	6-2	DM3000	25500	199.3	273	42	317	7:14	1	0.1	1	100	$P_1(2),P_1(4),P_1(5),BP_1(2),BP_1(4),BP_1(5)$,DARK,$N_2$PG
1999	F. Phillips	Double	6-2	DM3000	14948	116.8	181	47	303	7:34	1	0.1	1	100	$P_1(2),P_1(4),P_1(5),BP_1(2),BP_1(4),BP_1(5)$,DARK,$N_2$PG
			8-3	DM3000	1639	11.63	32	95	126	31:50	0.5	0.05	1	100	Continuous Spectra 7235-7405
			8-3	DM3000	877	10.33	36	213	250	6:58	1	0.05	1	200	$P_1(2),P_1(3),P_1(4),P_1(5),R_1(1),Q_1(2)$,DARK
2000	G. Klich	Double	6-2	DM3000	25881	231.8	263	43	305	7:31	1	0.1	1	100	$P_1(2),P_1(4),P_1(5),BP_1(2),BP_1(4),BP_1(5)$,DARK,OI,FRA
2001	M.Terkildsen	Double	6-2	DM3000				48		7:00	1	0.1	1	100	$P_1(2),P_1(4),P_1(5),BP_1(2),BP_1(4),BP_1(5)$,DARK,OI,FRA

Table 3-16. Data catalogue of Davis Spectrometer Data

4. Rotational Temperature Analysis

Development of analysis procedures for rotational temperature determination and error assessment, based on the 1990 data set, are discussed in this chapter. The author was responsible for all analysis code development and testing. Much of this work is published in Greet *et al.* (1998) "OH(6-2) spectra and rotational temperature measurements at Davis, Antarctica", Annales Geopyhsicae 16, 77-89. A copy of this manuscript is included in Appendix A.

The 1990 data set was selected as a 'test-bed' for analysis development, principally due to its consistent acquisition mode and manageable size. Where significant differences from subsequent data sets exist, they are noted in each section. Analysis improvements are discussed at the end.

Background features across the OH(6-2) region are examined in detail and assessed for potential contributions to P-branch line intensities. Where possible their presence is allowed for in the analysis. Implementation of the fast scan-segment acquisition mode, established at the end of 1996, relied on this detailed knowledge of background features.

4.1. Data selected for analysis development

Data selected in this study were collected at Davis over the interval from D090 to D270 (31 March - 27 September) 1990. Data acquisition is limited by day length and the observing period was further split into seven campaigns centred on new moon periods.

Instrument configuration has been described in chapter 3 but is summarised for this data set by the following:

- Field of view was ~6°, elevated 30° above the SE horizon, centred on 69.4°S, 80.8°E. (section 3.2.2.4).
- The instrument was operated without an appropriate higher-order blocking filter therefore second-order auroral contamination is also investigated.
- This work preceded refinement of the instrument function via the empirical fit method (and no laser profiles were available, see section 3.4.2). A triangular

instrument function of width 0.15nm was used in this case with Rowland ghost magnitudes 0.45% and 0.13% of the primary peak, displaced 0.275 and 0.535 nm at λ632.8 nm. An Argon doublet within the OH(6-2) band (λ846.5 nm), gave ghost displacements at 0.335 and 0.695 nm from the primary peak (compare section 3.3.6).

- Instrument spectral response is determined via reference to a secondary quartz-halogen lamp and the Dec-96 Eather LBS calibration at NML (section 3.6.1). The 1996 LBS calibration contains a small error (absolute temperatures ~1.6K too low) due to scattering from blackout curtains at NML (see section 3.5.5.3, Figure 3-37). This error does not alter the conclusions of this chapter.

- Spectra were generally accumulations of five sequential scans made over the interval λ837.5-856.0 nm at 0.005 nm steps and 0.1 s dwell, which took of the order of an hour to acquire (actual acquisition totals just under 31 minutes, thus approximately 26 minutes are spent stepping and repositioning for sequential scans). Major emission features in this spectral region are shown in Figure 4-1 for averaged spectra acquired at different levels of auroral activity (1990 spectra are binned in three groups by OI range and averaged).

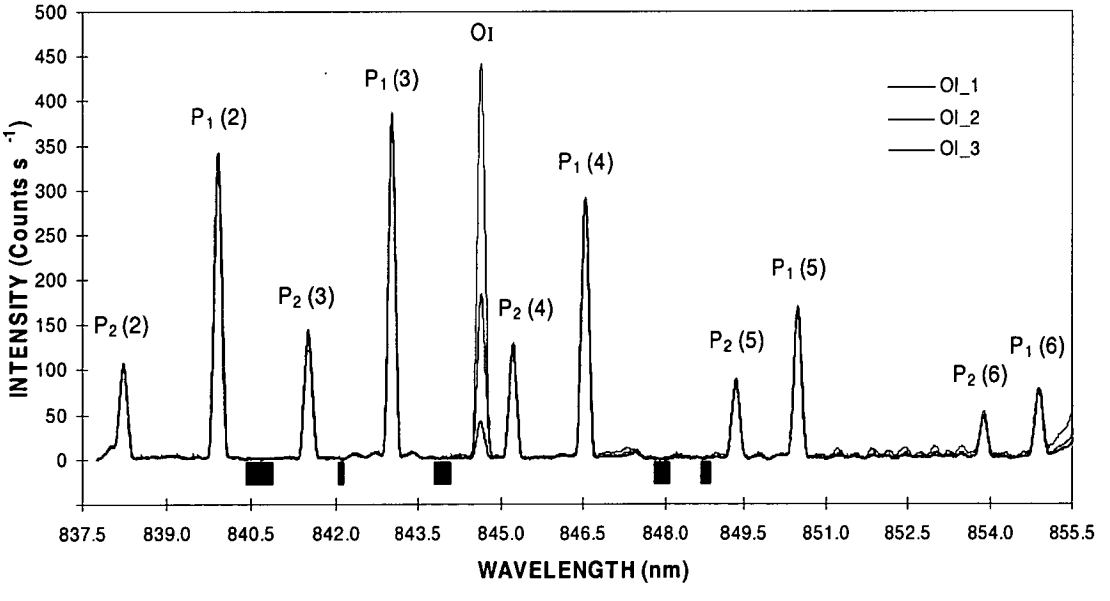

Figure 4-1. Averaged and smoothed spectra of OH(6-2) region at three levels of auroral activity (split by OI at λ844.6 nm). Smoothing was applied with a Gaussian filter of less than 0.02nm half-with. Significant features are labelled and black bands below the spectral profile show regions investigated for background sampling.

A principal reference data set consists of 104 spectra for which:

- clear skies were recorded (visual observation),
- the sun was more than 18° below the horizon,
- the moon was below the horizon, and
- the aurorally sensitive OI line at λ844.6 nm was less intense than the OH(6-2) $P_1(3)$ emission.

This data set contains the best spectra for the operating mode adopted in 1990. An expanded data set, of 277 spectra, was selected by incorporating criteria chosen near the upper limit of the range of values in the principal data set. Selection criteria for the expanded data set are that:

- the sun was more than 18° below the horizon.
- a linear fit across five background regions, identified by the black bands below the spectra in Figure 4-1, has a slope of less than 0.6 counts s^{-1} nm^{-1} (This amounts to a maximum difference between $P_1(2)$ and $P_1(5)$ due to a slope in the background of 6 counts s^{-1} and compares with an average peak signal for $P_1(3)$ in the principal data set of 385 counts s^{-1}); this criteria removes extreme moon and variable cloud influences.
- uncertainty in the temperature estimate due to counting statistics is less than 7 K; this eliminates spectra with significantly reduced intensities due to cloud cover.
- weighted standard deviation of the temperature, as calculated from different line pair ratios, is less than 10 K.
- $OI/P_1(3) < 2$; this criteria eliminates extreme auroral influences.

4.2. Identification of weak spectral features

Minor features in the spectra are from three main sources: aurorae, Rowland ghosts and minor OH-band emissions. Such features may contaminate the major lines used for rotational temperature measurements and background regions that must be subtracted when determining the intensity of each line. Knowledge of minor features facilitates selection of appropriate lines and background regions to minimize the spectral region scanned. An optimal instrument function may also be determined that minimizes contamination from known minor features. The possibility of auroral contamination is very high in Davis spectra. Rejection of all aurorally contaminated

spectra, as has been done by others [e.g. Myrabo *et al.*, (1987); Cogger *et al.*, (1988)] is not desirable, and thus a study of auroral detail is necessary.

4.2.1. Satellite lines

Table 4-1 gives wavelengths and Λ-doubling for the major P_1 branch lines in OH(6-2) spectra and nearby minor features, calculated from term energies given by Coxon (1980) and Coxon and Foster (1982).

line	ν_{vac}	λ_{air}	$\Delta\lambda$	λ_{mean}	λ_{obs}	I(221 K)	
	cm^{-1}	(nm)	(nm)	(nm)	(nm)	theory	observed
(a) OH(6-2) main branch lines							
$P_1(2)$f	11902.6	839.921	0.0101	839.916	839.92	85.7	scaled to 85.7
e	11902.8	839.91					
$P_1(3)$f	11858.8	843.026	0.0190	843.017	aligned	100.0	101.6 ± 0.2
e	11859.0	843.007					
$P_1(4)$f	11809.4	846.55	0.0305	846.535	846.54	76.7	77.2 ± 0.1
e	11809.8	846.519					
$P_1(5)$f	11754.5	850.505	0.0431	850.484	850.48	44.8	44.7 ± 0.1
e	11755.1	850.462					
(b) Weak features of interest							
$Q_1(4)$e	11928.9	838.073	0.083	838.032		6.1	4.9 ± 0.3
f	11930.0	837.99					
$Q_1(5)$e	11901.3	840.017	0.104	839.964	Blended with $P_1(2)$	1.8	Blended with $P_1(2)$
f	11902.7	839.912					
$Q_1(6)$e	11867.3	842.417	0.192	842.322	842.33	0.5	2.4 ± 0.6
f	11870.0	842.226					
†$P_2(12)$f	11864.2	842.639	0.094	842.686			
e	11862.9	842.733					
$^{Q}R_{12}(2)$e	11862.8	842.743	0.008	842.747	842.71	0.5	1.3 ± 0.3
f	11862.6	842.751					
$^{Q}R_{12}(3)$e	11862.4	842.771	0.001	842.771		0.1	
f	11862.4	842.771					
†$P_1(12)$e	11858.2	843.07	0.147	843.144	Blended with $P_1(3)$		Blended with $P_1(3)$
f	11856.1	843.217					
$^{Q}R_{12}(1)$e	11853.1	843.433	0.008	843.437	843.43	1.2	1.7 ± 0.3
f	11852.9	843.441					
$^{P}Q_{12}(2)$e	11796.9	847.451	0.019	847.46	847.44	1.5	2.0 ± 0.3
f	11796.6	847.47					
†$^{P}{}_1(13)$e	11760.3	850.086	0.167	850.179	Blended with $P_1(5)$ ghost		Blended with $P_1(5)$ ghost
f	11758.0	850.253					

Table 4-1 (a), (b). Wavenumbers, wavelengths, Λ-doubling and intensities compared with observed wavelengths and intensities (relative to $P_1(3)$) for the principal data set from (a) main branch lines and (b) proposed identifications of minor non-aurorally dependent spectral features near the main branch lines. All lines are from the OH(6-2) band except those marked by † which are from the OH(5-1) band as identified by Osterbrock et al. (1997).

Measured intensities for the main and satellite lines with those calculated for a rotational temperature of 221 K are compared in the last two columns in Table 4-1. Transition probabilities of Turnbull and Lowe (1989) were used in calculating main branch lines intensities. Goldman (1982) gives approximate transition probabilities for satellite lines relative to Mies (1974) values for the main branch transitions. In estimating transition probabilities for satellite lines consistent with Turnbull and Lowe values, it was assumed that the ratio of satellite line to main branch transition with the same upper state remained constant at the value given by Goldman.

4.2.2. Auroral Emissions

Selections of spectra from the expanded data set were grouped into three sets based on intensity of the aurorally sensitive OI (λ844.6nm) emission. Spectra in these three sets were averaged, using the $P_1(3)$ line to align each spectrum, and smoothed. Smoothing is only included to make small features more easily visible in the figures. Smoothing has a minor effect on widths and relative magnitudes of lines. Temperature analysis and relative scaling of features is performed only on unsmoothed data. Each of the smoothed, averaged spectra have been scaled to give a $P_1(3)$ count rate equivalent to an averaged principal spectrum (385 counts s^{-1}). Figure 4-2 shows spectral regions in the vicinity of $P_1(2)$, $P_1(3)$, $P_1(4)$ and $P_1(5)$ lines in expanded form. To illustrate small-scale features major lines have been truncated at 16 counts s^{-1}, approximately 4% of the maximum intensity of major P_1 branch lines, which are labelled for clarity.

Aurorally sensitive background features are apparent in Figure 4-2. Major auroral features which directly influence the OH(6-2) region are the N_2^+ Meinel (4-2) (λ827-878 nm) band and the N_2 1PG (3-2) (λ818-861 nm) band (Hecht *et al.*, 1987; Viereck and Deehr, 1989). Second-order lines from the auroral N_2^+ 1NG(1-2) (λ419-424 nm), N_2^+ 1NG(0-1) (λ422-428 nm) and various N_2 Vegard-Kaplan bands are also present. These bands are shown in Figure 4-3 as derived from programs provided by Gattinger [personal communication] and convolved with an instrument function equivalent to the Davis instrument. Band intensities, from Vallance-Jones (1974) [pp 126-134] are scaled relative to an IBC3 class aurora. Total system intensities are 882, 631, 152 and 55 kR for the N_2 1PG, N_2^+ Meinel, N_2^+ 1NG and N_2 Vegard-Kaplan systems respectively.

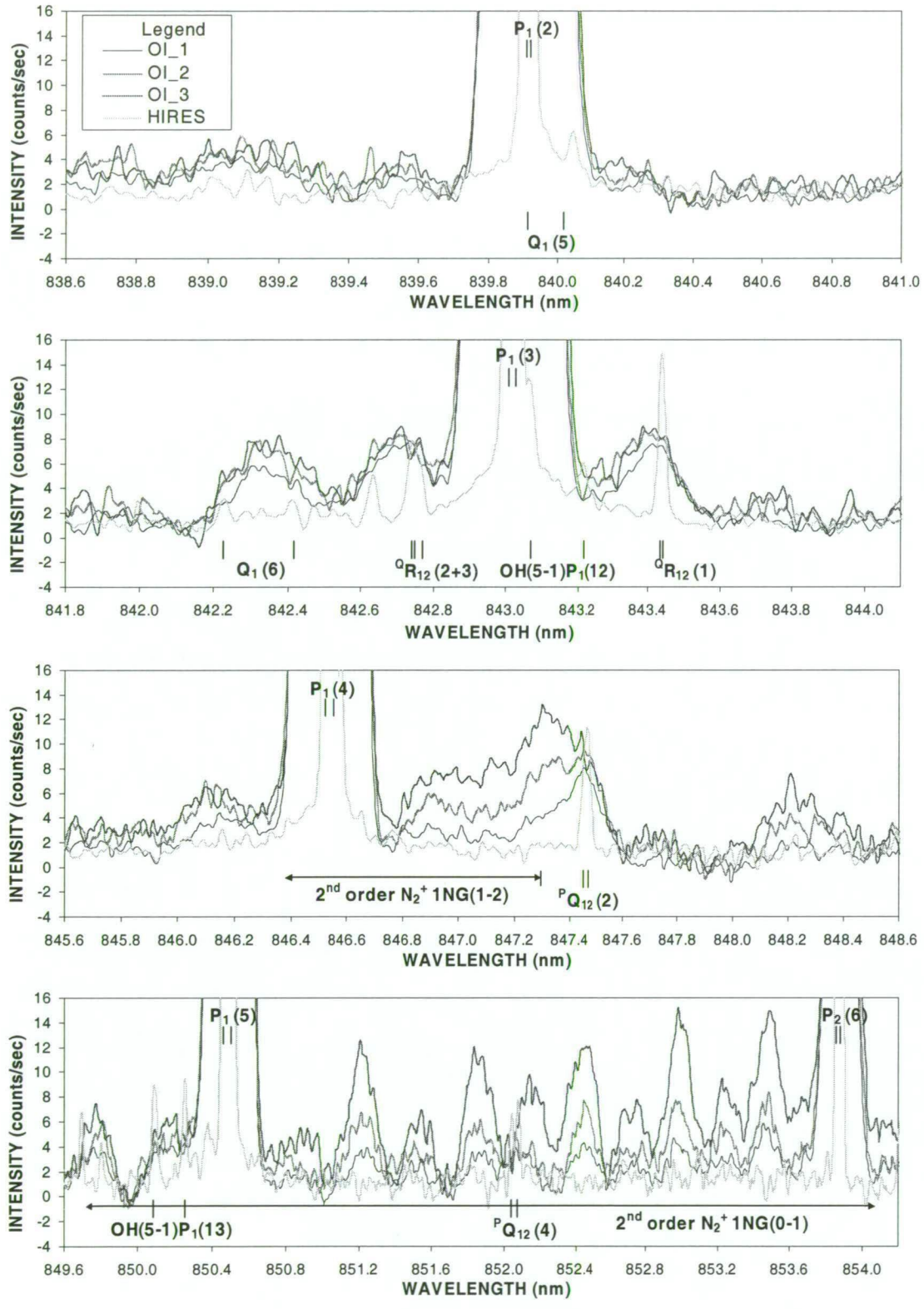

Figure 4-2. Averaged and smoothed spectra, at three levels of auroral activity, showing the dependence of weak spectral features in the vicinity of $P_1(2)$, $P_1(3)$, $P_1(4)$ and $P_1(5)$ lines of OH(6-2). Intensity is truncated at 16 counts s^{-1}. Main P-branch features are labelled and identification of weak spectral features is made below the spectra. Also shown is a spectrum from the HIRES (high-resolution echelle spectrograph) on the Keck 10-m telescope at Mauna Kea (Osterbrock et al. 1997) extracted from http://www.ucolick.org/~jfulb/OH.html and scaled to match $P_1(3)$ intensities.

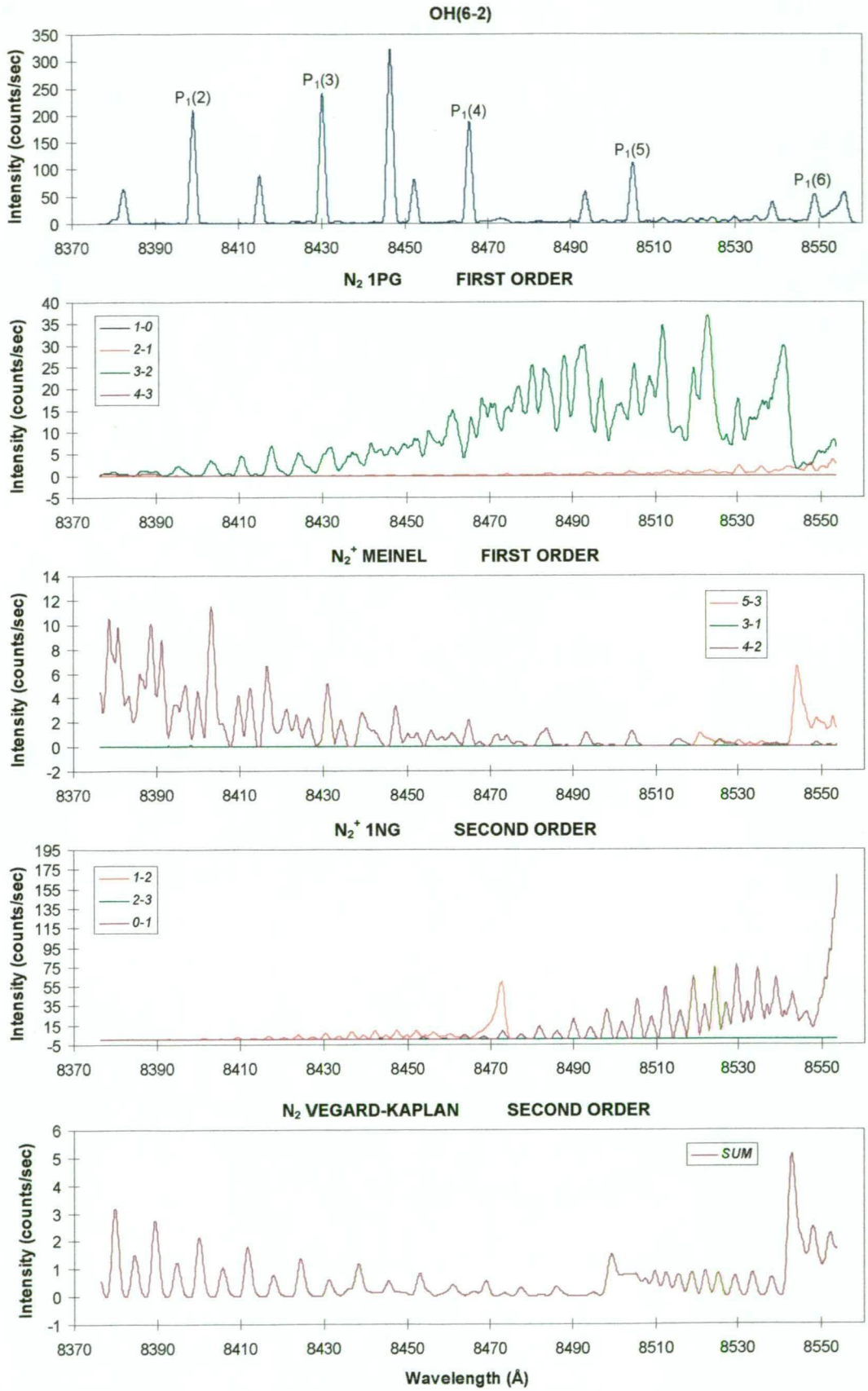

Figure 4-3. Structure of the nitrogen auroral bands (first order N_2 1PG and N_2^+ Meinel and N_2^+ 1NG and second order N_2 Vegard-Kaplan) underlying OH(6-2). Bands are calculated from theoretical spectra (Gattinger, private communication) and convolved with a 0.15 nm instrument function.

A spectrum from the HIRES (high-resolution echelle spectrograph) instrument on the Keck 10-m telescope at Mauna Kea (20°N, 155°W) is also shown overlayed on Figure 4-2 (Osterbrock *et al.,* 1997, spectrum image was extracted from www.ucolick.org/~jfulb/OH.html referenced in the paper). This spectrum, observed with an instrument resolution of ~0.02 nm in order 42, is scaled to match the $P_1(3)$ peak intensity. Clearly no auroral emissions are present, as would be expected at this latitude. Many of the underlying OH lines identified are resolved in the HIRES spectrum and it allows some estimate of their magnitude.

4.2.3. P_1 branch line contamination

$P_1(2)$ shows no evidence of contamination in Figure 4-2. Small features ±0.3 nm from the line are consistent with Rowland ghosts. Examination of a theoretical OH(6-2) spectrum shows that $Q_1(5)$ at λ839.964 nm (Λ-doubling of 0.104 nm), is coincident with $P_1(2)$. $Q_1(5)_f$ is apparent in the HIRES spectrum.

$P_1(3)$ shows three nearby features which are not aurorally sensitive and which are too strong to be solely due to ghosts. Originally, these were assigned to the OH(6-2) band features: $Q_1(6)$, and satellite lines $^{Q}R_{12}(2)$, $^{Q}R_{12}(3)$ and $^{Q}R_{12}(1)$. $^{Q}R_{12}(2)$ and $^{Q}R_{12}(3)$ are not resolvable with the Davis instrument or HIRES. Temperature analysis also indicated that a further minor emission existed under $P_1(3)$. Subsequently, Osterbrock *et al.* (1997) proposed high rotational-state OH(5-1) features in this region: OH(5-1)$P_2(12)$ (λ842.73 nm, not labelled in Figure 4-2) and OH(5-1)$P_1(12)$ (λ843.14 nm, which is evident in the HIRES spectrum). Some of these minor OH features are significantly broadened by Λ-doubling (see Table 4-1). Overlapped OH(6-2) $^{Q}R_{12}$(2 and 3) and OH(5-1)$P_2(12)$ features and the OH(6-2) $^{Q}R_{12}(1)$ feature are distorted by a superposed Rowland ghost from $P_1(3)$. Since the $P_1(12)$ lines are unthermalized and OH(5-1) intensity is unknown, a correction to $P_1(3)$ is impossible. $P_1(3)$ is consequently excluded from rotational temperature analysis.

$P_1(4)$ has a small auroral contribution, principally from the N_2 1PG(3-2) band, superimposed on the Rowland ghosts. The $^{P}Q_{12}(2)$ satellite emission is apparent approximately +1.0 nm from the $P_1(4)$ line and obvious in the HIRES spectrum. As auroral activity increases, a broader feature with a band head near the $^{P}Q_{12}(2)$ emission becomes apparent. This is principally due to second-order transmission of N_2^+ 1NG (1-2) band (λ419-424 nm).

$P_1(5)$ has an aurorally dependent, combined second order N_2^+ 1NG(0-1) (λ422-428 nm), and first-order N_2 1PG(3-2) feature under it. The aurorally sensitive sequence of alternating large and small background peaks, most readily apparent at wavelengths higher than the $P_1(5)$ line, are principally due to second-order N_2^+ 1NG(0-1)[†]. Satellite line $^PQ_{12}(4)$ is just discernable at λ852.06 nm, its location is made clear by the HIRES spectrum. Two Λ-doubled components of OH(5-1) $P_1(13)$ (at λ850.086 and 850.253 nm) are evident in the HIRES spectrum but are not apparent in the summed spectra as they are blended with the $P_1(5)$ ghost on the low wavelength side. These are unthermalised lines and would potentially be a problem if the instrument function were wider than its current value of 0.15 nm.

4.2.4. Atmospheric Absorption

None of the lines listed in Table 4-1 suffer significantly from atmospheric absorption. Water vapour is the only absorber of consequence in the wavelength range covered. A maximum concentration of 10 mm precipitable water is estimated for the Antarctic coastal site of Davis (see also http://www.cira.colostate.edu/climate /NVAP/NVAPCIRA.htm). Figure 4-4 plots the variation in water vapour mixing ratio obtained from twice-daily met-sonde flights conducted at Davis over 1998. Although the sondes reach different heights (typically 35 km in summer and 25 km in winter), most water vapour is contained below the tropopause (Salby (1996)).

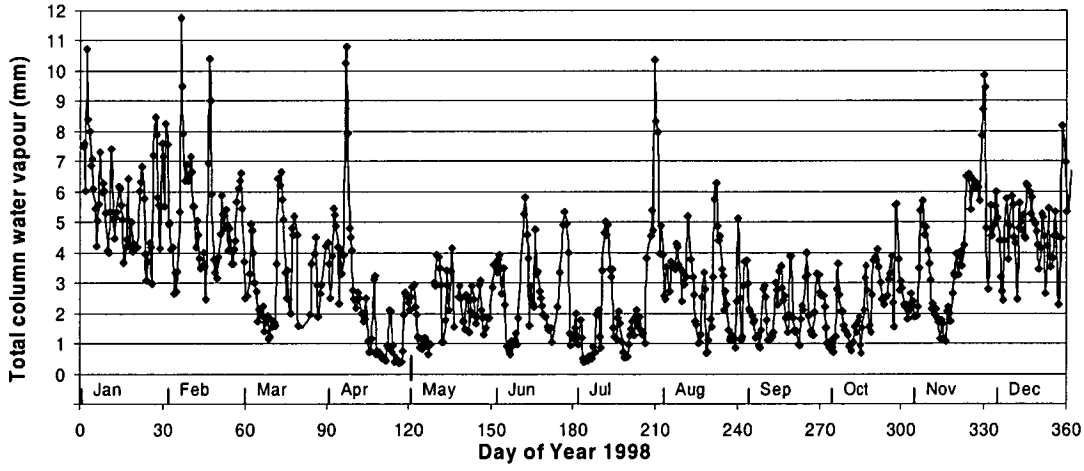

Figure 4-4. Total column water vapour from the twice-daily met-sondes at Davis over 1998.

[†] It was initially believed that an appropriate blocking filter was installed in the instrument in 1990, however this obvious alternating structure, combined with knowledge of the relative magnitudes of nitrogen auroral emissions (shown in Figure 4-3), that provided convincing proof that the filter was indeed left out.

Using high-resolution telluric absorption spectra (HITRAN96; Rothman *et al.* (1992) and equations in Turnbull and Lowe (1983) for absorption of a line of intensity *I*, viz.

$$I_{obs} = I_{true} \exp(-kH) \qquad \textit{Equation 4-1}$$

where H (cm^{-2}) is the amount of absorber along the path ($=N_{Avogadro}/22.4$ litres/mole $=2.69E+18\times mm_{H2O}$) and the absorption coefficient k (cm^2) for each absorbing line i is

$$k_i = \frac{S_i}{\pi} \frac{\alpha_i}{(\nu_i-\nu_o)^2+\alpha_i^2} \qquad \textit{Equation 4-2}$$

where S_i is the absorbing-line strength, α_i its air-broadened[†] half-width and $\nu_i-\nu_o$ the separation (in wavenumbers) of the absorbing line from the emission line of interest. The highest absorption calculated in this way for the P_1 Λ-components listed in Table 4-1 is 0.0002% [Figure 4-5]. The highest absorption for the Q_1 lines is 0.001%, for the R_1 lines is 0.011% and for the satellite lines is 0.0514%.

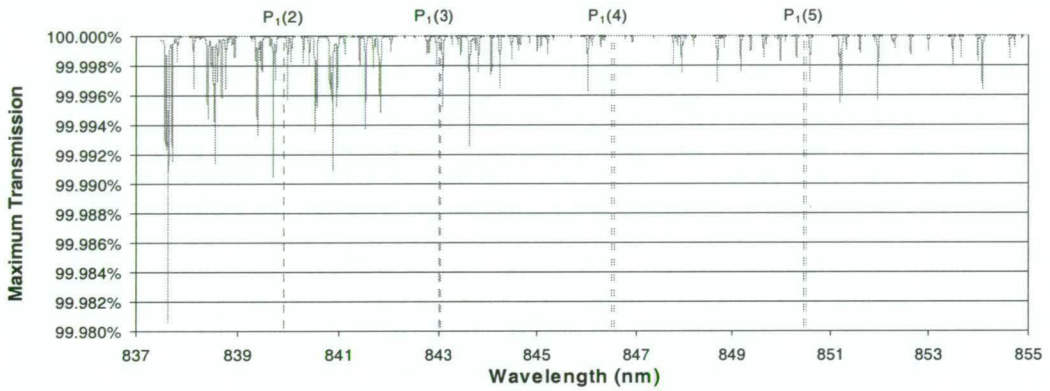

Figure 4-5. Water vapour absorption features over the OH(6-2) region, calculated using HITRAN96 with 10mm water vapour.P_1-branch line positions are marked and labelled.

In a more thorough treatment, Espy and Hammond (1995) model atmospheric absorption including seven major optically active atmospheric species and twenty-one trace species (with column abundances from U.S. Standard Atmosphere Supplements (1966)[‡]). Transmission coefficients for the major P, Q, and R-branch rotational lines in five OH bands (including OH(6-2)) are presented for (northern) mid- and high-latitude summer and winter conditions. Each Λ-doubled component of each OH line was given a Doppler broadened profile for the calculation. High latitude winter transmissions for the main P_1 and Q_1 are all greater than 99.7%. $R_1(2)$ has the greatest absorption of the lines listed at 98.7%. No satellite line transmissions were given.

[†] Self-broadened half-widths were used in error in Greet *et al.* (1998), however the resulting absorption factors are still negligible for this calculation.

[‡] Espy and Hammond's high-latitude winter H_20 density of 1.392E+22 is 3 orders of magnitude larger than that calculated here for 10mm H_20 (2.69E+19molec/cm^2). This discrepancy has not been resolved.

4.2.5. Solar Fraunhofer Absorption

Routine observations since 1995 are made throughout the observing season regardless of moon phase or cloud conditions. Spectra contaminated by moonlight or twilight have enhanced backgrounds containing Fraunhofer absorption lines.

Fraunhofer absorption can be seen in Figure 4-6 showing 326 co-added spectra, each of 5 scans, collected during moonlit conditions over 1996. A background is removed and the spectrum is arbitrarily scaled. A solar absorption spectrum [from http://mesola.obspm.fr/], convolved with the instrument function is scaled to fit. Major absorption features lie 0.68 nm below $P_1(5)$ [λ849.81 nm], 0.35 nm above $P_1(4)$ [λ846.88 nm] and 1.14 nm below $P_1(2)$ [λ838.78 nm].

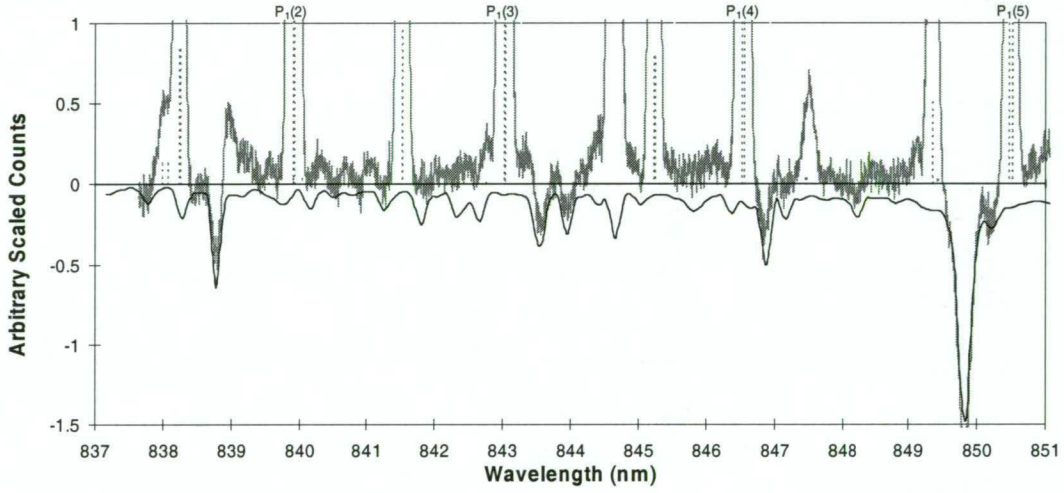

Figure 4-6. Solar Fraunhofer absorption features across the OH(6-2) band

4.3. Analysis Procedures

4.3.1. Aims and Previous Work

The analysis code for this work was developed using a PC based Borland C++ compiler. Prior to early 1994 considerable work had already been done on OH analysis routines in Fortran for VAX systems. Williams (1996) presents temperature results from the 1990 OH(8-3) spectra derived with these routines.

Significant differences exist between these two techniques; the Fortran procedure fitted Gaussians to each P-branch line, typically over a range of 3 half-widths or ±0.35 nm from the line centre. The background and slope fitted across this region varied for each emission line. No allowances were made for the instrument response across the scan region, auroral contamination (principally the N_2 1PG and N_2^+ Meinel

in first order, and second order N_2^+ 1NG), Rowland ghosts, Λ-doubling differences or satellite line blending (principally $Q_1(5)$ with $P_1(2)$ and OH(5-1) $P_2(12)$ with $P_1(3)$) (Williams, private communication).

The new analysis (Figure 4-7) summed total photon counts within an integration width around each P-branch line (typically 0.25 nm). Backgrounds for each line were estimated from several regions across the scan range where auroral, Rowland ghost and satellite line contributions were minimal. Correction factors were included for the instrument spectral response from LBS calibrations and the difference in Λ-doubling width based on a triangular (0.15nm fwhm) instrument function. Where possible, corrections were also made for satellite line contributions and auroral contamination. Each correction factor could be interactively switched to enable an immediate assessment of the effect on temperature and errors. Automated scripts allowed for the processing of large data sets once the procedures were established.

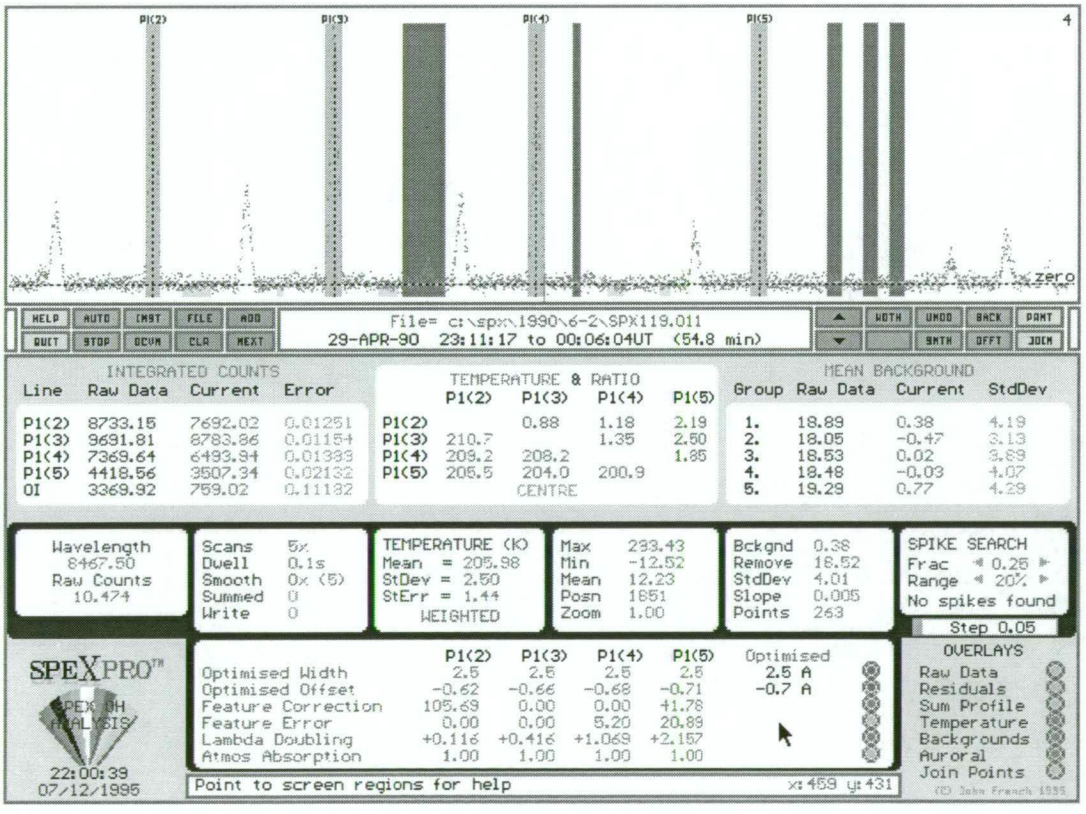

Figure 4-7. A screen capture from the C code analysis program. Interactive selection of correction factors enabled an immediate assessment of their effect. Automated scripts allowed for bulk data processing.

Figure 4-8 presents a flow diagram of the analysis procedure, which is generally followed in the subsequent discussion.

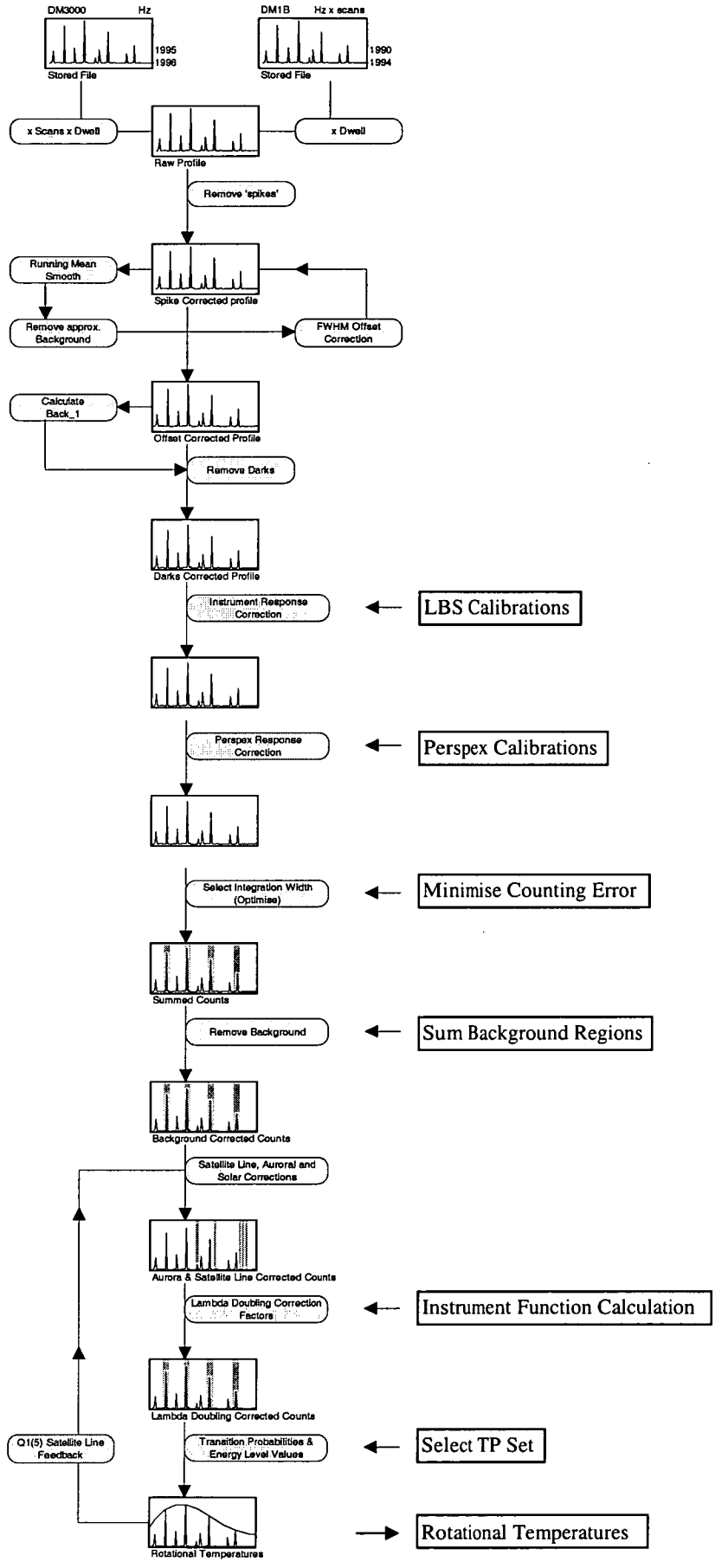

Figure 4-8. Flow diagram of the analysis procedure for OH(6-2) spectra

4.3.2. *Spike Corrections*

Raw spectra occasionally contained anomalous data points or 'spikes', due to electrical interference or cosmic ray strikes in the detector. These were usually only one sample point in duration but both up- and down-ward spikes were observed. Spikes of sufficient amplitude occurring within the integration region for P_1-branch lines or selected background regions may lead to significant temperature error. In order to detect both up- and down-going spikes the factor

$$\delta_i = abs\left(1-\frac{c_i}{\bar{c}}\right) \leq limit \qquad \textit{Equation 4-3}$$

was calculated for each spectral point c_i compared to the local mean $\bar{c}$ (three preceding and succeeding points). The point is corrected by interpolation if δ_i exceeds the limit value (0.95 was found to be suitable).

4.3.3. *Offset Correction*

During routine observations the spectrometer wavelength scale may drift in alignment from day-to-day but an accuracy of ±0.2 nm was generally maintained between alignments of the optical axis.

For correct sampling of the integration region an offset was determined for each P_1-branch line as the difference between the full width at half maximum centre wavelength for each peak in the raw spectrum and the mean of the theoretical Λ-doubled wavelength components (from Coxon and Foster (1982), see Table 4-1).

Raw spectra were first smoothed, by means of a Gaussian filter of half width less than 0.02 nm, so that noise did not influence the determination of fwhm values. A first approximation of the background was then removed so that an accurate estimate of the half maximum intensity could be determined. The mean count rate within the region λ840.425-840.875 nm was selected as a representative background.

A search for the maximum value ±0.4 nm from the known theoretical wavelength for each line identified the line peak. OH(6-2)P-branch lines are well isolated from other large emission features such as atomic oxygen (OI) emission at λ844.6 nm so that the correct peak was found with little difficulty (more care must be taken for the OH(8-3) branch however, as the oxygen ion (OII) emission at λ731.9 nm lies within 0.3 nm of the $P_1(2)$ line)

The wavelength mean of the two points greater than or equal to half the peak intensity defines the offset for each line from its theoretical value. [Figure 4-9]. When summing counts over the peak, the nearest point to the determined offset is chosen as the centre of the sum window and the width always includes an equal number of points on each side (always an odd number of points are summed).

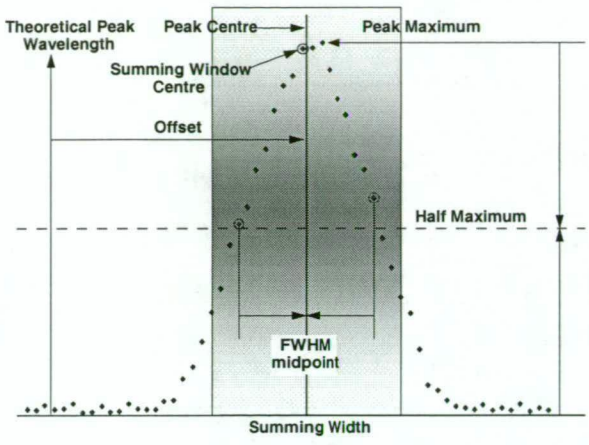

Figure 4-9. Offset determination

Initially only one offset value was used for each profile, viz. the mean of the four P_1-line offsets. It was later considered that several factors may influence the relative position of each peak, such as any non-linear effects in the mechanical scanning mechanism (deviations in the pitch of the lead screw, or stepper motor errors) and different intensities of the Λ-doubled components, which would yield an asymmetric peak. There is some evidence for this in the high-resolution echelle spectra of Osterbrock *et al.* (1996). Offsets for each P_1-branch line were therefore calculated separately and the mean value used for background and auroral emissions.

4.3.3.1. Observed Offsets in 1990

A histogram of the offset difference for each OH(6-2) P-branch line from the mean, for the full 1990 data set is shown in Figure 4-10. The mean differences are +0.0035 nm, -0.0003 nm, +0.0006 nm and -0.0039 nm for $P_1(2)$, $P_1(3)$, $P_1(4)$ and $P_1(5)$ respectively (all within one data point of the mean for 0.005nm step size).

Offset distribution for $P_1(2)$ is centred slightly higher that the mean value and broader on the high wavelength side, consistent with the location of $Q_1(5)$. The two Λ-doubled components of $Q_1(5)$ lie 0.0034 nm below and 0.1009 nm above the mean $P_1(2)$ wavelength and contribute about 2.1% (at 220K) to the measured $P_1(2)$ intensity.

The histogram for $P_1(3)$ shows a reasonably narrow and symmetrical distribution about the mean offset. Underlying $^{Q}R_{12}(2\&3)$ satellite lines and OH(5-1)$P_1(12)$

contribute about 1.3% in total but lie on either side of the $P_1(3)$ mean and does not detectably influence the offset.

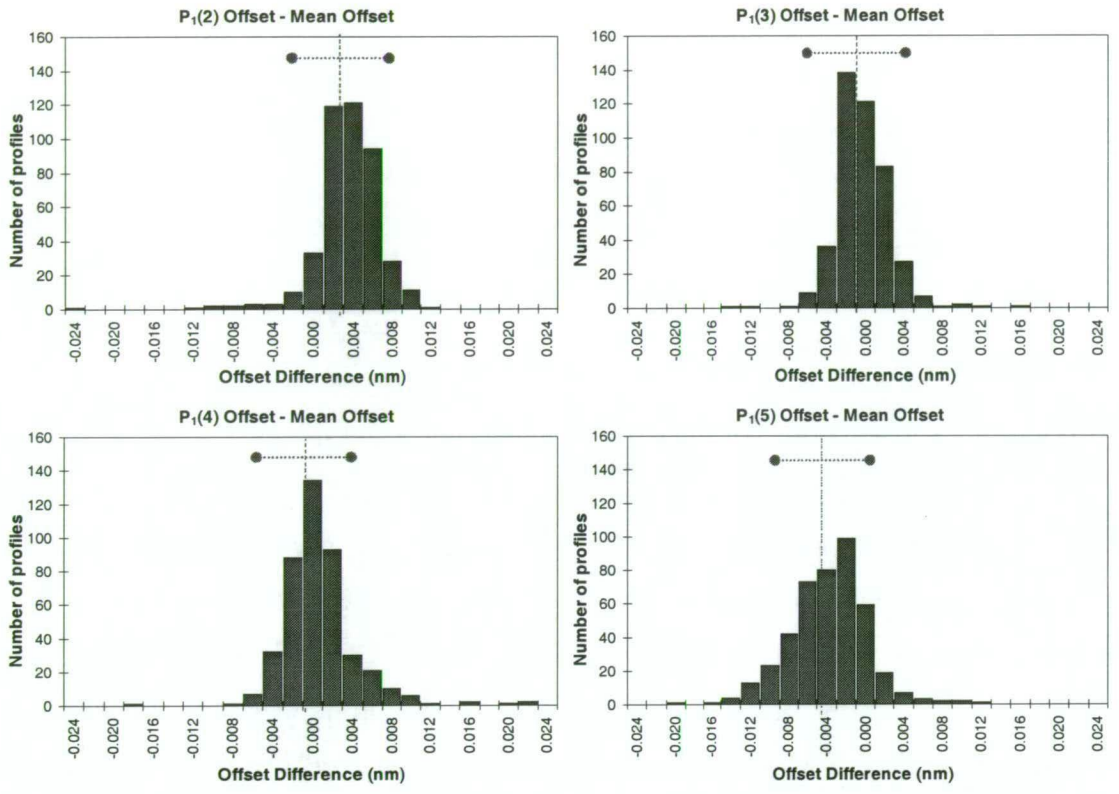

Figure 4-10. Histograms of the offset difference for each OH(6-2) P_1-branch line from the mean offset, for all 1990 data (429 profiles). Wavelength step size for these spectra is 0.005 nm (marked as dots). Mean values are plotted as dashed lines.

$P_1(4)$ distribution is also centred close to the mean offset but extends asymmetrically on the high wavelength side. This is consistent with a second order N_2^+ 1NG(1-2) band influence. Restricting the data set to spectra recorded during low auroral activity supports this conclusion as the offset distribution becomes more symmetrical.

$P_1(5)$ shows the broadest range of offset difference, suffering from the poorest signal to noise and influenced on each side by components of the N_2^+ 1NG(0-1) band in second order. It is also apparent that this offset is centred well below the mean (on average by one wavelength step). This is consistent with an influence from the Λ-doubled components of OH(5-1) $P_1(13)$ at λ850.086 nm and λ850.253 nm (at 0.399 and 0.231 nm below $P_1(5)$ respectively) identified in the high-resolution spectra of Osterbrock *et. al.* (1996).

Figure 4-11 shows the day-to-day variation in mean offset determined for the four P_1-branch lines. An overall trend toward increased wavelength is evident over the year, possibly due to a systematic re-positioning error or drift in optical alignment. Short-term variation may be due to temperature and pressure changes on the instrument.

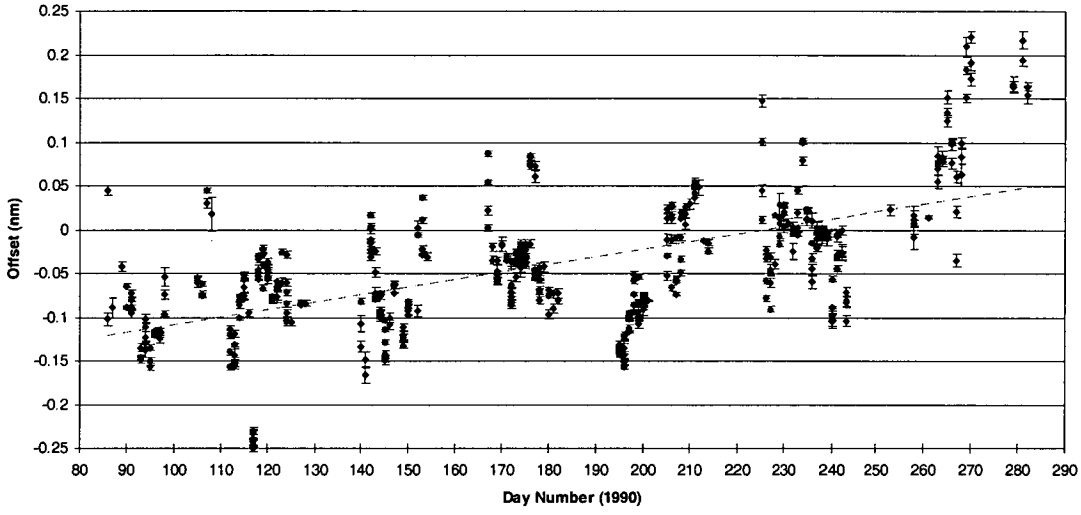

Figure 4-11. Variation in mean offsets during 1990.

4.3.3.2. Refractive Index changes.

Wavelength shift due to refractive index changes (n) of the air within the spectrometer can be calculated from Allen (1963), for air at pressure P (mmHg), temperature T (°C) and zero water vapour pressure via

$$n_{T,P} = (n_0\text{-}1)\frac{P(1+(1.049 - 0.0157T).10^6.P)}{720.883(1+0.003661T)} \qquad \textit{Equation 4-4}$$

where n_0 is the refractive index at temperature T =15°C and pressure P =760 mmHg (1013.25 HPa). The value of n_0 -1 in dry air at wavelength λ can be computed via the Cauchy formula in the CRC Handbook of Chemistry and Physics (1987) viz;

$$(n_0\text{-}1).10^7 = 2726.43 + \frac{12.288}{\lambda^2.10^{-8}} + \frac{0.3555}{\lambda^4.10^{-16}}. \qquad \textit{Equation 4-5}$$

For wavelengths in the OH(6-2) region, say λ840 nm, n_0 -1 $\approx$ 2.745x10^{-4}. Atmospheric pressure records show variations between 900 and 1015 hPa recorded from an AWS system at Davis. Temperature regulation in the old Davis lab in 1990 was not as good as in the new lab (18°C ± a few degrees) For the purpose of the calculation we can use say 10-30° as extreme values.

From the grating equation the diffraction pattern generated at any point is dependant on the optical path difference, $d\sin\theta$ between adjacent grooves. In a medium of refractive index n, the path difference becomes $n.d\sin\theta$, and for a small change in refractive index δn the grating equation becomes

$$m(\lambda+\delta\lambda) = (n+\delta n).2d\sin\theta\cos\phi \qquad \textit{Equation 4-6}$$

Figure 4-12 plots the change in wavelength (from STP: 15°C, 1013.25hPa) versus pressure for several values of temperature with the grating fixed to select λ840 nm. Slopes yield wavelengths shifts of 2.28×10^{-4} nm/hPa and -7.90×10^{-4} nm/°C at STP.

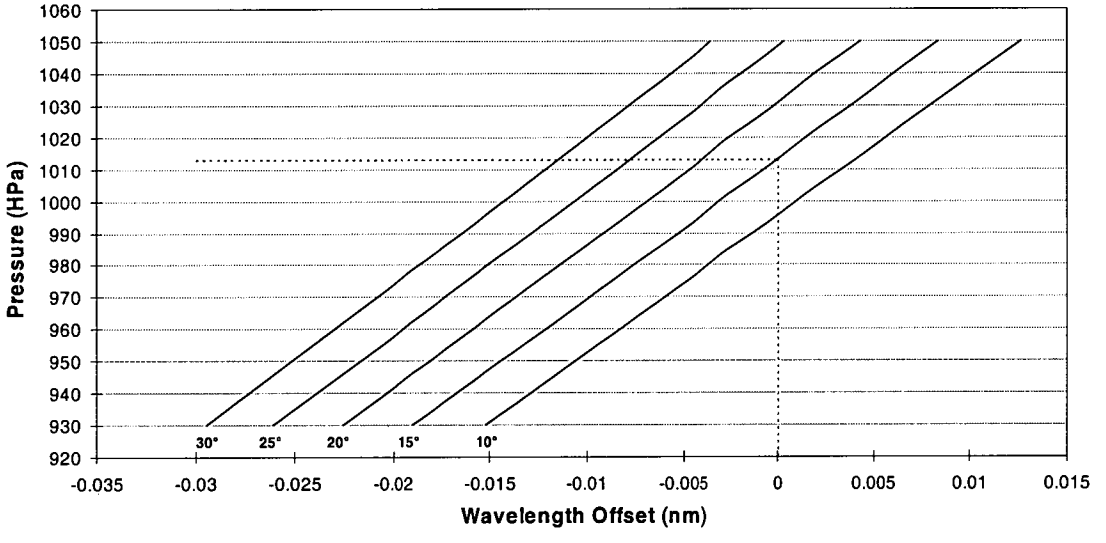

Figure 4-12. Isotherms of the change in wavelength versus pressure as a result of the change in refractive index at λ840 nm.

If, for example, the lab temperature increased by 5°C and the pressure dropped by 30 HPa over a period of time a net offset shift of +0.011 nm would be expected (about 2 sample points). This is an order of magnitude smaller than observed offset variation and implies that re-positioning (lead screw) errors are much greater.

4.3.4. Dark Count Measurement and Estimations

Backgrounds for each line are calculated separately in this analysis, thus it is only necessary to remove an estimate of the dark count so that the spectral response correction is *not* applied to it. Measurements of the dark count rate were only made intermittently in 1990 as no correction for spectral response was made in previous work with this instrument (Williams (1996), Hobbs *et al.* (1996)). In order that an accurate response correction is made for spectra not accompanied by a dark count measurement, an alternative estimate was calculated as a percentage of the measured background.

This percentage was determined from those spectra in the principle data set with accompanying dark count measurements. 39 of the 104 spectra in the principle data set had a measured dark count. A mean dark count of 40.7±16.1 counts/sec, was obtained from these measurements. The average count rate in the interval λ840.425-840.875 nm was chosen as a good background in each spectrum (referred to as background region 1). From the 39 spectra, a mean background of 50.4±16 counts/sec was obtained, thus 80±9% of the selected background region is due to dark counts. This value was chosen as a dark count estimate for all 1990 spectra.

Figure 4-13 plots the variation in background region 1 over 1990 for the principal and extended data sets. A suggestion of a slight decrease in the count rate during the winter months is possibly due to lower ambient temperatures, thus more efficient cooling of the photomultiplier. Clearly some backgrounds are influenced by twilight or moon contamination.

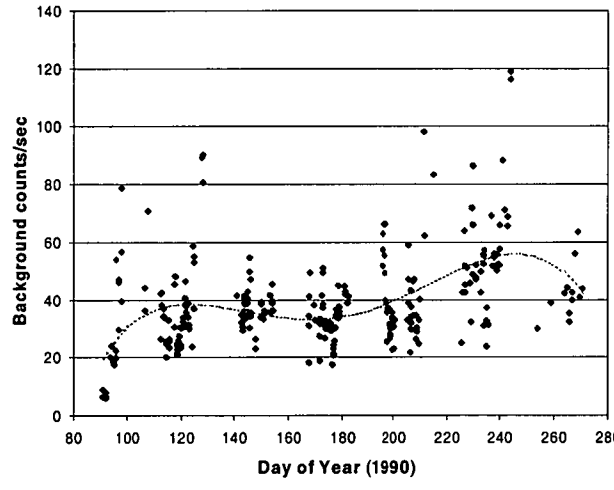

Figure 4-13. Variation in background for the principal (104 points in red) and extended (277 points in blue) data sets in 1990. Polynomial fit is to the extended set.

Figure 4-14 uses the entire data set (429 spectra) to show the effect on background of solar altitude (with limits on moon and auroral influence) and lunar altitude (with limits on solar and auroral influence). Selection criteria for sun and moon placed on the principal data set are derived from these.

No statistically significant auroral or cloud type (clear, patchy or overcast) influence was found on the background (with appropriate selection against moon and sun). This is expected, as the selected region has little auroral contamination, and the stellar background and continuum emissions (mainly $NO + O + M \rightarrow NO_2 + hv$) contribute only a small fraction (<0.5 R/A or ~1 count/sec, Chamberlain, 1961) to the measured counts. A small increase in counts was noted as a function of time from the start of a nightly observing session. This is believed due to a photomultiplier 'warm-up' effect as the shutter was closed and the EHT powered down during the

day, so the Peltier coolers were able to cool more efficiently. Minimum dark counts were therefore recorded during the first few spectra.

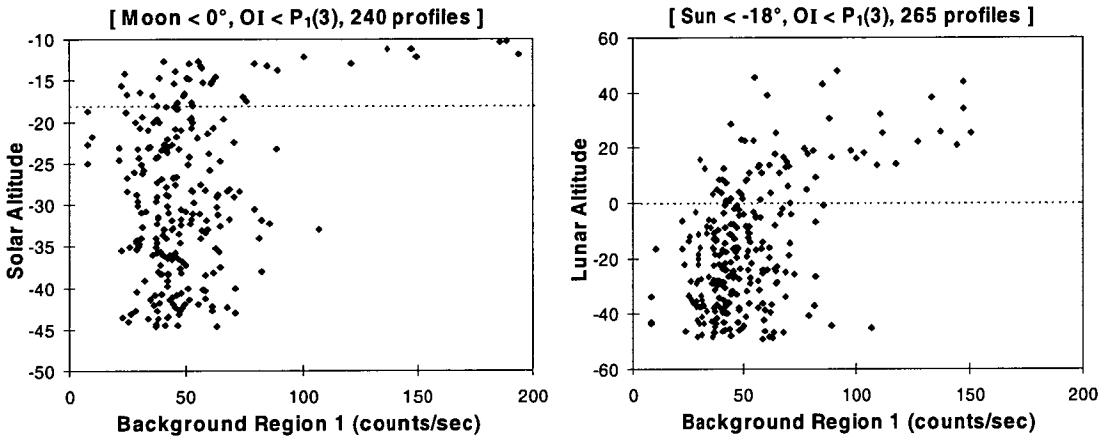

Figure 4-14. Left Panel: Background versus solar altitude for the full data set (429 profiles) with criteria set to limit moon and auroral influences (240 spectra). Right Panel: Background versus lunar altitude for the full data set with criteria set to limit sun and auroral influences (265 spectra). Dashed lines show selection criteria for the principal data set.

This method of dark estimation was not used for subsequent years, as regular dark samples were made from 1994 and they became an automated part of the fast scan-segment routine cycle from the end of 1996. Dark counts were reduced to about 8 counts/sec in 1995 with the instrument upgrade and pulse-amp discriminator change. On 22-Jul-96 (D204) an external air duct was fitted to the PMT cooler intake to improve cooling efficiency (air at ~ -20°C reduced the work required by the peltier devices) and further reduced dark counts to about 4 counts/sec [Figure 4-15].

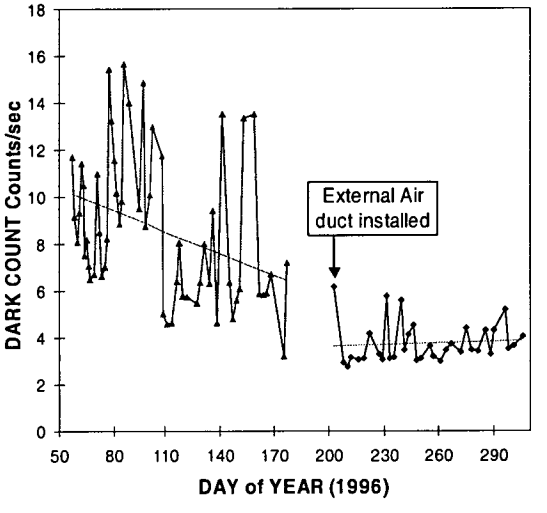

Figure 4-15. Dark counts in 1996 and the effect of the external air duct

4.3.5. Response Corrections

Instrument and Perspex response corrections have been derived in chapter 3.6. As stated previously they are referenced to the secondary calibration lamp and the Dec-1996 calibration of the Eather LBS (containing a small scattering error) in this study. Corrections are applied after subtraction of a dark count by means of quadratic

curves fit to these calibrations across the λ800-860 nm region. The same correction is applied to all spectra. The correction increases temperatures derived by an average 6.5 K and are shown for each ratio in Table 4-6. An uncertainty of 1.5 K in the correction is calculated from the variability in the calibration scans. These are listed in Table 4-7.

4.3.6. Backgrounds

Five background regions (marked in Figure 4-1 and listed in Table 4-2) all have minor contaminations. The background for each line was estimated as a fraction of nearby background regions [Table 4-3]. Fractions were chosen by examination of the average of principal spectra. Uncertainty in the background for all lines in an individual spectrum, e_b, is estimated to be $\sigma/\sqrt{n}$, where σ is the standard deviation of the n sample points in back_ 1.

Region	Start λ	Stop λ
Back_1	840.43	840.88
Back_2	842.06	842.15
Back_3	843.80	844.11
Back_4	847.81	848.07
Back_5	848.70	848.88

Table 4-2. Background regions

Region	Darks Estimate
Back_P_1(2)	(0.8837*Back_1)
Back_P_1(3)	(0.8851*Back_1+0.8859*Back_3)/2
Back_P_1(4)	(0.8447*Back_3+0.9089*Back_4)/2
Back_P_1(5)	(0.8943*Back_4)

Table 4-3. P-branch line background estimates

Fractional components of the backgrounds were removed in subsequent analysis by appropriate selection of the background intervals to balance the mean backgrounds derived from the averaged 1996 principle spectra. Intervals appropriate for each P-branch line are listed in Table 4-4.

Table 4-4. P-branch line background regions for subsequent years

Region	Background Estimate Region
Back_P_1(2)	840.55–840.85
Back_P_1(4)	(843.8–843.9+848.14–848.24+847.8–847.9)/3
Back_P_1(5)	847.9 – 848.45

4.3.7. Auroral Correction

Theoretical N_2 and N_2^+ spectra (see section 4.2.2) were calculated for a range of emission temperatures, convolved with the instrument function, corrected for instrument response, summed and fitted to the most 'aurorally active' average spectrum from Figure 4-2. A temperature of 500 K for the auroral N_2 emission region gave the best fit. A comparison of theoretical and measured auroral contributions in the vicinity of the major lines is shown in Figure 4-16.

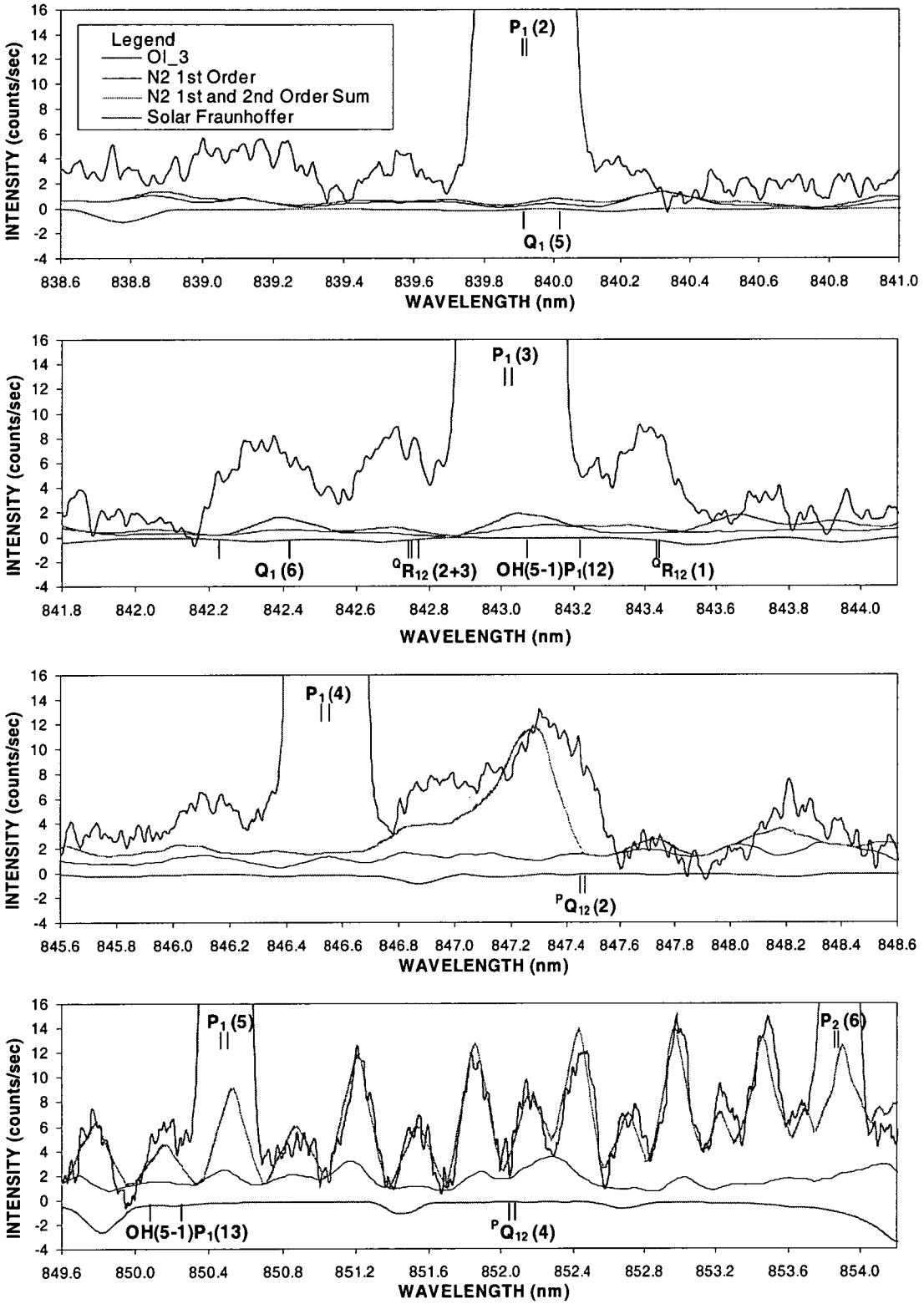

Figure 4-16. The most aurorally active spectrum from Figure 4-2, for which OI/P_1(3) average = 1.15, and showing the theoretical first and second order N_2 band auroral contamination fitted to the data and the theoretical auroral contamination for first order only. A solar Fraunhofer spectrum, arbitrarily scaled to fit the data, is plotted below the zero line. This contamination is from scattered moonlight. (Note that the Fraunhofer spectrum in Greet et al. (1998) is incorrectly offset 0.12 nm high, but is corrected here, (as advised by Dr. Tom Slanger, private comm. via. Bob Lowe)).

The combined theoretical auroral spectrum† was used to relate the sum under three N_2 auroral features, at λ851.9, λ852.4 and λ853.0 nm, to auroral contributions under the major P_1-branch lines. The sum of these three auroral features in each spectrum is used to calculate an auroral contribution, a_k, to subtract from the OH(6-2) $P_1(k)$ intensity measurements.

In Table 4-6, column A, the average auroral corrections for individual ratios are listed. Allowing for auroral corrections reduces the average temperature by 2 K. Use of an appropriate order-separating filter would obviate the need to allow for N_2^+ 1NG contamination. Estimated corrections for direct N_2 1PG and N_2^+ Meinel band auroral contamination, scaled to an OI/P_1(3) ratio of 1.0, are listed in column B of Table 4-6. The principal data set has an average OI/P_1(3) ratio of 0.28. Auroral intensity of the OI line is only weakly correlated with N_2 auroral emissions (sample time lag, altitude difference and OI emissions produced through dissociative excitation of O_2 all contribute), but it is the most intense auroral feature in the OH(6-2) spectral range.

4.3.8. Optimised Width

Emission line intensity was determined by summing counts over N wavelength increments centred on the P_1-branch line, and subtracting a background, b_k, with error e_b (which includes a contribution of photomultiplier dark count) and an estimated auroral contribution, a_k. Uncertainty in the auroral correction was estimated as half the auroral contamination of each line. Increasing the number of wavelength increments summed changes the relative error in the intensity measurements, which is calculated as

$$RE(k) = \frac{\sqrt{\sum_{i=1}^{N} C_i + (N.e_b)^2 + 0.25a_k^2}}{\sum_{i=1}^{N} (C_i - b_k) - a_k} \qquad \textit{Equation 4-7}$$

where C_i is the total number of counts at sample i. The value of N for which the relative error is minimized is termed the optimised width. The value varies for each line in the spectrum and with instrument bandpass, but for these data 51 points (=0.255nm) is a reasonable value for all lines with a 0.15 nm instrument bandpass.

† The instrument spectral response (fit over the λ800-860 nm region) was incorrectly applied to the second order N_2^+ 1NG and N_2 VK bands to generate this spectrum, hence the best fit to the aurorally active spectrum at 500K is too high. Later determinations indicate this is of the order of 250-300K. A value of 300K is used for subsequent analyses.

4.3.9. *Λ-doubling factors*

To make an accurate temperature estimate, each component of the Λ-doubled lines has to be summed over the same width. Because Λ-doubling is not resolved in these spectra, it was chosen to sum over a fixed width (of 0.255 nm) for all lines and allow for Λ-doubling using a factor calculated assuming a triangular instrument function† of 0.15 nm fwhm. The Λ-doubling correction factors for each line are listed in Table 4-5. They represent the fraction of an equivalent line with zero Λ-doubling contained within the summing width. Resulting temperature corrections for each ratio are listed in Table 4-6, column C. If Λ-doubling were not accounted for in the analysis, measured temperatures would decrease by 2 K.

Line	Λ-doubling factor
$P_1(2)$	0.9988
$P_1(3)$	0.9959
$P_1(4)$	0.9894
$P_1(5)$	0.9789

Table 4-5. Λ-doubling factors for a triangular 0.15nm instrument function

4.3.10. *$Q_1(5)$ correction*

The percentage contribution of $Q_1(5)$ to $P_1(2)$ varies with temperature. Theoretically, assuming that $Q_1(5)$ is thermalised, the ratio of $Q_1(5)$ intensity to $P_1(2)$ intensity amounts to 0.6% at 150 K, 1.7% at 200 K and 3.1% at 250 K (with Turnbull and Lowe (1989) transition probabilities). Pendleton *et al.* (1993) shows that the upper state of $Q_1(5)$ is slightly unthermalised (the deviation from thermalisation would not exceed 10%). This would make less than a 1 K temperature variation. When using the $P_1(2)$ line to calculate rotational temperature, contamination by $Q_1(5)$ can be allowed for. The magnitude of $Q_1(5)$ with respect to $P_1(2)$ is calculated by iteration of the final temperature. Correction for $Q_1(5)$ increases the derived temperature by the amounts shown in Table 4-6, column D. Average temperature is increased by 2.3 K.

4.3.11. *Transition Probability Sets*

Three sets of transition probabilities are published in the literature. Those of Turnbull and Lowe (1989) are used in this study. Columns F and G in Table 4-6 show how temperatures would have differed had the transition probabilities of Mies (1974) and

† Subsequent analyses used factors determined by the empirical fit method as discussed in section 3.4.2. These factors produce temperatures <0.2K warmer than the empirical fit method.

Langhoff *et al.* (1986) been used. Both are substantially lower (7 and 12 K respectively). An experimental investigation of transition probability ratios that show closest agreement to those of Langhoff *et al.* (1986) is discussed in chapter 5. Langhoff *et al.* (1986) values are used for subsequent analyses.

4.4. Temperature and Uncertainty Results

Rotational temperatures are calculated from ratios of any two of the measured P_1-branch lines after applying all corrections discussed in section 4.3. The error due to counting statistics in the temperature derived from an individual ratio of lines C_n and C_m is determined, taking into account relative line intensities, the sensitivity of each particular ratio to temperatures in the emission region, uncertainties in background estimates and contamination by minor emissions according to

$$T_{n,m} \pm \delta T = \frac{E_m - E_n}{k\, ln\left(\frac{C_n}{C_m} \pm \left(\frac{C_n}{C_m}\right)\sqrt{RE(n)^2 + RE(m)^2}\right).\left(\frac{A_m}{A_n}\right).\left(\frac{2J_m+1}{2J_n+1}\right)} \qquad \textit{Equation 4-8}$$

where $E_{m,n}$ are the energy term values, $A_{m,n}$ are transition probabilities, $J_{m,n}$ are rotational quantum numbers, k is Boltzmanns constant and the relative errors, *RE* for each line are from Equation 4-7.

Average temperatures and estimated uncertainties were derived for each of the six possible ratios. This approach was adopted to quantify the accuracy possible from individual line ratios and to determine if significant contamination of line intensities remains. If a line intensity is significantly mis-estimated, average temperatures derived from ratios using that line will be systematically different from temperatures derived from other ratios. For Davis 1990 data this enables estimation of the average contribution of the unthermalized OH(5-1)$P_1(12)$ emission to the measured $P_1(3)$ intensity.

Mean temperatures are also calculated for each spectrum. These are weighted averages of the temperatures derived from the $P_1(2)/P_1(4)$, $P_1(2)/P_1(5)$ and $P_1(4)/P_1(5)$ ratios, described henceforth as the weighted temperature.

4.4.1. Principle Data Set

Table 4-6 quantifies the effect on the temperature calculation for the principle data set of aurora, Λ-doubling, the $Q_1(5)$ line, instrument response and different transition probability sets, as described in section 4.3.

104 spectra	A	B	C	D	E	F	G
ratio	1st and 2nd order aurora	1st order aurora	Λ-doubling	$Q_1(5)$	Instrument response	Mies	Langhoff
$P_1(2)/P_1(3)$	-0.9K	-1.4K	+1.5K	+9.9K	+6.0K	-11.1K	-19.1K
$P_1(2)/P_1(4)$	-0.8K	-1.6K	+2.0K	+3.6K	+5.9K	-7.9K	-14.3K
$P_1(2)/P_1(5)$	-2.8K	-3.6K	+2.4K	+2.1K	+6.6K	-6.8K	-11.9K
$P_1(3)/P_1(4)$	-0.7K	-1.8K	+2.3k		+5.8K	-5.9K	-11.3K
$P_1(3)/P_1(5)$	-3.3K	-3.9K	+2.6K		+6.8K	-5.6K	-9.9K
$P_1(4)/P_1(5)$	-5.4K	-6.1K	+2.9K		+7.6K	-5.3K	-8.8K
Weighted average	-2.4K	-3.2K	+2.3K	+2.3K	+6.5K	-6.9K	-12.3K

Table 4-6. Temperature corrections for individual ratios and the weighted temperature correction (see text) for the principal data set from: (A) total auroral correction for principal data set; (B) auroral corrections for first-order contaminations, scaled to OI/P1 (3) = 1.0; (C) Λ-doubling; (D) Q_1 (5) under P_1 (2); (E) Instrument response correction (F) Mies (1974) and (G) Langhoff et al. (1986) transition probabilities.

Mean temperature for each of the ratios for the principal data set (104 spectra) is listed in Table 4-7, column A. The average weighted temperature is 221K. Mean temperatures for individual ratios range from 218 to 231 K with the mean temperature for $P_1(2)/P_1(3)$ being some 8K higher than for any other ratio. The standard deviation of the weighted temperatures is 10K and the standard error is 1K. The standard deviation and standard error for each of the ratios are listed in Table 4-7, columns B and C.

An average of the relative counting error for each ratio, $\sqrt{\mathrm{RE}(n)^2 + \mathrm{RE}(m)^2}$, converted to a temperature error via Equation 4-8, is listed in Table 4-7, column D. Weighting factors for the contribution of $P_1(2)/P_1(4)$, $P_1(2)/P_1(5)$ and $P_1(4)/P_1(5)$ temperatures to the weighted temperature are calculated inversely as the square of these temperature errors, determined separately for each spectrum. Average weighting factors are 0.32, 0.57 and 0.12, respectively. Average counting error for the temperatures of the principal spectra is 4 K. Errors calculated in this manner are lower limits for the error of each ratio. There is at least that degree of uncertainty inherent in the photons counted, the background estimate and possible auroral contamination.

104 spectra	A	B	C	D	E	F	G	H
ratio	Average temperature	Standard deviation	Standard error in mean	Counting error	SD Sampling Error	Instrument correction	Individual spectra error	Average temp error
$P_1(2)/P_1(3)$	230.7K	18.2K	1.8K	12.8K	11.0K	3.0K	17.1K	3.6K
$P_1(2)/P_1(4)$	222.5K	11.2K	1.1K	5.3K	7.7K	2.0K	9.6K	2.5K
$P_1(2)/P_1(5)$	220.8K	10.3K	1.0K	4.0K	6.4K	1.3K	7.7K	2.3K
$P_1(3)/P_1(4)$	217.6K	11.0K	1.1K	7.8K	8.6K	1.4K	11.7K	2.0K
$P_1(3)/P_1(5)$	218.1K	9.8K	1.0K	4.8K	7.5K	1.0K	8.9K	2.3K
$P_1(4)/P_1(5)$	218.9K	12.1K	1.2K	9.0K	8.7K	1.0K	12.6K	3.2K
Weighted average	221.0K	10.3K	1.0K	3.7K	7.1K	1.5K	8.1K	2.3K

Table 4-7. Average temperatures and uncertainty estimates for individual ratios and the weighted temperature (see text) for the principal data set. (A) average temperatures; (B) standard deviation; (C) standard error in the mean; (D) average 'counting error' for individual spectra; (E) standard deviation of `sampling errors'; (G) instrument correction uncertainty; (H) average error in individual spectra; (I) estimated error in the average temperatures

4.4.2. Sampling Errors

Counting errors do not include any estimate for variation in the intensity or temperature of the emitting region during the acquisition time of almost 1 hour. Coincident spectrometer and 6-channel photometric $P_1(2)$ observations existed for 131 spectra of the expanded data set. Assuming that the emitting region temperature was a constant 220 K (thus the variation was of photochemical origin and all lines changed the same way), a variation in the photometer measured $P_1(2)$ intensity at the time the spectrometer scanned the major lines can be converted to an equivalent temperature error in the appropriate ratios. The standard deviation of the temperature errors for each ratio is listed in Table 4-7, column E. By this method, an average error of 7.1 K can be associated with the time taken to acquire the spectra collected at Davis in 1990. If emission intensity decreases on average over the sample time, a cooler temperature is obtained, and vice versa. The mean temperature difference for the 131 spectra was found to be −1.1K as on average intensities were found to decrease over the night.

It has been reported that OH intensity decreases after sunset, although this effect varies between southern and northern hemispheres (Lowe *et al.*, 1996). It is thought to be at least partially linked to tidal variations, in which case significant latitudinal

variation would be expected. The average temperature difference for those spectra recorded prior to local midnight was –1.3 K, and for those after local midnight was –0.4K.

4.4.3. Error in the average temperature

An uncertainty in the instrument response correction is calculated from the repeatability uncertainty in the Eather LBS and secondary lamp calibration scans measured in 1996 and 1990[†]. These are converted to temperature errors and listed in Table 4-7, column F. An uncertainty of 1.5 K in the weighted temperature is associated with instrument calibration.

Average error in *individual spectra* is estimated as the square root of the sum of the squares of the independent error estimates:

- counting errors (Table 4-7, column D),
- sampling errors (Table 4-7, column E) and
- uncertainty in the instrument correction (Table 4-7, column F).

Uncertainties in the auroral corrections are insignificant for individual spectra. The average error for individual spectra is 8.1 K for the weighted temperature and is listed for all ratios in Table 4-7, column G.

Uncertainty in the *average temperatures* is estimated as the square root of the sum of the squares of:

- the standard error in the mean of the temperatures derived from the spectra (Table 4-7, column C),
- the uncertainty in the instrument correction (Table 4-7, column F),
- an estimated auroral correction uncertainty (half the average correction; Table 2, column D) and
- an estimate of the sampling error (taken as the whole mean difference, 1.1K).

For the average of the weighted temperatures this amounts to 2.3 K, and is listed for all ratios in Table 4-7, column H.

[†] Re-evaluation of the relative calibration uncertainties as discussed in section 3.6 yields slightly greater values when all secondary calibration scans made in 1990 are included. The weighted temperature uncertainty becomes 2.2K

4.4.4. Comparison of temperatures from each ratio

Average temperatures of the individual ratios (Table 4-7, column A) provide confirmation that $P_1(3)$ is overestimated. The $P_1(2)/P_1(3)$ average temperature is significantly high. Average $P_1(3)/P_1(4)$ and $P_1(3)/P_1(5)$ temperatures are low, but not significantly so. A comparison of the average $P_1(2)/P/(3)$ temperature with the independently derived average weighted temperature is consistent with a minor emission feature, believed to be $OH(5\text{-}1)P_1(12)$ (Osterbrock *et al.* (1997)), of magnitude 1.8% under the $P_1(3)$ line.

Discrepancy in the $P_1(2)/P_1(3)$ ratio mean temperature is not consistent with non-thermalisation of the $Q_1(5)$ emission, blended with $P_1(2)$. Non-thermalisation of the $Q_1(5)$ emission would result in a lower average temperature for the $P_1(2)/P_1(3)$ ratio. Similarly, non-thermalisation of $Q_1(5)$ would imply a low $P_1(2)/P_1(4)$ mean temperature. This is not supported by the results. $Q_1(5)$ thermalisation is consistent with the observation that $Q_1(4)$ is thermalised to the limit of the intensity uncertainty of these spectra (Table 4-1). However, $Q_1(6)$ is clearly not thermalised according to these measurements. Evidence that an Argon auroral emission contributes to the region under $Q_1(6)$ is presented in the discussion at the end of this chapter (section 4.5.2), thus any non-thermalisation is likely to be considerably less than indicated in Table 4-1.

Mean temperatures derived from ratios that include the $P_1(5)$ line provide no evidence for non-thermalisation of this line. Non-thermalisation of $P_1(5)$ would be reflected in high average temperatures for ratios involving this line. This confirms the results of Pendleton *et al.* (1993).

4.4.5. Expanded Data set

Selection criteria for the principal data set (104 spectra) limits the weighted counting error to 7 K and the weighted standard deviation (a weighted comparison of the $P_1(2)/P_1(4)$, $P_1(2)/P_1(5)$ and $P_1(4)/P_1(5)$ ratios to the weighted temperature) to 10K. The expanded data set, 277 spectra, maintains these criteria, but relaxes the auroral limitation criteria to $OI/P_1(3)<2.0$. Temperatures and uncertainties for the expanded data set are listed in Table 4-8. The average weighted temperature is 221K. The average $OI/P_1(3)$ ratio is 0.49. Comparing the average temperature of the $P_1(2)/P_1(3)$ ratio with the average weighted temperature, the magnitude of the contamination

under $P_1(3)$ is 1.1% (cf. 1.8% for the principal data set). The conclusions drawn from the principal data set are consistent with the expanded data set.

277 spectra	A	B	C	D	E	F	G
ratio	Average temperature	Standard deviation	Standard error in mean	Counting error	Auroral correction	Individual spectra error	Average temp error
$P_1(2)/P_1(3)$	226.7K	19.7K	1.2K	14.1K	-1.2K	18.1K	3.4K
$P_1(2)/P_1(4)$	222.4K	12.6K	0.8K	6.1K	-0.9K	10.0K	2.4K
$P_1(2)/P_1(5)$	221.0K	11.2K	0.7K	4.7K	-3.4K	8.0K	2.5K
$P_1(3)/P_1(4)$	220.1K	13.8K	0.8K	9.4K	-0.7K	12.8K	1.9K
$P_1(3)/P_1(5)$	219.6K	11.1K	0.7K	5.8K	-4.4K	9.5K	2.6K
$P_1(4)/P_1(5)$	219.7K	13.6K	0.8K	10.9K	-6.9K	14.0K	3.8K
Weighted average	221.0K	11.3K	0.7K	4.3K	-3.0K	8.4K	2.5K

Table 4-8. Average temperatures and uncertainty estimates for individual ratios and the weighted temperature (see text) for the expanded data set (see text, 277 spectra). (A) average temperatures; (B) standard deviation; (C) standard error in the mean; (D) average 'counting error' for individual spectra; (E) average auroral correction; (F) average error in individual spectra; (G) estimated error in the average temperatures

4.4.6. Seasonal Variations

Figure 4-17 shows the seasonal variation of the weighted temperatures of spectra in the expanded data set. Errors plotted are the maximum of the weighted standard deviation and the weighted average counting error. Generally, the weighted standard deviation is larger, but as this value may be fortuitously low, the weighted counting error has been set as a minimum error. Significant variability is seen in the data, as would be expected from wave and tidal activity. This variability is larger in the three mid-winter observing campaigns.

Also plotted in Figure 4-17 are CIRA 1986 model temperatures for 70°S and altitudes 86.3 km and 87.7 km (Fleming *et al.* (1990)). OH rotational temperatures from Davis are consistent with reported northern-hemisphere polar observations of an extended, warm, upper-mesosphere/mesopause winter period (Lübken and von Zahn (1991)). This is not reflected in the CIRA 1986 model (Lübken and von Zahn

(1991)). The Davis data presented are almost all confined to the winter period, although the first and last campaigns show some decrease in temperature. The mean of the weighted temperatures for the whole of the extended data set is 221.0±2.5K. Means for each new moon campaign period are given in Table 4-9.

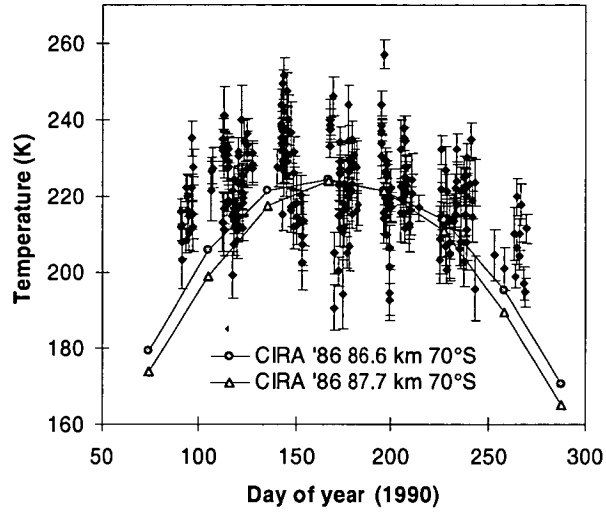

Figure 4-17. Seasonal temperature variation for the extended data set (see text) collected during 1990. Temperatures plotted are weighted temperatures for each of the 277 spectra. Error bars indicate the maximum of the weighted standard deviation and the weighted counting error (see text for definitions). CIRA model values are shown for 86.6 and 87.7 km and 70S.

DOY	n	Mean T	Std. Error
90-97	18	215.8K	1.8K
106-127	60	222.9K	1.1K
140-154	41	227.7K	1.9K
167-182	49	222.3K	1.7K
195-214	53	221.8K	1.5K
225-243	44	215.9K	1.3K
253-270	12	206.3K	2.3K

Table 4-9. The duration of each campaign, number of spectra (n), mean temperature and standard error in the mean

Given the uncertainty in the published OH(6-2) transition probabilities (cf. Turnbull and Lowe (1989); Table 4-6), which can yield temperatures up to 12 K lower than those listed here, the Davis winter temperatures are not inconsistent with the CIRA model midwinter value of 222K. For comparison, the Davis 1990 winter average temperature of 224.0±2.5 K [for months May, June and July (MJJ), a total of 161 spectra] is higher than the 86-km average temperature of 210 K, for the equivalent northern-hemisphere months of November, December and January (NDJ) from lidar and a variety of rocket techniques reported by Lübken and von Zahn (1991). NDJ averages of OH rotational temperature from Offermann and Gerndt (1990) for Oslo (60°N) of 217 K, and Myrabo (1986) for Longyearbyen (78°N) of 214 K, use Mies (1974) transition probabilities. For comparison, Davis MJJ temperatures using Mies transition probabilities are 217 K. Although these results are similar, comparisons between years are difficult because of reported positive correlations between mesospheric

temperatures and solar activity (Lübken and von Zahn (1991); Labitzke and Chanin, (1988); Sahai *et al.* (1996)) of at least 20 K between solar maximum and minimum. 1990 was a year of high solar activity, while the Longyearbyen average (Myrabo (1986)) comes from four winters, 1980-1985, which include years of low solar activity.

Williams (1996) reports 1987 Davis winter average temperatures, using the OH(8-3) emission, of 205±5K. This was obtained using Langhoff transition probabilities and no instrument response corrections were made.

Relative intensity estimates of summed OH(6-2) $P_1(2)$, $P_1(3)$, $P_1(4)$ and $P_1(5)$ lines are plotted against day of year in Figure 4-18. Only data from the principal data set are plotted. The sum of the $P_1(2)$, $P_1(3)$, $P_1(4)$ and $P_1(5)$ lines is 33% of the whole OH(6-2) band, for temperatures in the range 215-230 K. Similar to the temperature measurements, large variability is seen particularly in mid-to-late winter, suggestive of strong wave activity. There is a suggestion of a mid-winter minimum in intensity, with peaks in intensity occurring near the equinoxes. This is similar to the trend predicted by Le Texier *et al.* (1987), for the OH(5-3) band at high latitudes.

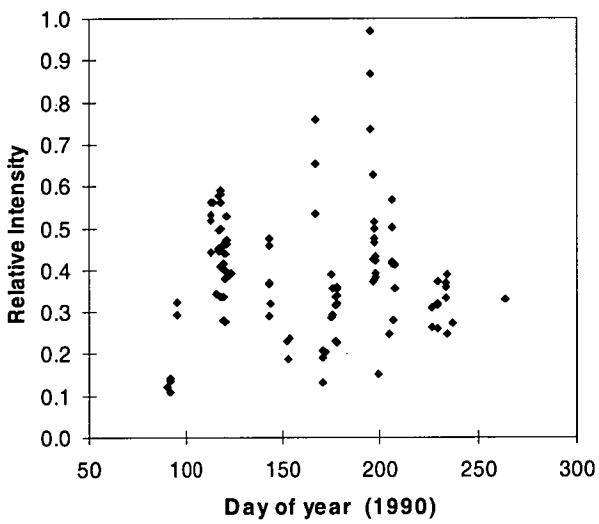

Figure 4-18. Seasonal OH(6-2) emission intensity variation for the principal data set (solar altitude < -18°, lunar altitude < 0°, no cloud, OI < P1(3) , 104 spectra) as a function of day of year, 1990.

4.4.7. Diurnal Variations

An attempt was made to determine a diurnal temperature variation. Temperatures were plotted against time and solar zenith angle, for the principal and expanded data sets, and for two- to three-week new moon campaign intervals. None of these plots, over the strictly limited hours of observations in dark skies, revealed any significant diurnal temperature variation. No attempt has been made to extract tidal, planetary or gravity- wave periodicities from these data.

Intensities for the principal data set are plotted against hours (UT) in Figure 4-19. Although the variability makes trend determinations difficult, there is a suggestion of a trend towards lower intensities through the night. A linear fit gives -1.8% per hour. A decrease is consistent with photochemical models where odd O and H are decreased at night in the absence of O_3 and H_2O photolysis [Battaner and Lopez-Moreno (1979), Moreels *et al.* (1977)]. Steady decreases have been observed in both ground based [e.g. Fiocco *et al.* (1970)] and satellite studies [e.g. Abreu and Yee (1989)], but not consistently so [e.g. Nakamura (1962), Dick (1972) and Takahashi and Batista (1981) observe a post midnight increase]. The diurnal trends are most likely influenced by tidal variations [Choi *et al.* (1998)].

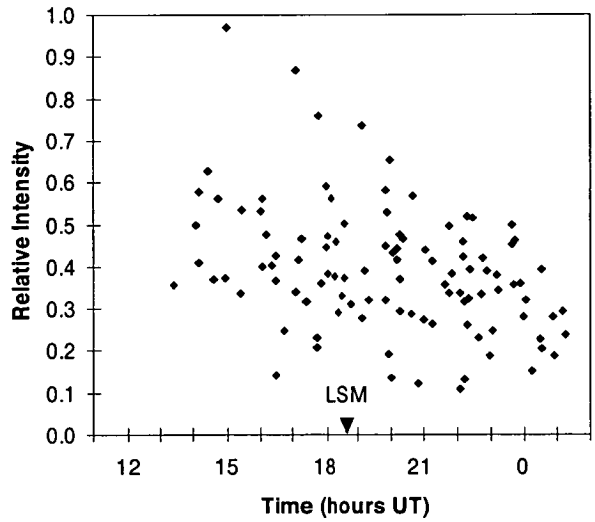

Figure 4-19. OH(6-2) emission intensity variation for the principal data set (solar alt <-18° lunar alt <0° no cloud, OI < P1(3), 104 spectra) as a function of time. The solid arrow indicates local solar midnight.

4.5. Discussion

Derivation of rotational temperatures from OH(6-2) spectra has been investigated in detail and a number of weak spectral features in the vicinity of P_1-branch lines have been noted which, if not correctly allowed for, will influence derived temperatures.

4.5.1. P_1 branch line influences

Resolution of our spectra and the technique of summing only over a 0.25 nm window centred on the line peaks, enables us to reduce the allowance necessary for $Q_1(5)$ contamination of the $P_1(2)$ line. Not all of both components of the Λ-doubled $Q_1(5)$ line fall inside the $P_1(2)$ sum window. Lower-resolution spectrometers, filter photometers and OH imaging systems will not be able to avoid most of the influence of the entire $Q_1(5)$ emission on $P_1(2)$. For such instruments, not allowing for $Q_1(5)$ influence will reduce the temperature derived from the $P_1(2)/P_1(3)$ ratio by some

10 K, $P_1(2)/P_1(4)$ by 4 K and $P_1(2)/P_1(5)$ by 3 K, for a rotational temperature of the order of 220K.

Centre of the $Q_1(6)$ line is some 0.70nm below the $P_1(3)$ line, but its large Λ-doubling (0.19 nm) needs to be considered. It is also important to avoid the regions of these features for background determinations. If all identified features in the vicinity of the $P_1(3)$ line were incorporated in the intensity of this line, considerable error would result. At 220 K the $P_1(3)$ intensity would be overestimated by some 7%, including an estimated average contribution from OH(5-1) $P_1(12)$ of 1.5%, resulting in an increase in the $P_1(2)/P_1(3)$ derived temperature by 41 K, and a reduction in the $P_1(3)/P_1(4)$ and $P_1(3)/P_1(5)$ temperatures by some 22 and 10 K, respectively.

The influence of $Q_1(5)$ on $P_1(2)$ and $Q_1(6)$, $^QR_{12}$ (1, 2, and 3) and OH(5-1)$P_1(12)$, on $P_1(3)$ alter the $P_1(2)/P_1(3)$ ratio in opposite senses, but in combination they result in a 2 K increase. Un-thermalised OH(5-1)$P_1(12)$ contamination makes the OH(6-2) $P_1(3)$ line unsuitable for absolute temperature measurements.

Solar Fraunhofer absorption features lie 0.68 nm below $P_1(5)$, 1.14 nm below $P_1(2)$ and 0.35 nm above $P_1(4)$ which may also influence temperatures derived from lower resolution instruments for data contaminated by moon or twilight.

Average temperatures of the $P_1(5)$ ratios provide evidence that this line is thermalised. There is no evidence that $Q_1(5)$ is not thermalised, but $Q_1(6)$ is measured significantly brighter (5 ± 1 times) than its theoretical thermalised intensity.

4.5.2. Argon Aurora

Later investigation has revealed an interesting source for the apparently large $Q_1(6)$ intensity: Argon aurora. This section is included in a rapid communication submission to the Journal of Atmospheric and Solar-Terrestrial Physics, entitled "Argon auroral emissions", Burns *et al.* (2001).

Argon makes up 0.9% of the atmosphere by volume at the Earth's surface. Only in situ measurements by mass spectrometers have been able to provide direct evidence of argon abundance throughout the atmosphere. In the altitude region 90 to 150 km the argon percentage rapidly drops to below 0.13% due to a combination of diffusive separation above the turbopause and an increase in the fraction of atomic oxygen

resulting from photo-dissociation of molecular oxygen. Auroral electrons can excite atmospheric species in this altitude range. The higher the electron energy, the lower the atmospheric region principally excited, and the greater the relative intensity of any argon emission.

An emission feature at λ842.4 nm, near the OH(6-2) $Q_1(6)$ line [see Figure 4-2], has been noted with an intensity several times brighter than expected compared with neighbouring OH features and N_2 auroral contributions [see Figure 4-16]. During strong aurora this feature may become as bright as the nearby $P_1(3)$ hydroxyl line. This auroral emission is identified as the λ842.46 nm line of argon. The argon identification was confirmed by the presence of a second argon line at λ840.82 nm. These lines are only significant at times of energetic electron precipitation and are not readily apparent in Davis spectra obtained during moderate auroral activity, thus they are not dominated by light pollution.

Figure 4-20(a) shows the sum of forty-five spectra, each consisting of five scans, collected during 1996 when riometer measurements show more than 1dB of absorption of 30 MHz galactic radiation, thus ensuring energetic auroral precipitation. Co-adding is necessary to reduce noise and background variability, which results from the combined influences of scanning and rapid fluctuations in intense aurora. Absolute intensities are calculated by comparison with the $P_1(3)$ hydroxyl line on the assumption that it constitutes 11% of the total OH(6-2) band intensity of 1.7kR [see section 3.6.6, Krassovsky *et al.* (1962)]. The intensity scale is truncated at 80R in Figure 4-20(a) but $P_1(3)$ peaks at approximately 180R and the atomic oxygen multiplet at λ844.6 nm is approximately 730R.

Auroral N_2^+ Meinel (mainly 4-2) and N_2 1PG(mainly 3-2) bands are fitted by a synthetic spectrum at 300 K (blue line) [see Figure 4-3, Gattinger and Vallance-Jones (1974)]. Hydroxyl features are fitted separately (red line), which include Rowland ghosts, satellite lines and the unthermalised OH(5-1) features marked (green lines) convolved with a 0.15 nm instrument function. The argon lines at λ840.82 and λ842.46nm are readily apparent, with intensities of approximately 11R and 17R amounting to 1.5% and 2.3% of the atomic oxygen multiplet intensity respectively.

Maximum λ842.46 nm argon intensity observed in an individual scan was 290 R. Ten individual spectra obtained when the argon line intensity at λ842.46 nm exceeds

100 R are co-added in Figure 4-20(b). An average increase in auroral activity during acquisition of these scans is apparent from the divergence from the synthetic N_2 spectra. Argon intensity in this combined spectrum (200 R) corresponds to 6% of the OI emission (3300 R).

Variation of Ar, O and N_2 densities with altitude implies that auroral Ar/O and Ar/N_2 intensity ratios are likely to be dependent on incident electron energy, although this is not straightforward (O/N_2 ratio is quite dynamic in aurora (Strickland *et. al.*, 1999) and the O profile is complicated by O_2 dissociative excitation (Hecht *et. al.*, 1991)).

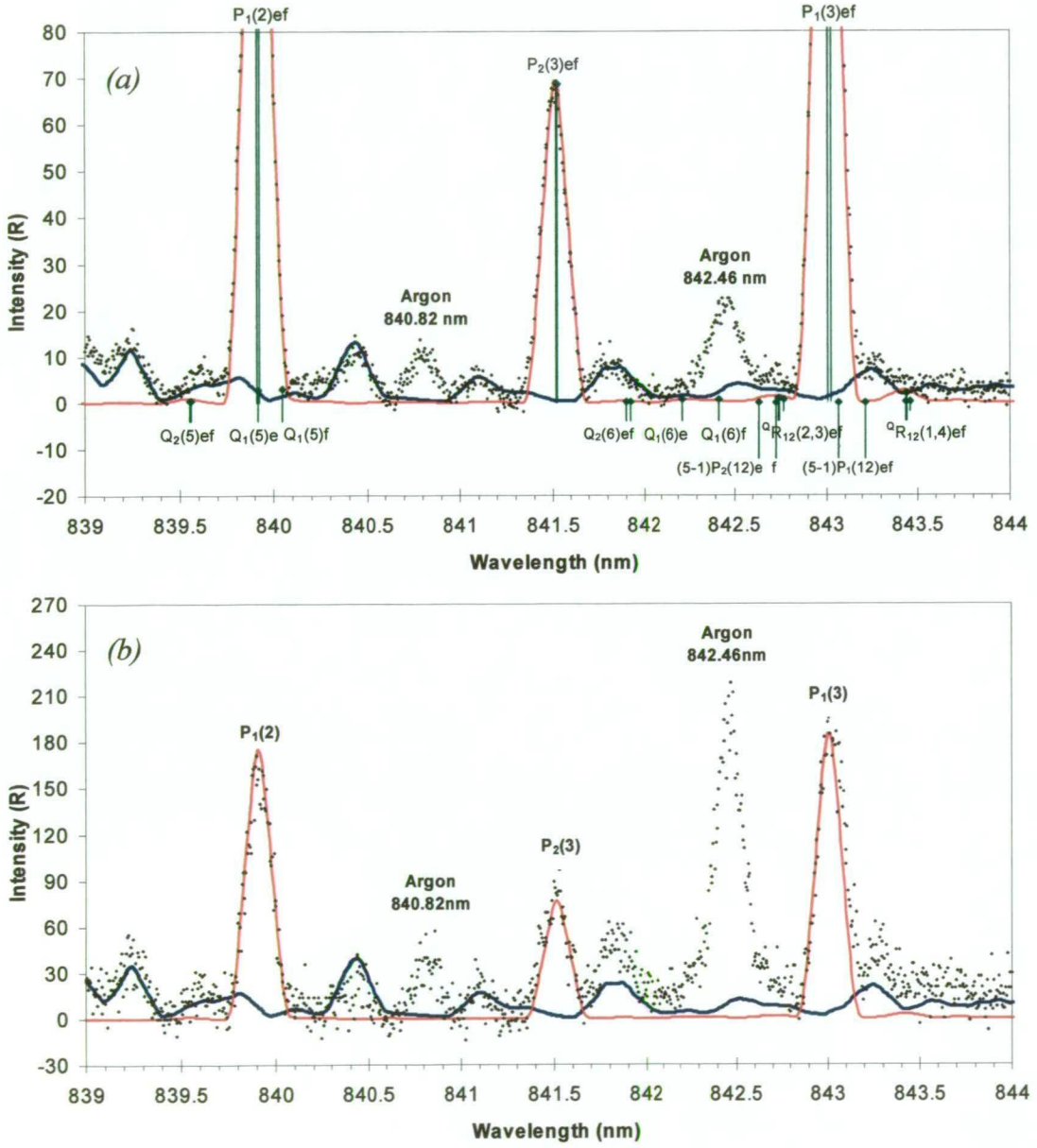

Figure 4-20. Argon aurora. (a) A spectrum obtained by co-adding 45 spectra, each consisting of 5 scans, collected when riometer measurements show energetic auroral precipitation in 1996. (b) Ten co-added spectral scans selected for Ar (λ842.46 nm) exceeding 100 R. Synthetic fits to nitrogen aurora (blue line) and hydroxyl airglow (red line) are included in each plot.

For intensity measurements derived from the average of the principal spectra in Table 4-1, an OI/$P_1(3)$ ratio of 0.28 implies an Ar/$P_1(3)$ contribution of 0.6-1.7 to the measurement of $Q_1(6)$. This accounts for most of the discrepancy between theoretical and measured $Q_1(6)$ intensities and the degree of thermalisation of the J'=6.5 state cannot be ascertained from these measurements.

Auroral argon lines at λ763.51, λ801.48, λ811.53, λ912.30 and λ965.78 nm may be up to 75% brighter than the argon line at λ842.46 nm [Worden (1995)]. Argon emissions during energetic aurora potentially allow remote sensing of argon densities across the altitude region where diffusive separation becomes significant.

4.5.3. Reducing temperature uncertainties

Uncertainty in the appropriate transition probabilities does not preclude determination of climate change if consistent values are used. Excluding this source of error, the Davis spectra from 1990, which are accumulated over a 1-hour interval, yield an average temperature uncertainty of 8 K (Table 4-7, column G). Most of this uncertainty is attributable to the non-simultaneous observations of the lines. This is avoided in Fourier transform instruments [eg Steed and Baker (1979)] or in CCD spectrometers where the whole spectrum is recorded simultaneously.

The detailed knowledge of background features acquired in this work provides considerable scope for improving the time resolution, thus accuracy, of OH(6-2) rotational temperatures obtained from measurements with the Davis spectrometer. Precise selection of only those wavelength intervals that determine line intensities, backgrounds and auroral estimates (Table 3-15, section 3.7.1.3) decreases the time required per spectra to 7.5 minutes.

Auroral influences can be significant but can generally be allowed for. It is, however, necessary to monitor an N_2 emission, rather than the brighter OI emission, for corrections to be made to temperature measurements.

The most significant uncertainty in average temperature determinations, which is difficult to reduce, is the instrument response calibration. In the Davis spectra from 1990 this amounts to 1.5K (Table 4-7, column F). More calibrations may reduce this uncertainty, but it will remain significant.

Solar cycle, seasonal, diurnal, tidal and planetary scale variations must also be accounted for in seeking climate-change variations. These variations will be discussed when a larger data set is analysed in chapter 6.

4.6. Conclusions

A Czerny-Turner scanning spectrometer has been used for detailed observations of OH(6-2) Meinel band emissions with the intention of establishing a data base for monitoring climate change in the Antarctic upper mesosphere. An investigation of weak spectral features including minor OH emission, nitrogen aurora, Fraunhofer and atmospheric absorption in relation to contamination of the main P_1-branch lines has shown:

- $Q_1(5)$ is coincident with $P_1(2)$. A correction can be calculated by iteration of the final temperature. It contributes ~1.7% of $P_1(2)$ at 200K.
- $Q_1(6)$, satellite lines $^{Q}R_{12}$ (1, 2, and 3), OH(5-1) $P_{1,2}(12)$ and an Argon auroral emission are within 1 nm of the $P_1(3)$ line. Non-thermalisation of the OH(5-1) $P_{1,2}(12)$ lines excluded calculation of a correction.
- the satellite line $^{P}Q_{12}(2)$ is within 1 nm at ~2% (at 200 K) of $P_1(4)$.
- most significant Fraunhofer absorption lines are 0.68 nm below $P_1(5)$, 0.35 nm above $P_1(4)$ and 1.14 nm below $P_1(2)$.
- atmospheric absorption is negligible.
- auroral activity has greatest influence on $P_1(5)$ due to the N_2 1PG(3-2) band. It can be allowed for by appropriate selection of the background.
- Average weighting factors of 0.32, 0.57 and 0.12 are derived for respective contributions of $P_1(2)/P_1(4)$, $P_1(2)/P_1(5)$ and $P_1(4)/P_1(5)$ ratios to the mean temperature. $P_1(2)/P_1(4)$ may be the most favourable ratio, in the auroral region however, due to the lower intensity, nearby Fraunhofer absorption and auroral contamination of $P_1(5)$.

From OH(6-2) observations at Davis in 1990, the average of the weighted temperatures from three possible ratios from three lines in the band was 221.0±2.3 K, using Turnbull and Lowe (1989) transition probabilities. Mid-winter average temperature is consistent with the 1986 CIRA mid-winter temperature, but this result is dependent on the choice of transition probabilities.

4.7. Improvements for subsequent analyses.

This section summarises changes and improvements that have been made to the data acquisition and analysis programs as a result of this study.

- Dark counts have been reduced from about 40 counts/sec in 1990 to about 8 counts/sec in 1995 by an upgrade of the pulse-amp discriminator and to about 5 counts/sec in 1996 by the installation of an external air duct.
- A second-order blocking filter was included from 1994, thus the second order N_2^+ 1NG bands were effectively removed from the spectrum. First order N_2 1PG and N_2^+ Meinel bands (recalculated at 300K) are accounted for in the selection of background intervals.
- New background regions, listed in Table 4-4, were determined from the spectral average of the principle data set from 1996. Intervals are selected to balance auroral, satellite line and solar Fraunhofer absorption contributions to each P_1-branch line sampled.
- Instrument functions were determined separately for each year and the Λ-doubling correction factors were determined from the empirical fit method (section 3.4.2) to replace those assuming a 0.15 nm fwhm triangular function.
- Instrument response corrections were re-determined for all years after the scattering problem at NML was resolved in 1999 (Table 3-13). The uncertainty in response corrections is reduced by an order of magnitude by careful calibration with the Eather LBS (section 3.6.5, Table 3-14).
- Transition probabilities of Turnbull and Lowe (1989) have been replaced by those of Langhoff *et al.* (1986). This is a result of an experimental investigation of P,Q and R branch line ratios discussed in chapter 5.
- Theoretical branch line wavelengths of Coxon and Foster (1982) were replaced by those of Goldman (1982). The maximum wavelength shift for the main P_1-branch lines is 0.0005 nm.
- A fast scanning routine was implemented at the end of 1996, which reduced the acquisition time per spectra to about 7½ minutes, thus substantially reducing the sampling error.

4.7.1. Time interpolation

Sampling error is further reduced by *time interpolation* of the emission intensities between successive scans to a common sample time. The principle is illustrated in Figure 4-21. Each of the P-branch line intensities, their background estimates and the OI, N_2 and Fraunhofer samples are interpolated to the time of the darks sample at the start of each scan cycle (nominally 7min 20sec in duration). Rotational temperatures are then determined from the interpolated values as above. Additional information on the rates of change of intensities and temperatures may be used as selection criteria to reject anomalous variations. This analysis procedure is applied exclusively to all spectra collected under the fast scanning routine adopted at the end of 1996. A comparison has also been made of the standard spectra and interpolated spectra analysis methods for the 1995 and 1996 data sets. Results from this are presented in section 6.2.9.

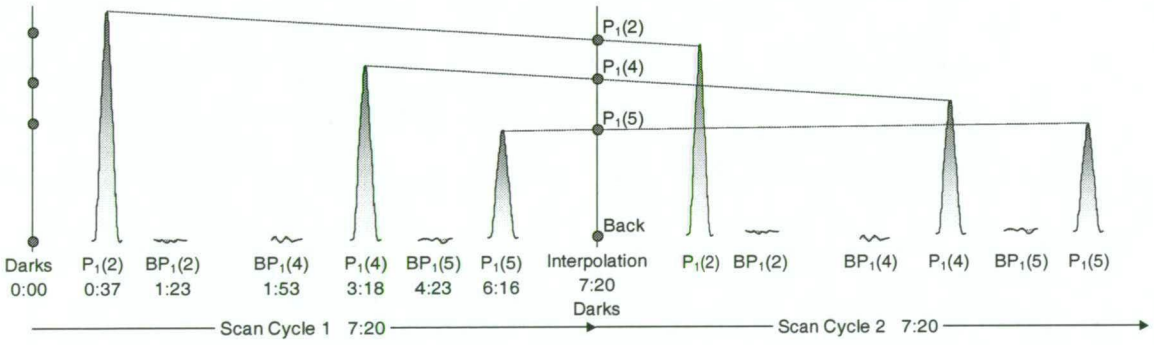

Figure 4-21. Illustration of the time interpolation of emission intensities. Sample times are in min:sec to the centre of the scan region.

5. Experimental Transition Probability Ratios

In section 4.3.11, three sets of published transition probabilities were introduced that were shown to yield a difference in the absolute rotational temperatures derived of some 12K. This chapter aims to determine an experimental set of values applicable to OH(6-2) for rotational states up to J'=4.5, by examination of the OH(6-2) Q_1/P_1 and R_1/P_1 airglow emission intensity ratios. This work is published in French *et al.* (2000) "Hydroxyl (6-2) airglow emission intensity ratios for rotational temperature determination" Annales Geophysicae 18, 1293-1303. A copy of this manuscript is included in appendix A.

5.1. Introduction

Rotational temperatures (T_{rot}) are derived by comparing the intensities of any two lines, from different upper rotational states (I_m, I_n), as has been discussed in section 2.3.9 and reiterated here in equation 5-1.

$$\frac{I_n}{I_m} = \frac{A_n (2J'_n+1)}{A_m (2J'_m+1)} exp(\frac{E_m-E_n}{kT_{rot}}) \qquad \textit{Equation 5-1}$$

where E_m, E_n are the initial rotational state energy levels (energy level values given by Coxon and Foster (1982) are used); J'_m and J'_n are the upper state, total angular momentum quantum numbers and k is Boltzmann's constant. Transition probabilities (A_n and A_m) apportion the fraction of the upper rotational state population that decays via the transitions measured.

Transition probabilities of Nelson *et al.* (1990), used by researchers for low Δv transitions (e.g., Lowe *et al.* (1991); Sivjee and Waltershied (1994); Mulligan *et al.* (1995)) do not cover the OH(6-2) band. Transition probabilities that include the $\Delta v = 4$ band have been published in Mies (1974) henceforth referred to as Mies; Turnbull and Lowe (1989) (henceforth T&L) and Langhoff *et al.* (1986) (henceforth LWR). Above the fundamental ($\Delta v=1$) sequence (which is strongly disturbed by vibrational-rotational coupling compared to the overtone transitions, $\Delta v>1$) the temperature variance from the choice of transition probabilities increases with Δv [T&L]. A 12K variation in OH(6-2) ($\Delta v=4$) temperatures has been calculated in section 4.4.1 (Table 4-6) depending on choice of transition probabilities.

An excited vibrational-rotational state may undergo transitions according to selection rules for ΔJ and Δk (see section 2.3.7). Six transitions are possible for the OH $X^2\Pi_{3/2}$ state; three within the same state which yield P, Q and R branches and three weaker transitions across to the spin-split $^2\Pi_{1/2}$ state† which yield the ^OP, ^PQ and ^QR satellite branches (see Figure 1-24).

It can be seen from equation 5-1 that for transitions arising from the same upper state $E_m = E_n$ and $J'_m = J'_n$ thus the intensity ratio I_n/I_m is a constant, independent of temperature and a direct measurement of A_n/A_m. A comparison of these ratio's from the five lowest rotational states of OH(6-2) derived from the transition probabilities of Mies, LWR and T&L are listed in Table 5-1 with the average variation between them. In this study, experimental measurements of line ratios from the same upper state, derived from night sky observations at Davis for the four lowest rotational states are compared with these published ratios in order to establish which set are most appropriate for the OH(6-2) temperature analysis.

Average temperatures derived from measurements of the four brightest OH(6-2) P_1-branch lines in spectra recorded at Davis in 1995 and 1996 using the transition probabilities of Mies, LWR, T&L and the experimentally determined ratios are compared at the end of this chapter [see table Table 5-8].

J'	Ratio	T&L	Mies	LWR	Variation
1.5	$Q_1(1)/P_1(2)$	1.42	1.365	1.33	6.6%
2.5	$Q_1(2)/P_1(3)$	0.49	0.46	0.44	10.8%
3.5	$Q_1(3)/P_1(4)$	0.244	0.228	0.213	13.6%
4.5	$Q_1(4)/P_1(5)$	0.145	0.132	0.123	16.5%
5.5	$Q_1(5)/P_1(6)$	0.094	0.086	0.078	18.6%
2.5	$R_1(1)/P_1(3)$	0.540	0.486	0.451	18.1%
3.5	$R_1(2)/P_1(4)$	0.678	0.590	0.523	26.0%
4.5	$R_1(3)/P_1(5)$	0.732	0.615	0.522	33.7%
5.5	$R_1(4)/P_1(6)$	0.756	0.613	0.500	41.1%

Table 5-1. Q_1/P_1 and R_1/P_1 ratios inferred from Mies, LWR and T&L compared with measured values.

† Note that the hydroxyl line nomenclature section in French *et al.* (2000), which is condensed from the descriptions in Osterbrock and Martel (1992) and Osterbrock *et al.* (1996, 1997) incorrectly refer to the $^2\Pi_{1/2}$ state as the first electronic excited state. The $^2\Pi_{1/2}$ state is of course the higher energy spin-split component of the ground state molecule and the first electronic excited state is $^2\Sigma^+$. This has been revised in section 2.3 and the same nomenclature is used in this section.

Goldman (1982) gives transition probabilities for satellite lines relative to Mies values for main branch transitions. These are listed as ratios of the appropriate OH(6-2) P_1-branch line intensities in Table 5-2.

J'	Ratio	$^{Q}R/P$	$^{P}Q/P$	$^{O}P/P$
1.5	sat./$P_1(2)$	0.015	0.018	0.006
2.5	sat./$P_1(3)$	0.005	0.014	0.006
3.5	sat./$P_1(4)$	0.002	0.011	0.006
4.5	sat./$P_1(5)$	0.001	0.009	0.005
5.5	sat./$P_1(6)$	0.000	0.008	0.004

Table 5-2. Satellite line ratios with respect to the appropriate P-branch line, as inferred from Goldman (1982).

5.2. Data for this study

Measurements reported here were collected at Davis during 1995, 1996 and 1997. Instrument configuration and calibration for these years are summarized as follows:

- The spectrometer had a six-degree field-of-view (fov) in the zenith.
- A cooled (-28°C) GaAs photomultiplier tube was used for photon detection.
- A blocking filter, limiting observations to first order, was used.
- Annual average spectral response functions were determined for each year from scans of the Eather LBS and secondary calibration lamp (see section 3.6). The Eather LBS source function from NML calibrations in Jan-99 was used, which corrected for scattering effects found in previous calibrations (see section 3.5.5).

Operating mode for determining OH rotational temperatures during 1997 consisted of successively scanning narrow wavelength intervals incorporating OH(6-2) $P_1(2)$, $P_1(4)$ and $P_1(5)$ emissions and appropriate background regions. Entrance and exit slit separations of 250 μm were used.

Between day-of-year (DOY) 182-229, 1997, additional wavelength regions were successively incorporated to measure the intensities needed to determine low rotational quantum number ($J' \leq 4.5$) line ratios. A step size of 0.01 nm and a dwell-time of 1 second were used.

Between DOY 230-295, slit separations were narrowed to 100 μm, reducing the width of the instrument function. This is near the limit to which reasonable

parallelism of entrance and exit slits can be maintained for this instrument. Step size was reduced to 0.005 nm and a dwell-time of 1 second maintained. Additional wavelength regions needed to determine individual line ratios were incorporated in separate campaigns over a number of nights, so that temperature measurements could be maintained. Figure 5-1 is a compilation of all spectral regions scanned.

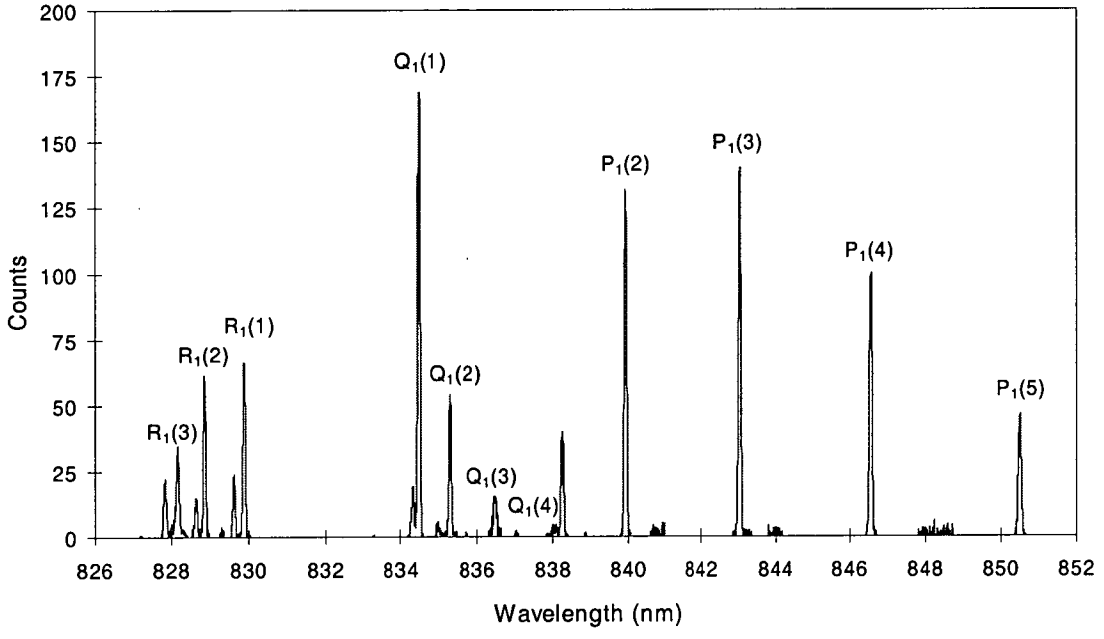

Figure 5-1. A compilation of spectral regions scanned with 100 micron slit separations, normalised to 100 counts for the $P_1(4)$ peak intensity. Major lines of interest are labelled. Apparent but not labelled are: $R_1(4+5)$ at λ827.8 nm, $R_2(3)$ at λ828.6 nm, $R_2(2)$ at λ829.6 nm, $Q_2(1)$ at λ834.3 nm, $Q_2(2)$ at λ835.0 nm and $P_2(2)$ at λ838.2 nm.

Knowledge of the instrument function is needed to allow for contamination by lines not fully separated from adjacent features. Instrument functions were determined using the empirical fit method discussed in section 3.4. At 100 μm slit separation, a slightly asymmetric, rounded instrument function of fwhm 0.071 nm is appropriate. The first ghosts are approximately 0.33% of the main peak, and displaced by 0.354 nm. For the second ghosts, an approximate magnitude of 0.18% and displacement of 0.71 nm were estimated. At 250 μm slit separation, an instrument function with fwhm 0.155 nm was similarly determined.

During 1995 and 1996 spectra were collected as continuous scans from λ837.5 nm to λ851.5 nm. Step size was 0.005 nm, dwell-time was 0.1 seconds and slit widths were 250 μm. Five scans were combined to give a spectrum for temperature analysis. From this data set, 279 spectra, obtained during optimal observing conditions and

with no significant auroral contamination, were chosen. These spectra are principally used to determine two satellite line ratios and to derive average temperatures from P_1 line ratio pairs for a comparison of transition probabilities.

A broad classification of sky conditions (clear, thin cirrus, patchy cloud, overcast, snow) was maintained through visual observation and reference to all-sky video records. Thin cirrus classification describes times when uniform thin high cirrus cloud, through which bright stars are visible, was apparent. In the cold Antarctic winters this is a common condition. Stratospheric haze is also often present, however as it can only be seen in forward scattered sunlight e.g. at twilight, its presence is ignored.

Only spectra that are free of auroral contamination are used in the intensity ratio determinations. In selecting against auroral contamination, reference was made to wide-angle (60 degree fov), zenith-oriented photometer measurements of the auroral N_2^+ 1NG band at λ428 nm.

Meteorological balloon flights, by employees of the Australian Bureau of Meteorology, were conducted twice daily during 1997 at Davis. Measurements taken allow calculation of the equivalent column density of water vapour above the site (Sturman and Tapper (1996)). Reference is made to these data when water absorption of emissions may be significant.

5.3. Determination of line ratios

Desired line intensities are determined after aligning and summing selected spectra. Unless specifically noted, spectra collected with 100 μm slit separations (0.071 nm fwhm instrument function) are used. Counts in a 0.125 nm region centred on the emission of interest are typically determined. The 'count region' occasionally varies, as will be indicated, to allow for difficulties with some emissions. A background level is determined for each emission of interest in the summed files.

The fraction of an emission within the count region, and contamination from nearby emissions, are determined using the instrument function. Allowance is made for Λ-doubling of the OH lines (see section 2.3.4). It is assumed that individual Λ-components are of equal intensity. An estimate of uncertainty in the derived ratios due to uncertainty in the instrument function is made by comparing line fractions

determined using the intrinsic width (worst case) and empirical fit (best case) methods (see section 3.4). The largest difference in any ratio was 0.2%, an amount insignificant compared with other uncertainties in the measurements.

Water vapour is the only absorber of consequence in the wavelength range covered. Using high-resolution telluric absorption spectra (HITRAN92; Rothman *et al.* (1992)) and the technique described in Turnbull and Lowe (1983), the transmission of each Λ-component has been checked. Where absorption by water vapour may be of concern, it is noted in the specific ratio determinations.

Possible intensity variations in the time taken to scan spectral components are also a source of error. $P_1(4)$ emissions in the 1995 and 1996 continuous scans (279 spectra) give an average intensity variation of -0.038% per minute, consistent with a tendency for decreasing hydroxyl intensity across the night at this site (see section 4.4.2). The time difference between measuring line intensities used to determine desired ratios are listed in Table 5-3, column B. The largest time difference is 7.4 minutes [for determining $Q_1(4)/P_1(5)$] and the shortest is 1.2 minutes [$Q_1(1)/P_1(2)$]. For each of the ratios determined, $P_1(4)$ intensity is monitored, and the average $P_1(4)$ intensity over the summed spectra is calculated as a 'percentage variation per minute'. These values are also listed in Table 5-3, column F along with the implied percentage error in the ratio being determined (Table 5-3, column G). Greatest uncertainty in the measured ratios, due to the time interval between measuring individual intensities, is -0.8% for the $R_1(3)/P_1(5)$ ratio. No allowance is made for minor variations possible due to the time interval between measuring the emissions.

Spectral response in 1997 was determined from 121 separate scans of the Eather LBS. Standard deviation of the individual scans was used to estimate uncertainty in the derived ratios due to the spectral response calibration (see section 3.6.5). These uncertainties, no greater than 0.3% for any ratio, are also listed in Table 5-3, column H and are insignificant compared to other sources of error for all ratios.

A range of cloud conditions has been accepted for the ratios derived. A value determined from 'clear sky' spectra is also presented for all ratios except the two satellite line ratios. No statistically significant difference is found between ratios determined under cloudy or clear conditions. In Table 5-3, column C are listed the

number of spectra summed in determining each ratio and the sky conditions under which those spectra were acquired (column D).

In determining some ratios, it was necessary to include spectra collected when the moon was above the horizon (Table 5-3, column E). Separate determination of the background for each emission allows for any spectral slope in moon-affected spectra. A solar spectrum was examined to ensure that Fraunhofer absorption did not affect the ratios determined.

An uncertainty is estimated for each ratio as the square-root of the sum of the squares of the relative errors of the individual line intensities. Emission intensity uncertainty includes allowance for counting statistics and uncertainties in estimates of the baseline, contamination by nearby emissions and any atmospheric absorption.

		A	B	C	D	E	F	G	H
Ratio	J'	fwhm (nm)	Δt min	No. of spectra	Sky	Moon	Slope %/min	Scan-time error %	Spectral error %
$Q_1(1)/P_1(2)$	1.5	0.071	1.2	232	cloudy	no	-0.004	-0.005	0.1
		0.071	1.2	6	clr	no	0.18	0.2	0.1
$Q_1(2)/P_1(3)$	2.5	0.071	3.8	74	clr	no	-0.05	-0.2	0.2
$Q_1(3)/P_1(4)$	3.5	0.071	4.3	59	clr+thc	yes	-0.07	-0.3	0.2
		0.071	4.3	30	clr	yes	0.04	0.2	0.2
		0.155	4.0	286	clr	yes	0.02	0.06	0.2
$Q_1(4)/P_1(5)$	4.5	0.071	7.4	174	clr+thc	no	-0.05	-0.3	0.2
		0.071	7.4	107	clr	no	-0.02	-0.15	0.2
		0.155	6.6	279	clr+thc	no	-0.04	-0.25	0.2
$R_1(1)/P_1(3)$	2.5	0.071	5.5	74	clr	no	-0.05	-0.3	0.2
$R_1(2)/P_1(4)$	3.4	0.071	4.2	46	clr	yes	-0.01	-0.03	0.3
		0.155	3.8	69	clr	no	-0.03	-0.1	0.3
$R_1(3)/P_1(5)$	4.5	0.071	6.5	66	clr	no	-0.13	-0.8	0.3
$^{Q}R_{12}(1)/P_1(2)$	1.5	0.155	1.9	279	clr+thc	no	-0.04	-0.07	0.1
$^{P}Q_{12}(2)/P_1(2)$	1.5	0.155	4.0	279	clr+thc	no	-0.04	-0.15	0.1

Table 5-3. Information on the data sets used to derive the indicated ratios. Included are the instrument function fwhm, the time taken to scan between the emissions, the number of spectra in the data set, the sky conditions (cloudy, clear = clr or thin cirrus = thc), whether the data set includes spectra collected when the moon was above the horizon, the average slope in the $P_1(4)$ intensity for the data set and the error in the ratio implied by the average intensity slope.

5.3.1. $Q_1(1)/P_1(2)$ [J'=1.5]

A sum of 232 spectra determined this ratio. All cloud conditions were accepted but the moon was always below the horizon. Figure 5-2 shows $Q_1(1)$ and $P_1(2)$ regions of the summed spectrum. Only 0.2% of the $Q_2(1)$ emission falls in the $Q_1(1)$ count region. 96% of the $Q_1(5)_e$ line (at λ839.91 nm) and 1.3% of the $Q_1(5)_f$ line (at λ840.04 nm) lie in the $P_1(2)$ count region.

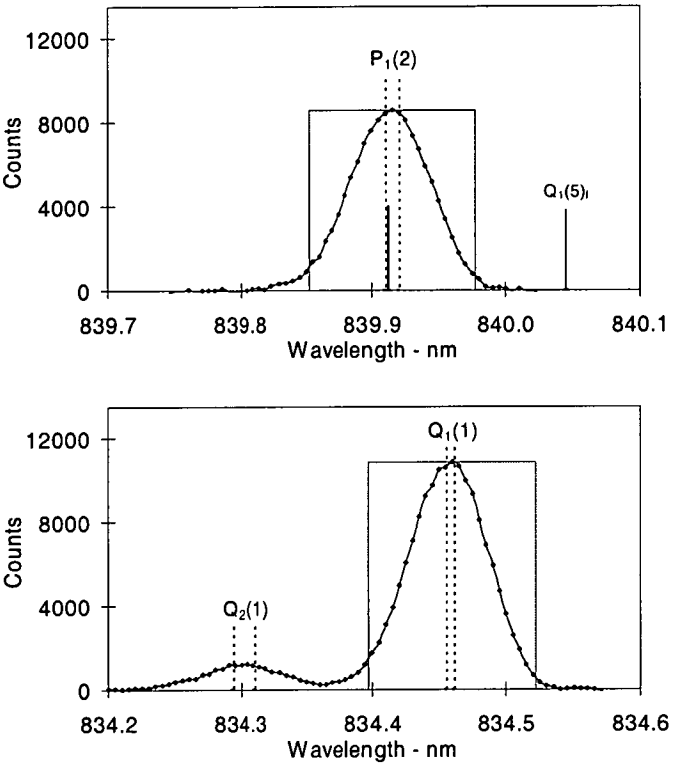

Figure 5-2. The 'count regions' for determination of the $Q_1(1)/P_1(2)$ ratio are indicated by rectangles centred on the relevant emissions. The $Q_1(5)_e$ line at λ839.91 nm, which contaminates the $P_1(2)$ emission, is marked but not labeled.

For a temperature of 200 K, estimates of total intensity of the $Q_1(5)$ emission with respect to the $P_1(2)$ emission for Mies, LWR and T&L transition probabilities varies between 1.6-1.7%. The range for a temperature of 240 K is 2.7-2.9%. A reasonable estimate of the $Q_1(5)$ intensity relative to the $P_1(2)$ intensity for winter temperatures above Davis is 2.2±0.8%. Taking $Q_1(5)$ contamination of this level into account, the $Q_1(1)/P_1(2)$ ratio is measured to be 1.261±0.012. This is the only ratio determined without any selection against cloud conditions. There were only six spectra collected under clear skies. These six spectra when combined yield a $Q_1(1)/P_1(2)$ ratio of 1.31±0.07.

Variations in intensity in the 1.2 minutes between measuring the two emissions, determined from variations in $P_1(4)$ intensity, average out to be insignificant (-0.005%, see Table 5-3). Dominant sources of uncertainty come from estimations of the $P_1(2)$ background and $Q_1(5)$ contamination.

5.3.2. $R_1(1)/P_1(3)$ and $Q_1(2)/P_1(3)$ [J'=2.5]

A sum of 74 spectra determined the $R_1(1)/P_1(3)$ and $Q_1(2)/P_1(3)$ ratios. Figure 5-3 shows $R_1(1)$, $Q_1(2)$ and $P_1(3)$ regions of the summed spectra. An estimated 61% of the un-thermalised OH(5-1) $P_1(12)_e$ line lies in the $P_1(3)$ count region. The OH(5-1) $P_1(12)_f$ line is 0.2 nm higher in wavelength than the peak of the $P_1(3)$ emission. From the summed spectrum, it is estimated that the OH(5-1) $P_1(12)_f$ line is 1.0±0.6% of the $P_1(3)$ intensity. This is lower than, but within estimated uncertainties of the value determined in section 4.5.1 of 1.5%.

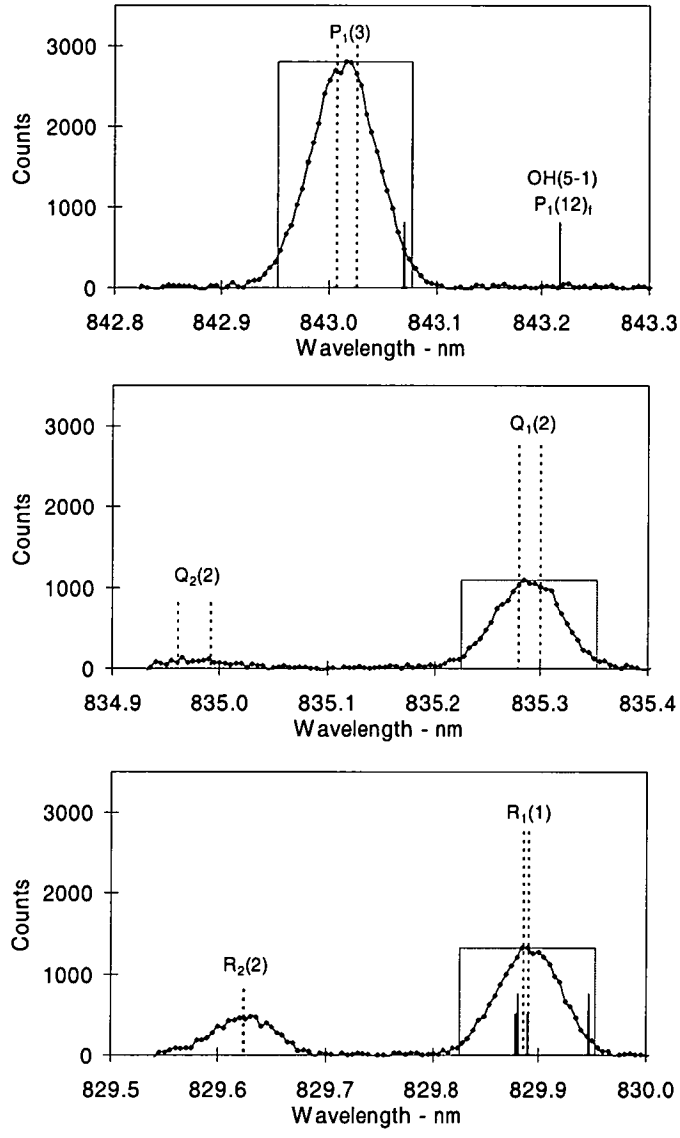

Figure 5-3. Spectral regions for evaluation of $Q_1(2)/P_1(3)$ and $R_1(1)/P_1(3)$ ratios. The locations of the contaminating lines, OH(5-1) $P_1(12)_e$ [at λ843.07 nm] (top panel) and $^QP_{21}(3)_e$ [λ829.88 nm], $^QP_{21}(3)_f$ [λ829.89 nm], OH(5-1) $P_2(10)_e$ [λ829.88 nm] and $P_2(10)_f$ [λ829.95 nm] (bottom panel), are marked without label.

95% of the OH(5-1) $P_2(10)_e$ line and 55% of the OH(5-1) $P_2(10)_f$ line lie in the $R_1(1)$ count region. The intensities of these un-thermalised lines are assumed equal to the measured OH(5-1)$P_1(12)_f$ intensity and ascribed an uncertainty amounting to 60% of the estimated contamination. 95% of the OH(6-2) satellite line $^QP_{21}(3)$ also lies in the $R_1(1)$ count region. Goldman (1982) gives transition probabilities for satellite lines consistent with Mies values for the major lines. For a temperature range of 200 to 240 K, these transition probabilities yield $^QP_{21}(3)/R_1(1)$ ratios ranging from 0.95% to 1.25%. A ratio of 1.1% is used to estimate the $^QP_{21}(3)$ contamination

with an uncertainty estimated as half the contamination value. The $R_1(1)/P_1(3)$ ratio is measured to be 0.436±0.016. The principal uncertainty results from estimations of the contamination of the $R_1(1)$ measurement.

The $Q_1(2)/P_1(3)$ ratio is measured to be 0.389±0.006. The main sources of uncertainty are in determination of the baseline for $Q_1(2)$ and in estimating OH(5-1) $P_1(12)_e$ contamination of the $P_1(3)$ intensity.

5.3.3. $R_1(2)/P_1(4)$ [J'=3.5]

A sum of 46 spectra determined the $R_1(2)/P_1(4)$ ratio. Figure 5-4 shows $R_1(2)$ and $P_1(4)$ regions of the summed spectrum. OH(9-4)$P_1(12)_f$ is blended with $R_1(2)$, but OH(9-4)$P_1(12)_e$ at λ828.725 nm is not discernible in Figure 5-4, therefore no allowance is made for this contaminant. Water vapour is potentially an absorber of the $R_1(2)$ emission, but the atmosphere above Davis in winter is very dry. Meteorological balloon flights at Davis station on the days these spectra were collected yield a water vapour column density of 1.8±1 mm cm^{-2}. This implies only 0.23% absorption of the $R_1(2)$ emission. An $R_1(2)/P_1(4)$ ratio of 0.514 ±0.013 is obtained from these spectra.

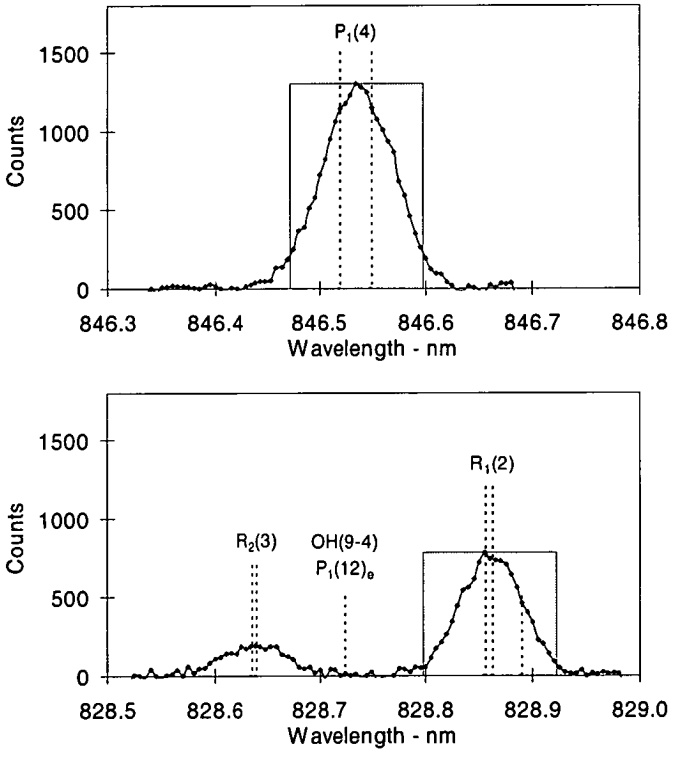

Figure 5-4. Summed spectral profiles showing the $R_1(2)$ and $P_1(4)$ spectral regions. OH(9-4) $P_1(12)_f$ at λ828.89 nm is marked without label.

A total of 69 spectra collected with 250 μm slit separations were also summed to obtain an independent estimation of this ratio. Count regions 0.25 nm wide centred on the respective emissions were selected. With this wider instrument function, it was necessary to allow for 6% of $R_2(3)$ under the $R_1(2)$ count region. Water vapour content was measured to be 3.5±1.5 mm cm^{-2}, implying a 0.45% $R_1(2)$ absorption. An $R_1(2)/P_1(4)$

ratio of 0.510±0.009 is measured. The larger number of suitable spectra, and the higher intensities obtained with the larger slit widths, yield a more accurate determination of the ratio. Principal source of uncertainty in both determinations comes from the background estimate of the $R_1(2)$ region.

5.3.4. $Q_1(3)/P_1(4)$ [J'=3.5]

A sum of 59 spectra was used to measured the $Q_1(3)/P_1(4)$ ratio. 72% of the OH(5-1) $P_1(11)_e$ emission lies in the $Q_1(3)$ count region. To obtain some estimate of the contribution of this feature, it is assumed to be of the same average relative magnitude as OH(5-1) $P_1(12)_f$ which was measured in section 5.3.2. Assuming an OH temperature of 220 K, OH(5-1)$P_1(11)_e$ emission amounts to 1.3% of the $P_1(4)$ intensity. Implied correction to the counts under the $Q_1(3)$ summing region is 5.5%. The $Q_1(3)/P_1(4)$ ratio is measured to be 0.179±0.012. For the 30 clear-sky spectra in this data set, the $Q_1(3)/P_1(4)$ ratio was 0.176±0.017. Principal sources of error come from estimation of the OH(5-1) $P_1(11)$ contamination and the low intensity of the $Q_1(3)$ emission.

A sum of 286 spectra acquired with 250 μm slit widths allow an independent estimation of the $Q_1(3)/P_1(4)$ ratio. Count regions 0.25 nm wide centred on the respective emissions were used. Figure 5-5 shows the summed spectrum around $Q_1(3)$ and $P_1(4)$. Potential contaminants of the $Q_1(3)$ emission, measured with this larger instrument function, are OH(5-1)$P_1(11)$, OH(6-2)$R_1(11)$ and OH(9-4)$P_1(13)_e$. Both OH(9-4)$P_1(13)_e$ and OH(6-2) $R_1(11)$ contaminations are insignificant with respect to uncertainty in the background level. OH(5-1)$P_1(11)_e$ remains the principal contaminant, with 89% of its total

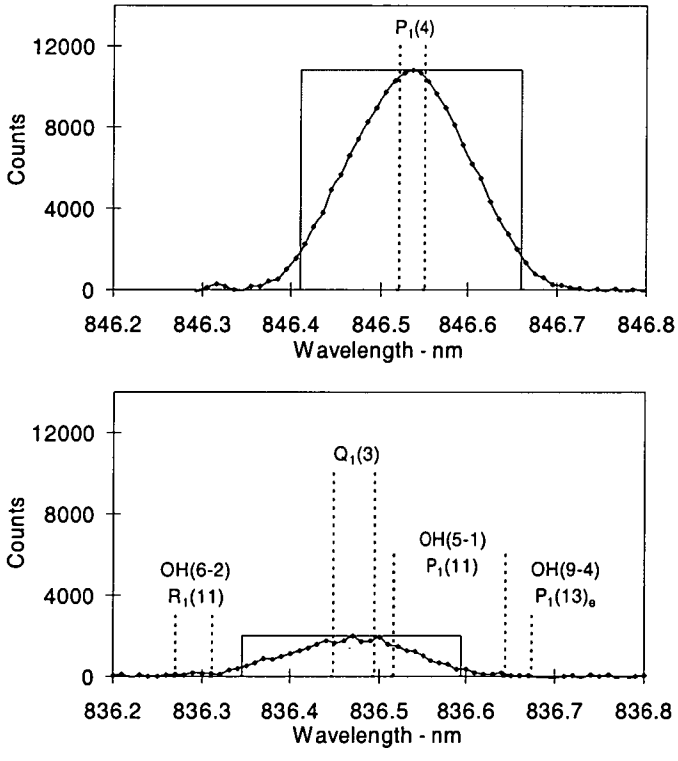

Figure 5-5. Summed profiles in the regions of $Q_1(3)$ and $P_1(4)$ obtained with a 0.155 nm instrument function.

intensity in the $Q_1(3)$ count region. 23% of the OH(5-1)$P_1(11)_f$ intensity also contaminates $Q_1(3)$. By assuming each is equivalent in average intensity to the measurement made of OH(5-1) $P_1(12)_f$, 7.7% of counts in the $Q_1(3)$ count region are estimated to result from the OH(5-1)$P_1(11)$ emission. The $Q_1(3)/P_1(4)$ ratio derived is 0.168±0.011. Principal uncertainty is in estimation of the OH(5-1)$P_1(11)$ contamination.

Since uncertainties associated with the $Q_1(3)/P_1(4)$ determinations are similar, an average value of 0.173±0.011 is appropriate. Uncertainty has not been reduced, due to its strong dependence on the method used to estimate OH(5-1)$P_1(11)$ contamination.

5.3.5. $R_1(3)/P_1(5)$ [J'=4.5]

A sum of 66 spectra was used to determine the $R_1(3)/P_1(5)$ ratio. Figure 5-6 shows the $R_1(3)$ and $P_1(5)$ regions of the summed spectrum. The $R_1(3)$ region is very crowded. An additional difficulty is that $R_1(3)$ may be significantly absorbed by atmospheric water vapour. The water column density over Davis when these spectra were acquired was measured to be 1.5±1 mm cm^{-2}. For this quantity of water vapour, the $R_1(3)_f$ line at λ828.164 nm is 0.45% absorbed and the $R_1(3)_e$ component at λ828.171 nm is 0.7% absorbed.

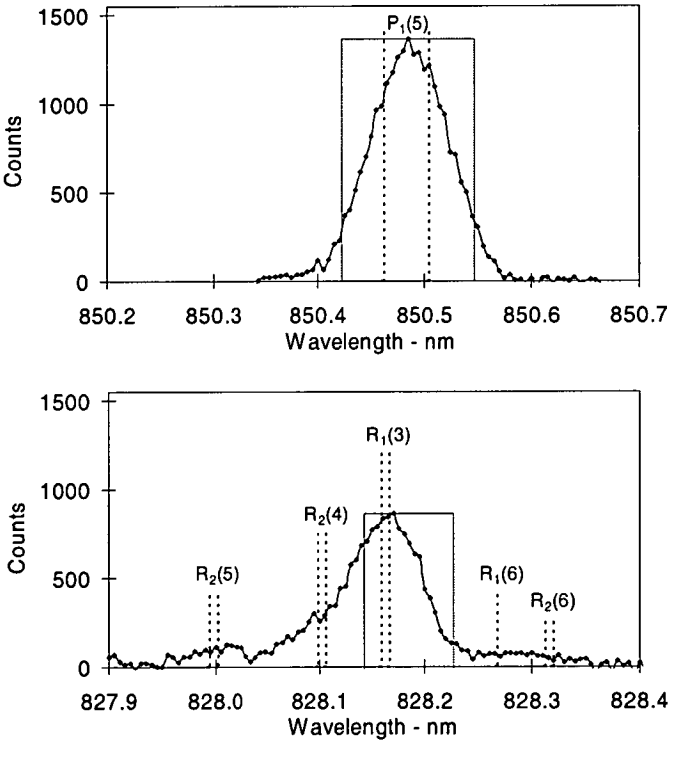

Figure 5-6. Summed profiles of $R_1(3)$ and $P_1(5)$ spectral regions. The $R_1(6)$ Λ-components are sufficiently close to be indistinguishable.

$R_1(3)$ emission is significantly contaminated on the low wavelength side by $R_2(4)$. Some allowance is made for this contamination by using an asymmetric $R_1(3)$ count region, from 0.0225 nm below the $R_1(3)$ centre wavelength to 0.0625 nm above. This reduces the $R_2(4)$

contamination of the $R_1(3)$ count region to 6.8% of the total $R_2(4)$ intensity. $R_2(4)$ intensity is estimated by counting from the $R_2(4)$ centre wavelength, 0.0625 nm towards lower wavelengths. 10% of the total $R_1(6)$ intensity lies within the $R_1(3)$ count region. $R_1(6)$ intensity is estimated using a count region from its centre wavelength, 0.0625 nm towards higher wavelengths. The $R_1(3)/P_1(5)$ ratio is measured as 0.483±0.017. Uncertainties in the estimation of $R_1(3)$ contaminants are the principal source of error.

5.3.6. $Q_1(4)/P_1(5)$ [J'=4.5]

A sum of 174 spectra were used to determine a $Q_1(4)/P_1(5)$ ratio of 0.107±0.009. The principal source of error is the low intensity of the $Q_1(4)$ emission.

A sum of 279 spectra from 1995 and 1996 were used to independently determine the $Q_1(4)/P_1(5)$ ratio. Figure 5-7 shows $Q_1(4)$ and $P_1(5)$ spectral regions of the summed file. The larger instrument function leads to an overlap of $P_2(2)$ emission with the less intense $Q_1(4)$ emission. This is partially compensated by defining an asymmetric $Q_1(4)$ count region, from 0.1425 nm below the $Q_1(4)$ central wavelength to 0.0625 nm above. Less than 0.8% of the $P_2(2)$ emission contaminates this $Q_1(4)$ count region. A $Q_1(4)/P_1(5)$ ratio of 0.094±0.004 is determined. Uncertainty in the estimate is lower than for 100 μm spectra due to increased $Q_1(4)$ intensity. This more reliable estimate of the $Q_1(4)/ P_1(5)$ ratio is used in further evaluations.

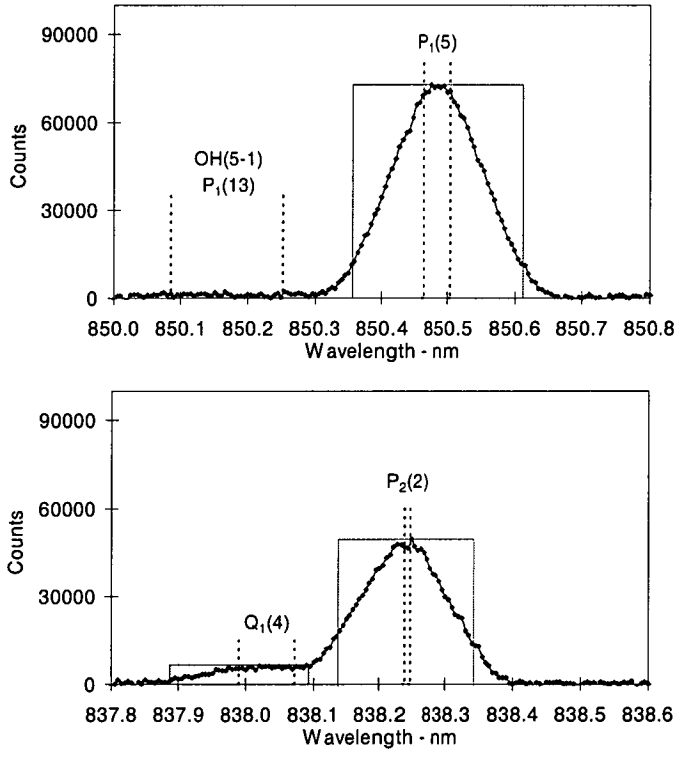

Figure 5-7. Summed profiles of the $Q_1(4)$ and $P_1(5)$ regions obtained with a 0.155 nm instrument function. The respective count regions are indicated by rectangles. The asymmetric count region chosen for the $Q_1(4)$ measurement is apparent.

5.3.7. Satellite line ratios: $^{P}Q_{12}(2)/P_1(2)$ and $^{Q}R_{12}(1)/P_1(2)$ [J'=1.5]

The 279 summed spectra from 1995 and 1996 were also used to estimate ratios of two OH(6-2) satellite lines. Figure 5-8 shows $P_1(2)$, $^{Q}R_{12}(1)$ [near $P_1(3)$] and $^{P}Q_{12}(2)$ [near $P_1(4)$] regions of the summed spectrum. Also shown overlayed are the $^{Q}R_{12}(1)$ and $^{P}Q_{12}(2)$ regions at 20 times magnification, so as to better display the satellite lines.

$^{P}Q_{12}(2)$ intensity is estimated from a centred count region, 0.205 nm wide, and $P_1(2)$ intensity is measured using a centred count region, 0.255 nm wide. The $P_1(2)$ count region is contaminated by 72.5% of the $Q_1(5)$ emission. $Q_1(5)$ intensity is estimated to be 2.2±0.8% of the $P_1(2)$ intensity, following section 5.3.1. A $^{P}Q_{12}(2)/P_1(2)$ ratio of 0.022±0.001 is obtained. This is significantly larger than the theoretical value of 0.018 determined from Goldman (1982). Conservative estimates of the uncertainties possible from all known contaminants are applied to the measured ratios, but if unknown contaminants exist their possible impact would be greatest on the lowest intensity features measured, such as the satellite lines.

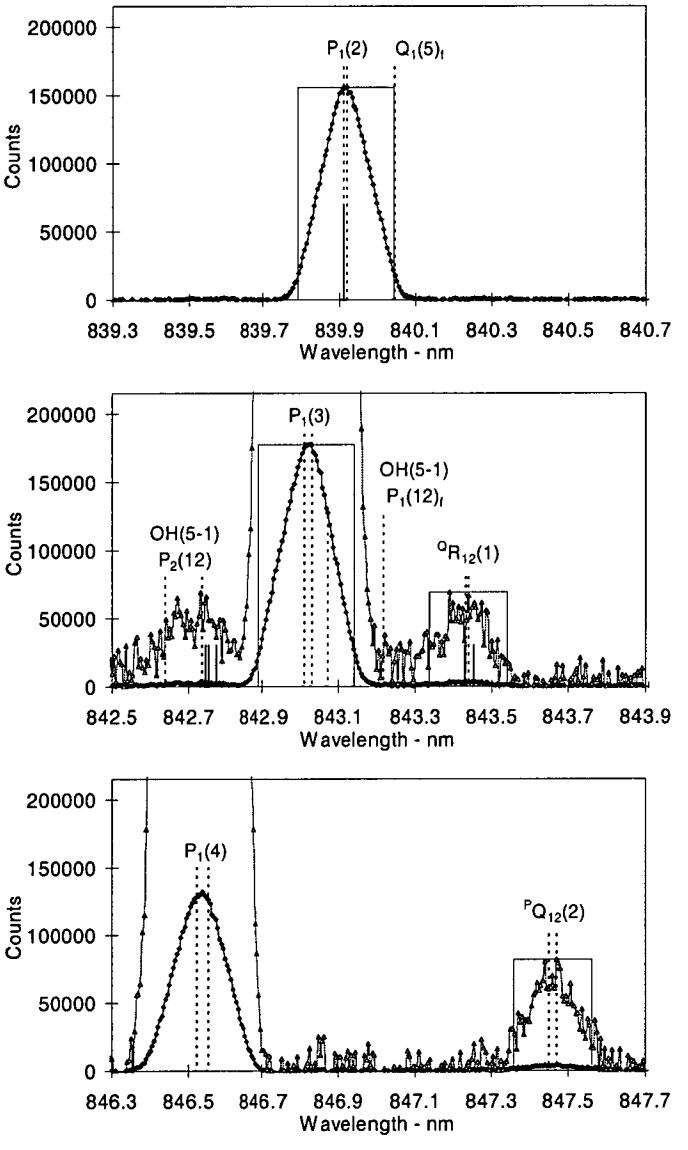

Figure 5-8. Summed profiles of the $P_1(2)$, $^{Q}R_{12}(1)$ and $^{P}Q_{12}(2)$ regions obtained with a 0.155 nm instrument function. The $^{Q}R_{12}(1)$ and $^{P}Q_{12}(2)$ regions are also shown at 20 times magnification to enhance the less intense emissions. The locations of the lines: $Q_1(5)_e$ [at λ839.91nm], $^{Q}R_{12}(2)$ [λ842.74 and λ842.75 nm], $^{Q}R_{12}(3)$ [λ842.77 nm], OH(5-1) $P_1(12)e$ [λ843.07 nm], and $^{Q}R_{12}(4)$ [λ843.43 and λ843.45 nm] are marked without label.

The $^{Q}R_{12}(1)$ emission has a number of contaminants. A count region 0.205 nm wide, centred on the $^{Q}R_{12}(1)$ emission was used. Contamination from OH(5-1) $P_1(12)$ Λ-components is relatively minor, with 1.2% of the OH(5-1)$P_1(12)$ intensity contaminating the $^{Q}R_{12}(1)$ count region. OH(5-1) $P_1(12)_f$ was estimated as 1.0±0.6% of the total $P_1(3)$ intensity as in section 5.3.2.

More significantly, the first ghost of $P_1(3)$ contaminates the $^{Q}R_{12}(1)$ count region. This contamination amounts to 0.23% of the $P_1(3)$ intensity. The $^{Q}R_{12}(1)$ line is blended with $^{Q}R_{12}(4)$ (see Figure 5-8). Goldman's (1982) transition probabilities give $^{Q}R_{12}(4)$ intensity as 2.3% of $^{Q}R_{12}(1)$ at 200 K and 3.1% at 240 K. A value of 2.7% was used to estimate the $^{Q}R_{12}(4)$ contamination. In total, 22% of the $^{Q}R_{12}(1)$ count region is estimated to come from contaminants. A $^{Q}R_{12}(1)/P_1(2)$ ratio of 0.014±0.002 is determined. This is not significantly different from the Goldman (1982) theoretical value of 0.015. Estimating the contamination of the $^{Q}R_{12}(1)$ count region is the greatest source of error, with $P_1(3)$ ghosts being the most significant contaminant.

5.3.8. Comparison with published line ratios.

Table 5-4 compares line ratios calculated from published transition probabilities of T&L, Mies and LWR, with the experimentally determined values. Experimental Q_1/P_1 ratios are significantly lower than any of the theoretical values, but closest to those of LWR. Measured R_1/P_1 ratios are also significantly lower than those derived from T&L and Mies, and lower, but within about twice the error of the LWR values.

J'	Ratio	T&L	Mies	LWR	Experimental
1.5	$Q_1(1)/P_1(2)$	1.42	1.365	1.33	1.261±0.012
2.5	$Q_1(2)/P_1(3)$	0.49	0.46	0.44	0.389±0.006
3.5	$Q_1(3)/P_1(4)$	0.244	0.228	0.213	0.173±0.011
4.5	$Q_1(4)/P_1(5)$	0.145	0.132	0.123	0.094±0.004
2.5	$R_1(1)/P_1(3)$	0.540	0.486	0.451	0.436±0.016
3.5	$R_1(2)/P_1(4)$	0.678	0.590	0.523	0.510±0.010
4.5	$R_1(3)/P_1(5)$	0.732	0.615	0.522	0.483±0.017

Table 5-4. Q_1/P_1 and R_1/P_1 ratios inferred from Mies, LWR and T&L compared with measured values.

Measured $^{Q}R_{12}(1)/P_1(2)$ ratio of 0.014±0.002 is not significantly different from the Goldman (1982) value, while the $^{P}Q_{12}(2)/P_1(2)$ value of 0.022±0.001 is significantly higher. Table 5-2 lists the satellite line ratios calculated from Goldman (1982).

5.4. *Comparison of temperatures derived*

In Table 5-4 experimental transition probability ratios have been derived for emissions arising from the *same* upper rotational state (J'). In order to determine a rotational temperature however, transitions arising from *different* rotational states need to be compared (according to equation 5-1). Thus, it is first necessary to establish how the total transition probability (the sum of the P, Q, R and satellite branch transition probabilities and henceforth referred to as the 'branch sum') varies between rotational states (J'). A comparison of these branch sums (excluding the weak satellite transitions) for vibrational bands from $v' = 6$ are shown in Table 5-5 for the T&L, Mies and LWR transition probability sets.

Strong rotational-vibrational coupling is known to exist for the OH molecule (see for example, Mies). The effect of this is most evident in the weak fundamental ($\Delta v = 1$) band where the branch sums increase rapidly with rotational level (J') and vary significantly between transition probability sets (between 3 and 20 times for the rotational levels shown). However the overtone transitions ($\Delta v>1$) yield relatively consistent branch sums (within 1.5% for those shown) for these rotational levels within all three sets of transition probabilities. It is the consistency of these branch sums that allows conversion of the experimentally determined transition probability ratios to relative (normalised to unity) transition probabilities and enable temperatures to be derived. That is we measure temperature independent ratios between branches (across the P_1, Q_1, R_1 table columns), but need to compare values over different rotational levels (down the J' table rows) and this can be done if the branch sums are equivalent or in a fixed ratio.

Choosing the 6-2 ($\Delta v = 4$) band, the variation in branch sums with J', normalised to the J'=1.5 value for each sets, is shown in Table 5-6. The variation is less than 1%, up to $J' = 4.5$. A 1% error in the OH(6-2) $P_1(2)/P_1(5)$ ratio corresponds to a 1.0 K average error in the derived temperature.

T&L, Mies and LWR do not list transition probabilities for the weak satellite lines, but an estimate of their contribution to the branch sums is made using the Goldman (1982) values, incorporated as a proportion of the P_1-branch transition. The variation in normalised branch sums up to J'=4.5 remains less than 1% for all transition probability sets and are also listed in Table 5-6.

		T&L			T&L	Mies	LWR
	J'	P_1	Q_1	R_1	Branch Sum	Branch Sum	Branch Sum
Δv=1 (6-5)	1.5	1.869	0.763		2.63	0.37	0.94
	2.5	3.012	0.297	0.000	3.31	1.42	1.68
	3.5	4.077	0.146	0.081	4.30	2.92	2.79
	4.5	5.139	0.080	0.413	5.63	4.90	4.29
	5.5	6.201	0.046	1.069	7.32	7.38	6.18
Δv=2 (6-4)	1.5	53.667	72.496		126.16	139.89	84.96
	2.5	65.306	29.700	30.863	125.87	139.83	85.38
	3.5	69.982	15.655	39.727	125.36	139.54	85.34
	4.5	72.568	9.429	42.527	124.52	138.96	85.09
	5.5	74.282	6.183	42.890	123.36	138.10	84.64
Δv=3 (6-3)	1.5	11.672	16.362		28.03	20.696	12.435
	2.5	14.019	6.703	7.278	28.00	20.726	12.494
	3.5	14.834	3.536	9.547	27.92	20.739	12.501
	4.5	15.196	2.132	10.432	27.76	20.726	12.480
	5.5	15.374	1.401	10.758	27.53	20.686	12.435
Δv=4 (6-2)	1.5	1.439	2.048		3.487	1.251	0.910
	2.5	1.719	0.839	0.928	3.486	1.253	0.914
	3.5	1.810	0.442	1.227	3.479	1.254	0.913
	4.5	1.845	0.267	1.351	3.463	1.253	0.911
	5.5	1.858	0.175	1.405	3.438	1.250	0.906
Δv=5 (6-1)	1.5	0.113	0.161		0.274	0.053	0.054
	2.5	0.134	0.066	0.074	0.274	0.052	0.054
	3.5	0.141	0.035	0.098	0.274	0.052	0.055
	4.5	0.144	0.021	0.108	0.273	0.052	0.055
	5.5	0.144	0.014	0.113	0.271	0.051	0.055

Table 5-5. Main branch transition probabilities from T&L, for v'=6 comparing vibrational bands Δv=1-5 and the lower five J' rotational levels, and the branch sums for T&L, Mies and LWR showing the consistency of branch sums with rotational level (J') except for the fundamental Δv=1 transitions affected strongly by rotational-vibrational coupling.

	T&L		Mies		LWR	
J'	$P_1Q_1R_1$	inc.sat.	$P_1Q_1R_1$	inc.sat.	$P_1Q_1R_1$	inc.sat.
1.5	1.000	1.000	1.000	1.000	1.000	1.000
2.5	1.000	0.997	1.002	0.999	1.004	1.002
3.5	0.998	0.992	1.002	0.997	1.003	0.998
4.5	0.993	0.990	1.002	0.999	1.001	0.999
5.5	0.986	0.977	0.999	0.990	0.996	0.987

Table 5-6. Normalised branch sums for the (6-2) band for T&L, Mies and LWR (normalised to the J'=1.5 branch sum in each case). Both normalized branch sums for the main P_1, Q_1 and R_1 transitions, and those determined by including the satellite lines from Goldman (1982) are shown. Normalised sums are consisted within 1% up to J'=4.5.

It is therefore reasonable to normalise the branch sums of each rotational level in vibrational bands other than for $\Delta v = 1$. Thus, we can equate the branch sums for each rotational level (J') to unity and write

$$\tilde{A}_{P_1(J')} + \tilde{A}_{Q_1(J')} + \tilde{A}_{R_1(J')} + \tilde{A}^{P}_{Q_1(J')} + \tilde{A}^{Q}_{R_1(J')} + \tilde{A}^{O}_{P_1(J')} = 1 \qquad \textit{Equation 5-2}$$

where the $\tilde{A}$ now represents a normalised or relative transition probability. Or equivalently, by dividing through by $P_1(J')$ we can write this in terms of the experimentally measured ratios for each J',

$$\frac{Q_1(J')}{P_1(J')} + \frac{R_1(J')}{P_1(J')} + \frac{P_1(J')}{P_1(J')} + \frac{{}^{P}Q_{12}(J')}{P_1(J')} + \frac{{}^{Q}R_{12}(J')}{P_1(J')} + \frac{{}^{O}P_{12}(J')}{P_1(J')} = \frac{1}{P_1(J')} \qquad \textit{Equation 5-3}$$

and then solve for each ratio to derive the relative transition probabilities listed in Table 5-7.

It has not been possible to measure all the ratios required up to the desired level of J'=4.5, but those missing are mainly low intensity satellite lines. Measurements that have been made can be extrapolated to estimate the ratios required, or the best available theoretical estimates can be used to supplement the experimental measurements.

The ${}^{Q}R_{12}(1)/P_1(2)$ ratio measured was equal to the Goldman (1982) theoretical value. No measured estimates of ${}^{O}P_{12}/P_1$ ratios are available. Thus, for the required ${}^{Q}R_{12}/P_1$ and ${}^{O}P_{12}/P_1$ ratios, the values of Goldman (1982) are used. For ${}^{P}Q_{12}/P_1$ ratios, the measured value is used for ${}^{P}Q_{12}(2)/P_1(2)$ [J' = 1.5] and the other required values are scaled proportionally. An uncertainty of half the estimated intensity is used for satellite lines for which no direct measurement is available. Errors are calculated as the RMS sum of the uncertainty in each ratio.

For example for J'=2.5 the measured values from Table 5-4 and the estimated Goldman (1982) equivalents for the satellite lines, substitute into equation 5-3 as

$0.389 + 0.436 + 1.0 + 0.0173 + 0.0053 + 0.0064 = 1/P_1(J')$ which gives $P_1(2.5) = 0.539$, and ratio substitution yields $Q_1(2.5) = 0.210$ and $R_1(2.5) = 0.235$ as listed in Table 5-7.

To make an allowance for $Q_1(5)$ which is blended with the $P_1(2)$ emission, values for the rotational level J'=5.5 are required. A $R_1(4)/P_1(6)$ ratio of 0.48 and a $Q_1(5)/P_1(6)$ ratio of 0.06 are estimated as being consistent with the trends of the measured Q_1/P_1

and R_1/P_1 ratios in Table 5-4. The trends in measured ratios, showing the estimated values for J'=5.5 is plotted in Figure 5-9. Recall that from section 4.3.10, $Q_1(5)$ contributes only about 1.7% (at 200 K) to the $P_1(2)$ line.

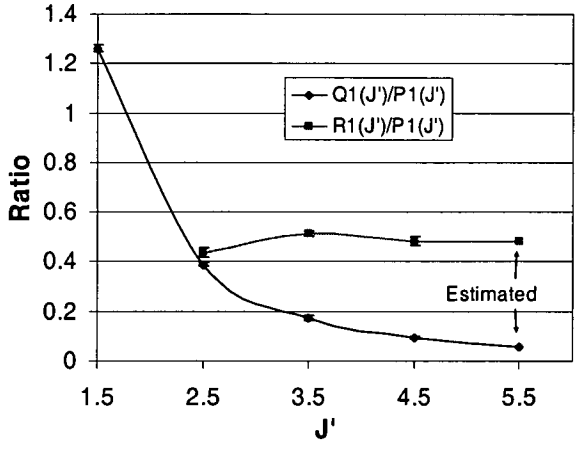

Figure 5-9. Trends in the measured Q_1/P_1 and R_1/P_1 ratios from Table 5-4 and showing the estimated values for J'=5.5 that enable a calculation for $Q_1(5)$.

J'	P_1-branch	Q_1-branch	R_1-branch	Sum
1.5	0.434±0.002	0.548±0.003		0.982±0.004
2.5	0.539±0.006	0.210±0.003	0.235±0.008	0.984±0.010
3.5	0.587±0.006	0.101±0.006	0.299±0.006	0.987±0.010
4.5	0.627±0.007	0.059±0.002	0.303±0.010	0.989±0.012
5.5	0.644	0.039	0.309	0.991

Table 5-7. Experimentally determined normalised transition probabilities ($\tilde{A}$) for the main lines in the OH(6-2) band, and the branch sum (the fraction of the total transition probability carried by the main P,Q,R branches).

Average temperatures, calculated for each of the six possible intensity ratios of $P_1(2)$, $P_1(3)$, $P_1(4)$ and $P_1(5)$ branch lines using the 279 1995 and 1996 spectra and derived using the Mies, LWR and T&L transition probabilities and now also for the experimentally determined normalised transition probabilities ratios are presented in Table 5-8.

Uncertainties listed in Table 5-8 are standard error-in-the-mean. A weighted average temperature is derived from temperatures determined using only the $P_1(2)/P_1(4)$, $P_1(2)/P_1(5)$ and $P_1(4)/P_1(5)$ ratios, weighted inversely as the square of the standard deviation for those ratios as described in section 4.4. Temperatures derived using the $P_1(3)$ intensity are not included in the weighted average because of contamination by the un-thermalised OH(5-1) $P_1(12)$ emission (see section 4.4.4).

As observed in section 4.4 the average temperature derived using the T&L transition probabilities is 6.9 K higher than for Mies values and 12.3 K higher than for LWR values. Weighted average temperature inferred from the experimentally determined line ratios is within measurement uncertainty of the LWR value.

Ratio	T&L	Mies	LWR	Experimental
$P_1(2)/P_1(3)$	222.0±1.5	211.7±1.3	204.3±1.3	200.7±1.2
$P_1(2)/P_1(4)$	**213.5±0.8**	**206.2±0.7**	**200.3±0.7**	**198.8±0.7**
$P_1(2)/P_1(5)$	**212.7±0.7**	**206.4±0.7**	**201.6±0.6**	**199.4±0.6**
$P_1(3)/P_1(4)$	209.3±0.9	203.7±0.8	198.8±0.8	198.8±0.8
$P_1(3)/P_1(5)$	210.5±0.7	205.3±0.7	201.3±0.6	199.4±0.6
$P_1(4)/P_1(5)$	**212.5±1.0**	**207.5±1.0**	**204.1±0.9**	**200.8±0.9**
Wtd.Average	**212.5**	**206.6**	**201.7**	**199.5**

Table 5-8. Average temperatures derived from the 279 1995 and 1996 spectra using the T&L, Mies and LWR transition probabilities, compared with the values obtained using the experimentally determined normalised transition probabilities. Those values contributing to the 'weighted average' are highlighted (see text).

Average temperatures derived from ratios using the $P_1(3)$ intensity with Mies and T&L transition probabilities show evidence of the OH(5-1)$P_1(12)$ contamination. In section 4.5.1 this evidence was used to estimate the average magnitude of OH(5-1)$P_1(12)$ contamination as 1.5% with T&L transition probabilities. Average temperatures derived using LWR transition probabilities show reduced evidence of this contamination, indicating that the magnitude of the contamination estimated in this manner is dependent on choice of transition probabilities. Temperatures inferred from the $P_1(2)/P_1(3)$ ratio are most sensitive to contamination of $P_1(3)$. That there is no evidence for OH(5-1)$P_1(12)$ contamination in averages of the experimentally determined temperatures may result from underestimation of the $Q_1(5)$ contamination of $P_1(2)$. The J'=5.5 experimental estimates are extrapolations, and the intra-band consistency of this state (Table 5-6) is least certain. If this is the reason for the lack of a signature of OH(5-1)$P_1(12)$ contamination, then the implied error in the experimentally derived weighted temperature average is of the order of –1 K.

The principal conclusion that OH(6-2) rotational temperatures are significantly lower than those determined using Mies and T&L transition probabilities remains valid.

5.5. Conclusions

Experimental measurements have been made of the temperature independent (same upper rotational state) Q_1/P_1 and R_1/P_1 emission line intensity ratios in co-added spectra collected at Davis in 1995, 1996 and 1997 accounting for instrument response, Λ-doubling and water vapour absorption and selecting only spectra that were free of auroral contamination and generally collected under moonless, clear sky conditions.

Using these ratios a set of normalised (total branch sum = 1) transition probabilities have been derived for J' up to 5.5 in the OH(6-2) band which are equivalent across the different J' and allow rotational temperature calculations. This is only possible because of the degree of consistency in the transition probability branch sums for $\Delta v > 1$. This method is not possible for the $\Delta v = 1$ bands which are strongly disturbed by vibrational-rotational coupling.

A comparison of the experimentally measured ratios and derived temperatures with those obtained using the published transition probabilities of T&L, Mies and LWR shows:

- Q_1/P_1 ratios for OH(6-2) band lines with J' up to 4.5 are measured to be significantly lower than implied by the three published sets of transition probabilities considered.

- R_1/P_1 ratios for OH(6-2) band lines with J' up to 4.5 are measured to be significantly lower than implied by T&L and Mies transition probabilities, and lower than LWR values by about twice the uncertainty in the measurement.

- Two satellite line ratios are measured. The measured $^{Q}R_{12}(1)/P_1(2)$ ratio is consistent with, while $^{P}Q_{12}(2)/P_1(2)$ is measured to be 20% larger than, Goldman (1982) theoretical values.

- OH(6-2) band rotational temperatures inferred from a set of experimentally determined fractions of J'-state transitions are 2 K lower than temperatures derived using LWR transition probabilities, 7 K lower than temperatures derived using Mies values and 13 K lower than values derived using T&L values.

It is important to note that no implication can be drawn from these experimental measurements with respect to absolute values of the transition probabilities. Variation in absolute values between the three published sets of OH(6-2) transition probabilities is far greater than the variation in their temperature-invariant line ratios. T&L transition probabilities are approximately 3.5, 3.95 and 4.6 times greater than LWR ratios for the low J', P_1-, Q_1- and R_1-branch transition probabilities respectively. Similarly Mies transition probabilities are approximately 1.3, 1.4 and 1.5 times greater than LWR values.

For comparison, the Q_1/P_1 and R_1/P_1 Mies, T&L and LWR ratios compared differ by between 7% and 34% (Table 5-1)

The conclusion that LWR OH(6-2) transition probabilities yield rotational temperatures most consistent with experimental measurements provides no direct evidence that absolute values of LWR transitional probabilities are experimentally preferred, however this set of transition probabilities are used in subsequent analysis in this work.

6. Temperature Variability & Trends

This chapter brings together eight years of OH(6-2) band rotational temperature measurements collected at Davis between 1990 and 2000; a total of 126,444 spectra yielding 1310 nightly average temperatures over the interval when measurements are possible [DOY 49 - 296]. Analysis procedures developed in chapter 4, the improvements suggested at the end of that chapter, and LWR transition probabilities (established as being closest to the experimentally determined ratios in chapter 5) are applied in obtaining final temperature results. Accuracy of the temperatures derived from this analysis are now considered optimal for the OH(6-2) band using the Davis scanning spectrometer. Nightly averaged temperatures are examined for seasonal variability, solar cycle association and long-term trends.

Much of this work has been accepted for publication in the Journal of Atmospheric and Solar-Terrestrial Physics entitled "Seasonal variations and inter-year trends in seven years of hydroxyl airglow rotational temperatures at Davis station (69°S, 78°E), Antarctica", Burns *et al.* (2001b). Earlier work, on subsets of these data, has also been published in Burns *et al.* (1998) "Monitoring the Antarctic mesopause region for signatures of climate change", Annals of Glaciology 27, 669-673 (a special edition on measurement of climate change in Antarctica) and in Burns *et al.* (2001a) "The Mesopause region above Davis, Antarctica (68.6°S, 78.0°E)" in "Long Term Changes and Trends in the Atmosphere" Ed. G. Beig, proceedings of the First International Workshop on Long Term Changes and Trends in the Atmosphere. Copies of these papers are included in appendix A.

6.1. Introduction

Seasonal variability, solar cycle association and long-term trends in mesopause region temperatures have been monitored by a number of observers. Full seasonal coverage is not possible at Davis with this instrument, but autumn, winter and spring results may be compared as nightly and monthly averages. Winter average temperatures, over the interval D106-258, are calculated to compare solar cycle and long-term trends.

6.1.1. Seasonal variability

Measurements of seasonal variations in temperature of the upper mesosphere from southern hemisphere sites are sparse (see Scheer (1995) for sites and also comments by Scheer *et al.* (1998) on Hecht *et al.* (1997)).

Clancy and Rusch (1989) (see also Clancy *et al.* (1994)) present a global five-year morphology of mesosphere temperatures derived from ultraviolet limb radiances measured by the Solar Mesosphere Explorer (SME) satellite. This technique measured sunlight scattered from the Earth's limb, so winter observations were not possible at high latitudes and summer observations are possibly contaminated by polar mesospheric clouds. For the upper mesosphere, at 70°S, monthly averages for four mainly equinoctial months were presented. After allowing for the 6-month seasonal difference, upper mesosphere monthly temperature averages reported for 70° latitude were similar between hemispheres.

Lübken *et al.* (1999) evaluated 24 falling sphere density measurements collected above Rothera (68°S, 68°W) in January and February 1998. They found January mesopause (87 km) temperatures not statistically significant different to equivalent northern hemisphere July measurements, However the southern upper mesosphere temperatures (around 82 km) were 7-8 K warmer than northern hemisphere equivalents by the end of February.

Williams (1996) gives an observing season average hydroxyl airglow temperature for Davis (69°S, 78°E) of 205±10 K from 139 OH(8-3) band spectra collected over seven months in 1987. These calculations do not account for the instrumental spectral response thus some doubt remains about absolute values. Monthly averages, however, show an abrupt post mid-winter cooling of 10 to 20 K.

Hydroxyl airglow intensity measurements have long been used to investigate seasonal temperature variations in the upper mesosphere in northern polar regions [see for example Shefov (1969a) and Myrabo (1986)]. There are uncertainties inherent with using hydroxyl temperatures for this purpose. Hydroxyl line intensities used to derive temperatures are integrated over the airglow emission layer that has a mean height of 87 km and mean thickness of 8 km (section 2.5 and Baker and Stair (1988)). She and Lowe (1998), from a comparison of hydroxyl airglow temperatures

with sodium lidar temperature profiles and utilising satellite determined hydroxyl profiles, concluded that hydroxyl rotational temperatures can be used as a proxy for temperatures at 87±4 km.

Seasonal variations in hydroxyl temperatures may be influenced by seasonal variations in average height and profile shape of the hydroxyl layer. Variability in nightly hydroxyl temperatures may result from gravity waves, tides, or height and profile variations coupled with variable sampling. It is as yet unknown if there are any significant latitudinal variations in the hydroxyl layer. It is assumed that values obtained by Baker and Stair (1988) and She and Lowe (1998) apply in polar regions.

6.1.2. Solar cycle variation

A number of publications have reported solar cycle associated variability in temperatures at hydroxyl altitudes.

- Shefov (1969a) shows solar cycle variations in hydroxyl rotational temperatures of order 25 K for Zvenigorod (56°N, 37°E) and 20 K for Abastumani (42°N, 43°E).

- Sahai *et al.* (1996), from observations over three winters, report a positive association between nightly hydroxyl-temperature averages at Calgary (53°N, 114°W) and the 10.7 cm solar flux of 0.32 K $(sfu)^{-1}$ [solar flux unit : sfu = 10^{-22} W m^{-2} Hz^{-1}]. This implies a 38 K solar cycle variation for a 120 sfu range [38 K:120 sfu].

- Labitske and Chanin (1988), using rocketsonde data from Heiss Island (81°N, 58°E), show solar-cycle temperature variations at 80 km of order 25 K.

- Lübken and von Zahn (1991) find a solar-variability associated temperature dependence at hydroxyl heights of 0.15 K $(sfu)^{-1}$ [18 K:120 sfu] for Andenes (69°N, 16°E).

- Bittner *et al.* (2000) analyse 2457 nights of hydroxyl temperatures above Wuppertal (51°N, 7°E) from the interval 1987 to 1995. They report positive correlations of temperature fluctuations with solar 10.7 cm flux for periods greater than ~30 days and negative correlations for periods less than ~10 days.

6.1.3. Long term trends

Several model studies indicate that the stratosphere and mesosphere will cool at a greater rate than warming of the troposphere due to increases in greenhouse gas concentrations, and that this cooling is expected to be greatest at high latitudes (section 1.2). Some observational evidence suggests that pronounced long-term cooling, in excess of model predictions, has already taken place (section 1.3). Mesopause region observations (summarised from section 1.3) include:

- Annual hydroxyl temperatures from a 39-year time-span collected at Zvenigorod (56°N, 37°E) and Abastumani (42°N, 43°E) show a 0.7 Ka^{-1} (K per annum) decrease (Golitsyn *et al.* (1996)).

- Bittner *et al.* (2000) report an increase in temperature variability of 0.8 K per decade (~16% per decade) in hydroxyl temperatures above Wuppertal (51°N, 7°E).

- Gadsden (1985, 1998) reports an increase in noctilucent cloud (~83 km) observations over north-western Europe. Hypotheses for this variation include a decrease (between 0.3 Ka^{-1}; Gadsden (1990) and 0.6 Ka^{-1}; Gadsden (1998)) in mesopause region summer temperatures and/or an increase in water vapour concentrations stemming from anthropogenic increases in tropospheric methane (Thomas *et al.* (1989)).

- Taubenheim *et al.* (1997), from a study of 33 years of radiowave reflection heights in summer, report a cooling of 0.6 Ka^{-1} in the column-mean temperature between the stratopause and 82 km.

- Clemesha *et al.* (1992), calculate a uniform cooling throughout the mesosphere of 0.3Ka^{-1} is necessary to account for a descent in the centroid height of the sodium layer over 15 years above Sao Jose dos Campos (23°S, 46°W).

Evidence has also been presented against large magnitude temperature trends in the upper mesosphere however. For example:

- Krueger and She (1999) find most of a 0.4±0.6 Ka^{-1} cooling derived from sodium lidar data at Fort Collins (41°N, 105°W) between 1990-1997 (underlying an

episodic increase attributed to the Pinatubo eruption) can be attributed to the decline in the solar cycle.

- Stegman (http://www.misu.su.se/~jacek/Ground/index2.html) finds limited evidence for a 0.5 Ka^{-1} increase in OH rotational temperatures between 1991 and 1998 (through solar minimum) at Sandkullen (59°N, 18°E).

- Lowe (priv. comm.) finds a small positive linear trend (0.07 Ka^{-1}) in OH(3-1) temperatures from Delaware observatory (43°N, 81°W) since 1990.

- Lübken (2000) compares in-situ measurements of polar-region, summer temperatures taken 30 years apart, at times of low solar activity, and finds no significant temperature trend in the upper mesosphere (75 - 85 km).

- Preliminary results of Sigernes *et al.* (http://fred.unis.no/OHNobs) find a nearly zero (+0.03±0.002 Ka^{-1}) temperature trend in over twenty years of winter (December and January) OH rotational temperatures at Adventdalen, Svalbard (78°N, 15°E).

6.2. Data selection criteria

A catalogue of the data presented here and the various instrument operating modes is given in Table 3-16. In order to maintain count rate equivalence to spectra collected in 1990, spectra in 1995 and 1996 were co-added in groups (typically of 5 scans) to yield a total accumulation time = (number of co-added scans) × (dwell time) / (step size) of 100 seconds per nm. The fast spectral-segment mode, used from the end of 1996, achieves this in a single scan.

Various operating modes in 1994 complicate the analysis of this year. Spectra up to D167 have 100 sec/nm accumulation times, so are processed individually. Spectra in the interval D182-209 and D212-216 have 50 sec/nm accumulation times, so two spectra are co-added before analysis. Spectra in the interval D210-211 and D217-294 have 15 sec/nm accumulation times. Insufficient spectra are available in these intervals to produce a nightly average if they are co-added in groups of 6 or 7 to yield equivalent count rates. Instead, spectra are processed individually, and a comparison is made of 1995 and 1996 nightly averages derived from single scan (20 sec/nm

accumulation times), and co-added spectra (100 sec/nm) to test the validity of this approach. (see section 6.3).

Instrument response corrections are applied as determined in section 3.5.5. Langhoff *et al.* (1986) transition probabilities are used, as determined most appropriate in chapter 5. Temperatures are derived as a weighted average of temperatures from three ratios possible from $P_1(2)$, $P_1(4)$ and $P_1(5)$ relative intensities (see section 4.4). $P_1(3)$ is not used because of blending with an unthermalised OH(5-4) emission (see section 4.5.1)

Different temperature derivation techniques are used on continuous (up to D269, 1996) and discrete-segment (from D269, 1996) spectra (see Figure 3-53). The P_1-line and background intensities for discrete-segment spectra are linearly interpolated to a common time between successive scans (see Figure 3-21). This approach is not feasible for continuous spectra due to long acquisition times. The effect of these different analysis techniques on the derived temperature averages is discussed in section 6.2.9.

Spectra are collected under all night-time conditions. Some spectra each year failed the analysis routines and were discarded. These spectra mostly suffered from very low signal-to-noise or highly variable auroral contamination in the background such that the offset search failed to find the correct emission peak or subtraction of the background from a line yielded a negative intensity.

For spectra that produced a temperature, acceptance of that temperature depends on a range of criteria. For all years, the following selection criteria are applied:

- weighted standard deviation of the temperatures derived for each of the three line-ratios is better than 15 K. This is a measure of the self-consistency of the three possible intensity ratio's.

- sufficient photon counts are measured in each line, so that the statistical uncertainty in the weighted temperature is less than 10 K. This is the weighted 'counting error' defined in section 4.4.1. There is at least this degree of uncertainty in individual spectra due to counting statistics. This criterion rejects spectra with significantly reduced intensities due to cloud cover.

- slope of a linear fit through the selected background regions is less than 0.6 counts s^{-1} nm^{-1}. This removes extreme background variability due to twilight or changing aurora or cloud cover.

- absolute magnitude of background intensities is less than 100 counts s^{-1}, which removes extreme moon and auroral contamination.

Additionally for discrete-segment spectra (from D269, 1996) the:

- rate of change of emission intensity is limited to 4% min^{-1} for $P_1(2)$ and $P_1(4)$ and to 5% min^{-1} for $P_1(5)$.

- rate of change of each background is limited to ±2 counts per minute.

The number of spectra rejected by these criteria for each year is listed in Table 6-1. Criteria 'Total' values refer to the total number of spectra rejected by that criterion alone. 'Running' is the total number of rejected spectra for each criteria applied sequentially across the columns. Percentages are calculated on the total that pass the analysis.

Values for the rejection limits were chosen by examination of weighted temperature and uncertainty against binned intervals of each particular criterion. Selection of criteria, and setting limits for them, is a somewhat arbitrary and iterative process. A lot depends on the subjective concept of what constitutes a 'bad' spectrum, which might bias the weighted mean. Ideally, a minimum number of criteria would be applied, that reject the maximum number of 'bad' spectra and retain the maximum number of 'good' spectra. Limits are generally set where the weighted temperature and uncertainty are no longer influenced by tighter restriction of that criterion.

In order that real temperature variations in the data do not influence the selection of criteria and limits, a long period of relatively consistent and stable temperatures is required. The most complete year of observations is 1998 and the interval from DOY 86 to 158 was selected for the purpose of evaluating selection criteria limits.

Year	Data Type	Total Spectra Scanned	Total that passed analysis	Total that pass all criteria	Daily Mean ±20K Subset		Number rejected by criteria							
							SD <15	CE <10	Slope <|0.6|	Back <100	$P_1(2)$ <4%/min	$P_1(4)$ <4%/min	$P_1(5)$ <5%/min	Back <3cts/min
1990	Continuous	466	457	328	325	Total	49	8	113	35				
				71.8%	71.1%	%	10.7%	1.8%	24.7%	7.7%				
						Running	49	7	71	2				
						%	10.7%	1.5%	15.5%	0.4%				
1994	Continuous	2305	1870	1042	933	Total	541	381	283	60				
				55.7%	49.9%	%	28.9%	20.4%	15.1%	3.2%				
						Running	541	167	118	2				
						%	28.9%	8.9%	6.3%	0.1%				
1995	5 sums	3883	3858	2813	2645	Total	549	128	555	337				
				72.9%	68.6%	%	14.2%	3.3%	14.4%	8.7%				
						Running	549	57	355	84				
						%	14.2%	1.5%	9.2%	2.2%				
1995	Continuous	18666	16022	7472	6319	Total	5116	416	2999	1219	1062	1632	2862	1047
				46.6%	39.4%	%	31.9%	2.6%	18.7%	7.6%	6.6%	10.2%	17.9%	6.5%
						Running	5116	138	1572	195	291	493	688	57
						%	31.9%	0.9%	9.8%	1.2%	1.8%	3.1%	4.3%	0.4%
1996	5 sums to D269	3354	3168	2253	2154	Total	376	171	582	274				
				71.1%	68.0%	%	11.9%	5.4%	18.4%	8.6%				
						Running	376	91	388	60				
						%	11.9%	2.9%	12.2%	1.9%				
1996	Continuous to D269	16773	14338	7801	6872	Total	3743	327	2601	913	785	1124	2079	1136
				54.4%	47.9%	%	26.1%	2.3%	18.1%	6.4%	5.5%	7.8%	14.5%	7.9%
						Running	3743	116	1497	174	183	287	442	95
						%	26.1%	0.8%	10.4%	1.2%	1.3%	2.0%	3.1%	0.7%

Year	Data Type	Total Spectra Scanned	Total that passed analysis	Total that pass all criteria	Daily Mean ±20K Subset		Number rejected by criteria							
							SD <15	CE <10	Slope <|0.6|	Back <100	$P_1(2)$ <4%/min	$P_1(4)$ <4%/min	$P_1(5)$ <5%/min	Back <3cts/min
1996	Segment from D270 $P_1(2)/P_1(4)$ only	1824	1647	770	684	Total		422	743	357	216	262		341
				46.8%	41.5%	%		25.6%	45.1%	21.7%	13.1%	15.9%		20.7%
						Running		422	402	11	10	24		8
						%		25.6%	24.4%	0.7%	0.6%	1.5%		0.5%
1997	Segment	20081	19680	14355	13828	Total	2343	2406	1786	1128	691	875	1842	1007
				72.9%	70.3%	%	11.9%	12.2%	9.1%	5.7%	3.5%	4.4%	9.4%	5.1%
						Running	2343	1350	764	117	146	190	337	78
						%	11.9%	6.9%	3.9%	0.6%	0.7%	1.0%	1.7%	0.4%
1998	Segment	25500	23915	16332	15987	Total	3137	2820	3747	3077	1007	1140	2629	2940
				68.3%	66.8%	%	13.1%	11.8%	15.7%	12.9%	4.2%	4.8%	11.0%	12.3%
						Running	3137	1475	1725	463	122	121	275	518
						%	13.1%	6.2%	7.2%	1.9%	0.5%	0.5%	1.1%	2.2%
1999	Segment	14948	13995	9960	9583	Total	1680	1693	1491	858	420	491	1140	1130
				71.2%	68.5%	%	12.0%	12.1%	10.7%	6.1%	3.0%	3.5%	8.1%	8.1%
						Running	1680	1024	706	124	74	82	177	168
						%	12.0%	7.3%	5.0%	0.9%	0.5%	0.6%	1.3%	1.2%
2000	Segment	26020	23054	15949	15479	Total	3710	3149	2827	2304	1048	1044	2649	2409
				69.2%	67.1%	%	16.1%	13.7%	12.3%	10.0%	4.5%	4.5%	11.5%	10.4%
						Running	3710	1480	987	208	118	133	306	163
						%	16.1%	6.4%	4.3%	0.9%	0.5%	0.6%	1.3%	0.7%

Table 6-1. Number of spectra rejected by the selection criteria for each year. 'Total' refers to the total number of spectra rejected by that criterion alone. 'Running' is the running total of rejected spectra for criteria applied sequentially across the columns. Percentages are calculated on the total that pass the analysis.

6.2.1. Standard deviation

If the intensity of each line has been measured correctly, then each line-pair ratio should yield the same temperature result. If temperatures are not consistent then at least one line had been misestimated. Figure 6-1 plots weighted standard deviation (SD) against weighted mean temperature for 7589 spectra that pass the analysis in the selected 1998 interval, with no other selection criteria applied.

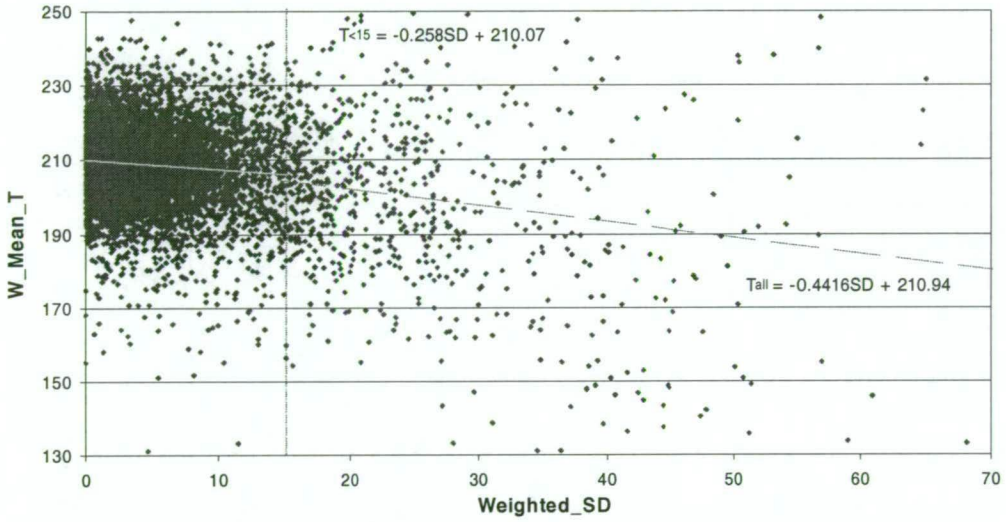

Figure 6-1. Weighted standard deviation vs weighted mean temperature for 7589 spectra in the interval DOY 86-158, 1998. A linear fit to all data is compared with a linear fit to points below the 15 K SD limit.

Fitted trends show high SD is associated with lower temperatures (slope -0.442). If SD is limited to 15 K the slope is reduced to -0.258. Figure 6-2 plots mean temperature derived for selected SD limits against that limit. Points are labelled with data percentiles and errors bars are standard error-in-the-mean. The 15 K limit is about the 90 percentile, thus about 10% of the data is rejected by this criterion.

Figure 6-3 shows the mean temperatures for selected SD bins. Data are labelled with the number of samples in each bin and error bars indicate standard error-in-the-mean. Mean temperatures are relatively consistent and within the error up to the SD 10-12 K bin. They then decline 2-3 K for bins out to SD 20-25 K, and are dramatically reduced beyond. From these, perhaps a tight restriction would be a SD limit of 10 K (rejecting ~20% of the data) and a wider one of 20 K (rejecting ~5%). A mid-ground value of 15 K was chosen.

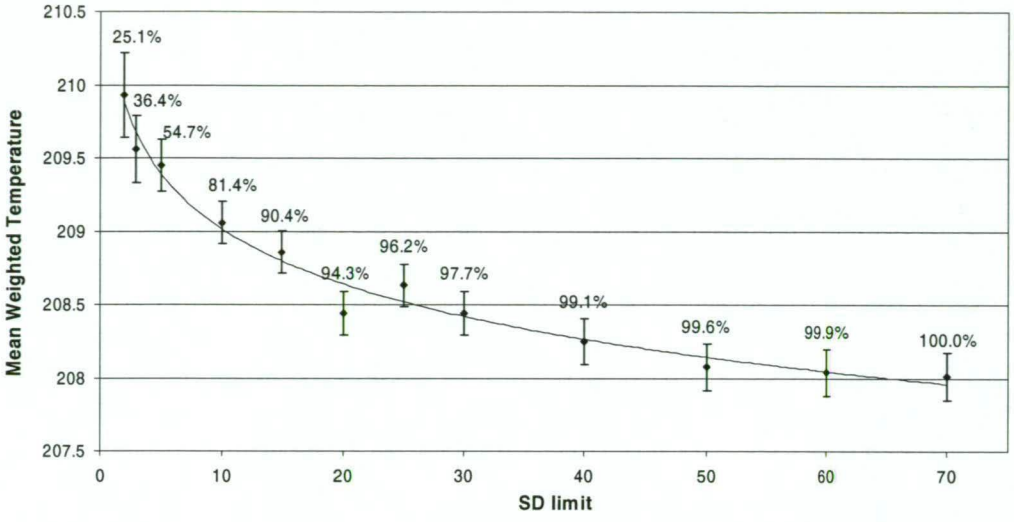

Figure 6-2. Mean weighted temperature plotted against the standard deviation limit applied. Points are labelled with data percentiles. The 15 K limit is approximately the 90 percentile, thus 10% of data is rejected by this criterion.

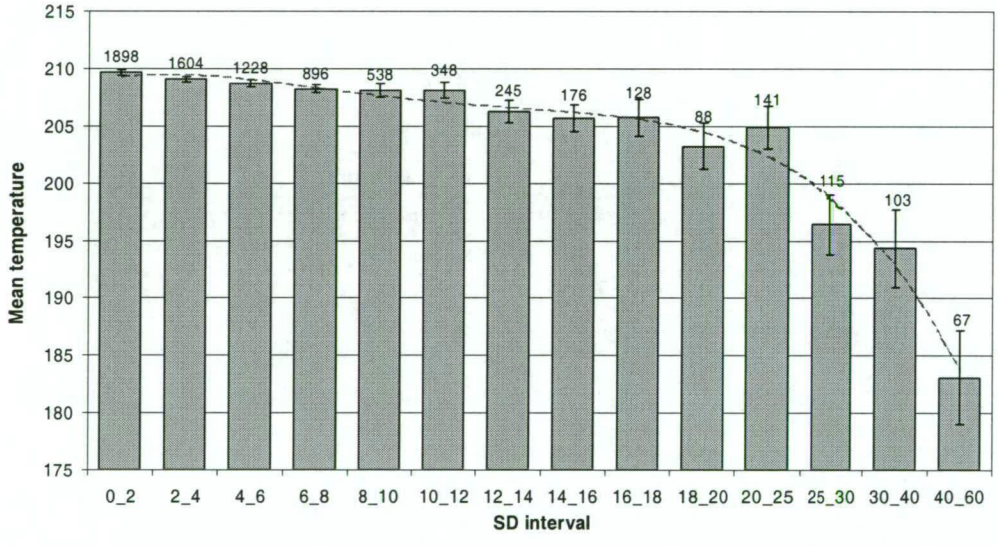

Figure 6-3. Mean temperatures calculated for selected SD bins. Data labels are the number of points in each bin and error bars show standard error-in-the-mean.

A physical explanation for the declining temperature trend with SD may lie in the OH photochemistry. It was shown in section 2.4.1 that calculated rate coefficients for the hydrogen-ozone reaction are temperature dependent (Table 2-4). Around 200 K, the production rate varies about 1.3%/K (using the Clyne and Monkhouse (1977) rate from Table 2-4). Thus, if temperature dependencies of loss mechanisms are small, a positive correlation of intensity with temperature of similar magnitude is expected (see Figure 6-16). High SD is likely to be associated with low intensity (due to

greater uncertainty in the intensity estimate) and thus also with low temperatures. A plot of SD versus integrated intensity [$P_1(2)+P_1(4)+P_1(5)$] shows that this relationship holds [Figure 6-4]. Placing too tight a limit on standard deviation may thus bias the selection to warmer temperatures. This provides justification for the decision not to restrict SD to the tighter 10 K.

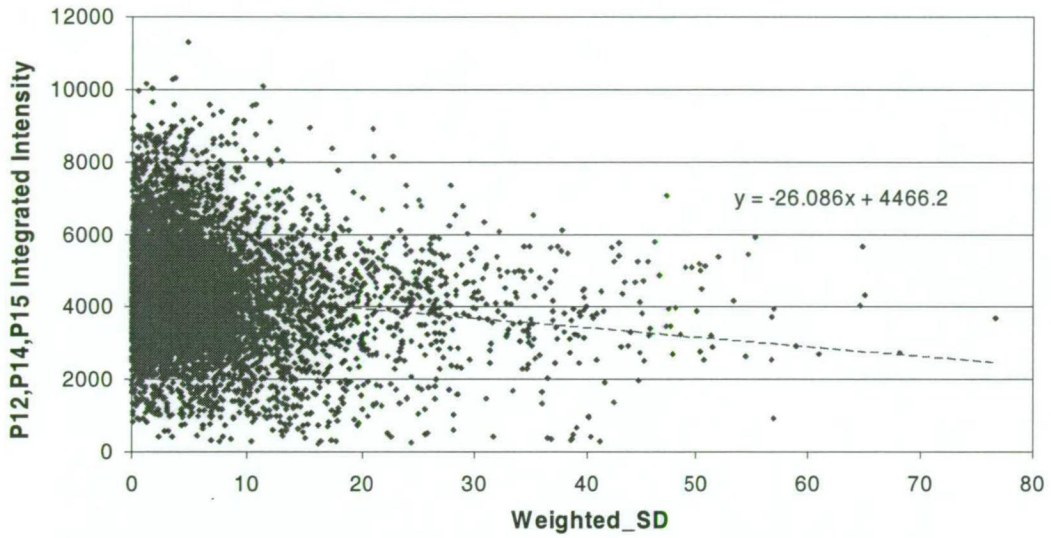

Figure 6-4. Integrated $P_1(2)+P_1(4)+P_1(5)$ intensity versus SD showing a similar trend to Figure 6-1. Temperature and intensity are correlated through the temperature dependence of the hydrogen-ozone reaction rate coefficient.

6.2.2. Counting error

Determination of a limit on counting error (CE) was approached in a similar manner to SD. Figure 6-5 shows weighted temperatures versus CE for all data in the interval. The distribution shows a much tighter cluster around the 6 K mean CE. Overall trend in this case shows an increase in temperature with CE, which is expected following the same temperature-intensity relationship argued above, as CE is proportional to the square-root of intensity via equation 4-7. However if the data are restricted to CE <10 K the trend is reversed. This can be seen more clearly in Figure 6-6 showing the mean temperature against selected CE limits for all data in the interval. The turning point is at about 13 K. It suggests that CE does not have a dominant influence on temperature below this level. Indeed, if the SD<15 criteria is applied this dependence vanishes (see also Figure 6-6), verifying that it is primarily controlled by the SD, which raised the temperature as the low intensity, low temperatures are preferentially removed.

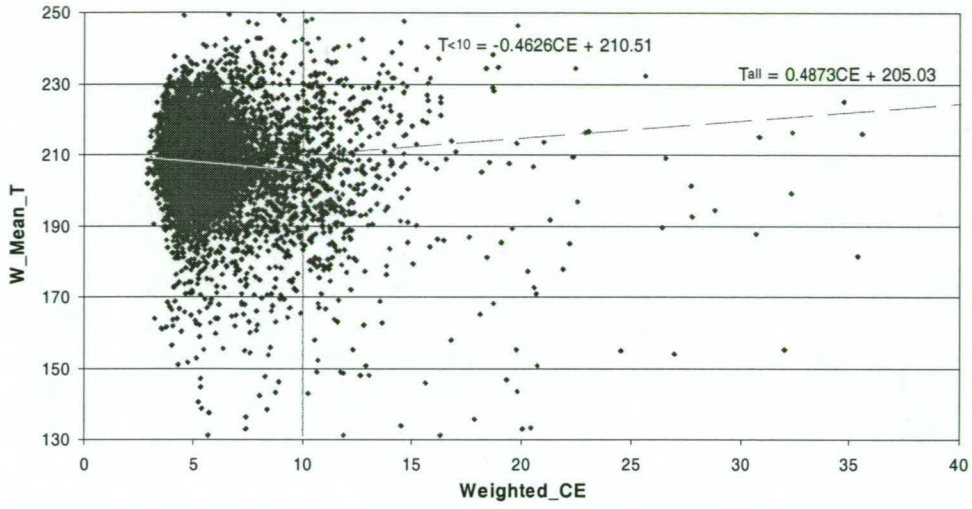

Figure 6-5. As for Figure 6-1 except for the weighted CE and a 10 K CE limit.

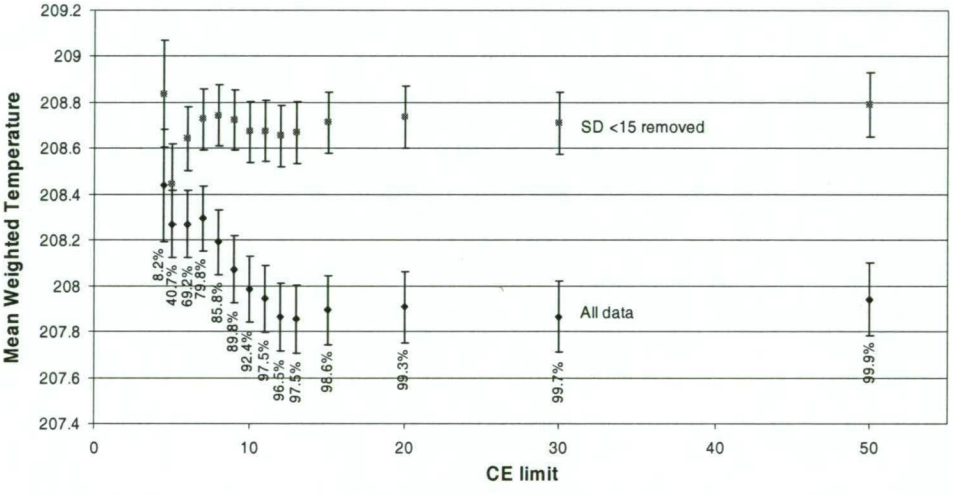

Figure 6-6. Mean weighted temperature against CE for all data (diamonds, labelled with percentiles) and with the SD<15 limit applied (squares).

Figure 6-7 shows mean temperatures derived for selected CE bins. Temperatures are relatively consistent, within the error out to the CE 10-11 K bin, after which they diverge and errors become larger. The limit selected on CE is consequently 10 K, which rejects about 8% of the data.

SD and CE are the primary rejection criteria as they represent the consistency and signal-to-noise uncertainty associated with measurement of each line in all spectra. Other selection criteria were examined to specifically reject data sampled during abnormal or atypical events, such as high levels of scattered moonlight and rapid auroral fluctuations. These are determined with both SD<15 and CE<10 criteria applied. At total of 6501 samples remain for the selected 1998 interval.

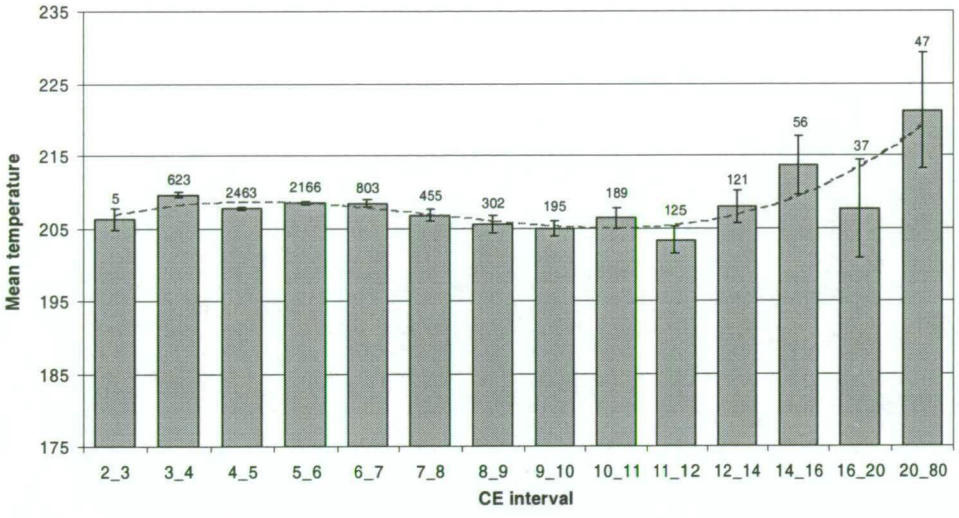

Figure 6-7. Mean temperatures calculated for selected CE bins. Data labels are the number of points in each bin and error bars show standard error-in-the-mean.

6.2.3. Background Slope

Figure 6-8 shows the distribution of background slope for the 6501 weighted temperatures of the 1998 interval with SD<15 and CE<10. Slope is calculated from the best linear fit through (time interpolated) averages of the wavelength intervals λ840.64-840.84, λ843.85-844.05 and λ847.85-848.60 nm (see Figure 3-53). Temperature shows a negative correlation with slope i.e. lower temperatures when the background increases with wavelength. This suggests an overestimate of $P_1(2)$ and/or underestimate of $P_1(5)$ with positive slope.

There is also a slight bias toward positive slope, which is expected as the dominant N_2 1PG(3-2) band increases across the region [see Figure 4-3] (thus aurora effects $P_1(5)$ to the greatest extent). Background regions for each P_1-branch line (Table 4-4) are selected to balance average auroral and Fraunhofer contributions. It is apparent that increased aurora leads to an overestimate of the $P_1(5)$ background, hence an underestimate of $P_1(5)$, and a lower temperature. A limit on background slope is therefore imposed to reject strong aurora contamination.

Figure 6-9 shows mean temperature for selected slope bins. Slope limits of ±0.6 counts/sec/nm were selected which rejects about 9% of the data. This is consistent with criteria used for analysis of 1990 data in chapter 4. A maximum temperature variation for an individual spectrum due to slope, is ±5 K with these limits. On average however the variation is balanced zero by the selection of background

regions. Mean temperature with ±0.6 counts/sec/nm limits is only 0.2 K lower than with ±0.2 counts/sec/nm limits for example.

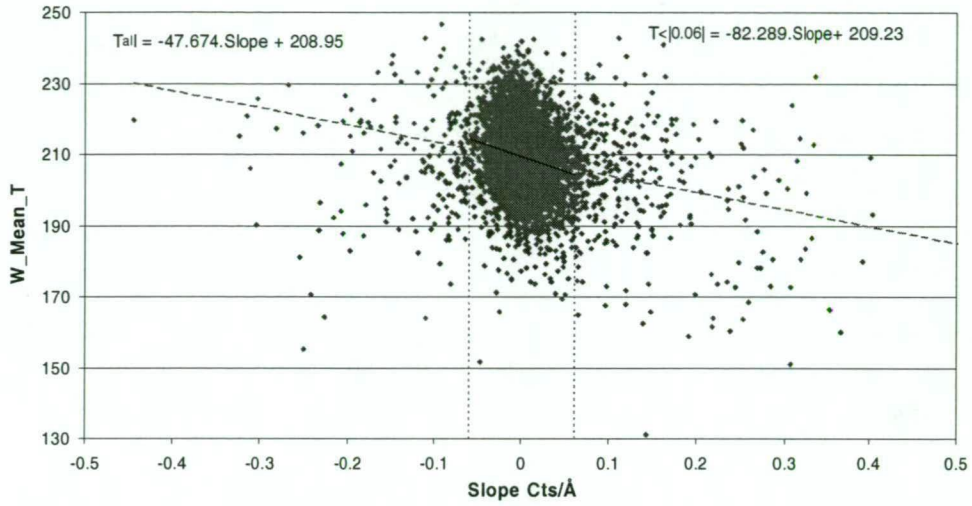

Figure 6-8. Weighted temperature versus slope for 6501 spectra in the selected 1998 interval with SD<15 and CE<10. A linear fit to all data is compared with a linear fit to points with slope <|0.6| counts/sec/nm.

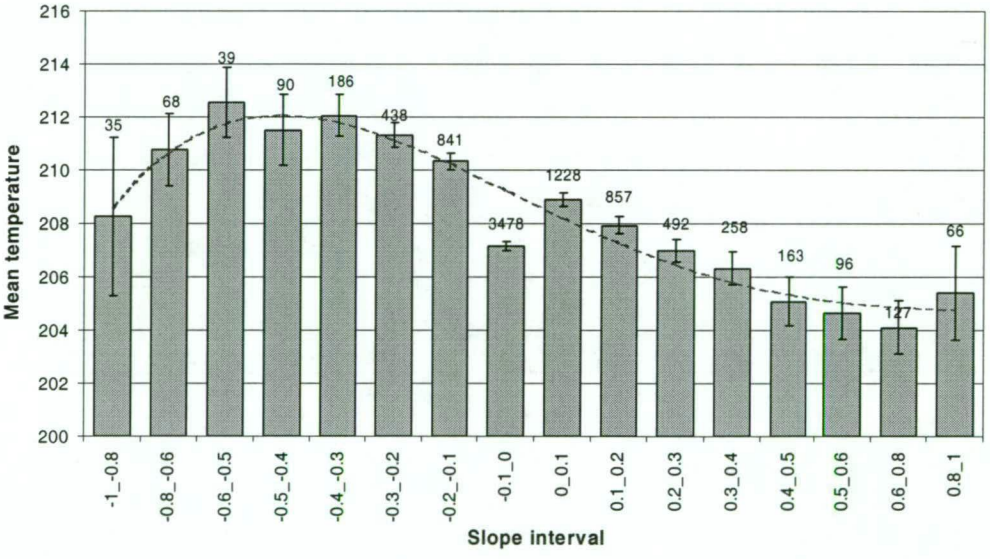

Figure 6-9. Mean temperature for selected slope bins. Data labels show the number of points in each bin and error bars show standard error-in-the-mean.

6.2.4. Background magnitude

A high background generally implies the spectrum is significantly contaminated by scattered moonlight or sunlight. Figure 6-10 shows clearly the 28 day lunar cycle in the $P_1(2)$ background (all data from 1998 with SD<15K, CE<10K and solar altitude <10° is plotted in this figure).

Figure 6-11 shows weighted temperature versus $P_1(2)$ background for the 6501 samples in the selected 1998 data interval with SD<15 K and CE<10 K. Both $P_1(4)$ and $P_1(5)$ have significantly more Fraunhofer absorption under them than $P_1(2)$ (see Figure 4-6). A slightly negative temperature trend is observed with increasing background, consistent with $P_1(4)$ and $P_1(5)$ being underestimated due to increased Fraunhofer absorption. $P_1(4)$ and $P_1(5)$ backgrounds yield similar results.

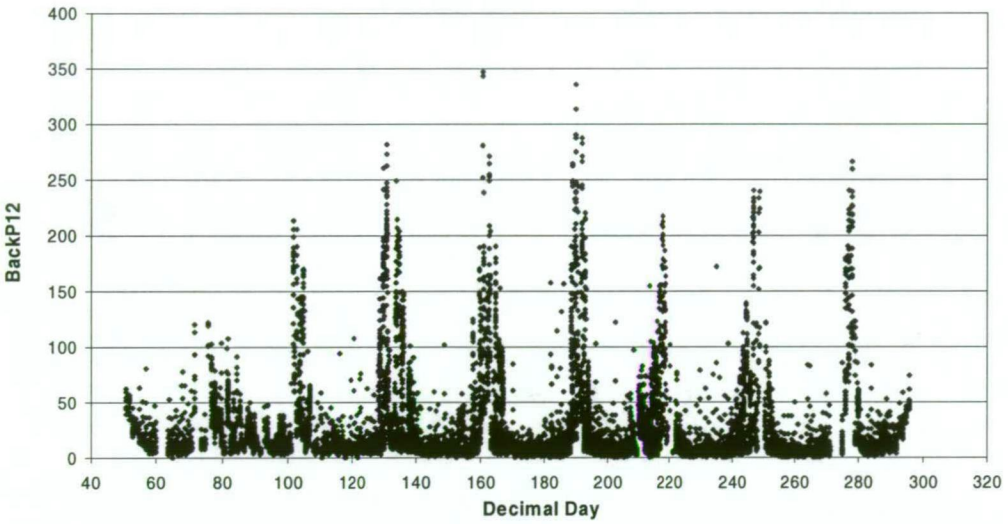

Figure 6-10. $P_1(2)$ backgrounds over 1998 (with SD<15 K,CE<10 K, sun<-10°) showing clearly the 28 day lunar cycle.

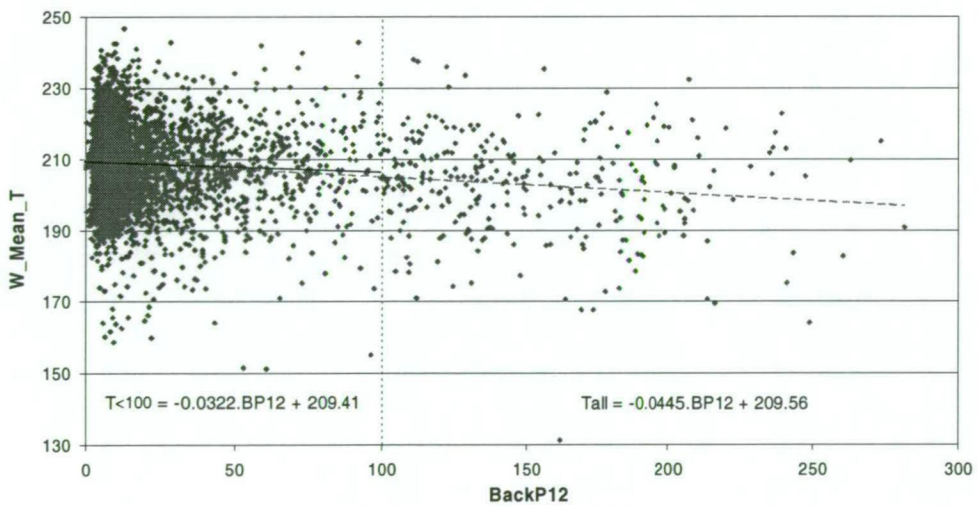

Figure 6-11. Weighted temperature versus $P_1(2)$ background. A linear trend for all 6501 samples is compared with a linear fit to those below 100 counts/sec.

Figure 6-12 shows mean temperature for selected background bins. Mean temperatures are relatively consistent out to the 75-100 counts/sec bin before they fall away. A similar results are obtained for $P_1(4)$ and $P_1(5)$ backgrounds. Background

limits for each background were thus set at 100 counts/sec, which rejects about 5% of the data. A maximum temperature variation of 3 K is implied with these limits.

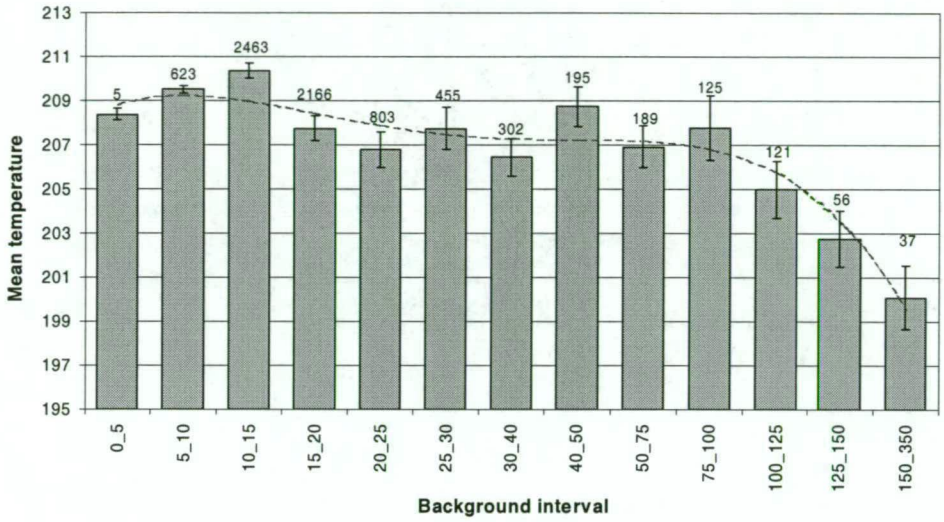

Figure 6-12. Mean temperature for selected background bins. Data labels are the number of points in each bin. Errors are standard error-in-the-mean.

6.2.5. Rates of change

Additional criteria were set on interpolated spectra to reject extreme rates of change in line intensities and backgrounds. These criteria were assessed with the aforementioned criteria limits set, i.e. SD<15 K, CE<10 K, Slope<|0.6| counts/sec/nm and backgrounds<100 counts/sec. A total of 5768 points in the 1998 sample data remain.

Figure 6-13 plots rates of change of $P_1(2)$, $P_1(4)$ and $P_1(5)$ emissions against weighted temperature separately and compares best-fit trends with and without the selected limits. $P_1(2)$ shows a relatively strong decreasing trend with increasing rate of change while $P_1(4)$ and $P_1(5)$ show very slight increasing, and decreasing trends respectively. A relatively high $P_1(2)$ intensity *is* associated with lower temperatures, but it is not clear why the rate of change is also associated.

As these criteria are not applied to the continuous scan spectra, limits were only set to reject outliers. A rate of 4% per minute on $P_1(2)$ and $P_1(4)$ allows for a 29% variation in emission intensity over the 7min 20sec cycle time. A 5% limit was set on $P_1(5)$ due to its lower intensity and this allows for a 37% variation over the cycle. Only about 2% of the remaining data are rejected by these limits.

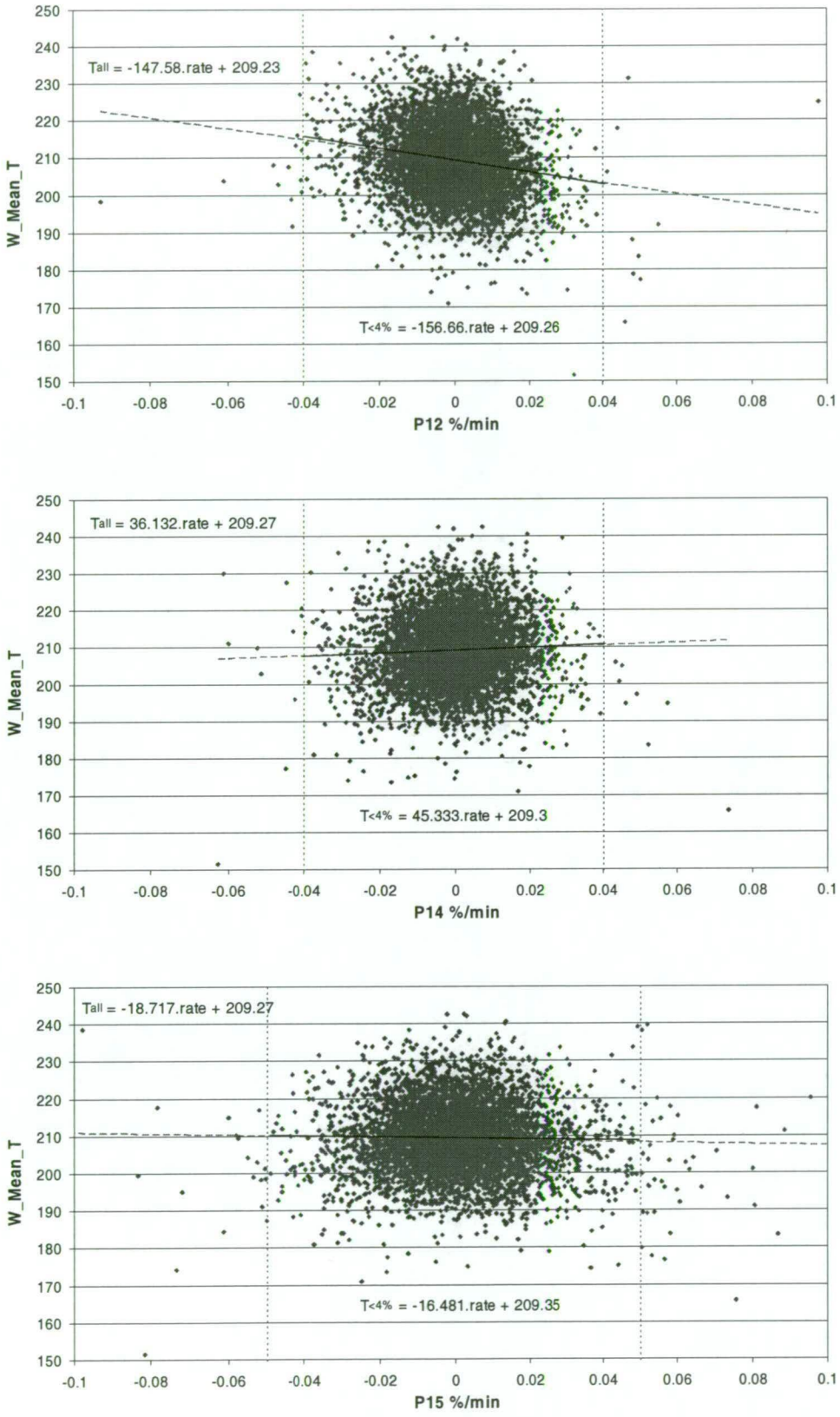

Figure 6-13. Rates of change of $P_1(2)$, $P_1(4)$ and $P_1(5)$ emission intensities over the ~7½ minute sample times against weighted temperature. Fitted trends compare all data with those below the selected rate limits.

Rate of change of background region 1 against temperature is plotted in Figure 6-14. No significant temperature relationship is evident. Rates of change for the other backgrounds are similar. Limits of ±3 counts per minute were set on background variability. This allows for a maximum variation of 22 counts over the cycle time, which is about twice the statistical counting error of the background limit. Again these limits were only set to reject outliers. A total of 1.2% of the remaining data is rejected by these criteria limits.

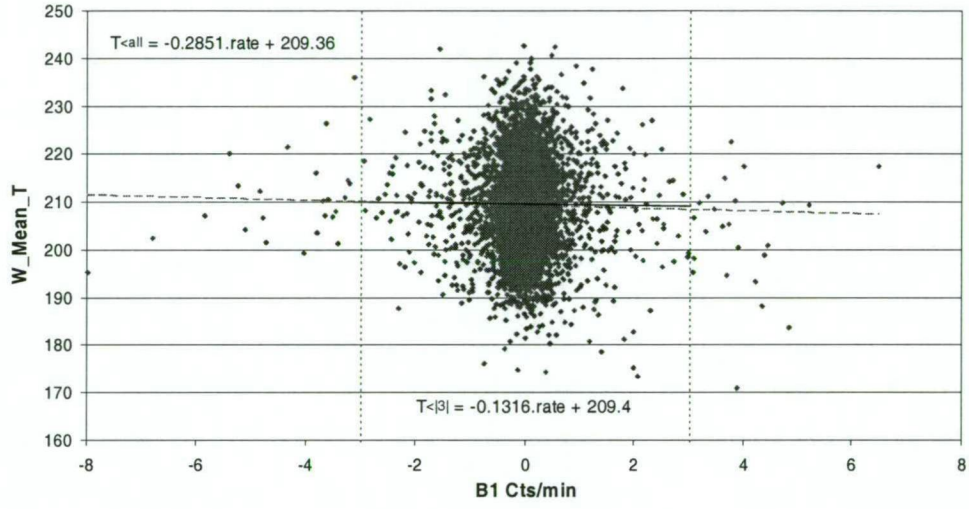

Figure 6-14. Rate of change of background 1 versus mean temperature.

Success of the selection criteria in removing possible influences can be judged by appropriate data splitting.

6.2.6. Moon influence

Table 6-2 shows average temperatures ($\overline{T}$) for the winter period (DOY 106-258) each year, for spectra collected with the moon either above or below the horizon. Average temperature differences for individual years are as great as 2.4 K (1998; warmer when moon up) and -2.3 K (1997). No trend is apparent, but the magnitude of the difference in some years is consistent with episodic 10-20 day variations in the Davis hydroxyl-temperatures of up to 30 K in relation to full moon periods. Table 6-2 also lists the percentage of spectra that were collected with moon above the horizon for each year. Typically this is ~40%, except in 1990 and 1994 when observations were campaign-based, centred on new-moon periods.

Year	No-moon		Moon		Both	$\Delta\overline{T}$ (K)	% Moon
	N	$\overline{T}$ (K)	N	$\overline{T}$ (K)	$\overline{T}$ (K)		
1990	221	215.8	55	214.1	215.5	-1.7	20%
1994	701	206.4	227	205.5	206.2	-0.9	24%
1995	1332	202.7	853	203.9	203.2	+1.2	39%
1996	1172	205.0	677	204.7	204.9	-0.3	37%
1997	6443	205.1	4816	202.8	204.1	-2.3	43%
1998	7852	204.4	5173	206.8	205.4	+2.4	40%
1999	3651	210.1	2917	208.3	209.3	-1.8	44%
2000	6594	208.3	5163	208.2	208.3	-0.1	44%

Table 6-2. Average temperatures obtained from winter (DOY 106-258) spectra split on whether the moon was above or below the horizon.

6.2.7. Cloud Influence

Cloud logs have been maintained by visual observation supplemented by all-sky auroral video records (see Figure 3-4). Observations are necessarily subject to different observers interpretation, but in an effort to reduce subjectivity, cloud is categorised only as clear, haze, patchy or overcast. Splitting data on the basis of clear or cloudy (haze, patchy or overcast) skies shows five of the eight years produce warmer OH temperatures when clouds are present (Table 6-3). However the average yearly difference is less than 0.3 K. For spectra that passed the selection criteria each year, the percentage collected under 'clear skies' varies between 23% and 58%.

Year	Clear		Cloudy		Both	$\Delta\overline{T}$ (K)	% Clear
	N	$\overline{T}$ (K)	N	$\overline{T}$ (K)	$\overline{T}$ (K)		
1990	138	213.9	101	216.9	215.2	+3.0	58%
1994	465	206.9	358	206.1	206.5	-0.8	57%
1995	518	203.0	1167	203.2	203.2	+0.2	31%
1996	426	204.3	1373	205.0	204.8	+0.7	24%
1997	4018	204.0	6548	204.3	204.2	+0.3	38%
1998	6967	206.0	5191	204.7	205.5	-1.3	57%
1999	1482	208.8	4902	209.2	209.1	+0.4	23%
2000	3539	208.9	7115	208.1	208.4	-0.8	33%

Table 6-3. Average temperatures obtained from winter (DOY 106-258) spectra split on whether the night sky was clear.

6.2.8. Auroral influence

It has been shown in section 4.2.2 that the major auroral features within the OH(6-2) region are the OI lines near λ844.6 nm, and N_2 1PG(3-2) [λ818-861 nm] and N_2^+ Meinel(4-2) [λ827-878 nm] bands (see also Hecht *et al.* (1987); Viereck and Deehr, (1989)). The OI emissions are relatively intense but easily avoided with the instrument resolution used and only weakly related to the N_2 bands that can directly influence derived temperatures.

Nitrogen auroral bands are ubiquitous but relatively weak in this spectral region. It is impossible to exclude all auroral N_2 band influences from spectra collected at Davis, thus possible auroral influence on temperature determinations from spectra that pass the selection criteria must be quantified.

Synthetic N_2 spectra have been fit to averaged OH spectra in the vicinity of the major P_1-branch lines for 1990 data in section 4.3.7. Using a similar approach (but now excluding second-order nitrogen bands) on an average of the continuous spectra in 1996, background regions were chosen (see Table 4-4) to balance influences of the weak N_2 auroral and Fraunhofer absorption features, on $P_1(2)$, $P_1(4)$ and $P_1(5)$.

During 1998, two N_2 1PG regions (Table 3-15) were monitored to attempt to quantify auroral influence on derived temperatures. No statistically significant relationship is found between the N_2 auroral emissions measured and hydroxyl temperature. This would indicate that the estimation of balanced backgrounds for each P-branch line was successful in accounting for auroral variability in the spectra that passed the selection criteria.

6.2.9. Comparison of analysis methods

Interpolation of intensities between consecutive spectra (section 4.7.1) is feasible when the time between spectra is only 7 minutes (from D269, 1996), but not appropriate for 40 minute (1994-1996) or 1 hour (1990) acquisition times.

Individual spectral-scans in 1995 and 1996 were retained, which enables a comparison of the individual-spectra and interpolated-spectra analysis methods. Acquire times for individual spectra are just under 8 minutes, but the accumulated count rate is 5 times less (20 sec per nm) which increases the statistical uncertainty.

Nevertheless, individual scans from 1995 and 1996 were processed with the interpolation method. Groups of four interpolated temperatures were averaged, to compare with the individual analysis temperatures derived from equivalent five- spectra sums [Figure 6-15].

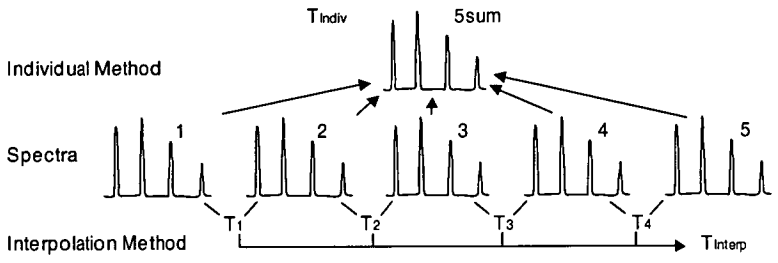

Figure 6-15. An illustration of the analysis method comparison.

For 1995, the average temperature derived from individual analysis (T_{indiv}) of 2643 five-spectra sums, that passed the selection criteria, was 1.0 K higher than that obtained from an appropriate average of single scans evaluated by the interpolation analysis (T_{interp}). A similar result (individual-spectra analysis 0.7 K higher) was obtained from 2145 five-spectra sums in 1996. As standard error-in-the-mean values are 0.23 and 0.26 K respectively, these are significant differences.

A small *increase* in average hydroxyl intensities during acquisition of spectra is implied, for 1995 and 1996 spectra that pass the selection criteria. This is in opposite sense to selected 1990 spectra in section 4.4.2, where an average *decrease* in hydroxyl intensity led to an underestimate of average temperature by ~1 K, due to the scan time. Line intensities, from the 1995 and 1996 interpolation analysis, do in-fact show an average intensity decrease over the acquisition time, consistent with 1990. However, $P_1(2)$ intensity decreases at a greater rate than $P_1(5)$ such that the net effect for five-spectra sums is on average a $P_1(5)$ increase, relative to $P_1(2)$, and a warmer temperature, as observed. As the magnitude of this correction is smaller than others errors assessed in chapter 4 no attempt is made to adjust temperature averages from the different analysis methods, or for possible scanning influences.

6.2.10. Temperature-intensity relationship

A positive relationship is found between temperature and emission intensity consistent with the temperature dependence of reaction 2-21. Figure 6-16 separates the relationship for $P_1(2)$, $P_1(4)$ and $P_1(5)$ using only clear sky data obtained in the interval D086-158, 1998. Slopes of 0.0061, 0.0087 and 0.0168 K/count/sec are obtained. Clear sky data across the whole year yields slopes of 0.0085, 0.0125 and 0.024 K/count/sec for $P_1(2)$, $P_1(4)$ and $P_1(5)$ respectively.

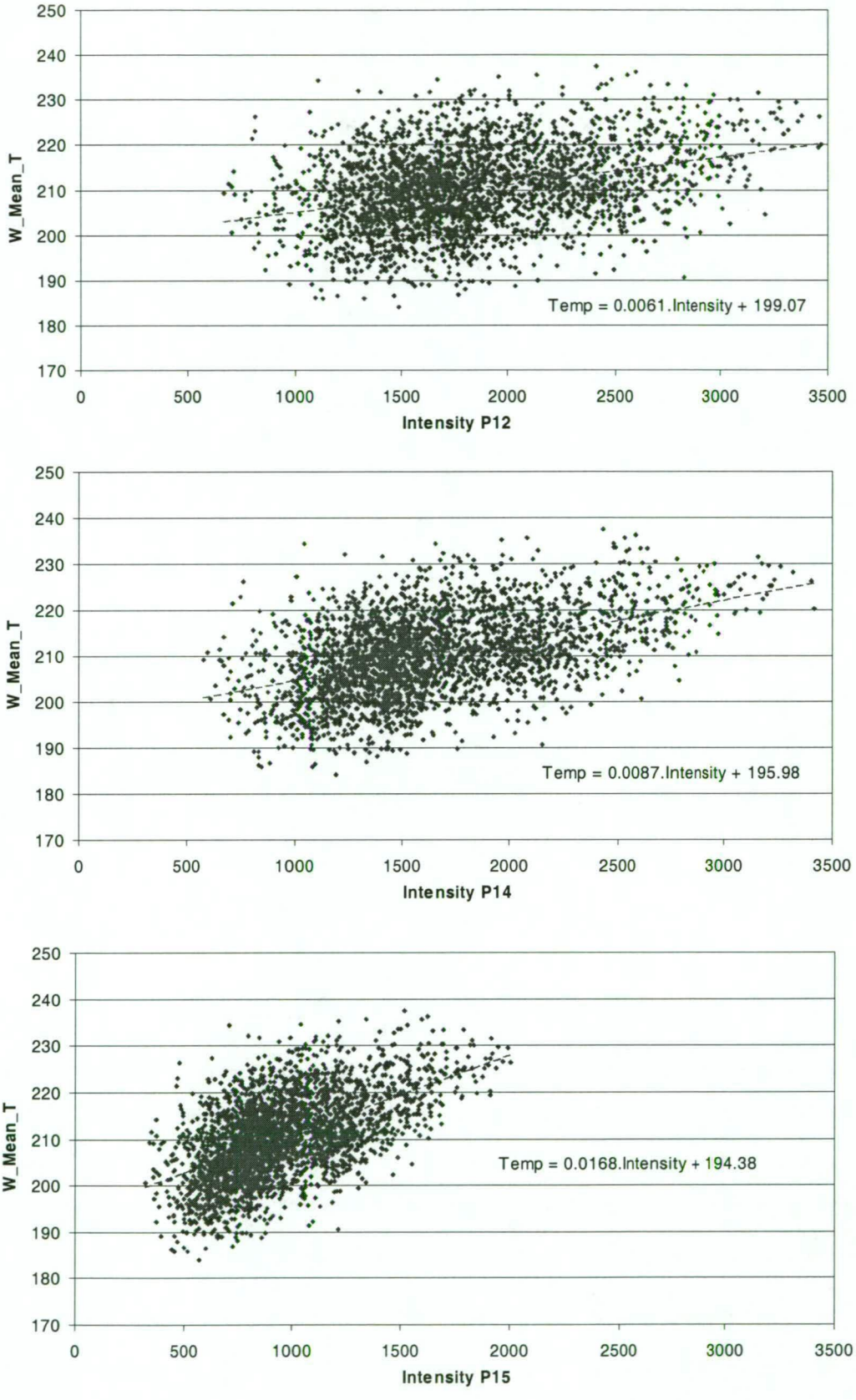

Figure 6-16. Comparison of the temperature-intensity relationship between $P_1(2)$ (top), $P_1(4)$ (center) and $P_1(5)$ (bottom) for clear sky data in the 1998 interval D086-158.

6.3. Temperatures and error estimates

6.3.1. Nightly Plots

Nightly plots have been produced for each observing session as a visual aid to data quality checking and selection. Several examples are shown in the following figures that cover the various operating modes. Four examples from 1998, collected with the fast scan-segment mode were selected to illustrate common features. Figures 6-21 and 6-22 show a comparison of the two different processing techniques for the same night in 1995, collected in the continuous scan mode. The former is processed as single scans using interpolation analysis and the latter as five-spectra sums with individual-spectra analysis. Figure 6-23 is an example of the continuous scan mode used in 1990.

In each figure, the top panel shows variation in $P_1(2)$, $P_1(4)$ and $P_1(5)$ emission intensity over the night. Wave structure with period 3-5 hours such as in Figure 6-17 and Figure 6-20 is often observed. Intensity enhancements around midnight (~1845UT) such as in Figure 6-18 and Figure 6-19 are also quite common. Overall nightly trends are not consistent, both increasing and decreasing intensities are observed.

An auroral indicator (either OI or an N_2 1PG band segment), mean background level, dark count rate, signal-to-noise and a Fraunhofer absorption index are all plotted in the second panel. Signal-to-noise is calculated as the average of the three P-branch line intensities divided by the average of their background samples.

Temperatures for each ratio (interpolated or individual-spectra), and weighted mean temperature with the maximum of the weighted counting error and weighted standard deviation as error bars, are shown in the third panel. Dots along the bottom of this plot indicate whether a particular temperature result passes all selection criteria. A nightly mean value is calculated from these.

Solar altitude, lunar altitude and phase (calculated using a PC based astronomical almanac program) and cloud cover (coded from visual observations and auroral imager video-tape) are plotted at the bottom. Daily F10.7 cm solar flux in the header is the observed value from the Canadian National Research Council's web site at http://www.drao.nrc.ca/icarus/www/current.txt.

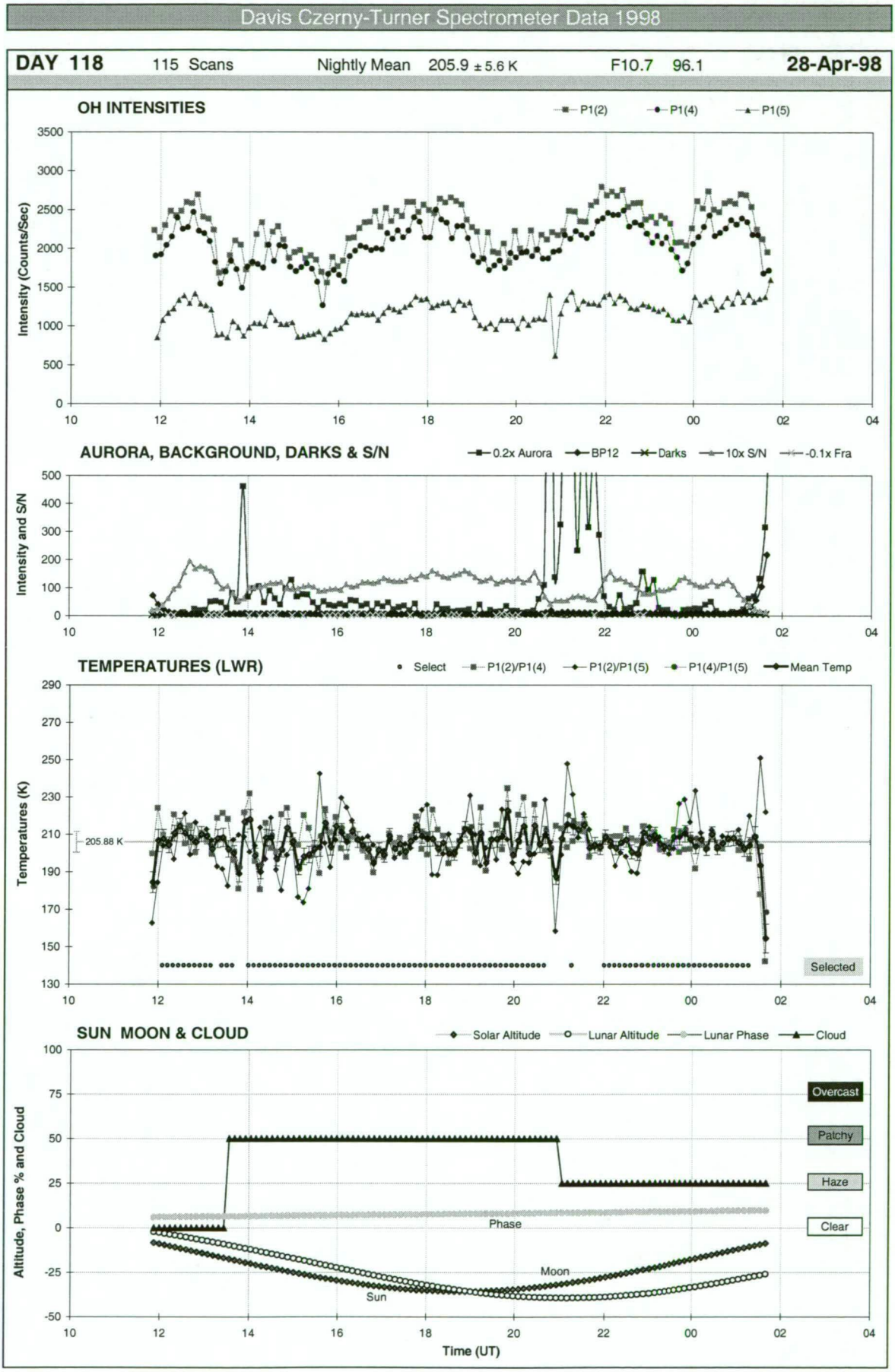

Figure 6-17. Nightly plot for D118, 1998

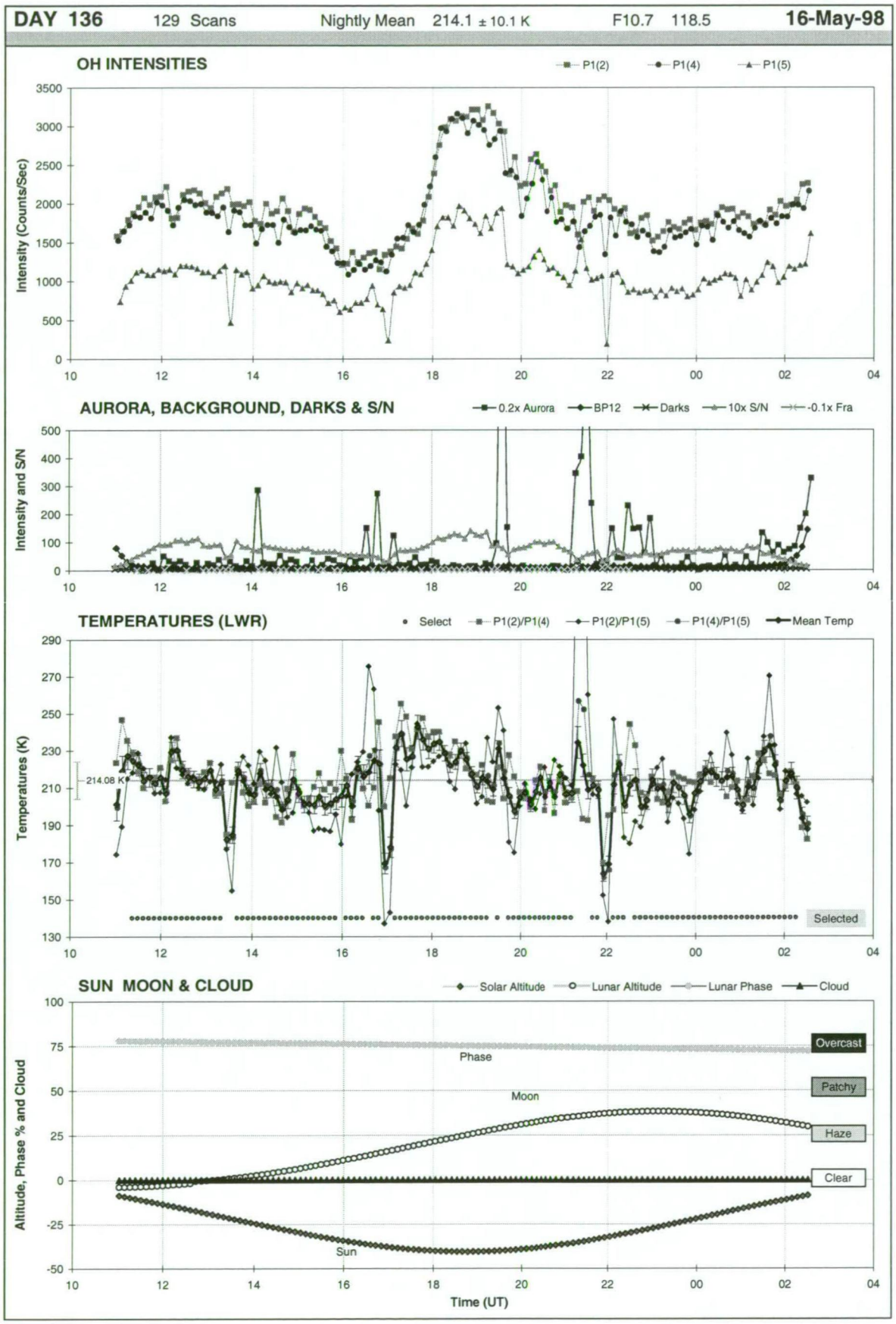

Figure 6-18. Nightly Plot for D136, 1998

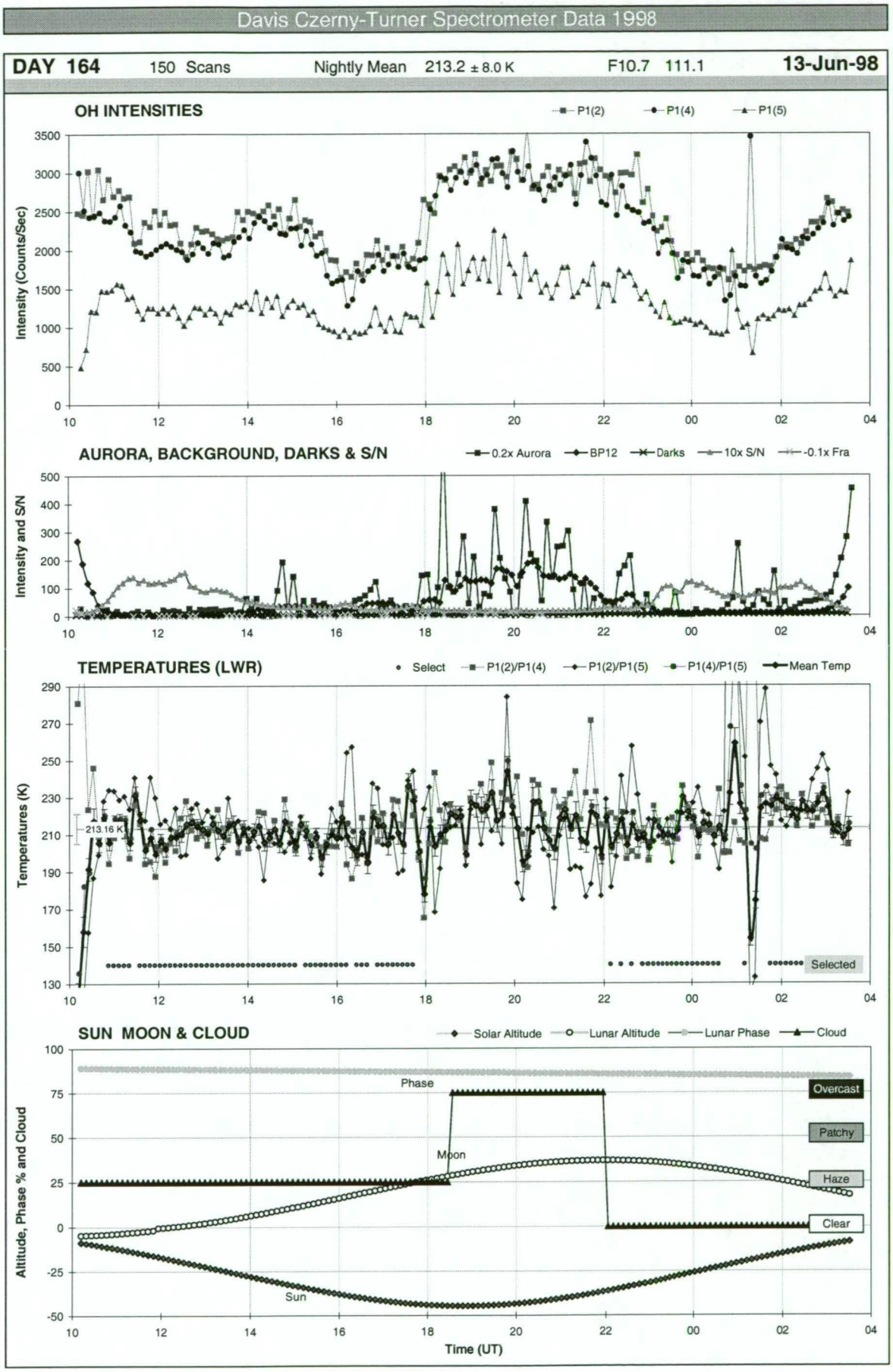

Figure 6-19. Nightly Plot for D164, 1998

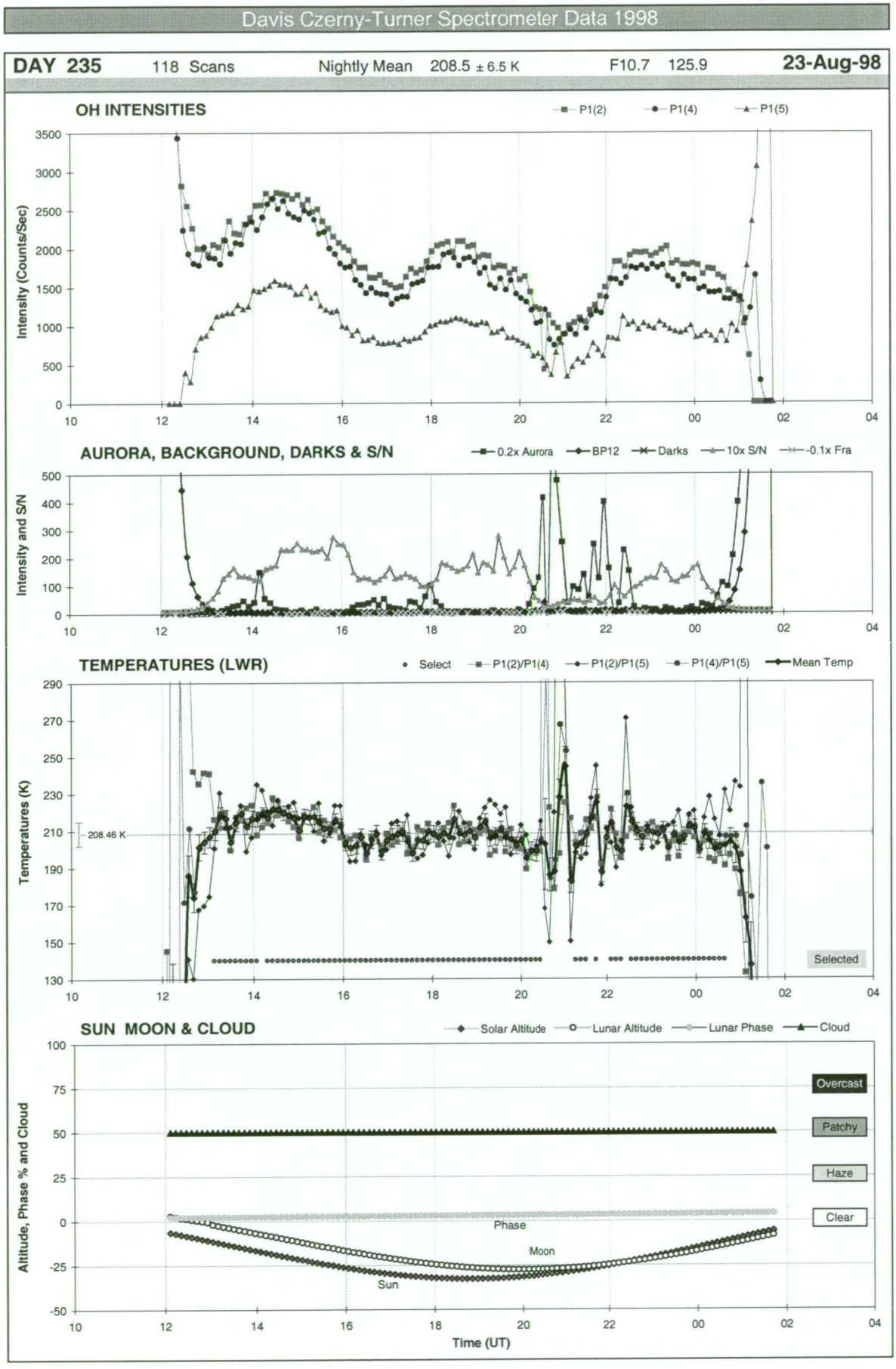

Figure 6-20. Nightly Plot for D235, 1998

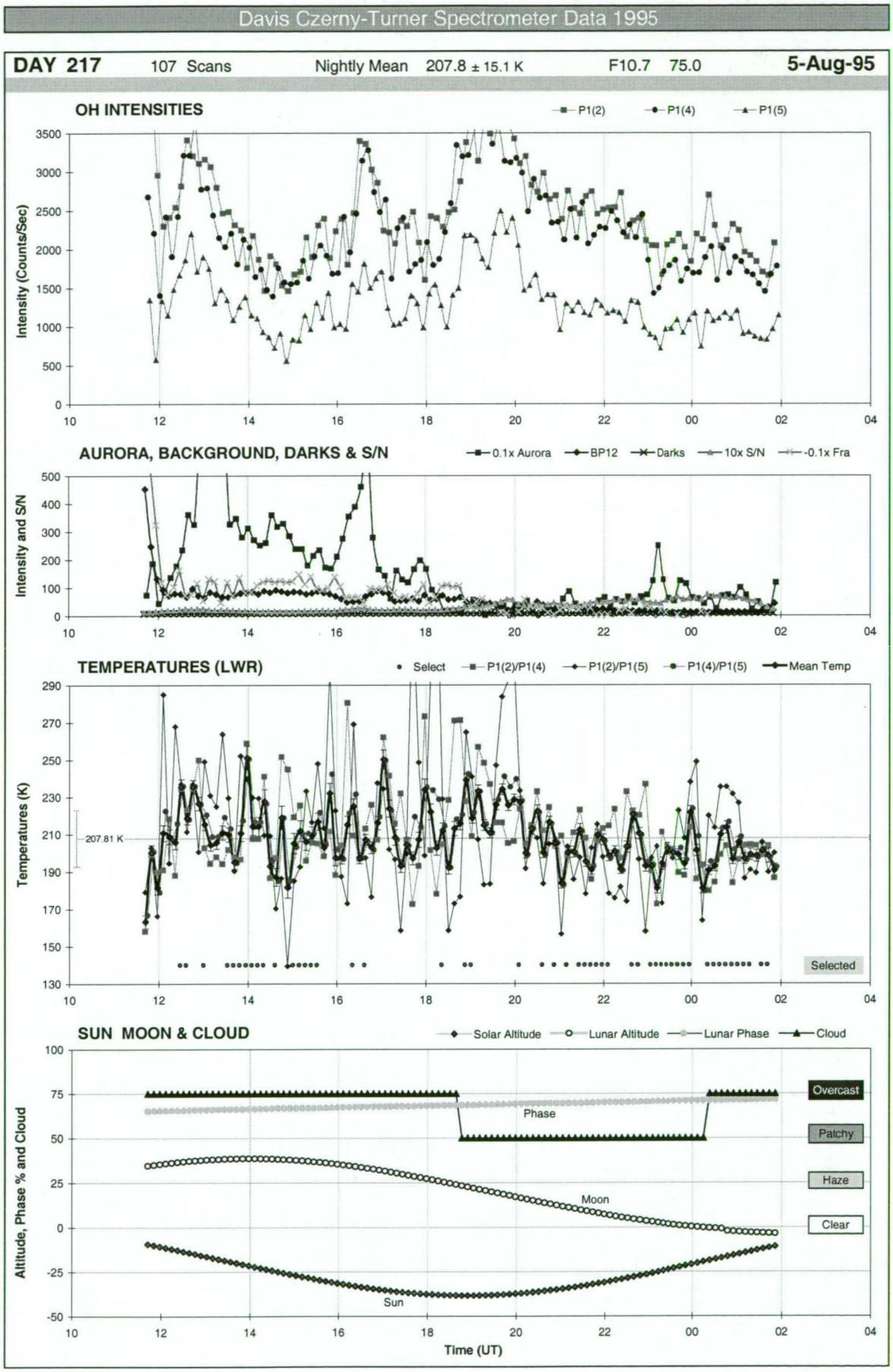

Figure 6-21. Nightly Plot from D217, 1995 – single scan interpolation analysis.

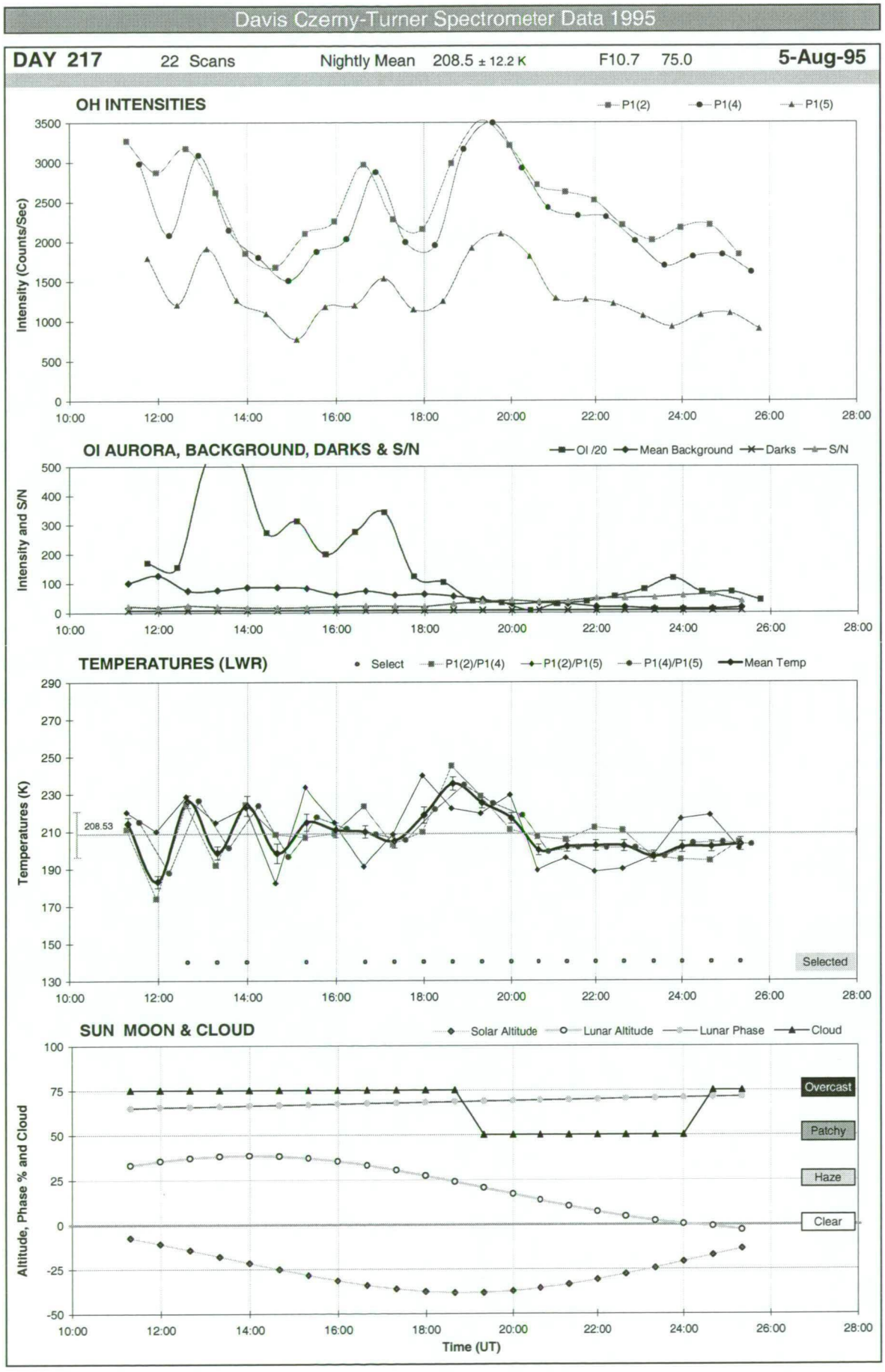

Figure 6-22. Nightly Plot from D217, 1995 – individual five summed spectra analysis

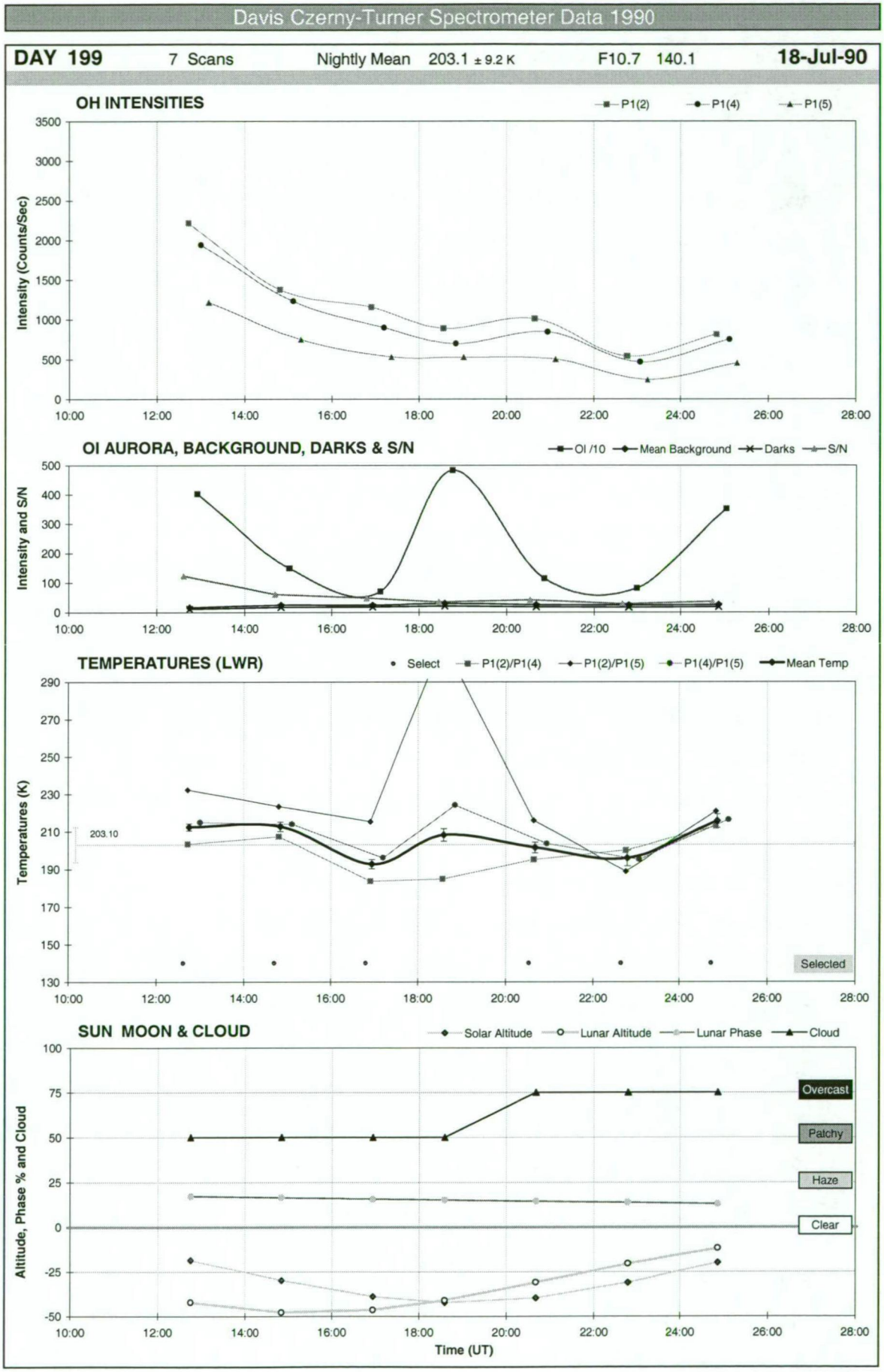

Figure 6-23. Nightly Plot from D199, 1990

Rejection of data contaminated by auroral emissions is evident in each example. Aurora may occur within the field-of-view for only a few spectral-cycles, (such as in Figure 6-18), but its impact on the derived temperature is readily apparent.

Figure 6-19 is a good example of the effect of moonlight scattered from cloud. A waning gibbous moon (approximately 85% illuminated) is rising during the first half of the evening and reaches a maximum elevation of 37° at about 22UT. Only haze (thin cirrus in patches) is observed until 1840UT, there is little scattered moonlight and good temperature results are obtained. Between 1840 and 22UT a thick band of cloud (alto-stratus and alto-cumulus) passed over the station. Background levels increased from ~10 counts/sec to ~160 counts/sec due to scattered light. Variability in $P_1(5)$ intensity is increased due to its proximity to the Fraunhofer absorption feature at λ849.8 nm and decreased signal-to-noise ratio. Temperatures are entirely rejected for this period due to high background, or large counting or standard deviation errors. At 22UT, the cloud band passed and the sky cleared. Good temperatures were obtained even though the moon was still near its maximum elevation.

Temperatures in the 1995 comparison example are significantly more variable for the single-spectra interpolation-analysis (Figure 6-21) than for the five-spectra-sums individual-spectra analysis (Figure 6-22), as would be expected. Enough interpolated temperatures pass the selection criteria to yield a nightly average however. In this example it is 0.7 K cooler than the five-spectra-sums analysis nightly mean. A standard error-in-the-mean of 2.6 K indicates that this is not a significant difference for nightly means (compared with annual mean in section 6.2.9). An analysis comparison was made of all 1995 and 1996 nightly averages treated in this way. On average, nightly means were 0.7 ± 4.1 K warmer in 1995 and 0.5 ± 3.4 K cooler in 1996 for the single-spectra analysis compared to the five-summed spectra analysis, i.e. not significantly different. Either method is therefore appropriate for derivation of nightly means in 1995 and 1996 and it is proposed that the use of single-scan analysis is also valid for the limited numbers of spectra available at the end of 1994.

Improvements in spectral acquisition methods over the years are obvious by comparison of the 1998 nightly plots with the example of 1990 data in Figure 6-23. Only 7 spectra (accumulations of five-scans over an hour-long period) were recorded

over this whole night (a maximum of 8 on any night) and one was rejected due to auroral contamination. Samples are spaced at two-hour intervals because they are alternated with scans of the OH(8-3) band.

Specific event analysis of fast acquisition data is not intended in this thesis, but clearly there are some very interesting cases. Figure 6-18 for example shows an intensity enhancement by almost 3 times in 2 hours after 17UT, apparently preceded by a temperature enhancement, an hour or so earlier, of almost 40 K. Figure 6-20 on the other hand shows no lag in correlated intensity and temperature variations. Many similar events in other years are available for future investigation.

6.3.2. Nightly Means

Nightly mean temperatures are determined from all spectra that pass the selection criteria each night with equal weight. Gravity waves and intensity enhancement events may produce substantial temperature excursions for short periods on a particular night, such as the example in Figure 6-18. So that outliers due to these events do not bias the nightly mean determination, individual temperatures are iteratively excluded if they are greater than 20 K from the nightly mean. A value of 20 K was chosen as twice the counting error for an individual sample. Total numbers of spectra rejected by this requirement for each year are also listed in Table 6-1. Typically it is around 2% of the remaining data.

A nightly mean must also contain more than a minimum number of spectra to be accepted. The minimum number of spectra required is three for 1990 and 1994 to D217, five for 1994 D218 forward and 1995 and 1996 five-spectra sums and ten for all other data. A winter-mean temperature (an average over 153 possible nights, D106-258) is calculated to test the effect of this requirement. Figure 6-24 plots variation in winter-mean temp as a function of the number of additional spectra required for a nightly average. Table 6-4 shows the maximum change in winter-mean temperature ($\overline{T}$) and the number of nightly averages that are gained or lost if the number of spectra required is halved (approximately) or doubled, respectively. For example in 1997, if 20 spectra are required for a nightly mean, eight nightly means are lost and the winter-mean temperature changes by at most 0.41 K, similarly if only 5 are required, two nights are gained and the temperature changed by 0.17 K.

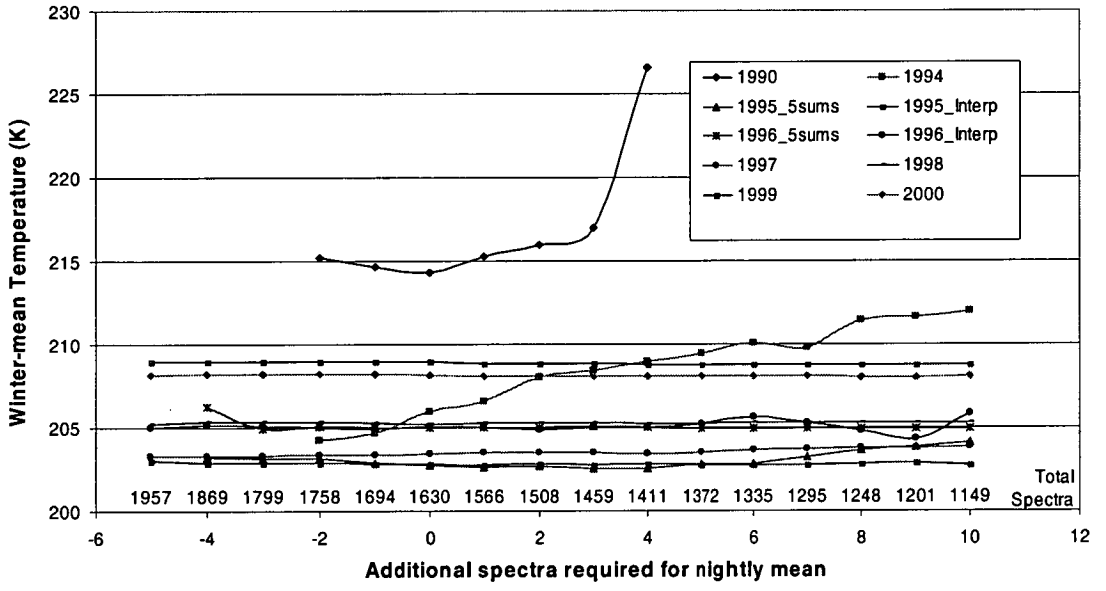

Figure 6-24. Effect on winter mean temperature of the number of spectra required for acceptance of a nightly mean. Zero corresponds to three spectra for 1990 and 1994, five for 1995 and 1996 5_sums and ten for the remainder. Labels along the bottom are the total number of spectra for all years.

Largest variations occur in 1994 and 1990, which have an average of only 9.5 and 4.5 spectra per night respectively, and which are collected only around new moon intervals over during the winter period.

Tides and gravity waves coupled with limited sampling periods influence the nightly average, but winter-mean temperatures do not appear to be sensitive to these influences beyond the magnitudes listed in Table 6-4. Uncertainty in the winter-mean temperature for the under-sampled 1990 and 1994 data sets will be addressed later.

		Max Change	Mean Temp	Max Change
Spectra required		20	10	5
2000	$\overline{T}$ (K)	0.10	208.14	0.06
	N	-7	141	+3
1999	$\overline{T}$ (K)	0.24	208.98	0.00
	N	-4	82	+0
1998	$\overline{T}$ (K)	0.08	205.23	0.13
	N	-7	144	+4
1997	$\overline{T}$ (K)	0.41	203.44	0.17
	N	-8	127	+2
1996 Interp	$\overline{T}$ (K)	1.51	205.09	0.23
	N	-72	95	+20
1995 Interp	$\overline{T}$ (K)	0.17	202.80	0.25
	N	-23	130	+10
Spectra required		10	5	3
1996 5_sums	$\overline{T}$ (K)	0.12	204.97	0.09
	N	-4	112	+3
1995 5_sums	$\overline{T}$ (K)	0.22	202.72	0.44
	N	-19	139	+8
Spectra required		6	3	2
1994	$\overline{T}$ (K)	2.52	205.93	1.25
	N	-16	81	+5
1990	$\overline{T}$ (K)	2.65	214.32	0.37
	N	-41	53	+9

Table 6-4. Maximum change in the winter mean (D106-259) if the number of spectra required is doubled or halved from the values chosen. The number of nightly averages that are lost or gained respectively are also listed.

All temperatures that pass the selection criteria and nightly means derived in the above manner are shown for each year in the following figures. Also plotted is the nightly MSIS-E-90 model temperature for 87 km altitude over Davis (constructed as the average of the 17 UT, 19 UT and 21 UT values), generated from the 'day of year profile' at http://nssdc.gsfc.nasa.gov/space/model/models/msis_n (Hedin (1991)).

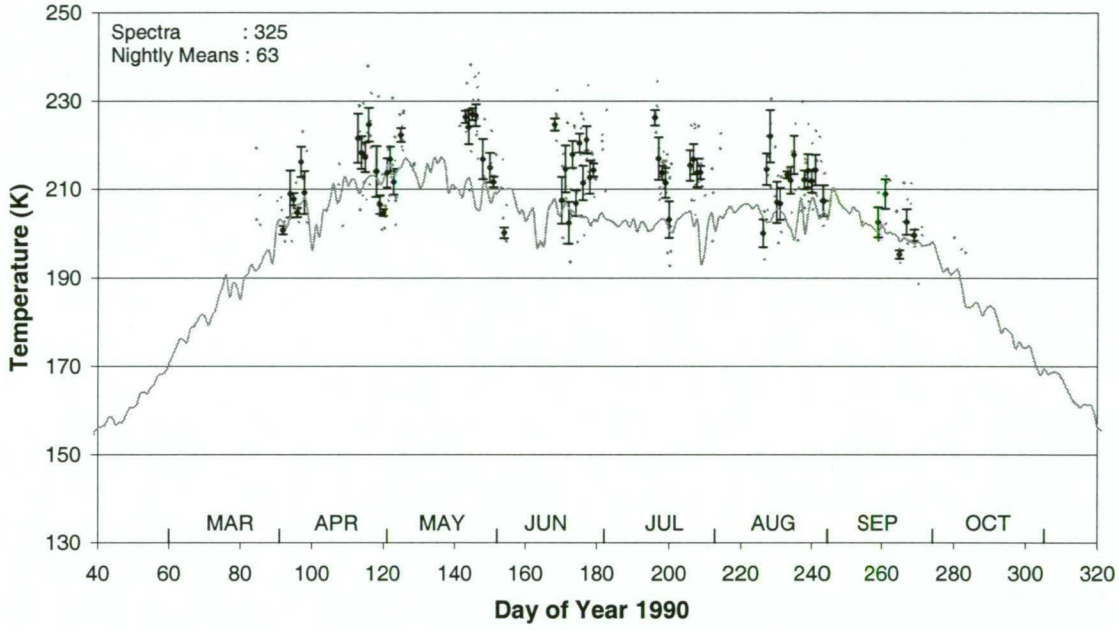

Figure 6-25. Individual temperatures (small dots), nightly means with standard error-in-the-mean error bars (large points) and MSIS-E-90 model (Hedin (1991)) nightly (17,19,21UT average) temperatures for 87 km over Davis (thin line) for 1990. Data gaps indicate full moon periods.

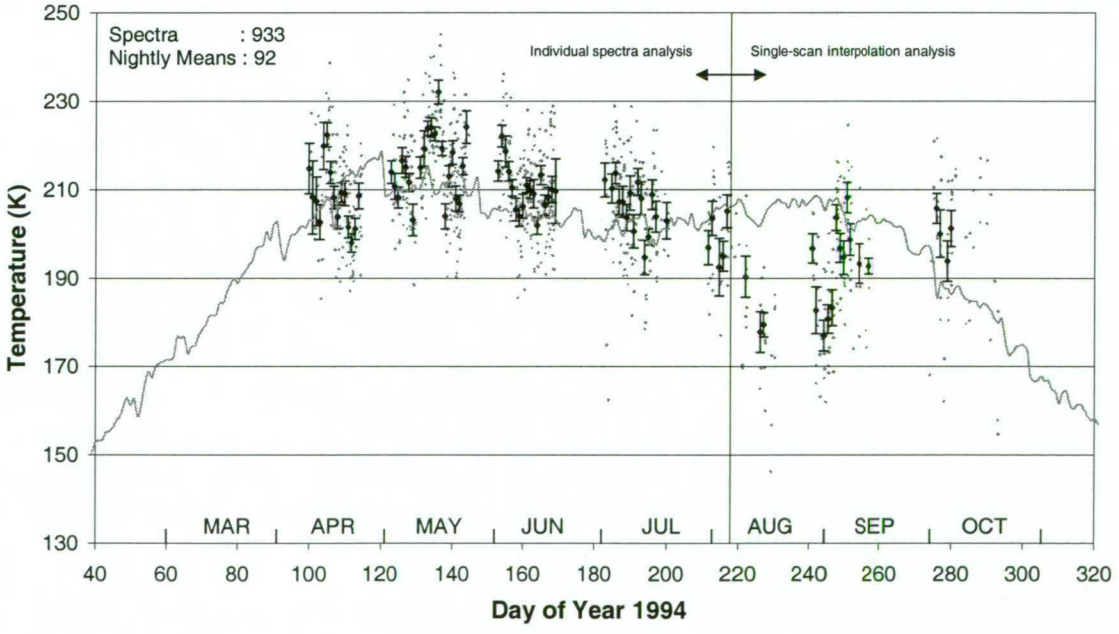

Figure 6-26. As for Figure 6-25 but for 1994. Data up to D217 are processed as equivalent 5-spectra sums with the individual-spectra analysis, and after D217 as single scans with the interpolation analysis. Greater uncertainty is consequently attached to the latter.

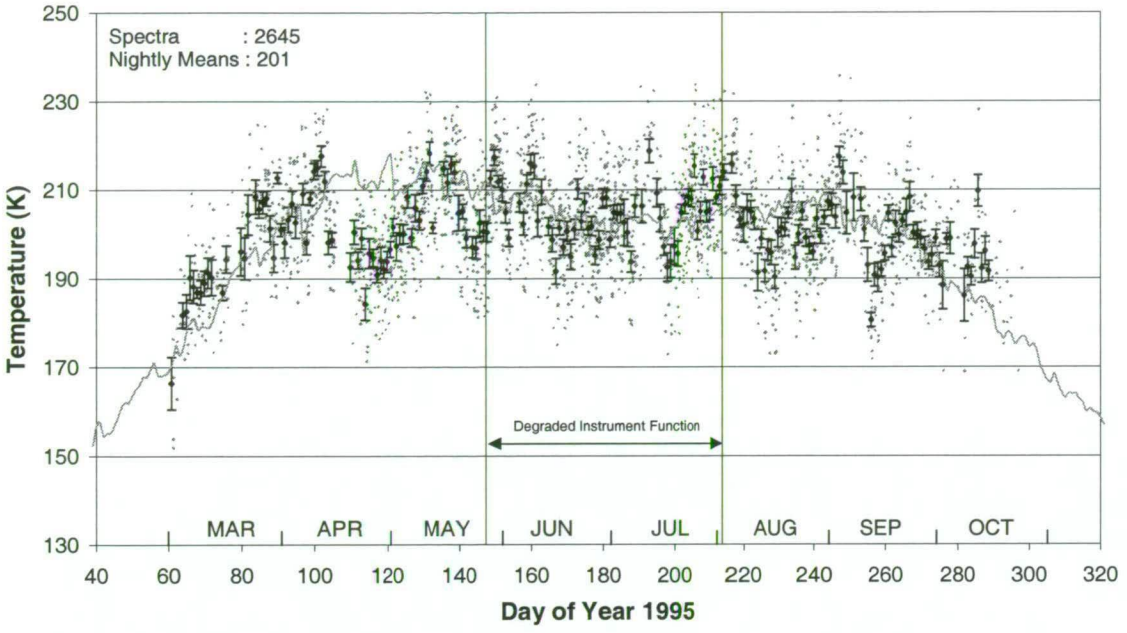

Figure 6-27. As for Figure 6-25 but for 1995. These results are from individual-spectra analysis of five-spectra sums. During the period from D147-D213 the instrument had a degraded instrument function due to slit a-parallelism. Larger uncertainties result in this period.

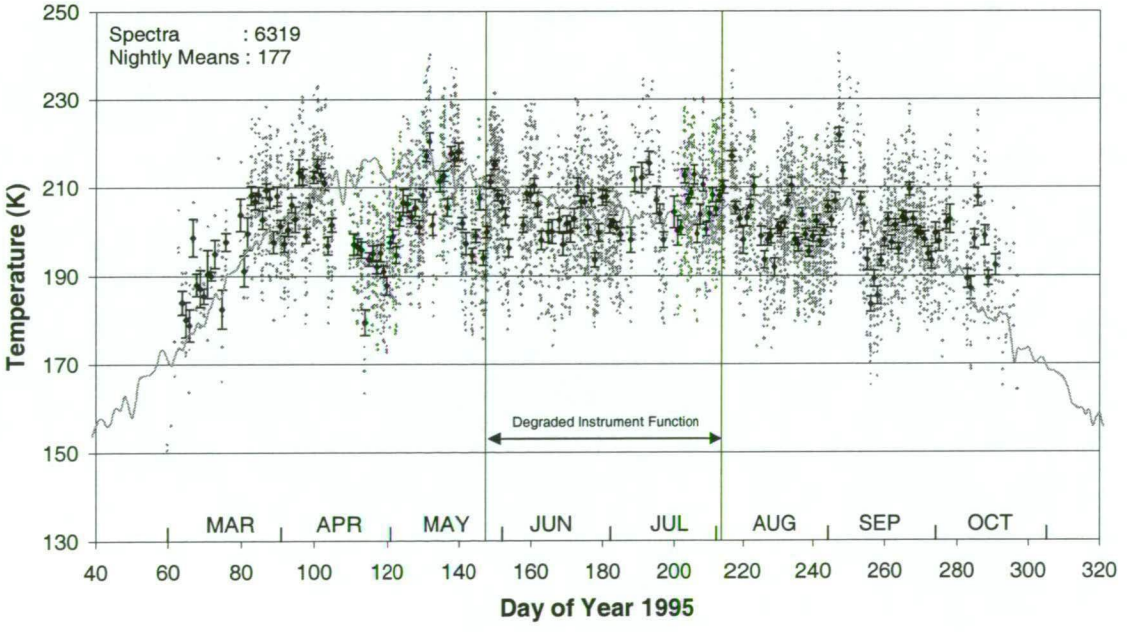

Figure 6-28. As for Figure 6-25 but for 1995. These results are from interpolation analysis of single scan spectra, which may be compared to Figure 6-27 above. Again, larger uncertainties are attached to the interval D147-D213 due to a degraded instrument function.

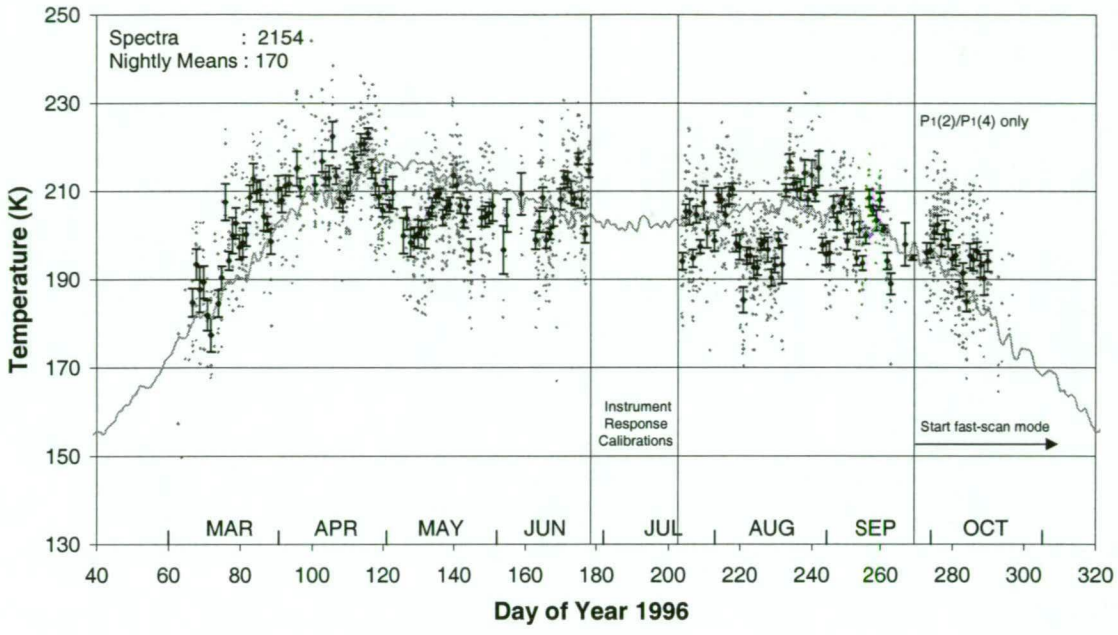

Figure 6-29. As for Figure 6-25 but for 1996. These results are from individual-spectra analysis of five-spectra sums. Instrument response calibrations (for 1996 and retrospectively for 1990, 1994 and 1995 using the Eather LBS) were conducted between D179 and D202. Fast scan-segment mode started on D269 but included only $P_1(2)$ and $P_1(4)$ ratios at that time. Interpolation analysis is used for these data.

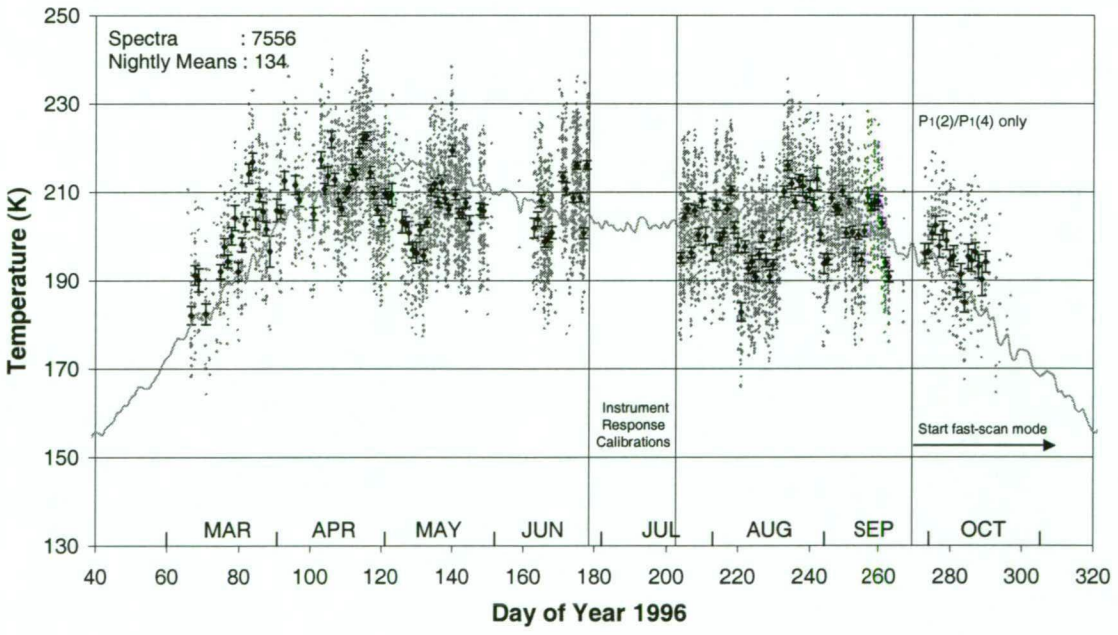

Figure 6-30. As for Figure 6-25 but for 1996. These results are from interpolation analysis of single scan spectra, which may be compared to Figure 6-29 above. The interpolated results from D269 are identical to Figure 6-29.

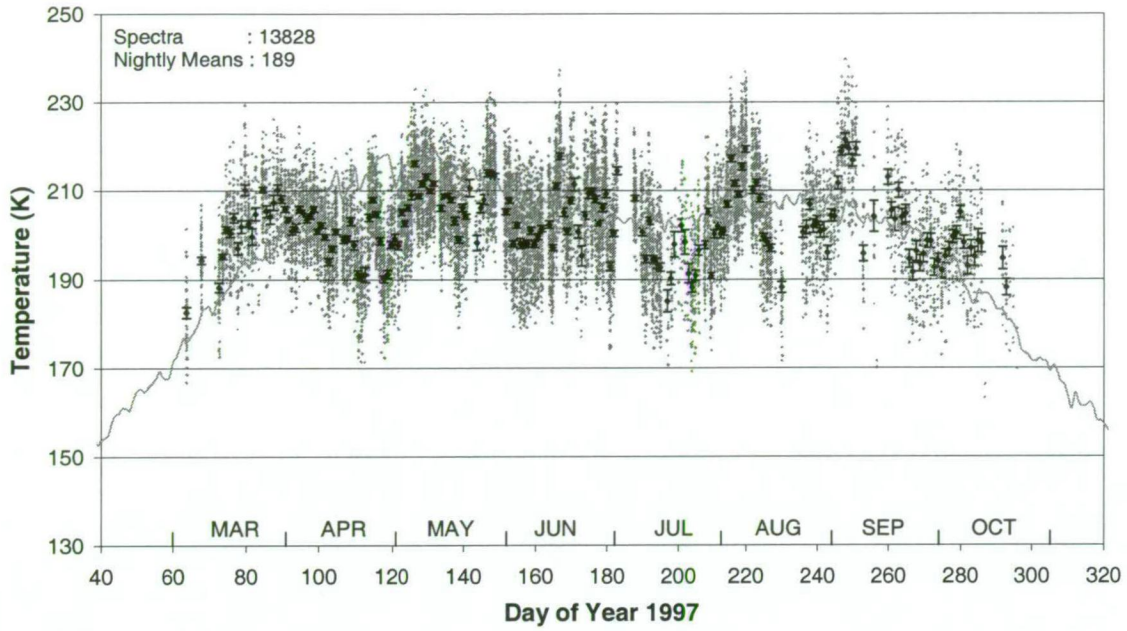

Figure 6-31. As for Figure 6-25 but for 1997. Interpolation analysis of single scan spectra. Note temperature dip in April.

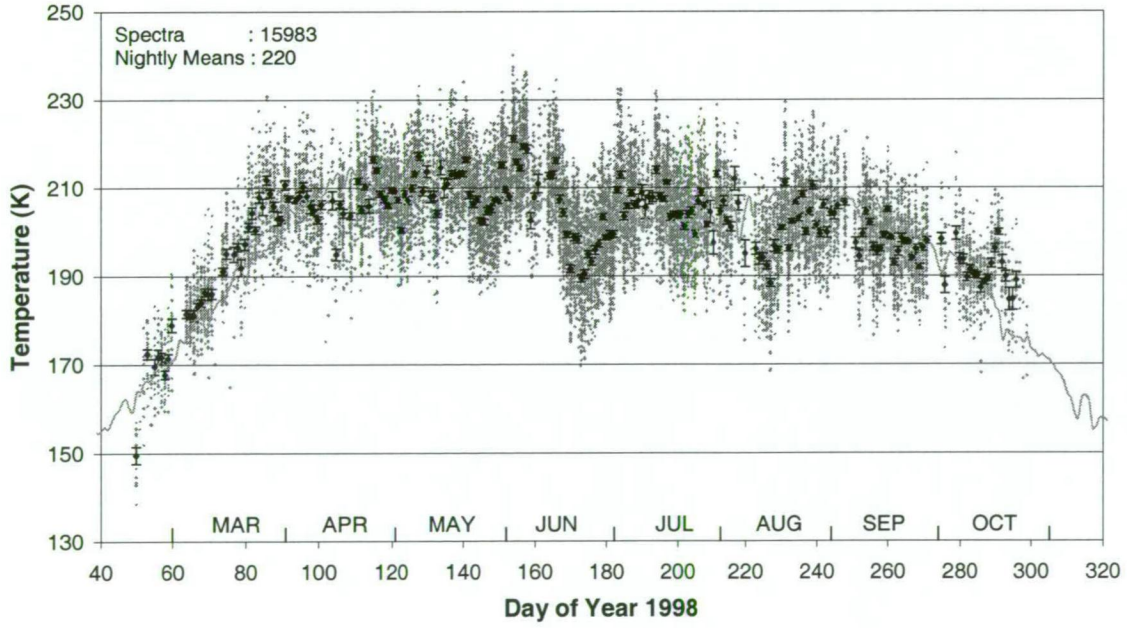

Figure 6-32. As for Figure 6-25 but for 1998. Interpolation analysis of single-scan spectra. Note temperature dips around D175 and D225.

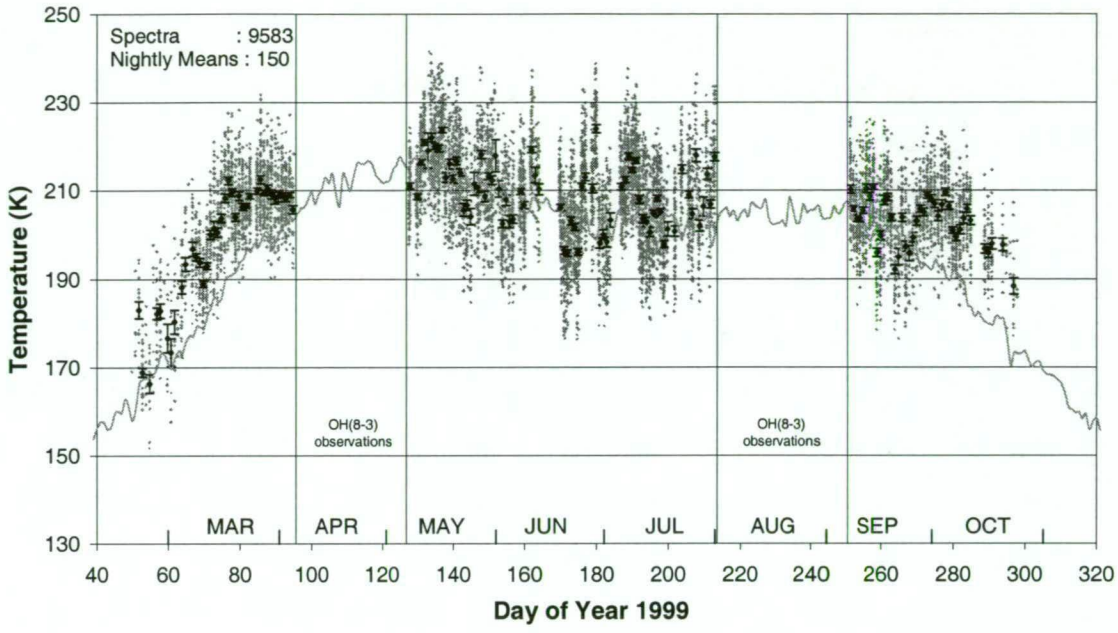

Figure 6-33. As for Figure 6-25 but for 1999. Interpolation analysis of single-scan spectra. Periods from D095-D126 and D213-D249 were used for campaigns of OH(8-3) measurements.

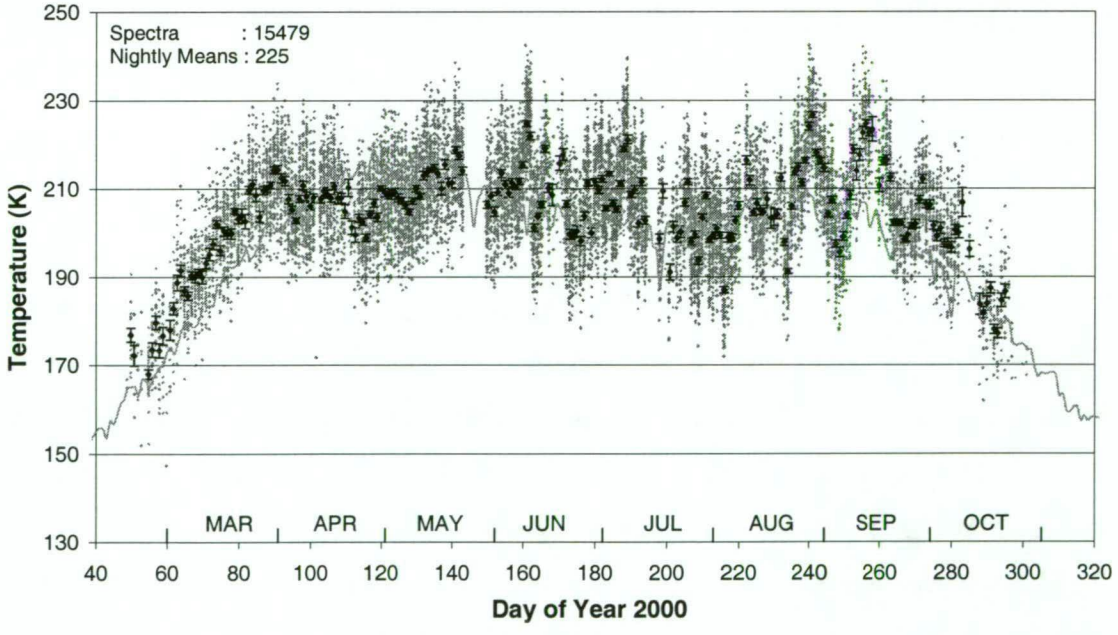

Figure 6-34. As for Figure 6-25 but for 2000. Interpolation analysis of single-scan spectra. Note temperature dip around D115 and oscillations between D230-280. Data gap around D145 due to a manual shutter being inadvertently closed.

6.3.3. Weighted nightly means

During the review of this thesis it was suggested by one referee that nightly averages could be derived using an average of all individual points weighted by their standard deviation. That is, no rejection criteria are applied and each spectrum contributes to the nightly mean according to its error. This method would avoid any bias being introduced to the nightly means by the application of selection criteria.

The 1998 data set was selected to test this method, as this year was used to derive the selection criteria in section 6.2. The referee suggested only the standard deviation weighting be used. This was tested, but widely scattered nightly averages were obtained as the standard deviation alone does not well represent the error in an individual spectrum (it can be fortuitously low by chance variation within the counting error). A better estimate of the error is the combined standard deviation and counting errors. Thus all individual temperatures from 1998 were weighted as $1/(SD^2+CE^2)$ for the weighted nightly mean calculations.

Figure 6-35 shows the weighted nightly means compared with the nightly averages derived via selection criteria (selected averages). Differences between comparable means (weighted-selected) are also shown. The requirement for a minimum number of 10 samples is applied to both sets of nightly means.

There are 29 more weighted nightly averages calculated (249) than those that pass the selection criteria (220), mostly at the start and end of the observing season, when selection criteria reject on the high background contamination. Comparing the same 220 nights, the annual mean is 0.68 K higher (201.17±0.7 K standard error) for the selection criteria means than for the weighted means (200.49±0.69 K), however the standard error in the difference is 1.0 K. Similarly, the winter (days 106-259) selection criteria mean is 0.78 K higher (205.23±0.55 K) compared to the weighted mean (204.45±0.55 K) but within the standard error in the difference (0.79 K). There is some suggestion of bias in the selection criteria toward higher temperatures, consistent with the temperature-intensity relationship described in section 6.2.1, but it is not significant.

There does however appear to be a number of weighted nightly means that are exceptionally low in Figure 6-35 compared to adjacent nights (eg nights 71, 92, 101-104, 160, 190, 219-221, 249). It is clear that most of these correspond to full moon

periods (see lunar phase plot in Figure 6-35), thus inadequate account of the high background and Fraunhofer absorption biases these weighted nightly means toward lower temperatures. Excluding lunar phase greater than 0.5 reduces the difference between annual averages to 0.4±1.0K. It is argued that the weighted means contain some spectra that are known to be badly contaminated by Fraunhofer absorption, high background counts, aurora or variable cloud conditions which may not be well represented by the counting and standard deviation errors alone. I would prefer to reject any contribution from these spectra. Perhaps a combination of selection criteria for extreme profiles and then weighted nightly means would be the best approach.

However, as the winter means derived from selected and weighted nightly averages are within one standard error-in-the-mean and as the same selection criteria are applied to each year it is not considered that any bias is introduced that will affect the following trend calculations.

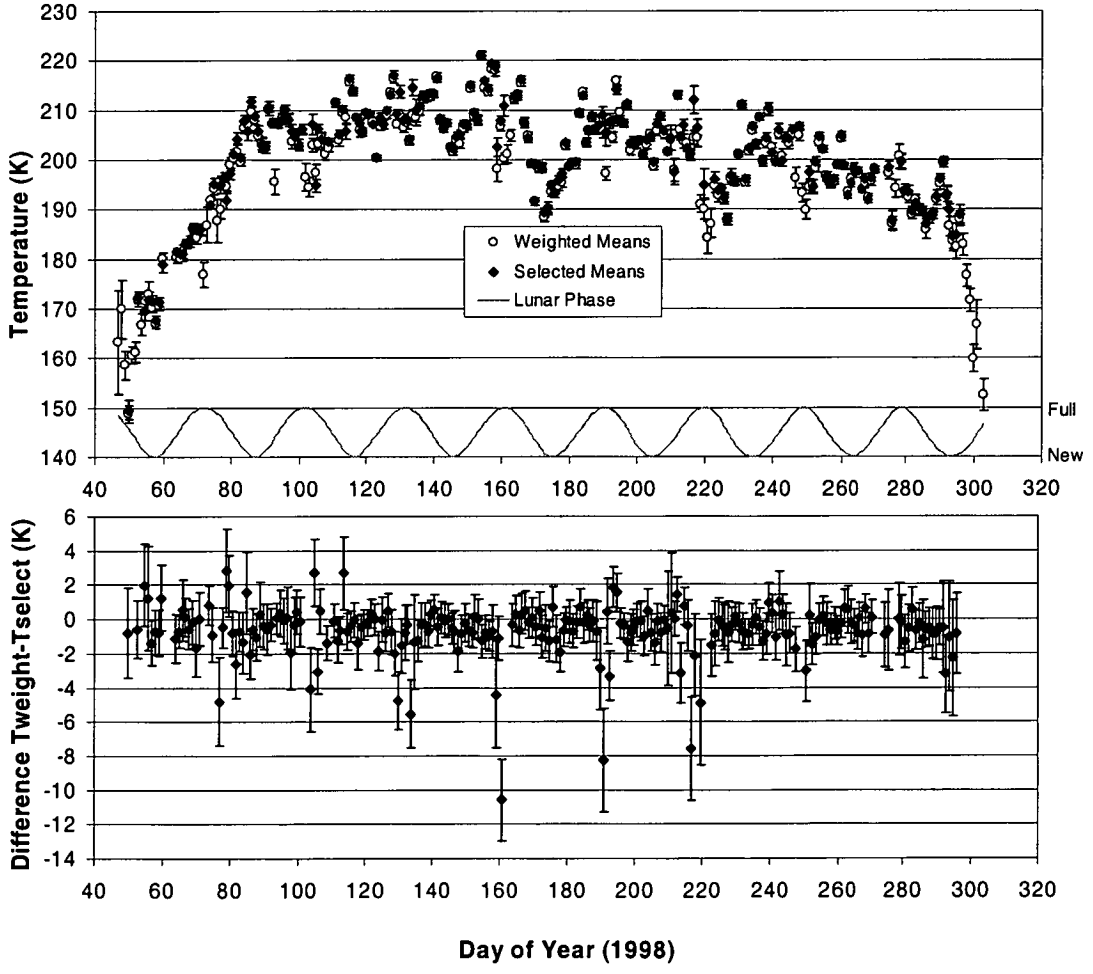

Figure 6-35. (Top panel) Nightly means (and standard error) derived via the selection criteria (closed diamonds) compared with weighted means (and weighted standard error) of all data (open circles) with lunar phase indicated on RHS and, (Bottom panel) the difference between comparable nights (Weighted – Selected) with standard difference-between-means error bars.

Combined nightly average temperatures and MSIS-E-90 model calculations at 87 km are plotted in Figure 6-36. Solar activity indicators also shown are the 10.7 cm solar flux values from http://www.drao.nrc.ca/icarus/www/current.txt and MgII composite index from ftp://susim.nrl.navy.mil/pub/uars/susim_v19r3_mgii_index.ascii.

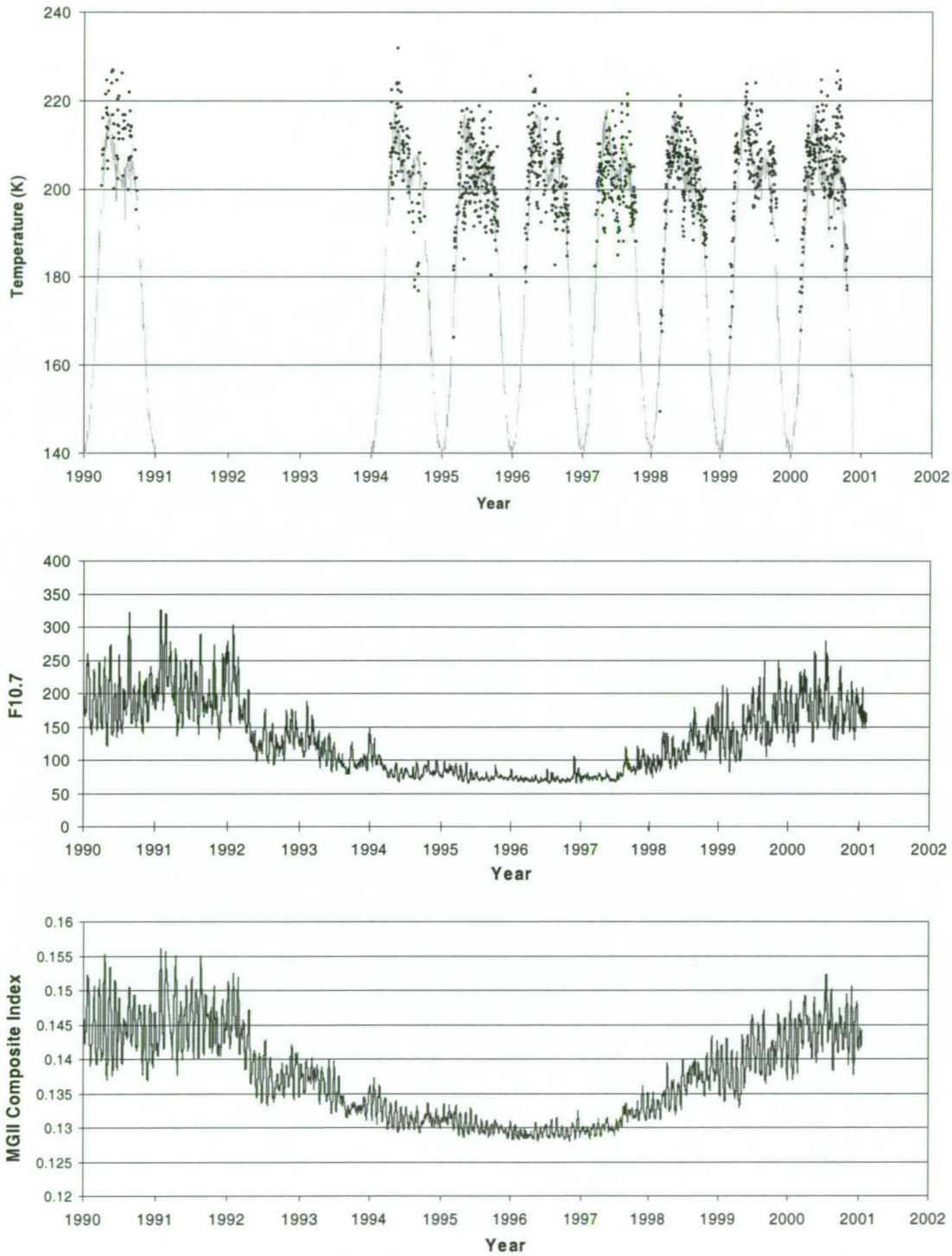

Figure 6-36. Top panel – combined nightly-mean temperatures for each year (blue points) with model calculations from MSIS-E-90 at 87 km (orange line). Centre panel – Solar 10.7 cm radio flux and Bottom Panel – Solar MgII composite index for equivalent years.

6.4. Discussion of Variability and Trends

Figure 6-37 shows nightly averaged temperatures against day-of-year for 1310 nights measured across all sampled years (1990, 1994-2000) and MSIS-E-90 model mean-nightly temperatures at 87 km for equivalent nights. MSIS-E-90 temperature variations at 87 km for the same day-of-year are considered to be at the model's noise level (Hedin, private communication via Bilitza).

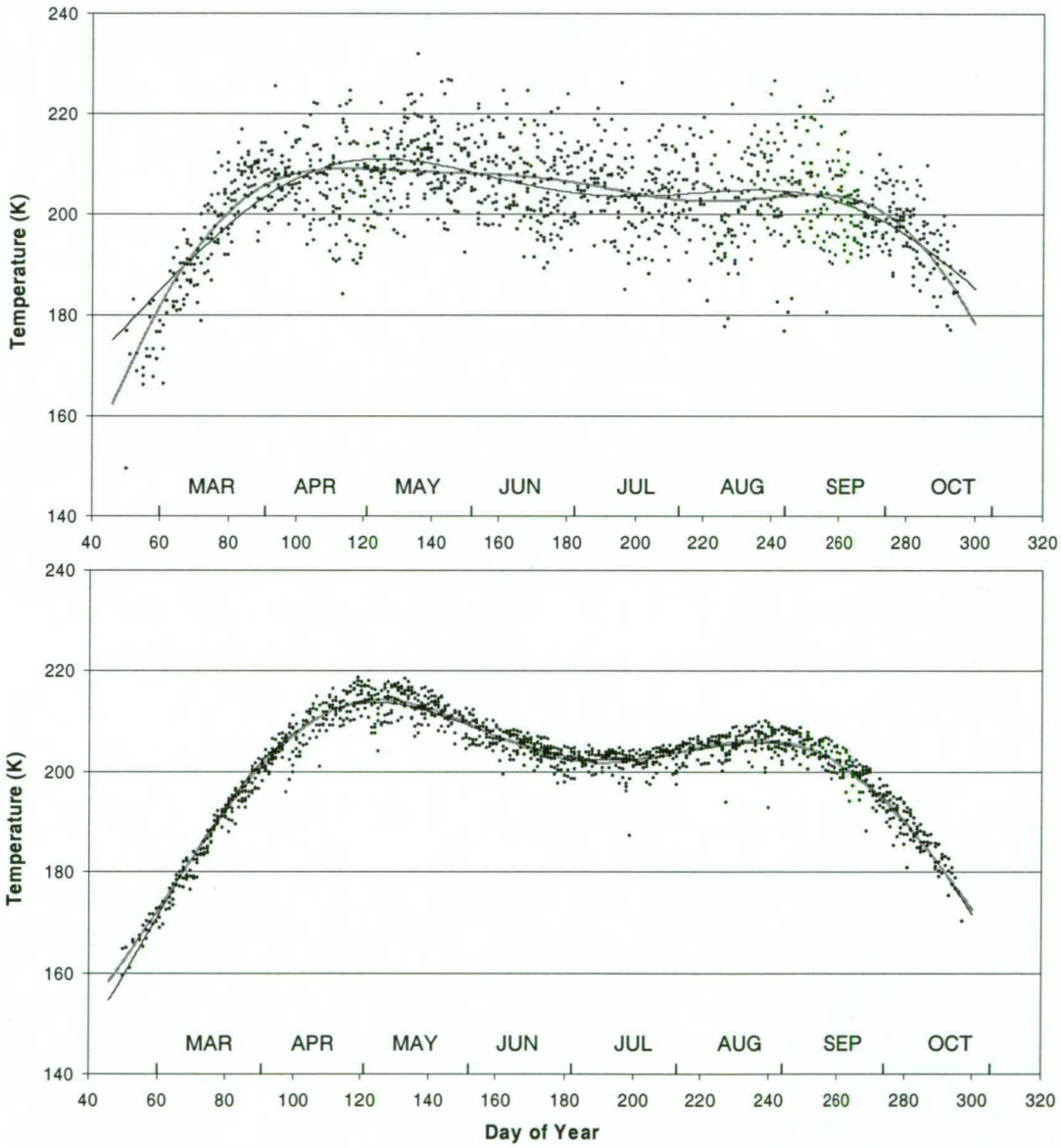

Figure 6-37. Top panel - Nightly-averaged temperatures against day-of-year for 1310 nights over all sampled years (1990, 1994-2000). Bottom panel – MSIS-E-90 model mean-nightly temperatures for equivalent nights. Fits to both data sets are mean, annual and semi-annual components (thin green line) and mean, annual, semi-annual and ter-annual components (thicker orange line).

Hydroxyl temperatures each year show a sharp, consistent rise before an abrupt levelling at ~D085. A slight downward trend is apparent across the winter months.

Increased temperature variability over winter is also apparent, particularly in comparison to the autumn interval. Only a small portion of the spring temperature decrease, from ~D265, is measured but the slope is more gradual than the autumn transition. All measured hydroxyl temperatures give the rise prior to D080 at 1.2 K per day (Kd^{-1}) compared with an MSIS-E-90 rate of 1.0 Kd^{-1}. Spring hydroxyl temperatures decrease at 0.65 Kd^{-1} from D275 compared with a model rate of 0.8 Kd^{-1}. Over the winter interval, D106-258 (mid-April to mid-September) observed temperatures decrease at only -0.04 Kd^{-1} (a total of 6 K) compared to the model at 0.07 Kd^{-1} (total 11K).

Periodic fits made to both OH and model temperatures are also shown in Figure 6-37. One is a fit of mean, annual and semi-annual components; the other also includes a ter-annual component. Amplitude and phase (day of maximum amplitude) coefficients for these fits are listed in Table 6-5. Fit coefficients over the whole year for MSIS-E-90 model are also listed.

The value of this comparison is limited by three main difficulties. Firstly, hydroxyl temperature samples do not cover a complete year. Model amplitudes are considerably greater for the fit over equivalent sample days, compared to the full year. Phase coefficients are reasonably consistent however.

		Annual Component		
	Mean	1st	2nd	3rd
Hydroxyl temperatures – Sampled Days (049-296)				
Amplitude (K)	190.77	23.84	10.35	
Phase (day)		176.10	94.03	
Amplitude (K)	180.94	41.35	22.17	6.48
Phase (day)		176.26	89.50	56.14
MSIS-E-90 temperatures – Equivalent Days				
Amplitude (K)	180.66	40.18	17.84	
Phase (day)		177.05	92.77	
Amplitude (K)	183.03	35.94	14.89	1.70
Phase (day)		176.68	93.43	60.94
MSIS-E-90 temperatures – All Year				
Amplitude (K)	185.02	33.90	13.32	
Phase (day)		176.80	94.81	
Amplitude (K)	185.02	33.90	13.32	2.88
Phase (day)		176.80	94.81	59.93

Table 6-5. Amplitude and phase (day of maximum) for the fitted curves in Figure 6-37, and for the MSIS-E-90 model for all days.

Secondly, MSIS-E-90 temperatures are derived with only annual and semi-annual components. It is apparent that the broad local minimum around midwinter is produced as a result. Clearly a fit extending only to a semi-annual term does not well represent the observed data. Fitted temperatures are too high at the start and end of the observing season, and a broad local minimum in mid-winter is generated. Including a ter-annual term provides a much better fit in spring and autumn and reduces the apparent midwinter minima.

Thirdly, hydroxyl temperature variations of up to 30 K in amplitude with periods between 10 and 25 days are occasional features of the Davis winter (see for example D230-280, 2000 in Figure 6-34 and D175 and D225, 1998 in Figure 6-32). These are most likely due to planetary wave activity (Scheer *et al.* (1994)) or changes in the mean circulation that enhance adiabatic cooling (upward-flow) or compressional heating (downward-flow). These events are sufficiently randomly distributed that, when all years are combined, there is no significant evidence supporting a local mid-winter temperature minima.

MSIS-E-90 temperatures presented in Figure 6-37 average 202.2 K while hydroxyl temperatures for the same 1310 nights average 203.5 K. Residual standard deviations (after extracting the periodic fit including ter-annual component) are 4.8 K and 1.1 K for hydroxyl and model temperatures respectively. MSIS-E-90 temperatures are stated to fit other observations (rocket and incoherent scatter radar data in the upper mesosphere and Handbook for MAP 16 tabulations in the lower atmosphere) to an overall standard deviation of 3 K (Hedin (1991)). In this case, if the 87 km, midnight average MSIS-E-90 model fit is extracted from the hydroxyl temperatures, a standard deviation of 4.3 K is obtained. Given previously noted uncertainties about hydroxyl altitude and profile variations, and MSIS-E-90 representation as only low-order spherical harmonics, agreement between model and hydroxyl temperatures is good.

In order to estimate a long-term trend, a hydroxyl-layer winter temperature is defined for each year as the mean of nightly averages over the interval D106–258 (centred on 1-Jul, D182). However, to take account of data gaps in individual years (1990, 1994, 1996 and 1999 in particular) each nightly mean is first corrected for the average winter slope for all years (-0.04 Kd^{-1}) to a temperature appropriate for 1 July (D182). The largest correction is -0.4 K for 1994, where the number of nightly averages in early winter is much greater than in late winter due to sampling mode changes. Mean and corrected-mean (annual 1 July) winter temperatures, associated errors, and the number of contributing nightly averages are listed for each year in Table 6-6. Solar F10.7 cm and MgII composite indices, averaged over the same nights (without correction) are also shown. Figure 6-38 plots corrected winter average temperatures with standard error-in-the-mean error bars. Best-fit linear trends show cooling at a rate of 2.24±0.09 Ka^{-1} between 1990 and 1995 and warming at 1.15±0.35 Ka^{-1} between 1995 and 2000. A solar cycle dependency is apparent. Winter temperatures

are plotted against average 10.7 cm solar flux in Figure 6-39 and against MgII composite index in Figure 6-40. Best-fit linear trends yield 0.066±0.015 K(sfu)$^{-1}$ and 490.6±125.5 K(MgII unit[1])$^{-1}$ respectively. Full solar cycle ranges for 10.7 cm solar flux (of 120 sfu), and for the MgII composite index (of 0.018), both imply hydroxyl-layer temperature variations of 8-9 K.

Year	1990	1994	1995	1996	1997	1998	1999	2000
Winter Nights	53	81	138	111	126	143	81	140
OH Temp	**214.32**	**205.93**	**202.77**	**204.94**	**203.36**	**205.23**	**209.09**	**208.12**
Error in Mean	0.96	1.22	0.63	0.70	0.69	0.55	0.78	0.63
OH Corrected	**214.18**	**205.53**	**202.84**	**205.02**	**203.14**	**205.20**	**208.94**	**208.14**
Error in Mean	0.91	1.10	0.64	0.66	0.72	0.50	0.73	0.65
Correction	-0.13	-0.40	0.07	0.08	-0.23	-0.03	-0.15	0.02
F10.7	186.45	82.66	74.20	71.06	75.75	117.03	157.87	178.52
Error in Mean	6.91	0.80	0.50	0.34	0.71	1.57	2.49	2.65
MgII	0.1441	0.1318	0.1302	0.1294	0.1303	0.1360	0.1407	0.1446
Error in Mean	0.0006	0.0001	0.0001	0.0001	0.0001	0.0002	0.0003	0.0003

Table 6-6. Winter-average temperatures – derived as an average of the nightly-average temperatures over the interval D106-258 for each year, corrected temperatures – derived by adjusting each nightly-average by the mean winter slope to an equivalent 1-Jul temperature, F10.7 cm and MgII composite solar activity indices averaged over the same days each year. Errors listed are standard error-in-the-mean values (standard deviation/sqrt(number of winter nights averaged)).

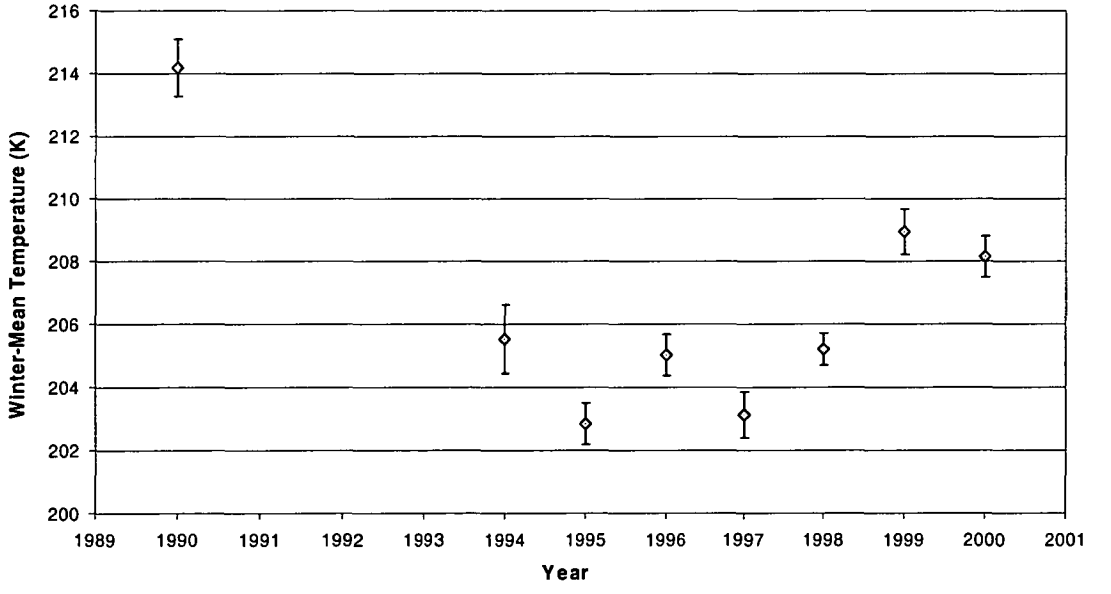

Figure 6-38. Corrected winter-average hydroxyl-layer temperatures above Davis. Error bars are ± one standard error. Cooling trend between 1990 and 1995 is at 2.24Ka^{-1} and warming trend between 1995 and 2000 is at 1.15Ka^{-1}.

[1] The MgII composite index is a core to wing ratio of several emission lines, defined for example at http://gome1.physik.uni-bremen.de/gome/. It is a dimensionless quantity.

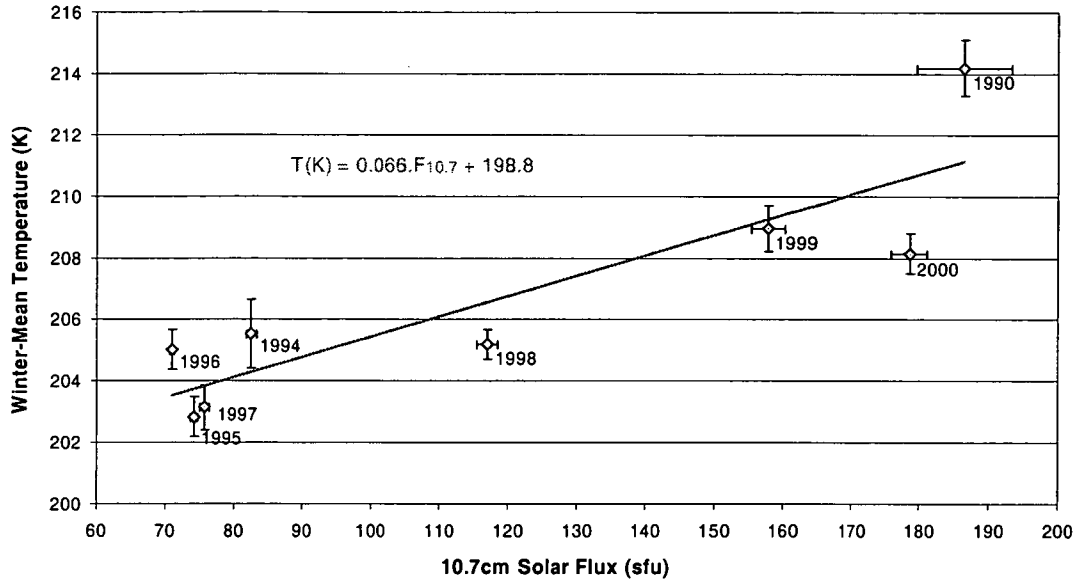

Figure 6-39. Winter-mean hydroxyl-layer temperatures against averaged 10.7 cm solar flux with a linear best-fit trend. Error bars are standard error-in-the mean values from Table 6-6.

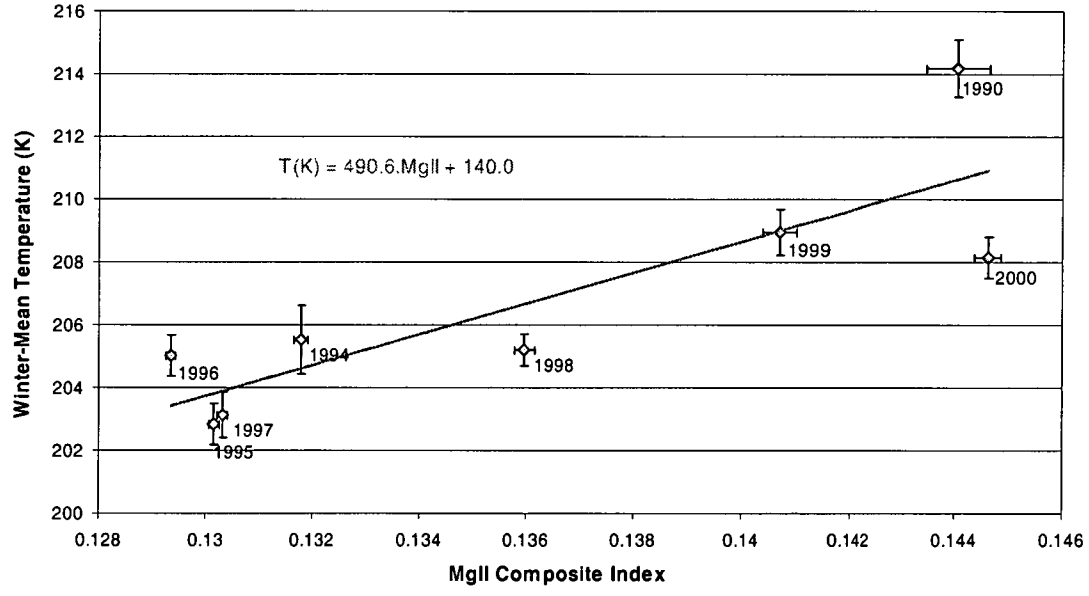

Figure 6-40. Winter-mean hydroxyl-layer temperatures against averaged MgII composite index with a linear best-fit trend. Error bars are standard error-in-the mean values from Table 6-6.

Only four years (1990, 1998, 1999 and 2000) have sufficient range in solar activity to determine a slope from a comparison with nightly temperature averages within the year (as per Sahai *et al.*, 1996). Slopes obtained are: 0.02, 0.02, 0.08 and -0.04 K(sfu)$^{-1}$ and 203.6, 406.4, 618.6 and 171.9 K(MgII unit)$^{-1}$ respectively. High variability in these slopes implies that the solar cycle variation in hydroxyl temperatures at Davis is not dominated by a direct influence manifested on time-scales of order of a day or so.

A multivariate fit involving long-term trend (L) and solar cycle (S) terms of the form

$$T = L.(\text{year}-1990) + S.F_{10.7} + C \qquad \textit{Equation 6-1}$$

has also been made on the corrected winter averages. Values derived for coefficients L and S were -0.482 ± 0.13 K/year (95% confidence limits -0.148 to -0.815 K/year) and 0.067 ± 0.008 K/sfu (95% confidence limits 0.088 to 0.045 K/sfu) respectively. The constant C was determined as 202.2 ± 1.4 K (95% confidence limits 205.8 to 199.5 K). The calculated fit is shown in Figure 6-41. If the solar cycle component of the fit is subtracted from the winter averages the residual long term trend shown in Figure 6-42 is obtained.

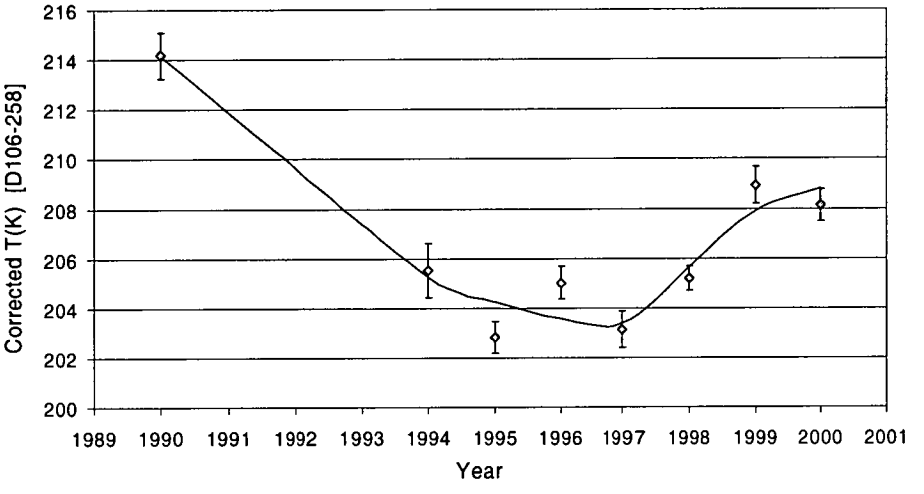

Figure 6-41. A multivariate long-term trend and solar cycle fit to the corrected winter averages of the form shown in equation 6-1.

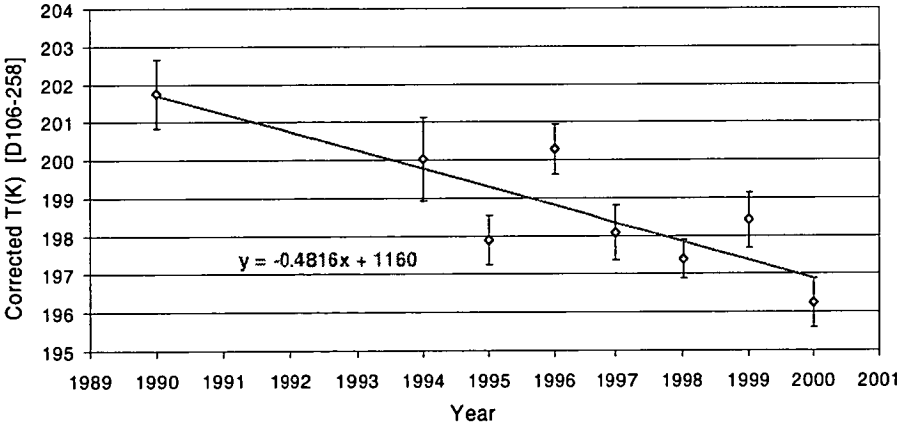

Figure 6-42. The long-term trend observed in the Davis winter temperatures with the fitted solar cycle component removed.

The progression of trends obtained by the multivariate analysis over the years of measurement are examined in Figure 6-43 for the solar cycle trend and in Figure 6-44 for the long-term trend. As each year is added the statistical significance of the trend

estimates has increased and the trend estimates have remained within the error of the previous measurement, i.e. the trend estimates have not diverged as the number of years of measurements has increased. Calculated in this way, some degree of long-term cooling in the winter average temperatures over Davis is now within 95% confidence limits.

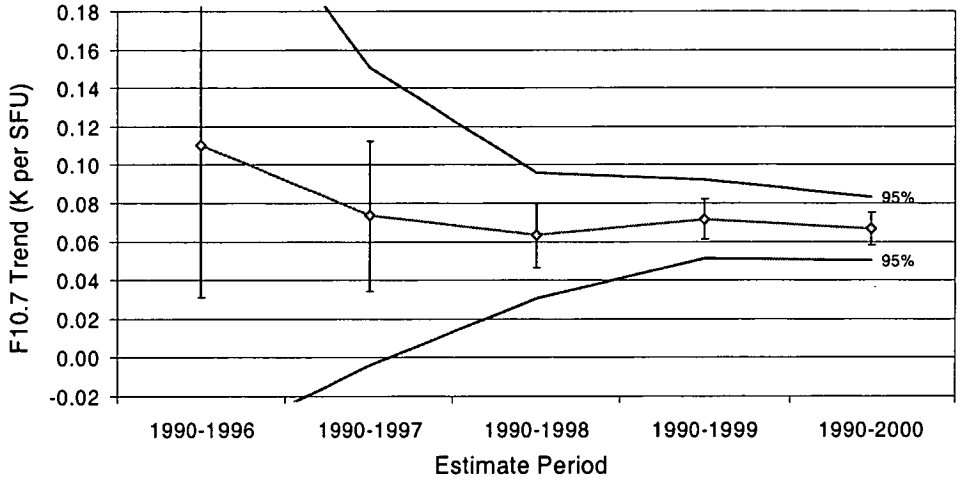

Figure 6-43. The progression of trends in the solar cycle trend estimate calculated over the years of measurement. One standard error and 95% confidence limits are shown.

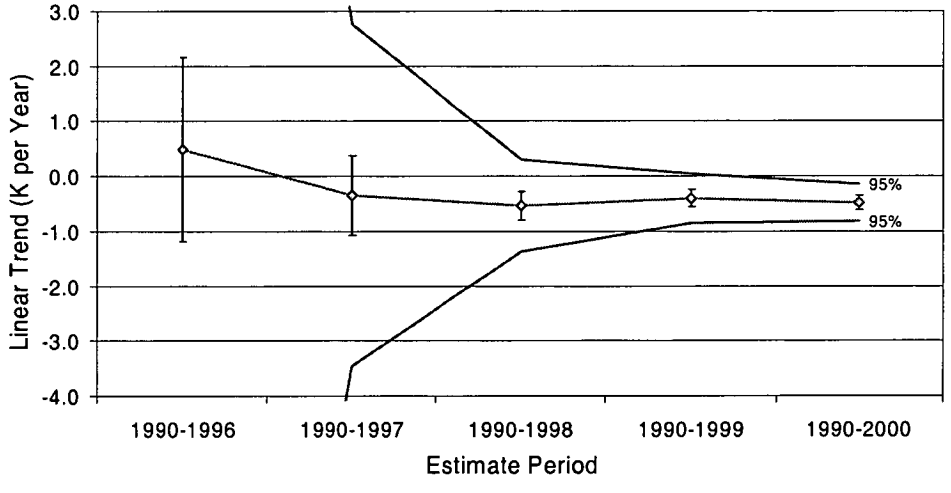

Figure 6-44. As for Figure 6-43 but for the long-term linear trend.

So far, the trend analysis has only been applied to the corrected winter mean temperatures [averaged for the 153 days between days 106 and 259]. Trends could of course be calculated for different day ranges, averaged for each year. Figure 6-45 for example, presents the multivariate trend analysis described above, for 70-day sliding window averages (shifted by one day) calculated for each year (1990-2000). So that the seasonal variation did not bias the trends, the best fit annual, semi-annual and ter-annual components (derived for all data as shown in Figure 6-37) were subtracted

from each year and temperature averages were corrected by the slope across the averaging window, to the window central day as previously described.

Variation in the solar cycle trend ranges between 0.025 K/sfu and 0.082 K/sfu, but is relatively consistent through the winter months around 0.06-0.07 K/sfu. In the long term trend variation, there is an indication that the cooling trend is greatest in the winter months, where it reaches -0.9K/year, but tends toward zero at the equinoxes, although the statistical significance decreases at these times. A best fit is obtained for the 70 day window centred on day 189 (0.063±0.002 K/sfu and -0.88±0.03 K/year).

These general tendencies persist with larger and smaller averaging windows but larger windows obviously smooth the variation and for windows smaller than about 30 days the trends are highly variable due to the effect of planetary scale variations in the data.

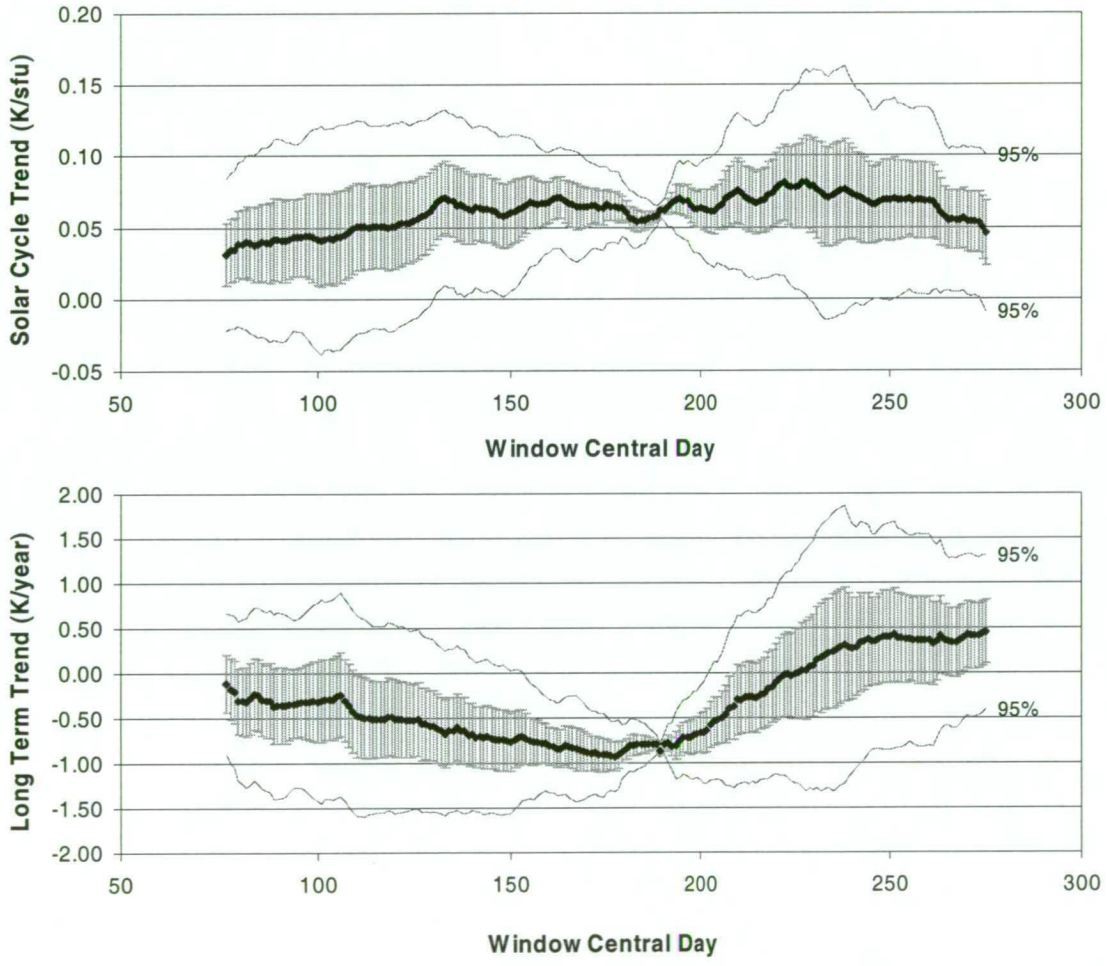

Figure 6-45. Results of the multivariate trend analysis calculated on 70-day sliding window temperature averages (corrected to the window centre) each year (1990-2000). One standard error and 95% confidence limits are also show.

6.5. Comparisons with other observations.

6.5.1. Seasonal variations

Lübken and von Zahn (1991) detail the mesosphere temperature structure above Andenes, Norway (69°N, 16°E) using 180 days of sodium lidar profiles and in-situ density measurements between 1980 and 1990. Winter and transition-season temperatures at 87 km for this northern-hemisphere latitude-equivalent of Davis are very similar to the hydroxyl temperatures presented here. An extensive (~6 month) winter season with a relatively constant temperature bounded by sharp seasonal transitions, particularly in the autumn, is apparent for both sites. Lübken and von Zahn (1991) list average monthly temperatures for nine months for mesospheric heights with a 1 km resolution. Davis hydroxyl-layer monthly averages, calculated as the average of corrected nightly-averages, are listed in Table 6-7 for comparison.

		Davis OH								SME		L&vZ	She&Lowe	
SH	Year	1990	1994	1995	1996	1997	1998	1999	2000	86.5 70°S	NH	87km 69°N	OH 43°N	Lidar 41°N 87km
Mar	Mean			**190.0**	**193.5**	**197.6**	**191.7**	**197.2**	**194.6**	198	Sep			
	Error			2.3	2.2	1.7	2.1	2.0	1.8	11				
	Count			23	22	20	25	28	31				204.0	210.0
Apr	Mean	**209.0**	**205.5**	**197.3**	**209.1**	**196.6**	**204.2**	**204.3**	**203.6**		Oct	209.3	5	6.2
	Error	1.9	1.8	1.6	1.1	0.9	0.8	0.8	0.6					
	Count	14	15	25	28	29	25	4	29					
May	Mean	**218.1**	**213.5**	**204.4**	**203.6**	**205.7**	**207.4**	**212.5**	**208.6**		Nov	213.4		
	Error	2.0	1.6	1.3	1.2	0.9	0.8	1.1	0.8					
	Count	10	21	28	26	27	31	24	25					
Jun	Mean	**212.4**	**209.4**	**202.7**	**206.2**	**202.6**	**203.7**	**205.8**	**208.8**		Dec	204.9		
	Error	2.2	1.2	1.2	1.9	1.1	1.7	1.6	1.2					
	Count	12	17	27	15	29	28	22	29				213.7	224.7
Jul	Mean	**215.3**	**205.9**	**205.1**	**202.4**	**198.0**	**206.7**	**208.3**	**205.6**		Jan	205.2	8.5	9.9
	Error	2.0	1.3	1.2	1.6	1.4	0.7	1.2	1.3					
	Count	9	17	28	9	23	31	26	27					
Aug	Mean	**213.8**	**190.3**	**203.7**	**203.7**	**206.6**	**203.2**		**209.4**		Feb	208.7		
	Error	1.5	3.2	1.1	1.5	1.5	1.2		1.7					
	Count	13	9	30	31	23	28		30					
Sep	Mean	**205.0**	**197.3**	**203.4**	**204.4**	**207.6**	**201.6**	**206.9**	**211.9**	222	Mar	202.1		
	Error	2.2	2.9	1.4	1.3	1.9	0.8	1.1	1.6	11				
	Count	5	9	28	22	24	24	24	29				200.3	202.4
Oct	Mean		**204.0**	**198.6**	**198.6**	**200.6**	**195.6**	**205.6**	**196.3**	200	Apr		7.3	10.6
	Error		2.4	1.8	1.1	1.1	1.0	1.3	2.1	11				
	Count		4	12	17	14	20	16	18					

Table 6-7. A comparison of Davis hydroxyl-layer monthly-mean temperatures with SME limb scattering data of Clancy and Rusch (1989) and northern hemisphere measurements of Lubken and von Zahn (1991) [L&vZ], and She and Lowe (1998) for equivalent months at 87 km altitude. Standard error-in-the-mean and number of nights contributing to each mean are also listed.

Variations due to planetary waves or mean flow changes, coupled with solar cycle variability obviously affect the monthly averages from year to year. Data contributing to Andenes monthly means cover a range of solar activity levels. Davis hydroxyl temperatures yield an average winter value, corrected to 1 July, of 207±4 K. The comparable average of the 87 km, Andenes, November to February monthly means is 208 K. Given the vertical profile of the hydroxyl layer and measured solar cycle dependence, the months that can be compared show no significant difference in magnitude or seasonal trend.

At high latitudes, a longer and colder winter season, with more rapid equinoctial transitions appears to be typical of both hemispheres when compared with northern hemisphere, mid-latitude observations, for example Nicie-jewski and Killeen (1995) [at Ann Arbor: 42.5°N], Mulligan *et al.* (1995) [at Maynooth: 53°N], and She and Lowe (1998) [at Delaware: 43°N and Fort Collins: 41°N]). Observations from the latter two are reproduced in Figure 6-46 and compared with the seasonal variation at Davis, 69°S, shifted by 6 months.

Clancy and Rusch (1989) present a climatology of monthly average mesosphere temperatures derived from ultraviolet limb radiances

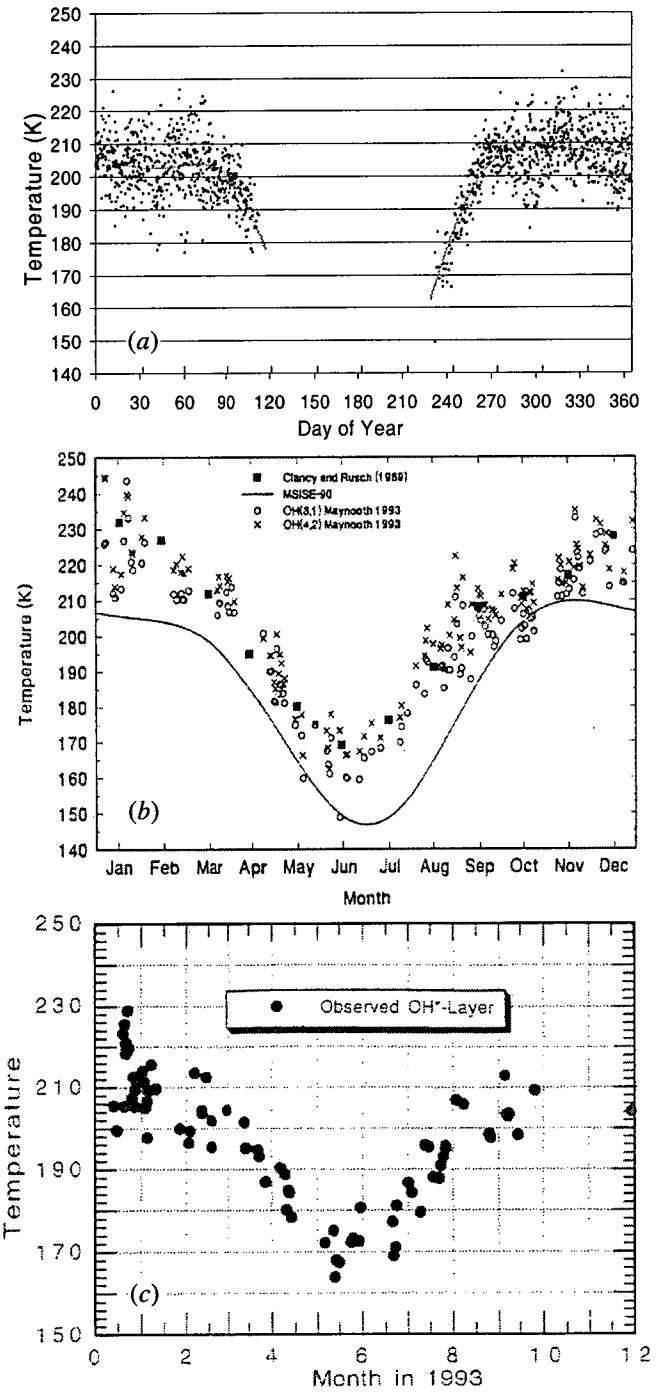

Figure 6-46. OH seasonal variations for (a) Davis (68°S) shifted 6 months, (b) Maynooth (53°N) from Mulligan et al. *(1995) including MSISE-90 and (c) Delaware (43°N) from She and Lowe (1998).*

measured by Solar Mesosphere Explorer (SME). Averages are calculated at 10° latitude and ~4 km altitude resolution for the 1982 - 1986 interval. Clancy and Rusch (1989) determine an 11 K uncertainty for monthly means at 90 km. Accuracy is slightly improved for the 86.5 km, 70°S values most suitable for comparison with Davis hydroxyl temperatures. Only three months are available for comparison. SME means for March (198 K), September (222 K) and October (200 K) compare with Davis average monthly means from 1990-2000 of 194 K, 206 K and 199 K respectively. The years compared cover a similar range of solar activity. March and October averages agree well, but September averages differ by ~17 K. The maximum September average in any year (212 K) is still 10 K lower than the SME value. Similarly, the SME 70°N, 86.5 km March temperature average of 218 K, is ~16 K greater than the Andenes (69°N) 87 km March average of 202 K (Clancy and Rusch (1989); Lübken and von Zahn (1991)). Andenes September or October averages are not available. SME monthly averages are significantly higher than comparable ground based measurements for the spring equinoctial month at 70° in both hemispheres.

Williams (1996) reports hydroxyl OH(8-3) rotational temperatures determined from 139 spectra collected at Davis in 1987. An 'observing season' (April to October) average of 205 +/-10 K is reported. This 'observing season' average may be lower than the winter average we determine, as some of a cooler spring transitional interval is included. Solar activity in 1987 was quiet but slightly more active than the lowest solar activity years. An uncertainty of 10 K makes the 'observing season' value not inconsistent with these measurements, but lack of instrument spectral-response correction raises a concern about 1987 absolute values. Williams (1996) reports an abrupt 10-20 K decrease in monthly temperatures after mid-winter. This is inconsistent with the gradual decrease across 'winter' (DOY 106-258), amounting to 6 K, found here. Likely reason for this discrepancy is the low number of spectra (~20 per month) contributing to the 1987 averages and the natural variability of temperatures at hydroxyl-layer altitudes.

6.5.2. Solar Cycle Variation and Long-term Trend.

Eight years of Davis winter averages yields a solar-cycle best-fit of 0.066 K $(sfu)^{-1}$ (8 K:120 sfu). Removing the least reliable winter averages (1990 and 1994), yields a

gradient of 0.05 K(sfu)$^{-1}$ (6 K:120 sfu). Reasons for being wary of 1990 and 1994 values include greater uncertainty in the spectral response calibrations (2 K, compared with 1 K for recent calibrations), larger sampling error due to longer acquisition times (comparisons with photometer determined intensities in section 3.4.2 suggest temperatures should be ~1 K warmer), low numbers of both spectra-per-night and nightly averages that contribute to the winter average and the off-zenith (60°) viewing angle used in 1990 (MSISE-90 model indicates the Davis zenith should be ~1 K cooler than the off-zenith region sampled).

Long-period planetary-scale fluctuations apparent in the Davis nightly averages, coupled with data collection centred on new moon intervals, also make 1990 and 1994 winter averages susceptible to variation. The magnitude of this variation can be estimated by applying the spacing of winter nights sampled in 1990 or 1994, to the 1998 data set (the most complete year). By progressively shifting the winter nights sampled by one day, 50 'test' mean-winter-values of the 1998 data were determined using the 1990 and 1994 sampling regimes. Averages of these 'test' winter-means were 204.9 K and 205.0 K respectively; compared to the 'true' 1998 winter mean of 205.2 K, however the range for both was 203-207 K and standard deviation 1.2 K.

Reported solar-cycle associated temperature variations at these altitudes are typically much greater (18-38 K per solar cycle) than is apparent in the Davis data (see section 6.1.2, Shefov (1969a); Labitske and Chanin (1988); Sahai *et al.* (1996); Lübken and von Zahn (1991)). Even though the Davis data only partially span a solar cycle at present and these are predominantly obtained during the minimum and rising phase of cycle 23 (1995-2000) a solar cycle dependence of magnitude as large as these reports does not appear to be within the statistical uncertainty in the multivariate analysis of the Davis observations calculated in section 6.4.

This analysis does support some long term cooling in the winter averages over Davis within 95% confidence limits. Large trends, such as the -0.7 K/year reported by Golitsyn *et al.* (1996) are well within these confidence limits both for the winter average and 70-day sliding window analyses. The cooling trend appears to be restricted to the winter months however, and lower, or possible zero trend rates consistent with other researchers (e.g. Lowe (priv.comm.), Krueger and She (1999)) may be obtained if the averages are taken across the whole year.

Bittner *et al.* (2000) report an increase of 0.8 K per decade (~16% per decade) in the standard deviation of residuals from the seasonal temperature trend above Wuppertal (51°N). Annual value of this standard deviation never exceeds 5.5 K for the Wuppertal data. Annual standard deviations of 'corrected' Davis winter temperatures are 6.6[1990], 9.9[1994], 7.6[1995], 7.0[1996], 8.1[1997], 6.0[1998], 6.6[1999], 7.7[2000] K. They range over 3.9 K, but show no significant trend. Davis temperatures show reduced variability in the transition periods before and after winter. This is particularly apparent for the autumn interval (Figure 6-37, D050-080). If a complete year of Davis data were available to determine the standard deviation of residuals, the magnitude may be reduced. This may account for the difference in magnitude between Davis and Wuppertal residuals. Latitudinal differences may also contribute.

6.6. Conclusions

Observations of hydroxyl (6-2) emissions at Davis have provided 1310 nightly mean temperatures from 126,444 spectra acquired over eight years. Seasonal variability and absolute magnitudes (206.6±3.7 K; average 1 July value) are consistent with a comparable northern hemisphere site (Lübken and von Zahn (1991)).

There is a gradual temperature decline across the central winter interval (-0.04 Kd^{-1}; D106 - 258). Temperatures during equinoctial transition periods show a sharp rise in autumn (at 1.2 Kd^{-1}; D049 - 080) and a more gradual spring decline (at -0.65 Kd^{-1}; D275 - 296). Comparable MSIS-E-90 model rates are 1.0 Kd^{-1} in autumn and -0.8 Kd^{-1} in spring.

Temperature variations of up to 30 K, with periods between 10 and 25 days are occasional features during winter. These are believed to be associated with planetary waves or changes in the mean flow that enhance adiabatic cooling or compressional heating.

A periodic fit to the seasonal variation is more appropriate if a ter-annual term is included. There is no significant evidence supporting a local mid-winter minima as represented in the MSIS-E-90 model.

There is no indication of a trend toward increased hydroxyl temperature variability as reported by Bittner *et al.* (2000).

Winter temperature averages for 8 years of Davis hydroxyl data are consistent with a positive solar cycle association of 0.066 K $(sfu)^{-1}$, considerably lower than most values reported in the literature. The solar activity association found in the winter means is not consistently reflected within individual years.

The multivariate analysis presented supports some cooling of the winter mean temperatures over Davis within 95% confident limits. Large cooling rates such as reported by Golitsyn *et al.* (1996) are well within these limits. The cooling trend appears to decreases toward the equinoxes however, and lower cooling rates, as reported by others, may be obtained if the temperature averages are derived across full years.

6.7. Recommendations for future work.

Recommendations for future work on the hydroxyl airglow project at Davis are as follows:

- Continued observation, at least through to the next solar minima in 2006 should enable a resolution of the coupled solar-cycle/long-term-trend association with hydroxyl temperatures above Davis. It is imperative that proper instrument calibration be maintained and changes to sampling mode minimized. Sampling should be as continuous as possible in order to derive accurate winter-mean temperatures.

- Analysis of OH(8-3) band spectrometer data will:
  a) extend the data set back to 1987
  b) enable an OH(6-2)/OH(8-3) temperature comparison for the alternate scans obtained in 1990 and
  c) Fill the two data gaps in 1999.

  Analysis routines for OH(8-3) spectra are already partially developed. A detailed examination of the background is required for proper background estimates.

- Six-channel photometer observations are available for 1984, 1987, 1990 and 1994 although different lines, in either the OH(8-3) or OH(6-2) bands, have been measured at various times over these years. Intensity variations have been examined in the 1990 set in section 4.4.2 to estimate a sampling error.

Temperature analysis of the 1984 data has been attempted previously (Williams (1987)) but a large differences between the three possible ratios were obtained, implying a misestimation or contamination of line intensities. A comparison of 1990 and 1994 photometer data with equivalent spectrometer data may enable an improved analysis.

- Extension of the observing season beyond current limits [D049-D296] will enable better characterization of the spring and autumn transition periods, and provide temperature measurements during the noctilucent cloud season. To this end a Fourier transform spectrometer is currently undergoing testing at Australian Antarctic Division (in collaboration with the University of Western Ontario) for deployment at Davis in 2002. This system monitors OH(4-2) and (3-1) band emissions between 1.2 and 1.6 μm, and incorporates a sun-tracking polarizer to preferentially reduce skylight contamination. It is anticipated that this system will also allow 24-hour observations over the midwinter period. Measurement of temperature, OH intensity and atomic oxygen emissions during the long twilight (considered too rapid at lower latitudes) is expected to provide information on changes in OH photochemistry between day and night.

- Large scale (up to 30 K) randomly distributed temperature variations are apparent in most years. Investigation of these events in comparison with the mean horizontal wind and implied vertical winds from a co-located 2MHz spaced antenna radar (operated in association with the University of Adelaide) is proposed.

- Future comparative studies may also be undertaken with the Lidar system installed at Davis in Feb-2001. Winds, temperatures and densities as a function of height may possibly extend as high as the mesopause, though this is at the limit of its range.

- Event analysis on a daily timescale also warrants further investigation. Several interesting examples are provided in section 6.3.1. Tide and gravity wave studies may be made in comparison with the OH scanning radiometer installed at Davis in 1999 and operated in association with the University of Western Ontario.

References

Abreu, J.A. and Yee, J.H. (1989) Diurnal and Seasonal Variation of the Nighttime OH (8-3) Emission at Low Latitudes, *Journal of Geophysical Research,* **94:**11949-11957.

Aiken, A.C., Chanin, M.L., Nash, J. and Kendig, D.J. (1991) Temperature trends in the lower mesosphere. *Geophysical Research Letters,* **18**:416-419.

Akmaev, R.A. and Fomichev, V.I. (1998) Cooling of the mesosphere and lower thermosphere due to doubling of CO_2. *Annales Geophysicae,* **16**:1501-1512.

Akmaev, R.A. and Fomichev, V.I. (2000) A model estimate of cooling in the mesosphere and lower thermosphere due to the CO2 increase over the last 3-4 decades. *Geophysical Research Letters* **27**:2113-2116.

Allen, C.W. (1963) Astrophysical Quantities, *University of London, Athlone Press, 2nd Edition*, London.

Armstrong, E.B. (1975) The Influence of a Gravity Wave on the Airglow Hydroxyl Rotational Temperature at Night, *Journal of Atmospheric and Terrestrial Physics* **37:**1585-1591.

Baker, D.J. and Stair Jr., A.T. (1988) Rocket Measurements of the Altitude Distrubitions of the Hydroxyl Airglow, *Physica Scripta,* **37:**611-622.

Bates, D.R. and Moiseiwitsch, B.L. (1956) Origin of the Meinel Hydroxyl System in the Night Airglow, *Journal of Atmospheric and Terrestrial Physics,* **8:**305-308.

Bates, D.R. and Nicolet, M. (1950) The photochemistry of atmospheric water vapor, *Journal of Geophysical Research,* **55**:301-327.

Battaner, E. and Lopez-Moreno, J.J.(1979) Time and Altitude Variations of Vibrationally Excited States of Atmospheric Hydroxyl, *Planetary and Space Science* **27:**1421-1428.

Berger, U. and Dameris, M. (1993) Cooling of the upper atmosphere due to CO_2 increases: a model study. *Annales Geophysicae* **11**:809-819.

Bittner, M., Offermann, D. and Graef, H.H. (2000) Mesopause temperature variability above a mid-latitude station in Europe. *Journal of Geophysical Research* **105 (D2)**:2045-2058.

Boyle, W. and Smith, G. (1970) Charge Coupled Semiconductor Devices, *Bell Systems Technical Journal*, **49**:587.

Broadfoot, A.L. and Kendall, K.R. (1968) The airglow spectrum 3100-10000Å, *Journal of Geophysical Research* **55**:301

Burns, G.B., French, W.J.R., Greet, P. A., Williams, P.F.B., Finlayson, K., Lowe, R.P. (1998) Monitoring the Antarctic mesopause region for signatures of climate change. *Annals of Glaciology* **27:**669-673.

Burns, G.B., French, W.J.R., Greet, P.A., Williams, P., Finlayson, K. and Lowe, R.P. (2001a) The Mesopause region above Davis, Antarctica (68.6°S, 78.0°E), in *Long Term Changes and Trends in the Atmosphere* Ed. Beig, G. *proceedings of the First International Workshop on Long Term Changes and Trends in the Atmosphere.*

Burns, G.B., French, W.J.R., Greet, P. A., Phillips, F.A., Williams, P.F.B., Finlayson, K. and Klich, G. (2001b) Seasonal Variations and inter-year trends in seven years of hydroxyl airglow rotational temperatures at Davis station (69°S, 78°E), Antarctica. *Journal of Atmospheric and Solar-Terrestrial Physics* (in press).

Burns, G.B., Williams, P.F.B., Lowe, R.P., French, W.J.R., Greet, P.A. and Monselesan, D.P. (2001) Argon Auroral emissions, *Journal of Atmospheric and Solar-Terrestrial Physics* (in press).

Chalamala, B.R. and Copeland, R.A. (1993) Collision dynamics of $OH(X^2\Pi_i,v=9)$, *Journal of Chemical Physics*, **99**:8 5807-5811

Chamberlain, J. W. (1961) Physics of the aurora and the airglow, *Academic Press*, New York.

Chamberlain, J.W. and Roesler, F.L. (1955) The OH Bands in the Infrared Airglow, *The Astrophysical Journal* **121:**541-547.

Choi, G.H., Monson, I.K., Wickwar, V.B. and Rees, D. (1998) Seasonal and diurnal variations of wind and temperature near the mesopause from Fabry-Perot interferometer observations of OH Meinel emissions. *Advances in Space Research* **21**:847-850.

Clancy, R.T. and Rusch, D.W. (1989) Climatology and trends of mesospheric (58-90 km) temperatures based upon 1982-1986 SME limb scattering profiles. *Journal of Geophysical Research* **94 (D3):** 3377-3393.

Clancy, R.T., Rusch, D.W. and Callan, M.T. (1994) Temperature minima in the average thermal structure of the middle mesosphere (70-80 km) from analysis of 40- to 92-km SME global temperature profiles. *Journal of Geophysical Research,* **99 (D9):**19001-19020.

Clancy, R.T., Sandor, B.J. and Rusch, D.W. (1994) Microwave observations and modeling of O_3, H_2O and HO_2 in the mesosphere. *Journal of Geophysical Research* **99**:D3, 5465-5473

Clemesha, B. R. Batista, P. P. and Simonich, D. M. (1997) Long-term and solar cycle changes in the atmospheric sodium layer. *Journal of Atmospheric and Solar-Terrestrial Physics* **59**:13, 1673-1678.

Clemesha, B.R., Simonich, D.M. and Batista, P.P. (1992) A long-term trend in the height of the atmospheric sodium layer: possible evidence for global change, *Geophysical Research Letters* **19**:457-460.

Clyne , M.A.A, and Monkhouse, P.P. (1977) Atomic resonance fluorescence for rate constants of rapid bimolecular reactions. Part 5. Hydrogen atom reactions: $H+NO_2$ and $H+O_3$. *J. chem. Soc. Farad. Trans. II* **73**:298.

Cogger, L.L., Elphinstone, R.D. and Giers, D.H. (1988) Wave characteristics obtained from OH rotational temperatures and 557.7 nm airglow intensities. *Journal of Atmospheric and Terrestrial Physics* **50**:943-949.

Connes, J. and Gush, H.P. (1960) *J.Phys. Radium* **21**:645.

Conway, R.R., Stevens, M.H., Cardon, J.G., Zasadil, S.E., Brown, C.M., Morrill, J.S. and Mount, G.H. (1996) Satellite measurements of hydroxyl in the mesosphere. *Geophysical Research Letters* **23(16)**:2093-2096.

Coxon, J.A. (1980) Optimum Molecular Constants and Term Values for the X2Pi(v<=5) and A2Sigma+(v<=3) States of OH, *Canadian Journal of Physics* **58:**933-949.

Coxon, J.A. and Foster, C.S. (1982) Rotational Analysis of Hydroxyl Vibration-Rotation Emission Bands: Molecular Constants for $OHX^2\Pi$, 6<=v<=10, *Canadian Journal of Physics* **60**:41-48.

Danilov, A.D. (1997) Long-term changes of the mesosphere and lower thermosphere temperature and composition. *Advances in Space Research* **20**:2137-2147.

Dick, K.A. (1972) Short Time-Interval Spectrometric Hydroxyl Emission Studies, *Annales Geophysicae* **28:**149-153.

Dunkerton, T.J. Delisi, D.P. and Baldwin, M.P. (1998) Middle atmosphere cooling trend in historical rocketsonde data. *Geophysical Research Letters* **25**:3371-3374.

Dyer, M.J., Knutsen,K. and Copeland, R.A. (1997) Energy Transfer in the ground state of OH: Measurements of OH(v=8,9,10) removal., *Journal of Chemical Physics*, **107**:19 7809-7815

East, S.A., Meredith, N.P., Harris, M.J., Rees, D., Wickwar, V.B., Monson, I.K. and Muller, H.G. (1995) First Summer results on winds in the upper mesosphere derived from the 843 nm Hydroxyl emission measured from the Bear Lake Observatory, Utah, *Journal of Atmospheric and Terrestrial Physics,* **57:**995-1008.

Eather, T.H. and Reasoner, D.L. (1969) Spectrometry of faint light sources with a tilting-filter photometer. *Applied Optics,* **8**:227-242.

Elsworth, Y.,Lopez-Moreno, J.J.,James, J.F. (1997) Hight Resolution Spectrography of Hydroxyl in the Night Airglow, *Journal of Atmospheric and Terrestrial Physics,* **59:**117-124

Espy, P.J. and Hammond, M.R. (1995) Atmospheric Trasmsission coefficients for hydroxyl rotational lines used in rotational temperature determinations. *J.Quant. Spectrosc. Radiat. Transfer,* **54**:879-889.

Espy, P.J. and Witt, G. (1996) Observation of a quasi 16-day oscillation in the polar summer mesospheric temperature. *Geophysical Research Letters.* **23**:1071-1074.

Etheridge, D.M., Steele, L.P., Langenfelds, R.L., Francey, R.J., Barnola, J.-M. and Morgan, V.I. (1998) Historical CO_2 records from the Law Dome DE08, DE08-2, and DSS ice cores. In *Trends: A Compendium of Data on Global Change.* Carbon Dioxide Information Analysis Center, Oak Ridge National Laboratory, U.S. Department of Energy, Oak Ridge, Tenn., U.S.A

Evans, W.F.J. and Llewellyn, E.J. (1972) Excitation Rates of the Vibrational Levels of Hydroxyl and Nightglow Intensities, *Planetary and Space Science* **20:**624-626.

Evans, W.F.J. and Llewellyn, E.J. (1973) Atomic Hydrogen Concentrations in the Mesosphere and the Hydroxyl Emissions, *Journal of Geophysical Research* **78:**323-326.

Evans, W.F.J., Llewellyn, E.J. and Vallance-Jones, A. (1973) Altitude Distribution of Hydroxyl Bands of the Delta v = 2 Sequence in the Nightglow, *Canadian Journal of Physics* **51:**1288-1292.

Fastie, W.G. (1952) A small plane grating monochromator, *Journal of the Optical Society of America,* **42**:641.

Fellgett, P. (1951) PhD Thesis, *Cambridge University*

Fiocco, G., Visconti, G. and Congeduti, F. (1970) Nocturnal Variation of the Intensity and Rotational Temperature of the OH (8,3) Band in the Airglow, *Nature* **228:**1079-1080.

Fleming, E.L., Chandra, S., Barnett, J.J. and Corney, M. (1990) Zonal mean temperature, pressure, zonal wind, and geopotential height as functions of latitude. *Advances in Space Research* **10(12)**:11-59.

Forsyth, R.J. and Wraight, P.C. (1987) A Survey of Research on Airglow Variability, *Planetary and Space Science* **35:**1449-1461.

French, W.J.R., Burns, G.B., Finlayson, K., Greet, P. A., Lowe, R.P. and Williams, P.F.B. (2000) Hydroxyl (6-2) airglow emission intensity ratios for rotational temperature determination. *Annales Geophysicae*, **18:**1293-1303.

French, W.J.R., Burns, G.B., Greet, P. A. and French, K. (2000) Antarctic Noctilucent Clouds: The upper atmosphere exposed to View, *The Physicist,* **37**:85-90.

Furguson, A.F. and Parkinson, D. (1963) The hydroxyl bands in the nightglow. *Planetary and Space Science*, **11**:149.

Gadsden, M. (1985) Observations of noctilucent clouds from North-West Europe. *Annales Geophysicae,* **3:**119-126.

Gadsden, M. (1990) A secular change in noctilucent cloud occurrence. *Journal of Atmospheric and Terrestrial Physics,* **52(4):**247-251.

Gadsden, M. (1998) The North-West Europe data on noctilucent clouds: a survey. *Journal of Atmospheric and Solar-Terrestrial Physics,* **60:**1163-1174.

Garcia, R.R. and Solomon, S. (1983) A numerical model of the zonally averaged dynamical and chemical structure of the middle atmosphere, *Journal of Geophysical Research* **88**:1379-1400.

Garcia, R.R. and Solomon, S. (1995) The effect of breaking gravity waves on the dynamical and chemical composition of the mesosphere and lower thermosphere. *Journal of Geophysical Research,* **90**:3850-3868.

Gattinger, R.L. (1968) *Canadian Journal of Physics,* **46**:1613.

Gattinger, R.L. (1969) Interpretation of Airglow Emissions - OH Emissions, *Annales Geophysicae* **4:**825-830.

Gattinger, R.L. and Vallance Jones, A.(1974) Quantitative Spectroscopy of the Aurora. II. The Spectrum of Medium Intensity Aurora Between 4500 and 8900 Å, *Canadian Journal of Physics* **52:**2343-2356.

Gattinger, R.L. and Vallance-Jones, A. (1972) Observation and interpretation of hydroxyl airglow emissions, *Physics and Chemistry of the Upper Atmosphere* 184-192. D.Reidel Dordrecht-Holland.

Goldman, A. (1982) Line Parameters for the Atmospheric Band System of OH, *Applied Optics* **21:**2100-2102.

Golitsyn, G.S., Semenov, A.I., Shefov, N.N., Fishkova, L.M., Lysenko, E.V. and Perov, S.P. (1996) Long-term temperature trends in the middle and upper atmosphere. *Geophysical Research Letters* **23**:1741-1744 .

Good, R.E. (1976) Determination of Atomic Oxygen Density from Rocket Borne Measurement of Hydroxyl Airglow, *Planetary and Space Science* **24**:389-395.

Greenblatt, G.D. and Wiesenfeld, J.R. (1982) Time-Resolved Emission Studies of Vibrationally Excited Hydroxyl Radicals: OH($X^2\Pi$, v=9), *Journal of Geophysical Research* **87:**11145-11152.

Greet, P. A., French, W.J.R., Burns, G.B., Williams, P.F.B., Lowe, R.P. and Finlayson, K. (1998) OH(6-2) spectra and rotational temperature measurements at Davis, Antarctica, *Annales Geophysicae* **16**:77-89.

Greet, P.A.,Innis, J.,Dyson, P.L. (1994) High-resolution Fabry-Perot observations of mesospheric OH(6-2) emissions, *Journal of Geophysical Research,* **21:**1153-1156.

Hamamatsu Photonics (1990) Photomultiplier Tubes Handbook, *Hamamatsu Electron Tubes Centre*, Japan.

Hansen, J., Fung, I.,Lacis, A., Rind, D., Lebedeff, R., Ruedy, R., Russell, G. and Stone, P. (1988) Global climate changes as forecast by Goddard Institute for Space Studies three-dimensional model, *Journal of Geophysical Research*, **93**:9341-9364.

Hansen, J., Sato, M., Lacis, A., Ruedy, R., Tegen, I., and Matthews, E. (1998) Perspective: Climate forcings in the industrial era, *Proc. Natl. Acad. Sci.* **22**:12753-12758.

Hansen, J.R. and Lebedeff, S. (1987) Global trends of measured surface temperature. *Journal of Geophysical Research,* **92:**13345-13372.

Hapgood, M.A. and Taylor, M.J. (1982) Analysis of Airglow image data. *Annales Geopyhsicae* **38:**805.

Harrison, A.W. (1970) Altitude Profile of Airglow Hydroxyl Emission, *Canadian Journal of Physics* **48** 2231-2234.

Hauchecorne, A., Chanin, M.L. and Keckhut, P. (1991) Climatology and trends of the middle atmosphere temperature (33-87 km) as seen by Rayleigh lidar over the south of France, *Journal of Geophysical Research* **96**:15297-15309.

Heaps, H.S. and Herzberg, G. (1952) Intensity distribution in the rotational-vibrational spectrum of the OH molecule, *Zeit. f. Phys* **133**:48-64.

Hecht, E. and Zajac, A. (1974) *Optics*, Addison-Wesley Publishing Company, USA.

Hecht, J. H.,Thayer, J. P.,Gutierrez, D.J.,McKenzie, D.L. (1997) Multi-instrument zenith observations of noctilucent clouds over Greenland on July 30/31,1995, *Journal of Geophysical Research* **102 (D2)**:1959-1970.

Hecht, J.H., Walterscheid, R.L., Sivjee, G.G., Christensen, A.B. and Pranke, J.B. (1987) Observations of Wave-Driven Fluctuations of OH Nightglow Emission from Sondre Stromfjord, Greenland, *Geophysical Research Letters* **92:**6091-6099.

Hecht, J.H., Walterscheid, R.L., Woithe, J., Campbell, L., Vincent, R.A. and Reid, I.M. (1997) Trends of airglow imager observations near Adelaide, Australia., *Geophysical Research Letters* **24:**587-590.

Hedin, A.E. (1991) Extension of the MSIS thermosphere model into the middle and lower atmosphere. *Journal of Geophysical Research* **96**:1159-1172.

Heppner, J.P. and Meredith, L.H. (1958) Nightglow emission altitudes from rocket measurements, *Journal of Geophysical Research* **63**:51-65.

Herman, R.C. and Hornbeck, G.A. (1953) Vibration-Rotation Bands of OH*, *The Astrophysical Journal* **118:**214-227.

Hernandez, G. and Killeen, T.L. (1988) Optical measurements of wind and kinetic temperatures in the upper atmosphere. *Advances in Space Research* **8**:149-213.

Herse, M., Moreels, G. and Clairemidi, J. (1980) Waves in the OH emissive layer: photogrammetry and topography. *Applied Optics* **19**,355.

Herzberg, G. (1939) Spectra of Diatomic Molecules, *Van Nostrand Reinhold Company, Canada.*

Herzberg, G. (1951) The atmospheres of the planets. *Journal of the Royal Astronomy Society of Canada* **45**:100-123.

Hickey, M.P. (1988a) Effects of Eddy Viscosity and Thermal Conduction and Coriolis Force in the Dynamics of Gravity Wave Driven Fluctuations in the OH Nightglow, *Journal of Geophysical Research* **93:**4077-4088.

Hickey, M.P. (1988b) Wavelength Dependence of Eddy Dissipation and Coriolis Force in the Dynamics of Gravity Wave Driven Fluctuations in the OH Nightglow, *Journal of Geophysical Research* **93**:4089-4101.

Hobbs, B.G.,Reid, I.M. and Greet, P.A. (1996) Mesospheric Rotational Temperatures determined from the OH(6-2) emission above Adelaide, Australia., *Journal of Atmospheric and Terrestrial Physics* **58:**1337-1344.

Holton, J.R. (1983) The role of gravity wave induced drag and diffusion in the momentum budget of the mesosphere. *Journal of Atmospheric Science* **40:**2497-2507.

Huang, T.Y.W. and Brasseur, G.P. (1993) Effect of long-term variability in a two dimensional interactive model of the middle atmosphere. *Journal of Geophysical Research* **98**:20413-20427.

Huber, K.P. and Herzberg, G. (1979) Molecular spectra and molecular structure IV. Constants of diatomic molecules, *Van Nostrand Reinhold Company* New York.

Innis, J.L., Phillips, F.A., Burns, G.B., Greet, P.A., French, W.J.R. and Dyson, P.L. (2000) Mesospheric temperatures from observations of the hydroxyl (6-2) emission above Davis, Antarctica: A comparison of rotational and Doppler measurements, Annales Geophysicae **19**:359-365.

IPCC (1994). Climate Change 1994: Radiative Forcing of Climate Change and an Evaluation of the IPCC IS92 Emission Scenarios [Houghton, J.T., L.G. Meira Filho, J.P. Bruce, Hoesung Lee, B.T. Callander, E.F. Haites, N. Harris, and K. Maskell (eds.)]. *Cambridge University Press*, Cambridge and New York, 339 pp.

IPCC (1996a). Climate Change 1995. The science of climate change. Technical summary, (eds) J.T. Houghton, L.G. Meira Filho, B.A. Callander, N. Harris, A. Kattenberg & K. Maskell, Intergovernmental Panel on Climate Change, *Cambridge University Press*, Cambridge.

IPCC (1996b). Climate Change 1995: The science of climate change. Contribution of Working Group I to the Second Assessment Report of the Intergovernmental Panel on Climate Change [Houghton, J.J., L.G. Meiro Filho, B.A. Callander, N. Harris, A. Kattenberg and K.Maskell (eds.)]. *Cambridge University Press*, Cambridge and New York, 584 pp.

Jacka, F. (1984) Application of Fabry-Perot spectrometers for measurement of upper atmosphere temperature and winds, *Ch2 in Middle Atmosphere Handbook for MAP* **13.**

Jenkins, F.A. and White, H.E. (1976) *Fundamentals of Optics*, McGraw-Hill, Kogakusha, Tokyo.

Johns, T.C., Carnell, R.E., Crossley, J.F., Gregory, J.M., Mitchell, J.F.B., Senior, C.A., Tett, S.F.B. and Wood, R.A. (1997) The second Hadley Centre coupled ocean-atmosphere GCM: Model description, spinup and validation, *Climate Dynamics* **13**:103-134.

Jones, P.D., New, M., Parker, D.E., Martin, S. and Rigor, I.G. (1999) Surface air temperature and its changes over the past 150 years. *Reviews of Geophysics* **37:**173-199.

Kaye, J.A. (1988) On the Possible Role of the Reaction $O + HO_2 \rightarrow OH + O_2$ in OH Airglow, *Journal of Geophysical Research* **93:**285-288.

Keckhut, P., Hauchecorne, A. and Chanin, M.L. (1995) Midlatitude long-term variability of the middle atmosphere: Trends and cycles and episodic changes, *Journal of Geophysical Research*, **100**:18887-18897.

Keckhut, P., Schmidlin, F.J., Hauchecorne, A. and Chanin, M.L. (1999) Stratospheric and Mesospheric cooling trend estimates from U.S. rocketsondes at low latitude stations (8°S-34°N), taking into account instrumental changes and natural variability, *Journal of Atmospheric and Solar-Terrestrial Physics* **61**:447-459.

Keeling, C.D. and Whorf, T.P. (2000) Atmospheric CO_2 Concentrations--Mauna Loa Observatory, Hawaii, 1958-1999 at http://cdiac.esd.ornl.gov/ndps/ndp001.html

Keyser, L.F. (1979) Absolute rate and temperature dependence of the reaction between hydrogen (^2S) atoms and ozone. *J. phys.Chem.* **83**:645.

Kitoh, A., Noda, A., Nikaidou, Y., Ose, T. and Tokioka, T. (1995) AMIP simulations of the MRI GCM. *Pap. Meteor. Geophys.*, **45.**

Knutsen,K., Dyer, M.J. and Copeland, R.A. (1996) Collisional removal of OH ($X^2\Pi$,v=7) by O_2,N_2, CO_2 and N_2, *Journal of Chemical Physics*, **104**:15 5598-5802

Kokin, G.A. and Lysenko, E.V. (1994) On temperature trends of the atmosphere from rocket and radiosonde data, *Journal of Atmospheric and Terrestrial Physics* **56**:1035-1040.

Krassovsky, V.I. (1956) The Aurora and the Airglow, Eds. Armstrong, E.B. and Dalgarno, A., *Pergamon Press*, London.

Krassovsky, V.I., Shefov, N.N. and Yarin, V.I. (1962) Atlas of the Airglow Spectrum 3000-12400 Å, *Planetary and Space Science* **9:**883-915.

Krueger, D.A. and She C.Y. (1999) Observer "long-term" temperature change in a midlatitude mesopause region in response to external perturbations. *Earth Plantes Space* **51**:809-814.

Kubota, M., Ishii, M., Shiokawa, K., Ejiri, M.K. and Ogawa, T. (1999) Height measurements of nightglow structures observed by all-sky imagers. *Advances in space Research*, **24**:593-596.

Kvifte, G. (1967) Hydroxyl rotational temperatures and intensities in the nightglow, *Planetary and Space Science* **15**:1515-1523.

Labitzke, K. and Chanin, M.-L. (1988) Changes in the middle atmosphere in winter related to the 11-year sunspot cycle, *Annales Geophysicae* **6**:643-644.

Langhoff, S.R., Bauschlicher Jr, C.W. and Taylor, P.R. (1989) *Journal of Chemical Physics*, **91**:5953

Langhoff, S.R., Werner, H.-J., Rosmus,R. (1986) Theoretical transition probabilities for the OH Meinel system. *Journal of Molecular Spectroscopy* **118**:507-529.

Le Texier, H.,Solomon, S. and Garcia, R.R. (1987) Seasonal Variability of the OH Meinel Bands, *Planetary and Space Science* **35**:977-989.

Lee, J.H., Michael, J.V., Payne, W.A. and Stief, L.J. (1978) Absolute rate of the reaction of hydrogen atoms with ozone from 219 to 360 K. *Journal of Chemical Physics* **69**:350.

Llewellyn, E.J.,Long, B.H. and Solheim, B.H. (1978) The Quenching of OH^* in the Atmosphere, *Planetary and Space Science* **26**:525-531.

Lopez-Moreno, J.J.,Rodrigo, R.,Moreno, F.,Lopez-Puertas, M. and Molina, A. (1987) Altitude Distribution of Vibrationally Excited States of Atmospheric Hydroxyl at levels v=2 to v=7, *Planetary and Space Science* **35**:1029-1038.

Lopez-Moreno, J.J.,Vidal, S.,Rodrigo, R.,Llewellyn, E.J. (1984) Rocket-Borne Photometric Measurements of $O_2(^1\Delta_g)$, Green Line and OH Meinel Bands in the Nightglow, *Annales Geophysicae* **2**:61-66.

Lowe, R.P. (1966) Interferometric spectra of the Earth's airglow. *Phil Trans Roy Soc London A*, **264**:163-170.

Lowe, R.P., Gilbert, K.L. and Turnbull, D.N. (1991) High Latitude Summer Observations of the Hydroxyl Airglow, *Planetary and Space Science* **39**:1263-1270.

Lowe, R.P., Le Blanc, L.M. and Gilbert, K.L. (1996) WINDII/UARS Observations of Twilight Behavior of the Hydroxyl Airglow, at Mid Latitudes, *Journal of Atmospheric and Terrestrial Physics* **58**:1863-1869.

Lübken, F.-J. (2000) Nearly zero temperature trend in the polar summer mesosphere. *Geophysical Research Letters* **27 (21)**:3603-3606.

Lübken, F.-J., Jarvis, M.J. and Jones, G.O.L. (1999) First in-situ temperature measurements at the Antarctic summer mesopause. *Geophysical Research Letters* **26 (24)**:3581-3584.

Lübken, F-J. and von Zahn, U. (1991) Thermal structure of the mesopause region at polar latitudes. *Journal of Geophysical Research* **96 (D11)**: 20841-20857.

Lysenko, E.V., Perov, S.P., Semenov, A.I., Shefov, N.N., Sukhodoev, V.A., Givishvili, G.V. and Leshchenko, L.N. (1999) Long-term trends of the yearly mean temperature at heights from 25 to 100 km, *Atmos. Oceanic Physics,* **35**:435-443.

Manabe, S., Stouffer, R.J., Spelman, M.J. and Bryan, K. (1991) Transient response of a coupled ocean-atmosphere model to gradual changes of atmospheric CO_2. Part I: Annual mean response. *Journal of Climate*, **4**:785-818.

McDade, I.C. and Llewellyn, E.J. (1987) Kinetic Parameters Related to Sources and Sinks of Vibrationally Excited OH in the Nightglow, *Journal of Geophysical Research* **92**:7643-7650.

McPherson, D.H. and Vallance Jones, A. (1960) A Study of the Latitude Dependence of OH Rotational Temperatures for Canadian Stations, *Journal of Atmospheric and Terrestrial Physics* **17:** 302-308.

Meinel, A.B. (1950) OH Emission Bands in the Spectrum of the Night Sky. *Astrophysics Journal* **3:**555-564.

Melo, S.M.L., Lowe, R.P. and Russell, J.P. (2000) Double peaked hydroxyl airglow profiles observed from WINDII/UARS. *Journal of Geophysical Research* **105**:12397-12403.

Meriwether Jr., J.W. (1975) High Latitude Airglow Observations of Correlated Short-Term Fluctuations in the Hydroxyl Meinel 8-3 Band Intensity and Rotational Temperature, *Planetary and Space Science* **23:**1211-1221.

Meriwether Jr., J.W. (1985) Ground Based Measurements of Mesosphere Temperatures by Optical Means, *MAP* **13:**1-18.

Meriwether Jr., J.W. (1989) A Review of the Photochemistry of Selected Nightglow Emissions from the Mesopause, *Journal of Geophysical Research* **94:**14629-14646.

Mies, F.H. (1974) Calculated Vibrational Transition Probabilities of OH(X2 Pi), *Journal of Molecular Spectroscopy* **53:**150-188.

Mohan, H and Shardanand (1975) Free Radical OH: A molecule of Astrophysical and Aeronomic Interest, *Scientific and Technical Information Office*, NASA, Washington DC.

Moreels, G. and Herse, M. (1977) Photographic evidence of waves around the 85 km level. *Planetary and Space Science* **25** 265-274.

Moreels, G., Megie, G., Vallance Jones, A. and Gattinger, R.L. (1977) An Oxygen-Hydrogen Atmospheric Model and its Application to the OH Emission Problem, *Journal of Atmospheric and Terrestrial Physics* **39:**551-570.

Moreels, G., Vallance-Jones, A. and Blamont, J.E. (1973) Balloon Observations of the 8-6 OH Band in the Day and Night Airglow, *Planetary and Space Science* **21:**1945-1955.

Mulligan, F.J., Horgan, D.F., Galligan, J.G. and Griffin, E.M. (1995) Mesopause temperatures and integrated brightness calculated from airglow OH emissions recorded at Maynooth (53.2°N, 6.4°W) during 1993. *Journal of Atmospheric and Terrestrial Physics* **57 (13):**1623-1637.

Murphy, J.M., (1992) A prediction of the transient response of climate. *Climate Research Technical Note*, No.32, Hadley Centre.

Murphy, R.E. (1971) Infrared emissions of OH in the fundamental and first overtone bands. *Journal of Chemical Physics* **54**:4852.

Myrabo, H.K. (1986) Winter-season mesopause and lower thermosphere temperatures in the northern polar region. *Planetary and Space Science* **34 (11):**1023-1029.

Myrabø, H.K., Deehr, C.S., Vierecck, R. and Henriksen, K. (1987) Polar Mesopause Gravity Wave Activity in the Sodium and Hydroxyl Night Airglow, *Journal of Geophysical Research* **92:**2527-2534.

Nagy, A.F., Liu, S.C. and Baker, D.J. (1976) Vibrationally-excited hydroxyl molecules in the lower atmosphere Geophysical Research Letters 3:731-734.

Nakamura, M. (1962) Diurnal Variation of OH Emission of the Nightglow, *Reports of Ionospheric and Space Physics in Japan* **15:**346-363.

Nelson Jr, D.D., Schiffman, A., Nesbitt, D.J., Orlando, J.J., Burkholder, J.B. (1990) $H+O_3$ Fourier-Transform Infrared mission and Laser Absorption Studies of $OH(X^2\Pi)$ Radical: An Experimental Dipole Moment Function and State-to-State Einstein A Coefficients, *Journal of Chemical Physics* **93:**7003-7019.

Nestorov, G., Pancheva, D. and Danilov, A.D. (1991) Climatic changes of the ionospheric radio wave absorption in the SW range, *Geomagnetism and Aeronomy* **31**:1070.

Niciejewski, R.J. and Killeen, T.L. (1995) Annual and semi-annual temperature oscillations in the upper mesosphere. *Geophysical Research Letters* **22 (23):**3243-3246.

Nicolet, M. (1970) *Annales Geophysicae* **26**:531.

Nicolet, M. (1971) Aeronomic reactions of hydrogen and ozone, in *Mesospheric Models and Related Experiments* (Ed. Fiocco, G.) pp 1-51 D.Reidel, Dordrecht.

Offermann, D. and R. Gerndt (1990) Upper-mesosphere temperatures from OH^* emissions, *Advances in Space Research*, **10(12)**:217-221.

Ohoyama, H., Kasai, T., Yoshimura, Y., Kimura, H. and Kuwata, K. (1985) Initial distribution of vibration of the OH radicals produced in the $H+O_3 \rightarrow OH(X^2\Pi)+O_2$ reaction. *Chem.Phys.Lett* **118**:263.

Osterbrock, D.E. and Martel, A.R. (1992) Sky spectra at a light-polluted site and the use of atomic and OH sky emission lines for wavelength calibration, *Publications of the Astronomical Society of the Pacific*, **104:**76-82, 1992.

Osterbrock, D.E., Fulbright, J.P. and Bida, T.A. (1997) Night-sky high-resolution spectral atlas of OH emission lines for Echelle spectrograph wavelength calibration II, *Publications of the Astronomical Society of the Pacific*, **109**:614-627.

Osterbrock, D.E., Fulbright, J.P., Martel, A.R., Keane, M.J., Trager, S.C. and Basri, G. (1996) Night-Sky High-Resolution Spectral Atlas of OH and O_2 Emission Lines for Echelle Spectrograph Wavelength Calibration, *Publications of the Astronomical Society of the Pacific* **108:**277-308.

Parker, D.E., Folland, C.K. and Jackson, M. (1995) Marine surface temperature observed variations and data requirements, *Climatic Change*, **31**:559-600.

Parker, D.E., Jones, P.D., Bevan, A. and Folland, C.K. (1994) Interdecadal changes of surface temperature since the 19th century, *Journal of Geophysical Research,* **99:**14373-14399.

Pendleton Jr., W.R., Espy, P.J., Hammond, M.R. (1993) Evidence for non-local-thermodynamic-equilibrium rotation in the OH Nightglow. *Journal of Geophysical Research* **98:**11567-11579.

Peterson, A.W.,Keiffaber, L.M., (1973) Photographic Parallax Heights of Infrared Airglow Structures, *Nature* **244:** 92-93.

Petit, J.R., Jouzel, J., Raynaud, D., Barkov, N. I., Barnola, J.-M. Basile, I., Bender, M., Chappellaz, J., Davis, M., Delaygue, G., Delmotte, M., Kotlyakov, V.M.,Legrande, M.,Lipenkov, V.Y., Lorius, C., Pepin, L., Ritz, C., Saltzman, E. and Stievenard, M. (1999) Climate and atmospheric history of the past 420,000 years from the Vostok ice core, Antarctica , *Nature*, **399:**429-436.

Phillips, L.F. and Schiff, H.I. (1962) Mass spectrometric studies of atom reactions III Reactions of hydrogen atoms with nitrogen dioxide and ozone. *Journal of Chemical Physics* **37**:1233.

Polanyi, J.C. and Woodall, K.B. (1972) Energy distribution among reaction products. VI. $F+H_2,D_2$, *The Journal of Chemical Physics*, **57**:4, 1574-1586

Portmann, R.W., Thomas, G.E., Solomon, S. and Garcia, R. R. (1995) The importance of dynamical feedbacks on doubled CO_2-induced changes in the thermal structure of the mesosphere *Geophysical Research Letters*, **22**:1733-1736.

Potter, A.E.Jr., Coltharp, R.N. and Worley, S.D. (1971) Mean Radiative Lifetime of Vibrationally Excited (v = 9) Hydroxyl. Rate of the Reaction of Vibrationally Excited Hydroxyl (v = 9) with Ozone., *The Journal of Chemical Physics*, **54:**992-997.

Rind, D., Suozzo, R. and Balachandran, N.K.(1998b) The GISS global climate/middle atmosphere model Part II: Model variability due to interactions between planetary waves, the mean circulation and gravity wave drag, *Journal of Atmospheric Science*, **45**:371-386.

Rind, D., Suozzo, R., Balachandran, N.K. and Prather, M.J. (1990) Climate change and the middle atmosphere. Part I: The doubled CO_2 climate. *Journal of Atmospheric Sciences*, **47**:475-494.

Rind, D., Suozzo, R., Balachandran, N.K., Lacis, A. and Russell, G. (1998a) The GISS global climate/middle atmosphere model Part 1:model structure and climatology. *Journal of Atmospheric Science,* **45**:329-370.

Roble, R.G. and Dickinson, R.E. (1989) How will the changes in carbon dioxide and methane modify the mean structure of the mesosphere and thermosphere ?. *Geophysical Research Letters* **16**:1441-1444.

Rogers, J.W.,Murphy, R.E.,Stair, A.T.Jr.,Ulwick, J.C.,Baker, K.D.,Jensen, L.L. (1973) Rocket-Borne Radiometric Measurements of OH in the Auroral Zone, *Journal of Geophysical Research* **78:**7023-7031.

Rothman, L., Gamache, R., Tipping, R., Rinsland, C., Smith, M., Benne,D., Malathy Devi,V., Flaud, J.M., Camy-Peyret, C., Perrin, A., Glodman, A., Massie, S., Brown, L.

and Toth, R. (1992) The HITRAN molecular data base: Editions of 1991 and 1992, *J. Quant. Spectrosc. Radiat. Transfer*, **48:**469-507.

Rowland, H.A. (1882) Preliminary notice of the results accomplished in the manufacture and theory of gratings for Optical purposes. *London, Edinburgh and Dublin Philosophical Magazine* **13**:469.

Russell, G.L., Miller, J.R. and Rind, D. (1995) A Coupled Atmosphere-Ocean Model for Transient Climate Change Studies, *Atmosphere-Ocean*, **33(4)**:683-730.

Sahai, Y., Giers, D.H., Cogger, L.L., Fagundes, P.R. and Garbe, G.P. (1996) Solar Flux and Seasonal Variations of the Mesopause Temperatures at 51°N, *Journal of Atmospheric and Terrestrial Physics* **58:**1927-1934.

Salby, M.L. (1996) Water Vapour, in *Fundamentals of Atmospheric Physics*, Academic Press, New York.

Sandor, B.J. and Clancy, R.T (1998) Mesospheric OH_x chemistry from diurnal microwave observations of HO_2, O_3 and H_2O, *Journal of Geophysical Research*, **103**:D11, 13337-13351.

Sappey, A.D. and Copeland, R.A. (1990) Collision dynamics of $OH(X^2\Pi,v=12)$, *Journal of Chemical Physics*, **93**:8 5741-5746.

Scheer, J. (1995) What can be learned from rotational temperatures derived from ground-based airglow observations about the aeronomy of the southern hemisphere, *Advances in Space Research.*, **16(5):**61-69.

Scheer, J., Reisin, E.R., Espy, J.P., Bittner, M., Graef, H.H., Offermann, D., Ammosov, P.P., and Ignatyev, V.M. (1994) Large Scale Structures in Hydroxyl Rotational Temperatures during DYNA, *Journal of Atmospheric and Terrestrial Physics* **56:**1701-1715.

Scheer, J., Reisin, E.R., Greet, P.A., Dyson, P.L., Smith, R.W. and Hernandez, G. (1998) Comments on paper: 'Trends of airglow imager observations near Adelaide, Australia' by J.H. Hecht, R.E. Walterscheid, J. Woithe, L. Campbell, R.A. Vincent and I.M. Reid, *Geophysical Research Letters* **25:**21-22.

Sharpe, M.R. and Irish, D. (1978) Stray light in diffraction grating monochromators, *Optica Acta* **25**:861-893.

She, C.Y. and Lowe, R.P. (1998) Seasonal temperature variations in the mesopause region at mid-latitude: comparison of lidar and hydroxyl rotational temperatures using WINDII/UARS OH height profiles. *Journal of Atmospheric and Solar-Terrestrial Physics* **60**:1573-1583.

She, C.Y., Thiel, S.W. and Krueger, D.A. (1998) Observed episodic warming at 86 and 100 km between 1990 and 1997: Effects of Mt Pinatubo eruption. *Geophysical Research Letters* **25**:497-500.

She, C.Y., Yu, J.R. and Chen, H. (1993) Observed thermal structure at a midlatitude mesopause. *Geophysical Research Letters* **20**:567-570.

Shefov, N.N. (1969a) Hydroxyl Emission of the Upper Atmosphere - I. The Behaviour During a Solar Cycle, Seasons and Geomagnetic Disturbances, *Planetary and Space Science* **17:**797-813.

Shefov, N.N. (1969b) Hydroxyl Emission of the Upper Atmosphere - II. Effects of a Sunlit Atmosphere, *Planetary and Space Science* **17:**1629-1639.

Shefov, N.N. (1971) Hydroxyl Emission of the Upper Atmosphere - III. Diurnal Variations, *Planetary and Space Science* **19**:129-136.

Shepherd, G.G., Anger, C.D., Brace, L.H., Burrows, J.R., Heikkila, W.J., Hoffmann, J., Maier, E.J. and Whitteker, T.H. (1973) An observation of polar aurora and airglow from the ISIS-II spacecraft, *Planetary and Space Science* **21**:819.

Sivjee, G.G. and Hamwey, R.M. (1987) Temperature and Chemistry of the Polar Mesopause OH, *Journal of Geophysical Research* **92:**4663-4672.

Sivjee, G.G. and Walterscheid, R.L. (1994) Six-Hour Zonally Symmetric Tidal Oscillations of the Winter Mesopause Over the South Pole Station., *Planetary and Space Science* **42:**447-453.

Sivjee, G.G., Dick, K.A.and Feldman, P.D. (1972) Temporal Variations in Night-time Hydroxyl Rotational Temperature, *Planetary and Space Science* **20:**261-269.

Spencer, J.E. and Glass, G.P. (1977) Some reactions of OH v=1, *Int J. Chem. Kinetics*, **9**:111.

Sridharan, U.C., Klein, F.S. and Kaufman, F. (1985) Detailed course of the O + HO_2 reaction, *Journal of Chemical Physics* **82**:592-593.

Steed, A.J. and Baker, D.J. (1979) Night-sky spectral emission measurements (λ0.9-2.3μm) using a field widened interferometer-spectrometer, *Applied Optics*, **18**:3386-3389.

Stevens, W.J., Das, G., Wahl, A.C., Krauss, M. and Neumann, D. (1974) Study of the ground state potential curve and dipole moment of OH by the method of optimised valence configurations. *Journal of Chemical Physics* **61**:3686.

Streit, A.E. and Johnston, H.S. (1976) Reactions and quenching of vibrationally excited hydroxyl radicals, *Journal of Chemical Physics* **64**:95-103.

Stubbs, L.C.,Boyd, J.S. and Bond, F.R. (1983) Measurement of the OH Rotational Temperature at Mawson, East Antarctica, *Planetary and Space Science* **31:**923-932

Sturman, A. P. and N. J. Tapper (1996) The weather and climate of Australia and New Zealand, *Oxford University Press*, Melbourne.

Suzuki, K. and Tohmatsu, T. (1976) An Interpretation of the Rotational Temperature of the Airglow Hydroxyl Emissions, *Planetary and Space Science* **24:**665-671.

Takahashi, H. and Batista, P.P. (1981) Simultaneous Measurements of OH(9,4), (8,3), (7,2), (6,2) and (5,1) Bands in the Airglow, *Journal of Geophysical Research* **86:**5632-5642.

Takahashi, H., Clemesha, B.R., Sahai, Y. (1974) Nightlow OH (8-3) Band Intensities and Rotational temperatures at 23°S, *Planetary and Space Science* **22:**1323-1329.

Taubenheim, J., Entzian, G. and Berendorf, K. (1997) Long-term decrease of mesospheric temperature, 1963-1995, inferred from radiowave reflection heights. *Advances in Space Research* **20 (11)**:2059-2063.

Taubenheim, J., von Cossart, G and Entzian, G.(1990) Evidence of CO_2-induced progressive cooling of the middle atmosphere derived from radio observations. *Advances in Space Research* **10**:171-174.

Taylor, M.J., Turnbull, D.N. and Lowe, R.P. (1991) Coincident Imaging and Spectrometric Observations of Zenith OH Nightglow Structure, *Geophysical Research Letters* **18:**1349-1352.

Thomas, G.E. (1996a) Global Change in the Mesosphere-Lower Thermosphere Region: Has it Already Arrived?, *Journal of Atmospheric and Terrestrial Physics* **58:**1629-1656.

Thomas, G.E. (1996b) Is the Polar Mesosphere the Miners Canary of Global Change ?, *Advances in Space Research* **18:**149-158.

Thomas, G.E., Olivero, J.J., Jensen, E.J., Schroeder, W. and Toon, O.B. (1989) Relation between increasing methane and the presence of ice clouds at the mesopause. *Nature* **338:**490-492.

Torr, D.G. (1985) The photochemistry of the upper atmosphere, chapter 5 in *The photochemistry of atmospheres, Earth, the other planets, and comets*, Academic Press, Inc Ed. Levine, J.S.

Turnbull, D.N. and Lowe, R.P. (1983) Vibrational population distribution in the hydroxyl night airglow, *Canadian Journal of Physics*, **61**:244-250.

Turnbull, D.N. and Lowe, R.P. (1988) An empirical determination of the dipole moment function of $OH(X^2\Pi)$. *Journal of Chemical Physics,* **89**:2763.

Turnbull, D.N. and Lowe, R.P. (1989) New Hydroxyl Transition Probabilities and their Importance in Airglow Studies, *Planetary and Space Science* **37:**723-738.

Vallance Jones, A. (1973) The Infrared Spectrum of the Airglow, *Space Science Reviews* **15**:355-400.

Vallance Jones, A. (1974) Aurora *Geophysical and Astrophysics Monographs*, D.Reidel Publishing Company, Dordrecht, Holland.

Viereck, R.A. and Deehr, C.S. (1989) On the Interaction Between Gravity Waves and the OH Meinel (6-2) and the O_2 Atmospheric (0-1) Bands in the Polar Night Airglow, *Journal of Geophysical Research* **94:**5397-5404.

von Zahn, U. (1990) Temperature and altitude of the polar mesopause in summer. *Advances in Space Research* **10**:(12)223:(12)231

von Zahn, U., Fricke, K.H., Gerndt, R., Blix, T. (1987) Mesospheric Temperatures and the OH Layer Height as Derived from Ground-Based Lidar and OH^* Spectrometry, *Journal of Atmospheric and Terrestrial Physics* **49:**863-869.

von Zahn, U., Hoffner, J., Eska, V. and Alpers, M. (1996) The mesopause altitude: Only two distinctive levels worldwide ?. *Geophysical Research Letters* **23**:3231-3234

Wallace, L. (1962) The OH Nightglow Emission, *Journal of Atmospheric Sciences* **19**:1-16.

Walterscheid, R.L., Schubert, G. and Straus, J.M. (1987) A Dynamical Chemical Model of Wave-Driven Fluctuations in the OH Nightglow, *Journal of Geophysical Research* **92:**1241-1254.

Walterscheid, R.L.,Sivjee, G.G.,Schubert, G.,Hamwey, R.M. (1986) Large-Amplitude Semidiurnal Temperature Variations in the Polar Mesopause: Evidence of a Pseudotide, *Nature* **324:**347-349.

Watanabe, T.,Nakamura, M.,Ogawa, T. (1981) Rocket Measurements of O_2 Atmospheric and OH Meinel Bands in the Airglow, *Journal of Geophysical Research* **86:**5768-5774.

Weast, R.C., Astle, M.J. and Beyer, W.H (Eds) (1987) CRC Handbook of Chemistry and Physics, *CRC Press*, Boca Raton, Florida.

Werner, H-J, Rosmus, P. and Reinsch, E-A. (1983) *Journal of Chemical Physics* **79**:905-916.

Wiens, R.H. and Weill, G. (1973) Diurnal, Annual and Solar Cycle Variations of Hydroxyl and Sodium Nightglow Intensities in the Europe-Africa Sector, *Planetary and Space Science* **21:**1011-1027.

Williams, P.F.B. (1987) OH Nightglow Observations and Temperature Determinations at Davis, Antarctica, *A.N.A.R.E. Research Notes* **48:**176-186.

Williams, P.F.B. (1996) OH Rotational Temperatures at Davis, Antarctica, via Scanning Spectrometer. *Planetary and Space Science* **44:**163-170.

Winick, J.R. (1983) Photochemical processes in the mesosphere and lower thermosphere, in *Solar-Terrestrial Physics*, Ed. Carovillano, r.l. and Forbes, J.M. pg 677-732 D. Reidel, Hingham, Mass.

Wolfe, W.L. (1997) *Introduction to Imaging Spectrometers*, SPIE - International Society for Optical Engineering, Bellingham, Washington.

Wood, R.W. (1937) *Nature* **140**:723.

Worden, E.F. (1995) Argon, in *Line spectra of the elements*, Reader, J. and Corlis, C.H. (Eds.). In *Handbook of Chemistry and Physics*, 76th Edition, Lide, D.R. (Ed.). CRC Press.

Appendix A – Copies of published papers

The following refereed papers have been published in association with this work.

OH(6-2) spectra and rotational temperature measurements at Davis, Antarctica,
Greet, P. A., French, W.J.R., Burns, G.B., Williams, P.F.B., Lowe, R.P. and Finlayson, K.
Annales Geophysicae **16**:77-89 (1998).

Argon Auroral emissions.
Burns, G.B., Williams, P.F.B., Lowe, R.P., French, W.J.R., Greet, P.A. and Monselesan, D.P.
Journal of Atmospheric and Solar-Terrestrial Physics (2001 in press)

Hydroxyl (6-2) airglow emission intensity ratios for rotational temperature determination.
French, W.J.R., Burns, G.B., Finlayson, K., Greet, P. A., Lowe, R.P. and Williams, P.F.B.
Annales Geophysicae, **18:**1293-1303 (2000).

Seasonal Variations and inter-year trends in seven years of hydroxyl airglow rotational temperatures at Davis station (69°S, 78°E), Antarctica.
Burns, G.B., French, W.J.R., Greet, P. A., Phillips, F.A., Williams, P.F.B., Finlayson, K. and Klich, G. *Journal of Atmospheric and Solar-Terrestrial Physics* (2001 in press).

Monitoring the Antarctic mesopause region for signatures of climate change
Burns, G.B., French, W.J.R., Greet, P. A., Williams, P.F.B., Finlayson, K., Lowe, R.P.
Annals of Glaciology **27:**669-673 (1998)

The Mesopause region above Davis, Antarctica (68.6°S, 78.0°E)
Burns, G.B., French, W.J.R., Greet, P.A., Williams, P., Finlayson, K. and Lowe, R.P. in *Long Term Changes and Trends in the Atmosphere* Ed. Beig, G. *proceedings of the First International Workshop on Long Term Changes and Trends in the Atmosphere.* (2001)

Antarctic Noctilucent Clouds: The upper atmosphere exposed to View
French, W.J.R., Burns, G.B., Greet, P. A. and French, K.
The Physicist **37**:85-90. (2000).

Appendix B – Tungsten Lamps

Halogen Cycle, Aging and Failure modes of Tungsten lamps

Factors affecting the longevity and stability of tungsten halide, or quartz halogen lamps used in our low brightness source calibration lamps are considered in this Appendix (see section 3.5.4.1). References for this section are from http://www.misty.com/people/don/bulb1.html and http://modarch.gsfc.nasa.gov:80/EOS/TEXT/40/1538_SRCA_In1_0.txt unless otherwise cited.

Figure B-1 shows pictures of the tungsten halide bulb used in the Eather LBS in comparison with a new bulb.

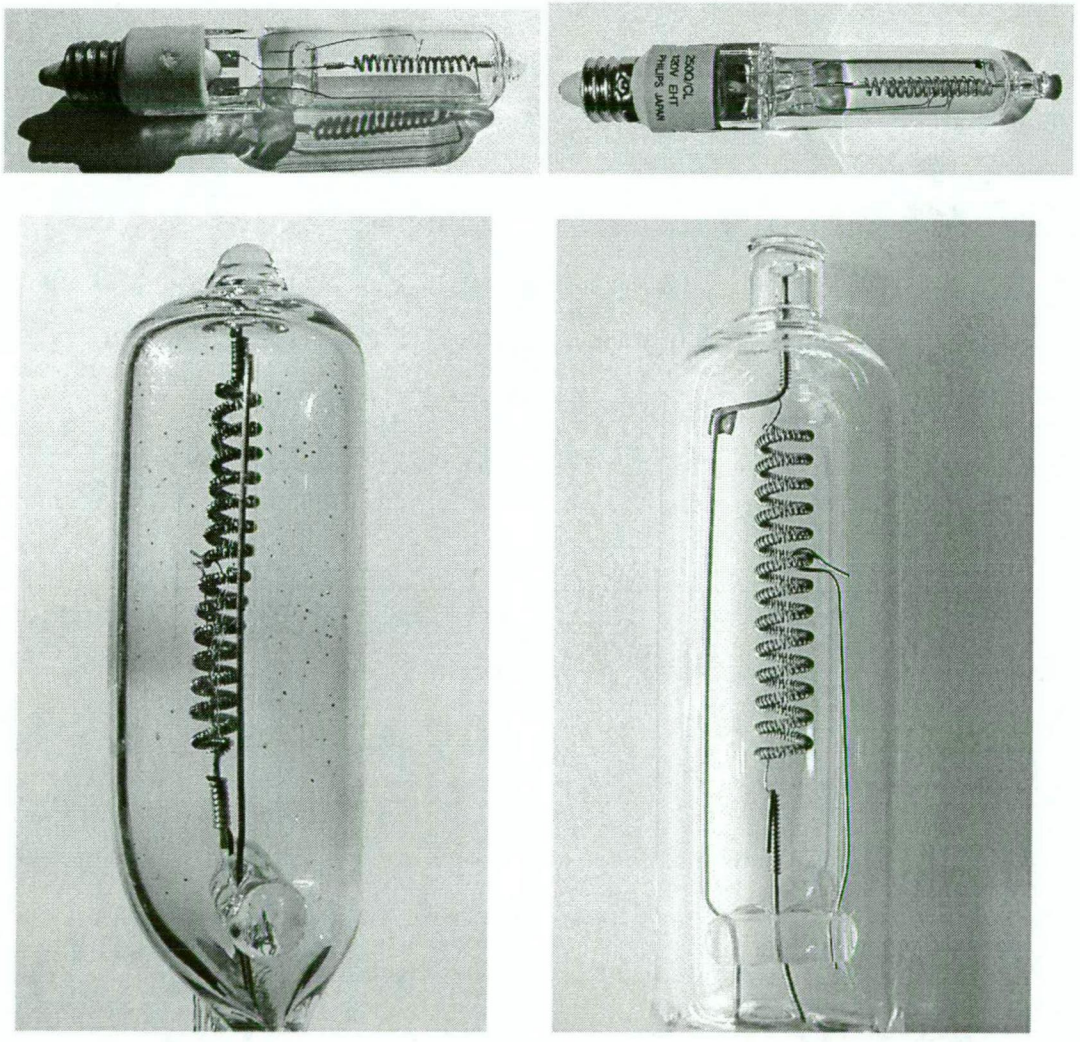

Figure B-1-1. The old and the new. The actual quartz halogen bulb used from 1995 in the Eather LBS (on the left) is compared with a new bulb on the right. Pictures were taken in Feb-2000. The old coiled-coil tungsten filament is dark and crystalline. Tungsten is deposited on the quartz envelope near the centre hanger. Loose flecks of the metal are also distributed around the envelope walls.

The Halogen Cycle

Common construction of quartz halogen lamps comprises a tungsten filament, an inert fill gas such as krypton, xenon or argon but with a trace of halogen gas, usually bromine or iodine, housed in a small quartz glass envelope. A tungsten filament operates at extreme temperatures (around 3000°C) and the metal constantly evaporates. In the vicinity of the glass wall of the bulb tungsten vapour cools below 800°C, and can combine with the reactive halogen gas forming gaseous tungsten-halide. This molecule can freely migrate back to the hot filament where it decomposes. Tungsten metal is deposited back on the filament and the halogen is released to the gas. This ongoing process is known as the *halogen cycle*, which extends the life of the filament and provides greater efficiency. Conventional incandescent bulbs contain only the inert gas. There is no mechanism for the tungsten to be transported back to the filament so it is simply deposited on the glass bulb, eventually darkening it.

Failure modes

Failure modes of both types are the same, usually from melting or vibration breakage of a thin spot in an aging filament. Thin spots develop as evaporation and deposition of tungsten occurs in an uneven manner. With less mass and decreased cross-sectional area, these thinned sections heat up faster, run hotter and evaporate at a greater rate than the rest of the filament. In addition, the temperature gradients give rise to Soret diffusion; thermally induced mass transport from areas of high temperature to low temperature. Thinning and temperature overshoot are amplified in this cycle until the filament fails when the melting point is attained at 3410°C.

Another mode called *necking* occurs where the filament endpoints are attached to the lead wires (and also at the hanger attachment points where long filaments are used). Due to heat being dissipated though the lead wires the filament is much cooler at these points, to the point where it can react with the halogen gas as occurs on the cooler glass surface in the halogen cycle. This erodes the filament at the endpoints and it can eventually break under its own weight.

Soft starting and De-rating

A large current is drawn when the lamp is first switched on as the resistance of a cold filament is less than at operating temperature. The current surge can be more than ten times the normal operating level and thus most bulbs fail as they are switched on, and most often at the necked endpoints. Slowly ramping up the current or *soft starting* reduces the superheating in thin sections and the likelihood of failure on start-up.

Operating the lamp lower than the rated power will also extend the life of the filament by reducing the evaporation rate, but in order for the halogen cycle to work, the bulb surface must be very hot, generally over 250°C. If the bulb is dimmed excessively both the removal of tungsten from the inner surface of the bulb by the halide gas, and the decomposition of tungsten halide at the filament will be severely diminished. Generally, halogen lamps cannot be significantly de-rated. (Johnson, 1993). Klipstein (1996) reports that halogen bulbs should work normally at voltages as low as 90% of what they were designed for, and possibly lower if the bulb is in an enclosure that conserves heat.

AC versus DC

It is observed that operating a lamp with DC current can substantially *reduce* filament life, by factors of 3 or more (Johnson 1993), but the effects are dependent on the lamp operating temperature, filament diameter and the gas fill and pressure. A small percentage of tungsten atoms are ionised by UV radiating from the filament, the electric field around the filament or by free electrons. In the polarised field these ions migrate toward the negative terminal, either within the vapour or more readily along the filament surfaces by electro-migration. Surface migration rates are anisotropic, being dependent on the orientation of the crystallographic plane at the surface. As a result *notching* occurs, manifested at a sawtooth structure along the filament. The valleys or constrictions of each notch give rise to localised overheating, increased evaporation and Soret effect transport from the valleys to the peaks, and the process rapidly accelerates until the filament is weakened and breaks.

Electro-migration notching is eliminated if AC current is used at any frequency greater than about 1 cycle/min. However, reversing the polarity of a DC current with

a time scale much greater than this is observed to *increase* the development of notches in the direction of the original current polarity. It appears that the lamp filament, after a few minutes of DC operation develops enough structure to establish notch formation regardless of subsequent current flow. (Johnson 1993).

Notching effects on lamp life are also greatly reduced in larger diameter (high current) filaments where surface features are small compared to filament diameter and high temperature filaments where the rate of evaporation far exceeds the surface migration of material. The transitions occur at greater than about 1 mil (.0254 mm) diameter and at about 2700K for gas filled lamps (higher if the gas is pressurised)

Failure of the quartz bulb

As the bulb must be able to withstand extreme temperatures it is usually made of quartz. Any organic material or salts, say from a fingerprint, are extremely detrimental to hot quartz. Organic material will carbonise, leaving a dark spot that will absorb radiation and become excessively hot. Salts can leach into hot quartz and weaken it and other contaminants may crystallise it. Any of these mechanisms may cause the bulb to crack or shatter (these bulbs should therefore be suitably enclosed).

Recommendations

A tungsten-halide lamp is still the most suitable option currently available for a low brightness source given the constraints of instrument design and view angle. Their use may be optimised if the following conditions are met:

- A high current, low voltage filament is selected. This implies a short, thick filament less prone to shock or vibration damage and obviates the need for hangers, which may cause necking in the middle of the filament.
- AC voltage is used so as to eliminate electro-migration notching and surface diffusion. Any frequency greater than 1 cycle/min is suitable. This is not implemented for our current LBS units as precision DC systems are in place).
- It is operated close to its design rating to ensure adequate tungsten halide cycling. Typically no less than 90% is suitable.
- Soft starting is employed to reduce excessive current flow on startup and improve the filaments ability to survive necking.
- Care is taken to ensure the quartz envelope remains clean.

Appendix C – Examiners Reports

This thesis was submitted to the University of Tasmania on 18-Sep-2001, Examiners reports were received on 14-May-2002. Comments from the two referees are included here in *italics*. I have addresses the revisions and corrections suggested in normal text.

Referee 1

I should first like to say that this work represents a careful assessment not only of the measurements made and their associated errors, but also a degree of scientific interpretation that sets it above many other similar works. I would therefore rank this as an excellent thesis, and congratulate the candidate. I find both his work and conclusions well justified and scientifically sound, and do not hesitate to recommend that the degree be awarded on those grounds. However, I have noted some textual errors and points that the candidate may wish to elaborate and clarify to the satisfaction of the Head of School.

On page 7, in paragraph 4, the author states that Rind et al. (1990) sees a warming in the lower winter mesosphere as well as in the upper summer mesosphere. This does not necessarily lead to the strong latitudinal gradient as mentioned on page 8 (top). The author might also mention the warming in the lower winter mesosphere is accompanied by a strong cooling in the upper winter mesosphere, and this, along with the warming in the upper summer mesosphere, does lead to the strong latitudinal temperature gradient mentioned on page 8.

Added "cooling of the winter upper mesosphere" as advised

On page 15, the Stegman measurements from 1991 through 1998 are said to span a declining solar cycle. However, the measurements span a declining solar cycle from 91 to 96 only. The 1997-98 measurements take place during the increasing phase of the next solar cycle. Similarly on page 16, rather than covering a single trend in solar activity as stated by the author, the Lowe measurements from 1990 through 2000 span the maximum of solar cycle 22, through its minimum, and onto the peak of cycle 23.

Changed sentences to read "Though their data span solar minimum (decreasing 1991-1996, increase 1996-1998) it was not yet possible to infer a rotational temperature – solar flux relationship." For the Stegman reference and " .. spans the maximum of solar cycle 22, through its minimum and onto the peak of cycle 23 .." for the Lowe measurements.

On page 17, the author has practiced the time-honoured tradition of "chi-by-eye" on the Bittner data. At the best of times this is a rather dangerous technique (see, for example, Weatherhead et al, 1998, JGR 103, pp 17149-17162 for a discussion of how correlation and unequally sampled time series can lead to false trends even with several seasons of data in the series). However, in this case Bittner himself is reluctant to assign a long-term temperature trend to his data in a paper that deals with long-term trends. I think that the author's speculation of the trend should be eliminated, or at least the reluctance of Bittner to assign a trend to this data should be acknowledged.

Removed speculation of the long term trend, and added a note on Bittner's observed correlation with the QBO.

On pages 18 and 19, the Danalov measurements are mentioned but summarized in neither the text nor the table. Also, the results of Clemesha 1992 have been superseded by Clemesha BR, Batista PP, Simonich DM, 1997, JASTP 59, pp. 1673-1678.

The Danilov paper is a review of trends in a range of atmospheric parameters (ionospheric reflection heights, critical frequencies, ionospheric storm occurrence frequencies, 558 and 630 nm intensity), only one temperature trend is reported, that of Kokin and Lysenko (1994). Danilov (1997) has been added to that observation in the table.

The Clemesha *et. al.* (1997) update has been included in the text and table, it confirms the trend in the previous (1992) work.

At the bottom of page 19, I believe the term "homosphere" is being misused in this case. The term refers to the region of the atmosphere that is well mixed. That is, the proportions of species do not change with altitude and the mean molecular weight remains nearly constant. The boundary for this, the turbopause, varies between 115 km (winter) and 106 km (summer), considerably above the mesopause (Hall CM, Manson AH, Meek CE, 1998, JGR 103, pp. 28769-28773).

It was appropriate to just replace the term with "atmosphere".

On page 23 in the discussion of the parameters critical for the performance of spectrometers, one should mention the focal length of the instrument.

Added focal length.

On Page 26 and 27, you list your energies in decreasing magnitude. However, being pedantic, the translational energy of a room temperature molecule is ~0.04 eV, whilst electronic transitions can be several eV and vibrational transitions several tenths of eV. Better to say that the internal energies are listed in decreasing order.

Changed paragraph to read "The first describes the bulk motion of the molecule as a whole, the next three terms (in order of decreasing magnitude) involve the internal motion of the

nuclear framework of the molecule ...". Also added magnitudes in the discussion of each component.

On page 30, near the end of the second paragraph on the page, So = 0 and not ½.
Corrected as advised.

On page 34, the second paragraph reads: "Transitions also occur between vibrational and rotational levels of molecules in any given electronic state". As you are speaking generally here, one should add: "... in any given electronic state that possesses a permanent dipole moment", or make the statement specific to OH molecules.
Added statement as advised.

On page 38, in the second paragraph, the author correctly states that the number of transitions that stochastically occur before thermalization constitutes unthermalized behaviour. However, there is an inference in the third paragraph that this number of "quick" transitions is constant over the rotational levels, and as the population of a given level becomes less, the percentage of unthermalized transitions increases. This interpretation, unfortunately, is not correct. The Pendleton et al. (1993) reference (and particularly the Polanyi reference therein) instead indicate that some high-lying rotational levels have populations in excess of what would be expected if they were thermalized with the translational energy field. These levels are populated in the highly exothermic hydroxyl formation process. However, they do not readily move to lower levels through the exchange rotational and translational energy due to the separations between adjacent levels being much greater than kT. They are therefore very poor at exchanging rotational and translational energy. This population of high-lying levels tends to represent the nascent population of OH, and it is the fact that the populations are higher than expected from Boltzmann collisional equilibrium that leads to non-LTE emission. A better measure of where one might expect this breakdown to occur would be to look at the separation between adjacent energy levels, and suspect those whose separation is greater than kT.
Revised the misinterpretation and added two pages to the discussion of un-thermalised behaviour (pages 39 and 40, two pages should therefore be added to the following comments) including examination of the separation between adjacent energy levels compared to the translational energy at various temperatures, as suggested (Figures 2-10, 2-11 and 2-12). Added the Polanyi and Woodall reference.

On page 42, in the discussion concerning the perhydroxyl reaction, the author may wish to present the relatively recent direct observation of these species in the atmosphere made by

Sandor and Clancy (1998, JGR 103, pp. 13337-13351) and Clancy et al. (1994, JGR 99, pp. 5465-5473).

Paragraph 3 on page 44 was modified to include the results in the references listed.

The discussion of OH quenching on pages 42 and 43 tends to focus on early, phenomenological quenching rates but ignores laboratory measurements. It should bring into the discussion the measurements of the SRI group (the various authors are Knutsen, Dyer and Copeland) that measure the quenching of v' = 8, 10 and 11 (1997, Journal of Chemical Physics 107,7809-7815), of v' = 7 (1996, JCP 104, 5798-5893), v' = 9 (1993, JCP 99, 5807-5811), and v' = 12 (1990, JCP 93,5741- 5746).

Paragraph 3 on page 47, and table 5-2 were added to discuss these laboratory measurements of quenching rates. Sappey and Copeland (1990), Chalamala and Copeland (1993), Knutsen et. al. (1996) and Dyer et. al. (1997) references were added.

On page 45, just under Equation 2-33, the author states: "In equilibrium, the rate of formation of ozone by 2-33 must balance its destruction in the hydrogen-ozone reaction (2-21)". However, the author started this section with: "During the day... ". In fact, during the day the dominant loss mechanism for ozone is photolysis (2- 32) and not 2-21. The statement should be modified to read: "During the night, the equilibrium rate of formation of ozone. ".

Modified statement as suggested (now on page 48).

In section 3.1, if the FPS room is important enough to mention, the author should spell out what FPS is.

The reference to the Fabry-Perot Spectrometer room was removed.

On page 62, the author should replace colloquialisms such as "way above" with "above" or "significantly more".

Changed term to "much higher".

On page 81, 3 lines from the bottom, the work "change" should be "changed", and in the next line "Consequent" should be "Consequently".

Corrected as advised.

On page 100, one may also wish to consider whether the diffusing screens in the source have a spectral characteristic. It is well known that diffusing screens made of "opal glass" diffuse well below 500 nm, but become increasingly transparent above that wavelength. Thus, the shorter wavelengths are scattered more effectively whilst the red end of the spectrum maintains more of a beam characteristic. This is less of a problem with ground glass, but is dependent upon the "gauge" of the grinding. The net effect is that the red end of the spectrum

may not be well diffused, and this will lead to the signal changing with the orientation of the LBS. Is there any sensitivity observed?

The diffusing screens in the source *are* likely to have some spectral characteristic, but this is accounted for in the calibration at NML. That is, the LBS is calibrated as it is used at Davis, the complete unit with the diffusing screens fixed in position in front of the bulb. No effect of the LBS orientation has been observed (it can be oriented at 0, 90, 180 and 270° on the instrument at Davis). The spectral characteristics of the screens separately can be tested during the next NML calibrations.

Another effect that can beset low brightness sources with a flat final diffusing screen is that of multiple reflections. This is particularly true if the side of the screen facing the instrument is not frosted. Light may then reflect off the slit mechanism surfaces, back to the diffuser, and off the diffuser back into the instrument. This will also lead to sensitivity in the orientation of the LBS, and sensitivity to the distance between the LBS and the spectrometer slits.

It would be good if you could comment on these effects in both your field calibration and laboratory calibration systems. That is, do you see these effects whilst attempting to calibrate the LBS at NML? Could these effects affect your field transfer calibrations? It would be an advantage to be able to state in the literature that no sensitivity to orientation or distance could be observed with the LBS.

A test for multiple reflections was carried out on the instrument at Davis on day 278, 1998. The LBS was positioned normal to, and then tilted slightly (~20°) relative to the optical axis. No change in the spectral response was observed.

A masking test, where all but a small portion of the front diffusing screen was masked off and compared to the full screen was also made on days 118-119, 1997. Again no significant difference in the (normalised) spectral response was observed.

These tests have not been preformed at NML, however the Davis system has much greater sensitivity, and is therefore the more appropriate place to test these effects.

I have added the sentence "No spectral response sensitivity to LBS orientation (diffusivity), off axis tilt (multiple reflections) or view area of the front diffusing screen (uniformity) was observed for these calibrations" on page 111.

I am afraid that section 3.6 needs some re-working. As written, it is confusing with regard to nomenclature being used inconsistently. For example, the abscissae in Figures 3-47 and 3-48 are labeled "Intensity (Counts/sec)". As an optical intensity has a specific meaning, and does not have this unit, this should be changed to either "Counting Rate (Counts/sec)", or "Response to source (Counts/sec)". The units then distinguish between and are consistent with your definitions of "response to source", "instrument response" and "source function"

defined at the top of page 110. It would also help to clarify things if you would give the units of these three parameters when you define them on page 110.

The abscissa in Figure 3-47 is relabelled "Response (counts/sec)". Figure 3-48 was labelled "Relative Intensity" and is relabelled "Normalised Response". Units have been added to the definitions of E(λ), R(λ) and I(λ) at the top of page (112). I was using the generic term of "intensity", meaning light brightness measured by the instrument rather than the specific SI quantities of "Radiant Intensity" [in Watts per steradian] or "Luminous Intensity" [in Lumen per Steradian].

On page 112 you begin to use the term "response factor", which is apparently your "response to source" defined on page 110. Again you should keep the terminology consistent, labeling the abscissae on figures 3-49 and 3-50 and table 3-12 as "Response to source (Counts/sec)" rather than "Normalised Intensity" and "Response Factor", respectively.

Response factor was introduced merely as a term to describe the evaluation of a response function at a particular wavelength (eg the P-branch lines). I.e. response function is a function of wavelength, response factor is a single value at a given wavelength. I have replaced the term with "Evaluation of R(λ)" where appropriate.

Figures 3-49 and 3-50 are <u>not</u> in units of Counts/sec as they have been normalised at $P_1(3)$. I.e. it is a ratio of the response function (in counts/sec) to the response at $P_1(3)$ (in counts/sec) thus it is a dimensionless quantity. I have changed the abscissa in each case to "Normalised Response".

By the time you reach section 3.6.5 and 3.6.6 your terminology has broken down completely. Your definition of "instrument response" on page 110 has become efficiency on page 116. Perhaps a more consistent terminology, which avoids the ambiguity of "system efficiency" used in a discussion of optics, would be "relative instrument response" and "absolute instrument response". Similarly the terms "spectral response" and "spectral response calibrations" on pages 114 and 115, respectively, are not defined.

Section 3.6.6 is an attempt to calculate how efficiently the instrument converts radiance seen at the input to counts per second out of the detector as a function of wavelength, and has units of Counts/sec/Rayleigh, whereas the previous measurements of the relative instrument response are dimensionless. I still think system efficiency is an appropriate term, especially as it is defined in this context in the first paragraph, and the units are given at the top of the second paragraph. Nevertheless, I have replaced system efficiency with absolute instrument response throughout section 3.6.6 as appropriate.

Spectral response and spectral response calibrations have been changed to instrument response and instrument response calibrations respectively in section 3.6.5.

Finally, I am not certain that constantly relating the errors in "response to source" to temperature uncertainty in K is all that enlightening. The section gives the impression that the primary calibration parameter is the response to source. However, your temperature calculations require the instrument response function. It is this function that you should be comparing. Whilst is interesting to note that the uncertainty is dominated by the measurement error of your "response to source" rather than that in your "source function", this should be expected as you integrated longer in obtaining your "source function". However, your total temperature error is due to the uncertainty in your "instrument response" function, and it is this uncertainty that must be propagated through your calculation of temperature in equation 4-8.

The relating of errors in the instrument response to an error in K (at about the mean winter mesopause temperature of 200K) was a suggestion of my supervisor to give a feel for the magnitude of the uncertainty in the final temperature result due to each component, and to allow a comparison with other sources of error.

I have attempted to maintain separation between the two components required to derive an instrument response I(λ), namely the calibrations carried out at NML (determination of the source function E(λ)) and the calibrations carried out at Davis (determination of the response to the source R(λ)). This was initially done as we could not get a consistent calibration of E(λ) (until Dec-99) at NML and the two components required for the instrument response were entered separately into the analysis program so they could be more easily modified.

Tables 3-8 and 3-13 compare the magnitudes of E(λ)) and R(λ) respectively. Errors from the two components are brought together in Table 3-14 so that a comparison of the magnitude of each error can be made. (Both are about the 0.2K level)

It is interesting to note that you have not included the instrument response in that equation, nor have you propagated that error in your determination of temperature uncertainty on page 145. The multiplicative nature of the instrument response will correlate counting and instrument response errors, which your sum-of -squares will not do. Thus, you must propagate your error calculation properly in equation 4-8 accounting for counting errors, background subtraction errors, and the combined errors of your source function and response to source that go into your instrument response function.

That is true, but there is more to it than that. Equation 4-8 shows only the error due to the counting statistics for each line (including a background and aurora contamination estimate). It does not show the subtraction of darks and the error in the darks estimate, the instrument response correction and its error, the Perspex response correction and its error, the estimate of $Q_1(5)$ under $P_1(2)$ and its error, the Λ-doubling correction and its error, or the error due to

the time taken to scan across the spectrum. All these must be included in the temperature and error calculation (and are dealt with in turn in section 4.3). Equation 4-8 would be horrendous if all of these terms were included. (see also later comments)

On page 122, in your first bullet on that page, you refer to back to section 3.5.5.3 to discuss the light scattering errors. You mention that the blackout curtain scattering does not alter the conclusions of this study, but the effect on the instrument response would appear to be of order 25% according to figure 3-37. However, as a result of the many measurements you made, I may have misunderstood exactly to which curve you are referring. If possible, you should refer to an exact figure/curve or state the error here.

The error due to scattering does not alter the conclusions of Chapter 4 which are listed in section 4.6. I have changed "conclusions of this study" to "conclusions of this chapter".

The scattering effect in the Jan-97 and Dec-97 NML calibration does result in temperatures too low by an average 1.1K and 1.4K at 200K respectively (see Table 3-8), or by 1.6K for the 1990 data. I have added the statement "(absolute temperatures ~1.6K too low)".

Figure 3-37 is the correct figure (added this reference). This figure shows the error over the 700-900 nm range. It does amount to 25% over this range, however the OH(6-2) range is only from 837.5-855.5 where the error is less than 2%.

The Jan-97 and Dec-97 calibrations were not used in further analysis (Chapters 5 and 6) but as the conclusions were not changed the values in chapter 4 were not changed so as to maintain consistency with the published paper. This is noted in section 4.7 (Improvements for subsequent analyses).

On page 130, you should state the units of H (i.e. cm^{-2}) and k (cm^2), as these are not SI quantities.

Units stated as advised.

At the bottom of page 139, the author should quantify the amount of contamination expected from starlight as well as from the NO+O+M -> NO_2 + hv continuum (Sivjee and Hamwey, 1987; Swenson et al, 1985, GRL 12, pp 97-100 and references therein).

Although Sivjee and Hamwey identify the "relative level of background light intensity over the wavelength range covered .." as a source of error in estimating emission intensities from Hydroxyl bands the contribution from starlight is not quantified in this paper and they do not mention the NO_2 continuum.

Swenson *et. al.* 1985 does deal with the NO_2 continuum associated with a ram effect on satellites and the space shuttle. It refers to measurements of "ram-glow" on the shuttle tail pod between 4000 and 8000Å. This glow, attributed to the NO_2 continuum shows a spectral peak around 7000Å. Extrapolation to 8400Å gives an intensity around 10% of the peak

value, but the radiant intensity of the emission in not quantified, let alone an atmospheric emission. The Fontijn *et. al.* (1964) and Paulsen *et. al.* (1970) references within Swenson *et. al.* (1985) that refer to measurements of the NO_2 spectrum are both laboratory experiments and are normalised in Swenson *et. al.* (1985) for comparison.

Chamberlain (1961) [p360] however, does quantify the combined atmospheric continuum and astronomical light emission intensity, peaking at ~6000Å at about 4R/Å. Taking 10% of this value yields less than 0.5R/Å for the 8400Å region, or approximately 1 count/sec using the absolute response calculation in section 3.6.6. This estimate has been added to the text on page 139 (now 141).

The author mentions on page 141 that the best-fit temperature for the auroral corrections was 500 K. This is quite high, as most authors see temperatures in the range of 250-300 K. Although this discrepancy was noted in the footnote on page 143, it is unclear whether auroral corrections were made using a temperature of 500 K or the 250-300 K temperatures. As the contribution to the OH is effectively an extrapolation of the band shape, and as the rotational temperature controls this shape, the temperature used would appear to make a great deal of difference. The author should clarify whether the corrections were made using the correct temperatures, or whether the combination of improper instrument response function and unphysical temperature produce the same band shape.

The problem with this early determination of the best fit for the combined N_2 theoretical profile was that it was made against an averaged spectrum from the 1990 data set (the analysis was developed on this data and is the basis for chapter 4). In 1990 the instrument did not contain a second order blocking filter so it was necessary to include second order N_2^+ 1NG and N_2 VK bands into the fitting. Unfortunately all these theoretical N_2 profiles were combined before the instrument response correction was applied, whereas the instrument response over λ400-430nm, should have been applied to the second order profiles. This error was detected during the analysis development for subsequent years where the blocking filter was included, thus no second-order profiles were included in the fit and 250-300K was an appropriate temperature for the fit.

The value of 500K has remained in this chapter to remain consisted with the published paper. The footnote is added in section 4.3.8 to identify the error. The second point in section 4.7 (Improvements for subsequent analyses) states that a temperature of 300K was used subsequently. I have added "A value of 300K is used for subsequent analyses" to the footnote.

On page 143 the author states that the OI line intensity is only weakly correlated with the nitrogen auroral emissions. However, Vallance-Jones (1974. Aurora. Reidel, Dordrecht) and Myrabo (1986. Planet. Space Sci. 34, pp. 1023-1029) list this emission as produced only

by electron bombardment and not produced in the nightglow. Why then would one expect it to be only weakly correlated with auroral emissions? (See note on section 4.5.2, below)

The difference in sampling time due to the time taken to scan across the region in 1990 (about 4 minutes between when the OI is sampled at 8446Å to the N_2 lines used at ~8524Å) is most likely why the OI and N_2 emissions are not well correlated.

However, as you also note in your comment on section 4.5.2, below, the OI produced quite effectively by dissociative excitation of molecular oxygen and the non-straightforward relationship between deposition altitude and the O/N2 emission ratio also contribute to the lack of correlation. I have added "(sample time lag, altitude difference and OI emissions produced through dissociative excitation of O_2 all contribute)" to that paragraph.

Also on page 143, the variable Neb in equation 4-7 is not defined.

Ne_b corrected to read $N.e_b$. I.e. N times the error in the background, where N is the width of the summing interval of the emission line.

On page 145 in equation 4-8, as has been mentioned earlier, the author has neglected the instrument response function and its associated uncertainty in the calculation of the temperature and its resulting uncertainty. As a result, the uncertainty estimate is incorrect and under-estimated. Since the instrument response function enters into the equation as a multiplicative factor to the line strength (or dividing the counting rate), its propagation in equation 4-8 should be calculated in a standard fashion. It is this final error that should be included in Table 4.8.

Equation 4-8 shows only the error due to counting statistics. Many corrections and errors that are applied to the data are not shown here (see earlier comment on equation 4-8) for simplicity (this is stated in the paragraph above equation 4-8, i.e. "after applying all the corrections discussed in section 4-3"). I have added specifically "error due to counting statistics" in the paragraph above equation 4-8 to help clarify this. The instrument response function is not neglected. Darks are removed prior to the (multiplicative) instrument and Perspex response corrections are applied to each point in each spectrum (as depicted in the flow diagram in Figure 4-8). Thus all counting estimates (lines, backgrounds and auroral estimate) have been corrected for these response functions. The error in the response correction (together with the other errors listed in Tables 4-7 and 4-8) is included in the individual spectra and average temperature errors in Tables 4-8 (for the expanded data set) and 4-7 (for the principle data set) as described in section 4.4.3.

In section 4.5.2 the author uses the OI 844.6 nm emission as indicative as electron impact on atomic oxygen, and goes on to state that its ratio with Ar should vary with incident electron energy as compared to the Ar ratio to nitrogen emissions. However, this oxygen emission is

also produced quite effectively by dissociative excitation of molecular oxygen (Hecht et al, 1991, JGR 96 P 5757-5776), which would have an altitude profile similar to that the molecular nitrogen emissions. Hence, it must be corrected for this component before it can be used to infer altitude. In addition, the O/N_2 ratio can be quite dynamic in aurora, and the effects of changes in this can dominate the variations in the oxygen to nitrogen emission ratio (Strickland et al., 1999, JGR 104, p. 33-44). That is, the relationship between deposition altitude and the ratio of 01 844.6 to molecular nitrogen is not straightforward. The author should correct this or make mention of the complicating behaviour of molecular oxygen components and the variation of 0 to N_2 in aurora.

The statement in section 4.5.2 only claims that these ratios are likely to be dependent on incident electron energy in that the more energetic, the more Ar is likely to be excited. The O excitation from O_2 dissociation would certainly complicate any attempt to extract the incident particle energy (or infer altitude). I have added "although this is not straightforward (O/N_2 ratio is quite dynamic in aurora (Strickland *et. al.*, 1999) and the O profile is complicated by O_2 dissociative excitation (Hecht *et. al.*, 1991))."

At the bottom of page 161 the author's statement makes it sound as if only the $\Delta v = 1$ sequence is disturbed by vibrational-rotational coupling. Although strong in this sequence, it occurs throughout the hydroxyl manifold. It is that coupling, combined with variations in the dipole moment function, that result in the differences between the Turnbull and Lowe, Langhoff and Mies transition probabilities. That is, if there were no vibrational-rotational coupling, one would not need to account for variations in the dipole moment function with inter-nuclear distance.

Altered sentence to read "Above the fundamental ($\Delta v=1$) sequence (which is strongly disturbed by vibrational-rotational coupling compared to the overtone transitions, $\Delta v>1$) the temperature variance from the choice of transition probabilities increases with Δv [T&L]."

It is unclear to what the last paragraph on page 162 is referring. Should there be a table reference?

This part of the introduction only describes what is covered in this chapter. I have inserted a forward reference "[see Table 5-8]".

Think that section 5.4 is rather confusing and could use substantial re-writing. I believe you should begin with an expanded section that describes what you are attempting to do. That is, the first, rather terse, single-sentence paragraph should be expanded, using equations to demonstrate your statements. I think this would clearly point the reader in the direction you are attempting to go, and would alleviate some of the semantic difficulties inherent in trying to describe a mathematical equation. For example, the second paragraph states: "If the

relative proportions of the upper state that decay via possible transitions differ depending upon. .. ". I find this statement to be very unclear.

I think this lack of clarity extends to page 178, where it is entirely unclear what was done to the data. How does the author "determine the fraction of the upper state that decays via each transition"? What is your normalization factor? That is, what are you dividing the P, Q and R branch intensities by to arrive at the numbers in Table 5-7? Once again, you should show an equation that details how you are going from your data to the numbers in the table. One can assume that you have summed the intensity of the P, Q, and R transitions with an estimate of the satellite transmission for each level to arrive at a normalizing factor. If so, then you should state this. Do you then repeat that procedure for each level, or do you use the nominalization factor determined from a particular level for all the rest? How, precisely, are the J=5.5 level numbers determined? That is, what are the trends and how did you determine the extrapolation?

Section 5.4 has been substantially re-written, including a more descriptive discussion on how the intensity ratios are converted to normalised transition probabilities that are comparable across different rotational levels. This discussion is supported by appropriate equations and an example calculation for J'=2.5 to derive the values in Table 5-7. More consistent terminology has been used throughout the section, particularly 'branch sums' is defined in the discussion and replaces 'J'-component sums' and variants and 'normalized transition probabilities', defined in equation 5-2 replaced 'fractions of the upper state that decay ..' and 'relative proportions of the upper state..' and variants. Figure 5-9 has been added to indicate how the J'=5.5 values were estimated. An additional half page summary has also been added to the conclusions in section 5.5. Two pages have been added to this section overall.

The statement concerning the Lübken results is slightly misleading. The Lübken (1999) results for the mesopause show no significant difference between the northern and southern hemispheres. They do, however, see a 7-8 K difference at the 82 km point late in summer.

Corrected paragraph to read "They found January mesopause (87 km) temperatures not statistically significant different to equivalent northern hemisphere July measurements, However the southern upper mesosphere temperatures (around 82 km) were 7-8 K warmer than northern hemisphere equivalents by the end of February."

On page 185, the Stegman results span 1991 through 1998, which represent both decreasing and increasing solar activity levels.

Altered sentence to read "between 1991 and 1998 (through solar minimum)"

On page 191, the author attempts to discard outliers. However, in doing so, there may well be biases introduced in the data. As the author points out, the winter season is characterized

by a strong correlation between radiance and temperature, and the standard deviation of low radiance nights will be greater. Hence, one is selecting higher temperatures through the selection of smaller standard deviations.

I was very aware of the potential of the selection criteria to introduce bias into the temperature averages, this is why the detailed examination of the effect of each selection criteria on the weighted mean temperature was undertaken in section 6.2. As I point out in the second last paragraph in the introduction of section 6.2 (page 189). "Values for the rejection limits were chosen by examination of weighted temperature and uncertainty against binned intervals of each particular criterion. Selection of criteria, and setting limits for them, is a somewhat arbitrary and iterative process. A lot depends on the subjective concept of what constitutes a 'bad' spectrum, which might bias the weighted mean ...".

The bias introduced by the standard deviation limit of 15K placed on the weighted average temperature from the 3 possible ratios is 0.04K in the 1998 data, with the other selection criteria applied. I consider the consistency of the three possibly temperatures derived from the line ratios is a good measure of the quality of the spectrum and this criteria is sufficiently wide to reject only those spectra where at least one line is badly contaminated.

I would not claim the association of radiance and temperature is strong, only that a positive relationship was found (see section 6.2.10). R-squared determination coefficients for Figure 6-16 are 0.10 for $P_1(2)$, 0.20 for $P_1(4)$ and 0.29 for $P_1(5)$. I.e. less than 30% of the variance in intensity is attributable to the weighted temperature.

Similarly, lower radiance may be associated with particular dynamical conditions, which will then be selectively eliminated in this process. The removal of outliers in this fashion, selecting only on standard deviation, risks eliminating a class of data when there is an underlying relationship. The danger lies in then using that selected data set to find trends in those same relationships. For example, in Figure 6-4 the standard deviation is plotted against the $P_1(4)$ intensity. However, the intensity of the $P_1(4)$ is itself a function of temperature. Here it would be better to use the integral of the lines rather than a single rotational line.

$P_1(4)$ in Figure 6-4 was replaced with integrated intensity as suggested.

I would suggest that the averages and trends be determined using all the data, but using an analysis whereby the individual points are weighted by their standard deviations. One may also wish to present the trends in this section first using the entire data set, and then using the selected data in order to demonstrate that the selection process did not create the trends. I certainly do not dispute the interpretations, but believe the author could make a better case for them by not eliminating data purely on the basis of standard deviation.

I have added section 6.3.3 "Weighted nightly means" and Figure 6.35 - which contains a comparison of the weighted nightly means calculated as suggested, with those calculated via the selection criteria for the 1998 data set (on which the data selection criteria were derived). Weighted nightly means are shown to be influenced by lunar phase as there is inadequate representation of background and Fraunhofer absorption in the standard deviation and counting errors (compared with the selection criteria means in section 6.2.6). As the winter means derived from selected and weighted nightly averages are within one standard error-in-the-mean and as the same selection criteria are applied to each year it is not considered that any bias is introduced that will affect the trend calculations.

Finally, I think you might be trying too hard to demonstrate that a cooling trend exists. You consistently ascribe an increasing solar activity trend to data sets that show increasing OH temperatures even though the data sets actually span both increasing and decreasing solar activity. The fact that a large solar cycle variation and a trend could conspire to give the weak solar cycle variation and no trend observed in your own data does not explain why the Sahai data sets (as well as others) show such a strong solar-cycle dependency. Presumably the same secular trends were at work when that data was acquired. I think a better question is, could these data sets, which span different solar cycles or parts of solar cycles, be combined with your own to unambiguously infer the strength of secular trends and solar cycle effects.

I appreciate the difficulty in making any assessment of long term trends in 8 years of data when there is an underlying 11-year solar cycle variation and individual years contain randomly distributed planetary scale variations of magnitude up to 30 K. Nevertheless I believe the calculation of winter average temperatures and their variation with respect to the average solar flux calculated over the same interval remains a valid comparison. I have added the multivariate (solar F10.7 and linear long term trend) analysis on pages 232-234 in order to quantify the statistical significance of the solar cycle and cooling trends obtained.

The statements referring to which part of the solar cycle is spanned by other observations have been corrected as per previous comments. The speculation about a larger magnitude solar cycle dependence coupled with a larger long term cooling trend conspiring to match the Golitsyn *et. al.* (1996) trend (pages 238 and 240) have been replaced with statements reflecting the statistical uncertainty derived for solar cycle dependence and linear trend from the (added) multivariate analysis in comparison with these observations.

The question of combining data sets is something that is very worthwhile and something that I have recently been invited to contribute to, in a review of Mesospheric temperature trends by the Mesospheric temperature trends assessment group (MTTA). Due for publication in Reviews of Geophysics later this year.

Referee 2

This is an outstanding thesis and I recommend that the candidate be awarded the PhD degree. It is a detailed experimental investigation of the determination of temperatures in the Antarctic mesosphere from observations of hydroxyl airglow emissions. The work is important primarily because the mesospheric temperature is regarded as a sensitive indicator of climate change and it is a difficult region to monitor other than through remote sensing from the ground or from satellites. The candidate gives a concise review of those aspects of the mesosphere important for his project, showing that he has a good knowledge of the relevant literature and is able to extract and summarise relevant material and ideas.

An essential aspect of monitoring climate change is the accumulation of accurate data over many years. Again this is particularly difficult when measuring mesospheric temperatures because the temperatures are low and the expected variations are small. Great care and attention to detail is needed to ensure that specific instruments provide accurate relative temperatures from hour to hour, day to day, and year to year. But to be of most value, accurate absolute values of temperature are needed and this requires extreme care and competence, especially for observation at high latitudes where auroral emissions so readily contaminate the measurements. The candidate has addressed these issues thoroughly and his work now sets the benchmark for others to reach.

The observing instrument used in the study is a scanning spectrometer. Spectroscopy is a well- developed area of physics in which exciting and important new developments continue to occur. Even the well-established areas of theory and experiment have subtleties that can easily escape the unwary so it is only the very best students who are able to show convincingly that they have a good, comprehensive understanding of both the theory of spectroscopy and the details of spectrometer design, operation and calibration. The candidate has shown that he has a thorough understanding of the theory and experimental techniques. His discussion of spectroscopic theory is very clear and concise, much better and more informative than many textbooks! His discussion of instrumental features and operation are a model for other students, particularly as it shows the importance of accounting for various instrumental effects which invariably occur with spectrometers.

The most impressive aspect of this thesis overall is the attention to important details, particularly in evaluating the performance of the main instrument used, striving to obtain reliable absolute calibration, and dealing with auroral contamination. The level to which each of these has been addressed shows a desire and a tenacity to achieve the very best and not be satisfied with the "status quo". An example of this is the investigation of the

calibration procedures used by the National Measurement Laboratory. Many others students would have accepted the NML calibrations without much questioning because they were provided by "the experts".

Mesospheric temperatures obtained over several years have been analysed carefully, compared with the best model available, and compared with measurements obtained by others. Agreements and disagreements with models and other measurements are identified and discussed. The need for ongoing measurements to monitor climate change is stressed. Several papers have already been published on this work and it is already gaining recognition as being a leading contribution to the study of mesospheric temperatures.

The presentation of the thesis is excellent as the candidate has taken advantage of modem "desktop" publishing techniques. There are, inevitably, some typos and I have listed the few I noticed.

p Contents i: 5^{th} *last line replace "appropriated" with "appropriate"*

p Contents ii: 8^{th} *last line replace "(-0.65 K/day)" with "(-0.65 K/day"*

p2: 2^{nd} *last line (and possibly elsewhere), replace "Earths" with "Earth's"*

p27: 7^{th} *last line replace "hydrogen like" with "hydrogen-like",*

p30: 7^{th} *line replace "pared" with "paired"'*

p31: 8^{th} *line replace "its" with "their"*

p32: 8^{th} *line (and possibly elsewhere), replace "Planks" with "Planck's"'*

p33: 10^{th} *line replace "its" with "their",*

6^{th} *last line replace "expresses" with "expressed".*

p36: 20^{th} *line replace "molecules" with "molecule's".*

p77: Figure 3-26. Units need to be specified on vertical scales

p78: Figure 3-27. Units need to be specified on horizontal scale

p79: Figure 3-28. Units need to be specified on horizontal scale

p81: 9^{th} *last line, replace "at covering the spectrometers" with "covering the spectrometer's"*

2^{nd} *last line, replace "Consequence" with "Consequently"*

Last line. Full stop required at end of sentence.

P83: 2^{nd} *last sentence reads awkwardly. I suggest "...calibrations for the limited wavelength range below λ660 nm over which they can be compared.".*

pl00: 5^{th} *last line, replace "Full" with "full".*

pl04: 4^{th} *line, replace "differences ...has" with "differences ... have"*

p117: 2nd last line, insert "by" or "with" in "maintained reference".

p122: 4^{th} *line, replace "ghosts" with "ghost"*

p123: *3rd and 11th lines, degree sign needed after "18"*

p125: *3rd last line, "[pp 126-]" needs second page number*

p144: *2nd last line, change to read "...E and F in Table 4-6 show"*

Each of these typographical errors or axis labels have been corrected as advised.

P180: *2nd dot point should read "...but the differences are on the borderline of significance"*

Note that on p175 5th last line it is stated that "...R_l/P_l ratios are not significantly different from LWR values". This is not strictly correct according to Table 5-4. The dot point in the conclusion is a more accurate statement. You should modify the statement on p175 accordingly.

Modified both the dot point and paragraph on p175. The point to be made is "Measured R_l/P_l ratios are also significantly lower than those derived from T&L and Mies, and lower, but within about twice the error of the LWR values."